Imperial College

Characterisation of Adherent Microbubbles for Molecular Targeted Ultrasound

A thesis submitted to Imperial College London for the degree of Doctor of Philosophy

Jonathan Philip Casey

Imperial College London,

Imaged Sciences Department

10/31/2013

Declaration of Originality

All work is original and that of the author, except where noted. Where concepts, figures or other information have come from external source they have been referenced. All outside works referred to are listed in Chapter 8

- Jonathan Casey

i. Abstract

Molecular imaging is a field of medicine which can offer great potential for both diagnostic and therapeutic purposes. Within this field contrast enhanced ultrasound displays the possibility of making molecular imaging a cost effective viable tool in an increasingly diverse set of clinical situations. One of the current challenges associated with this technique is how one differentiates the signal for adherent microbubbles from those produced by the bulk non-adherent population.

The first part of this thesis acoustically examines the response of single microbubbles under the effects of adhesion and compares the response observed with that of the MBs non-adherent counterpart. It was found experimentally that differences could be observed in both the 2nd harmonic signals generation and in the stability over repeated exposure. These differences could be utilised as the basis for discretisation imaging strategies.

The second section of this thesis attempts to characterize these differences in terms of current theoretical models. A more comprehensive modelling strategy is utilised for the fitting of increasingly complex theoretical models. Good agreement was found with the outputs of this fitting procedure with previously reported parameters. Further detail could also be observed in the form of various size/resonance effects which have not previously been reported. There was little observed difference between the parameters extracted for the adherent and non-adherent MBs although it was suggested that the effective elasticity of an adherent MB could be elevated in comparison to its non-adherent counterpart in the region of resonance. Efforts will be required to control and account for some of the variability observed in MB response before this can be stated definitively however.

ii. Acknowledgement

There are numerous people who I have to thank for their support over the years which have made this work possible.

Firstly, a heartfelt thanks to my supervisors Rob Eckersley and Mengxing Tang for their support and belief in my ability to achieve this. It has been an interesting and (believe it or not!) enjoyable time being part of the group. The chance to bounce ideas around and get into heated discussions in meetings has been entertaining and your help and support has been invaluable, Cheers.

Many friends have helped me over the years, typically this help came in liquid form at a very reasonable price from the union but without it I think I'd have probably lost my mind somewhere along the way (The jury is still out as to whether this is actually true anyway!) Special mentions to Ryan and Lukasz for the many BBQs, Emma for being my drinking partner in crime, Kirsten and Richard for enduring the fun of Hammersmith hospital and making life bearable there, Duncan, my older brother for getting me into this mess in the first place (I blame you for everything!) and Dan for brightening my otherwise boring day with tales of your latest shenanigans. You've all helped make this a reality so thank you.

The last thanks goes to my parents, none of this would have been possible your continued support. Not content with one layabout son refusing to enter the real world you willingly encouraged and supported me in the same endeavour, I cannot thank you enough - if you're lucky I may even become a functioning member of society now*.

*I wouldn't hold your breath!

iii. Table of Contents

a. Abbreviations

AM	Amplitude modulation
AWG	Arbitrary waveform generator
CTR	Contrast tissue ratio
MB	Microbubble
MI	Mechanical index
PE	Pulse-Echo
PI	Pulse inversion
PNP	Peak negative pressure
PRF	Pulse repetition frequency
RP	Rayleigh-Plesset
SH	Sub-harmonic
SNR	Signal to noise ration
STD	Standard difference
STP	Standard temperature and pressure
UCA	Ultrasound contrast agent
US	Ultrasound

b. List of figures

c. List of Tables

1 Introduction

1.1 Background

Molecular imaging is the visualisation of biochemical events at the cellular or molecular level using non-invasive imaging techniques [1]. A number of pathologies express molecular markers to regulate certain processes during the pathology progression. Detection of these bio-markers can lead to an early diagnosis and therefore earlier treatment and as such in an area of intense study.

Pathologies such as atherosclerosis [2], cancer detection [3]–[5], Alzheimer's [6] and cardio-vascular disease [7] are all examples of current targets, the imaging of which often lies with the development of probes capable of targeting bio-markers such as inflammation [8], angiogenesis [9] or cell adhesion molecules [10].

In addition to the imaging and diagnosis of pathologies, molecular imaging also offers a great deal of potential in therapeutics [11]–[13]. It does this by two methods: firstly, if one can incorporate a therapeutic molecule into the targeting probe, then site-specific drug or gene delivery can be achieved. This can have the twin impact of reducing the required dosage of a treatment whilst ensuring that the therapy is delivered precisely to the point at which it is required [14], [15].

The second potential for targeted imaging for therapeutics is in the field of drug discovery. By attaching a targeting probe to certain parts of a drug candidate, it is then possible to track the progression of a drug - more importantly, the metabolites of a drug - as it passes through and interacts with the system [16], [17].

To develop a targeting probe for successful in vivo application, a number of criteria have to be fulfilled [1], [18]:

- They must have a high affinity for the target site and good pharmacodynamics. That is, the probe must specifically bind to a target area whilst not being expelled from the system too rapidly, preventing imaging, and simultaneously not disrupting the system adversely in terms of toxicity or immune response.
- Must be able to overcome the physical/chemical barriers to adhesion, be it high blood flow/shear rate, or the ability to cross membranes (i.e. cell membranes, blood brain barrier).

- The probe must be able to be attached to an imaging label or contrast agent capable of being imaged, preferably with high sensitivity, rapidly and in high resolution.
- The signal from the probe when bound to the target sight must be able to be differentiated from the background image, noise and response from unbound probes.

Typical targeting probes make use of either simple small molecule interactions i.e. peptides, enzyme substrates, or larger, more complex interactions such as antibody-antigen or protein interactions. Once a likely targeting probe has been identified, it needs to be incorporated into a contrast agent [19].

The choice of contrast agent depends on the imaging modality being used. Currently one of the most commonly used imaging modalities for molecular imaging is the radio tracing techniques of PET (positron emission tomography) [20]. This technique works by the incorporation of a radioactive atom into the structure of the imaging probe itself. This atom then decays via positron emission. When the positron encounters an electron the particles annihilate and two gamma waves are created, which travel 180° apart from each other. By detecting the gamma waves from multiple annihilation events, the position of the radio tracer can be determined. This technique is highly sensitive, requiring only pico-Mole concentrations of tracer [20], making it ideal for purposes such as drug discovering [21].

There are a number of drawbacks associated with PET for molecular imaging though. The radio tracers typically have a half-life of 20–120 minutes (Carbon^{11} and Fluorine^{18} being the most commonly used). This means that a cyclotron and rapid synthesis are required to produce the tracer with enough time for imaging. The imaging itself requires a large and expensive scanner to detect the annihilation events, and even then a resolution of the order of 3mm is typical [22]. Scan time is also an issue, taking tens of minutes to complete, and the processing of data needs to be conducted offline, meaning that real-time scanning is not viable.

These are some of the issues facing the gold standard in vivo molecular imaging technique. However, other molecular imaging techniques such as single photon-emission computed tomography (SPECT), magnetic resonance imaging (MRI) and magnetic resonance spectroscopy (MRS), each have their own specific issues. These include the high cost of the equipment used and the additional expense of ancillary services, the immobility of the equipment, and the time taken for a scan – of the order of minutes to hours – all of which inhibit the applicability of molecular imaging.

(Pysz et al. [19] provides a comprehensive review of the available imaging modalities and their relative merits; however, for brevity this will not be covered here.

1.2 Potential of Ultrasound Imaging

1.2.1 Overview

Ultrasound (US) scanning is one of the most prevalent imaging modalities in use today. It provides a quick and low-cost way of non-invasively observing internal structures. Further to its well-known uses in obstetrics, US is also used in the examination and diagnosis of problems pertaining to blood perfusion [23], [24], tumours/lesions [25], [26] and glandular defects (e.g. thyroid, prostate) [27], [28]. In addition, US is also used as a guide for surgery in procedures such as the placement of needles for biopsies and fluid extraction [29]

Even in their earliest incarnations, US scanning units were relatively small in comparison to other imaging modality machines. With the increasing advances in computer processor power, units are becoming commonly attached to laptops or as small standalone units, further diversifying US applications as a portable diagnosis unit. When compared to other imaging modalities – namely PET/SPECT, MRI, and CT/X-ray – in terms of, cost, ease of use and scanning time, it is easy to see the advantages of US. Furthermore US provides enhanced resolution in comparison to PET/SPECT with the additional advantage of not requiring ionising radiation. (please refer to [19] for a full comparison of the imaging modalities).

Where US falls behind the other imaging modalities is in the level of contrast and hence the level of discernable features/detail of images. To improve on this, the field of US contrast agents (UCAs) has been widely investigated since their initial postulation. This came after the discovery by Gramiak et al. [30] that it was possible to detect the presence of bubbles in the bloodstream, after an increase in contrast was noted in the right ventricle following an agitated saline injection.

For the duration of this thesis, when discussing UCAs, this can be taken as synonymous with microbubbles (MBs), the most common form of UCA (cf. Section 2.3). Initial approaches into developing UCAs had little understanding of the physical makeup of a good UCA [31]; however, this is being rectified with intensive study both in academia and by companies with a vested interest in producing the benchmark UCA.

Current research is being utilized to probe the physico-chemical characteristics of UCAs using both experimental (cf. Section 3.2) and now increasingly computational methods (cf. Section 2.5 and Chapter 6) in order to determine the ideal parameters of an UCA [32]–[34]. More recently, efforts have been made to selectively target UCA on areas of interest for the purpose of enhanced

imaging for functional molecular scanning, as well as drug and gene delivery [11], [35]. Chapter 2 will explore the current standing of this research in greater detail and show the directions of current study.

1.2.2 **Molecular Targeting**

In addition to the low cost, mobility and fast acquisition times inherent to US, contrast-enhanced ultrasound has a number of additional benefits concerning targeted imagery. MBs' surface architecture is easily modified to incorporate targeting probes (cf. Section 2.4.3). Spatial resolution can be attained similar to that of MRI (for high frequency and/or near field applications) and is considerably higher than that attainable with PET, whilst having sufficient sensitivity to detect the response from single MBs.

There are a number of associated disadvantages as well. MBs by their nature are restricted targets within the vasculature system (cf. Section 2.3) and as such any molecular expression has to be present on the endothelium (cf. Section 2.4.3). Similarly, due to the nature of US scanning, whole body scans are unfeasible and imaging of the lungs or brain is problematic (cf. Section 2.2).

With particular reference to molecular imaging, there are two standout issues that need to be addressed when using contrast-enhanced US. The first is how one ensures that a MB can become – and more importantly, remains – adherent to a target site. The targeting probes used for MBs are essentially the same as used for other imaging modalities i.e. peptides, anti-bodies, proteins. However, the contrast agent they are expected to label is approximately 3 orders of magnitude larger in physical size; for example, (F^{18})fluorodeoxyglucose (a commonly used radiotracer in PET imaging) has a diameter ≈ $1x10^{-9}$ m, whereas a typical MB has a diameter ≈ $3x10^{-6}$ m. This increase in size means that the forces the binding ligands are expected to cope with are vastly different.

Limited to the vasculature as MBs are, this means that overcoming forces due to blood flow and shear rates, as well as buoyancy start becoming a significant issue, particularly in the larger vasculature. Methods for increasing the binding affinity and increasing the attachment rate are covered in Sections 2.4.3 and 2.6, respectively.

The second issue with contrast-enhanced US for molecular imaging, and the main focus for this thesis, is how one differentiates and discriminates between the signals produced from adherent MBs compared with those freely circulating. US imaging is sensitive to the response from a single MB [36]; however, in the course of usual imaging, something of the order of 10^9 MBs are injected. When

this is coupled with the issues with binding rates it results in comparatively low concentrations of adherent MBs in the presence of a large concentration of freely circulating contrast agent.

Current methods used to separate these signals either rely on the differential clearance time from the body of adherent and non-adherent MBs [37], or by using a combination of filtering techniques [38]. These will be fully discussed in Section 2.7.

1.3 Aims and Objectives of this Thesis

There is growing evidence to suggest that the boundary conditions imposed by adhesion (i.e. proximity to a boundary surface and the functionalization of the MB surface) bring about changes in radial dynamic response of MBs [39]–[42]. These changes are predominantly attributed to the presence of a boundary.

The actual process of adhesion on the dynamics of MBs has not been thoroughly explored. One of the few examples of this type of investigation suggests that there could be changes in the magnitude and frequency content of the MB response [43]; however, this is a purely optical study and the acoustic verification of this has not been presented.

The working hypothesis for this thesis was that MB adherence alters the acoustic signal generated by a MB in response to US insonation and that this difference can be acoustically observed and discretised. As such, any observed difference could then form the basis of an improved molecular imaging method using US.

The specific aims of this thesis were to:

- *Create a method for the reproducible examination of MBs under tightly controlled conditions.*
- *Examine MBs under a variety of boundary conditions to observe the effect of adhesion on the acoustic emission from MB under US insonation.*
- *Highlight any secondary phenomena that occur as a function of MB adherence.*
- *Account for any observed differences in terms of the fundamental physics of the situation and suggest methods for their exploitation in the differentiation of adherent MB signals in a clinical setting.*

1.4 Guide to Thesis

Chapter 2: Bubble Theory

In this chapter, a broad overview of ultrasound Imaging, contrast agents and imaging is presented. This describes from first principles the different factors that affect US imaging and the way in which ultrasound contrast agents provide improvement to the quality and applicability of US. The constituent components of a MB are examined and their effect on the MB dynamics is described in terms of the most prevalent theoretical models. The evolution of these models in complexity is explained, with reference to the observed phenomena they represent and the methods by which physical meaning is attached to the model parameters. In addition, secondary considerations concerning the dynamics of MBs, such as boundary conditions and radiation forces, are also discussed. Lastly, the implications that these effects have on imaging strategies is covered, including the effects brought about by targeted MBs for molecular imaging purposes.

Chapter 3: Materials and Methods

This chapter describes the experimental methods available for the interrogation of MB characteristics, along with the associated benefits and drawbacks of each approach. This culminates in the rationale behind focussing on the acoustic characterisation of single MBs.

Following this, the experimental setup devised for the conduction of single bubble acoustic characterisation experiments is presented. This constitutes methods for the insonation of a MB, the recording of the scattered response, and optical sizing of the MB. For validation purposes, a well-documented, commercially available MB (SonoVue, Bracco Diagnostics Inc., Geneva) is characterised, and the results are presented in conjunction with those from literature. Good agreement is achieved between the result from this study, previously reported data and the associated theory. Furthermore, this study served as a method to highlight areas of improvement in terms of pulse design and setup to ensure the maximum potential data could be extracted from subsequent studies.

Aspects of this work, particularly that of Sections 3.4 and 3.5 were presented at the IPEM, Physics & Technology of Medical Ultrasound conference, 2011, York, UK under the title "*Acoustic Characterisation of Single Ultrasound Contrast Agents: Applications in targeted imaging and therapy.*"

Chapter 4: Single Bubble Acoustic Characterisation and Stability Measurement of Adherent Microbubbles*

In this chapter, the modification of the surface of MBs with functional ligands for targeting purposes is examined, in terms of the effect adhesion it has on MB dynamics. In-house produced MBs were utilised that had the ability to incorporate binding ligands on their surface. The Biotin – Streptavidin ligand pair was used for targeting. Specifically, this chapter examines changes in the fundamental and 2nd harmonic frequency bands, allowing for resonance frequencies to be extracted. The stability of MB response to repeated insonation and the shape of the time-domain envelope were also examined.

There was little difference observed between the control, functionalized and adherent MBs in terms of the fundamental scattering properties. Examination of the 2nd harmonic showed that there was a change in the MB radius of peak 2nd harmonic generation, indicating an increase in the resonance frequency of approximately 19% (when normalized against the resonance frequency of an unencapsulated MB of the same size) due to adherence.

MB stability was seen to be closely tied with MB resonance with significant signal loss occurring for resonant MBs. The change in resonance size between the adherent and non-adherent MB cases was also observed in this stability data. The shape of MB response was also tied with resonance. MB at resonance showed a distinct trend to behave in a compression-dominated manner. No distinction could be made between the adherent and non-adherent MBs in terms of response asymmetry.

*Adapted from [44] *Single Bubble Acoustic Characterisation and Stability Measurement of Adherent Microbubbles,* accepted for publication in Ultrasound in Medicine and Biology 2013 May; 39(5):903-14.

This work was also presented at The IEEE International Ultrasonics Symposium, 2011. Orlando, FL under the title "*Single Bubble Acoustic Characterisation and Stability Measurement of Adherent Microbubbles*"**.**

Further aspects were also presented at The 17th European Symposium on Ultrasound Contrast Imaging, 2012. Rotterdam, NL under the title "*Size dependant asymmetrical microbubble response*"**.**

Chapter 5: Sub-Harmonic Characterisation of Adherent Microbubbles

This chapter continues the characterisation of the in-house development MBs as used in Chapter 4 by examining the sub-harmonic (SH) scattering regime. The characterisation was performed using a similar insonation pulse to that used in Chapter 4, albeit at a higher insonation pressure due to experimental constraints. It was hypothesised that the use of SH could provide a method to better differentiate between adherent and non-adherent MBs, based on the shift in resonance frequency observed in Chapter 4.

SH signals were shown to be produced for all MB test cases (i.e. functionalized, adherent etc.). These SH were most prevalent in a narrow size and frequency region. This region was found in the radial size region of 2.2–3.4μm and frequency range 0.8–1.4 MHz. This corresponds well with the literature prediction of the region for peak SH signal generation. Between the adherent and non-adherent test cases there was no observed statistical difference in these scattering regions. One of the possible reasons for this non-observance could be the high degree of variability of response that was present throughout the experimental sections of this thesis.

This work was presented at The IEEE International Ultrasonics Symposium, 2012. Dresden, Germany. Under the title "*Sub-Harmonic Characterisation of Single Adherent Microbubbles***".**

In addition aspects of the work were also presented at the Microbubble Symposium: Fabrication, Characterisation and Translational Applications, 2012. Leeds, UK. Under the title *"Single Bubble Sub-harmonic Characterisation of Lipid Shelled Microbubbles: Effect of Functionalization and Adherence."*

Chapter 6: Computational Modelling

In this chapter, numerical models are used to provide some theoretical underpinning to the observed experimental effects. The choice of model used can have a significant impact on the behaviour exhibited in simulation and a number of models have been developed with specific applications in mind. As such, a number of models are explored here; these range from simple linear models used for small amplitude oscillation through to the incorporation of non-linear shell properties and the inclusion of boundary effects.

These models are parameterised using the experimentally gathered data in the preceding chapters. The method used for this parameterisation is a new approach that does away with many of the assumptions used in other characterisation studies. As such, it is able to provide a detailed

view of how the parameters change to accommodate observed phenomena as well as illustrating the interdependence between the parameters.

Shell properties such as “strain-softening” and “shear-thinning” are observed and accounted for, as well as a resonance dependence on parameters such as the surface tension at break-up and buckling radius. Using the derived parameters, the experimental results from the preceding chapters can be recreated. The effect of adhesion is explored in terms of changing model parameters.

Chapter 7: Discussion and conclusions

This chapter summarises the key findings of this thesis and their implications to the field. A number of improvements are suggested, along with some possible avenues for the progression of this work. This culminates in a final conclusion for the thesis.

2 Bubble Theory

2.1 Abstract

In this chapter the background theory of US and contrast enhanced imaging is presented. The composition of MBs is explained and the function of each constituent part is described. The theoretical models used to describe MB have developed alongside the advancement in the technology and practices used in their study. This progression is outlined and the key theoretical models applicable to this study are highlighted along with methods of their implementation and limitations.

Secondary effects brought about by experimental conditions are covered with their possible implications for experimental design and for applications in real world function. Lastly current clinical imaging strategies are discussed along with those specific for molecular imaging.

2.2 Principles of Ultrasound

Ultrasound (US) works by directing high frequency (typically in the MHz range) sound pulses through a medium (in this instance the body) and the detection of subsequent reflected/scattered echoes created as the pulses pass from one medium to another of differing physical properties.

The reflections and scattering of the pulses are produced as the wave fronts encounter a boundary between different physical properties; for example, density (ρ) or compressibility. This change in material property results in a variation in the speed of sound of the medium and consequently a change in the acoustic impedance (Z), given by Equation 2-1, where c is the speed of sound in the medium.

$$Z = \rho c$$

Equation 2-1

The energy of the reflected (E_R) and transmitted (E_T) waves due to the boundary is then given by Equation 2-2 and Equation 2-3 where the subscripts 0 and 1 refer to the first and second mediums the wave passes through (this is the idealized case where there are no losses e.g. thermal losses etc.):

$$E_R = \left(\frac{Z_1 - Z_0}{Z_1 + Z_0}\right)^2$$

Equation 2-2

$$E_T = 1 - E_R$$

Equation 2-3

In accordance with these relationships, it is evident that the larger the difference in impedance between the two media, the larger the echo produced. This causes some problems for US when the wave encounters a medium of vastly different density/compressibility i.e. solid or gas as found in bone or the lungs, respectively. For the case of bone for example, with acoustic impedances of 1.69 kg/(s.m^2) and 5.32 kg/(s.m^2) as found in muscle fibre and bone respectively [45] one finds that approximately 52% of the incident energy is reflected and 48% of the energy is

transmitted. The same process occurs on the back surface of the bone as the transmitted sound propagates back into the tissue. In this instance 27% of the energy is reflected back into the bone leaving only 35% of the original signal intensity to propagate beyond the bone. The reflected signal from structures on the far side of a bone barrier will undergo the same reduction in intensity on the return journey to the transducer resulting in very low signal from those structures and subsequent artefacts known as shadowing. Figure 2-1 below shows an example of an US image through the chest cavity [46]. The structures seen at the top of the image are the subcutaneous layers of skin, fat and muscle. The ribs are numbered 1 and the shadowing artefacts they produce are labelled 2. One can also see that as depth increases the intensity and contrast achieved is dramatically diminished.

Figure 2-1: Rib shadowing artefacts produced by the acoustic impedance mismatch of tissue and bone in the imaging of the chest cavity. Figure reproduced from [46]

Conversely one can see that if the impedance of the two media is similar then most of the wave energy will be transmitted through, resulting in a low echo response. When this is examined with reference to Table 2-1, one can observe that the majority of tissue in the body has very similar impedance. This almost uniformity of tissue allows for a near constant speed of sound to be estimated and allows for depth information to be reliably obtained (as a time of flight measurement). The near uniformity also allows for good depth penetration to be achieved and reduces artefacts due to signal reverberation.

The attainable (axial) resolution of US systems is limited by the spatial pulse length (spatial pulse length is the product of the wavelength and the number of cycles). As a rough rule of thumb the smallest axially resolvable object is limited to half the spatial pulse length. A typical imaging pulse contains two or three cycles. Clinical US typically operates at frequencies of up to 15 MHz, although in certain cases, for example ophthalmic examination, frequencies of up to and exceeding 50 MHz have been utilized. Taking an example of a 2-cycle imaging pulse and using the relationship expressed in Equation 2-4. Where c is the speed of sound; taken as approximately 1540 ms^{-1} for soft tissue in the body, (Table 2-1 provides examples of the observed speed of sound in different media), f is the frequency of the US pulse and λ is the associated wavelength. This gives a limit of resolvable objects of approximately 100 μm at 15 MHz and 30 μm at 50 MHz. In reality, the actual resolution limit is comprised of many other factors and varies depending on transducer aperture, focal length, pulse length, depth and frequency. Reference [47] provides a good overview of these factors and their effect on the attainable resolution.

$$c = f\lambda$$

Equation 2-4

It has been shown that very high spatial resolution can be obtained by the application of very high frequency ranges; however, there is a trade-off associated with such high frequencies. As the frequency is increased the signal attenuates at an increased rate (see Equation 2-5, where $\propto$ is the attenuation factor for the medium given in $dBcm^{-1}MHz^{-1}$, L is the distance in cm through the medium, and f is the US pulse frequency in MHz) In fact the attenuation coefficient increases as a function of the square of the frequency however most attenuation coefficients are given at a specific frequency, in Table 2-1 these are given at a 1 MHz transmit frequency. This increase in attenuation is because waves of higher frequency have a smaller wavelength and are more likely to interact with the medium and hence dissipate their energy as scattering or heating. Imaging depth can be seen to be inversely proportional to frequency, consequently there has to be some concessions made between depth penetration and resolution depending on the situation and organ to be examined [31]: for organs such as the liver, the typical range of US used is around 2-5MHz, whereas as earlier stated, ophthalmic uses can use frequencies up to 50MHz due to the small nature of the area of study and the shallow depth penetration needed.

$$Attenuation\ (dB) = \propto L\ f$$

Equation 2-5

Some typical examples of attenuation factors are given in Table 2-1.

Material	Speed of Sound (m/s)	Acoustic Impedance (Rayl*10^{-6})	Attenuation (dB/cm*MHz) @ 1MHz
Air	330	0.0004	1.64[+]
Water	1480	1.48	0.0022
Blood	1584	1.61	0.20
Liver	1595	1.65	0.50
Kidney	1560	1.62	1
Fat	1478	1.38	0.48
Brain	1560	—	0.60
Average Human Soft Tissue	1540	1.63	0.54
Bone	4080	7.8	20

Table 2-1: Speed of sound, impedance and attenuation for body tissues [48], [49]**. Attenuation values given for a 1 MHz transmit frequency. [+] value for air taken at 20°C and 60% relative humidity** [50]**. 1 Rayl =1 Pa.s/m**

2.3 Ultrasound Contrast Agents Overview

The role of contrast agents will be briefly discussed here before a full exploration of their properties in Chapter 2. US contrast agents (UCAs) enhance the magnitude of received echo and thereby improve the contrast of an image, allowing for smaller structures to be observed. This contrast is achieved by the introduction of microbubbles (MBs) of gas into the bloodstream. Other contrast media do exist, such as liquid nano-droplets [51], [52] (upon insonation, these droplets undergo phase transition into a gas and subsequently act as MBs of gas. As such, the main body of work will principally focus solely on the behaviour of MBs). These bubbles have markedly different acoustic impedance than the surrounding medium (blood/tissue); thus, one can see that by applying Equation 2-2 the reflected sound energy from the bubble will be significantly enhanced compared with the surrounding tissue.

For a UCA to be effective it must fulfil a number of criteria. They must be able to enter and persist in the bloodstream for long enough to allow for the bubbles to reach the site of interest and imaging to take place; this itself introduces a number of factors. The size of the MB has to be such that it can pass through all parts of the vascular system, and as such is limited by capillary diameter. Therefore, making them comparable in size to red blood cells (≤8μm) is the obvious solution. If the MBs were to be larger, they would run the risk of becoming lodged somewhere in the system, possibly resulting in an embolism. Another benefit to this size range is that at typical clinical US frequencies (1–7 MHz), this size range of MB experiences resonance, thereby increasing their response to US. Additionally, care should be taken to ensure that once introduced the MBs do not aggregate in the system, which could also result in the aforementioned situation.

The UCA must also be highly echogenic. This ensures that low volumes of MBs are required; a desirable trait for a number of reasons. As earlier stated, when discussing the reflection and transmission of US signals, pockets of gas create virtual barriers to the further transmission of US waves. By the same token, a high density of UCA in one area also constitutes an area of high attenuation. This is shown in Figure 2-2 by the steadily decreasing depth penetration of the US as the MB concentration increases.

Another reason for keeping the quantity of contrast agent low is so that the introduction does not result in a perturbation of the system from the norm, either in the form of toxicity – the agent used should be as non-harmful as possible but using very low doses reduces this risk – or changes in blood perfusion or organ function as a result of the UCA being present. This also applies to the pathways of excretion for the agents: it is not permissible for the contrast agent to become irreversibly bound in the system, so the body must be able to metabolize the agent away. Either the metabolites must also be bio-compatible, or the body must be able to excrete the agents out by some other path e.g. exhalation.

Other desirable characteristics for MBs include the ease of preparation of the bubbles – there is little point in having a highly versatile and portable US unit if it requires a full laboratory to produce a contrast agent that needs to be administered within a short time scale, as is the case of positron emission tomography (PET) imaging. Further to this, the effective shelf-life for created bubbles needs to be considered, ideally the agents will have a long shelf-life under standard temperature and pressure (STP) conditions, eliminating the need for specialized storage. Whilst in a hospital setting these demands are easily met if required this is not the case in more remote or rural settings where US could provide a vital diagnostic tool.

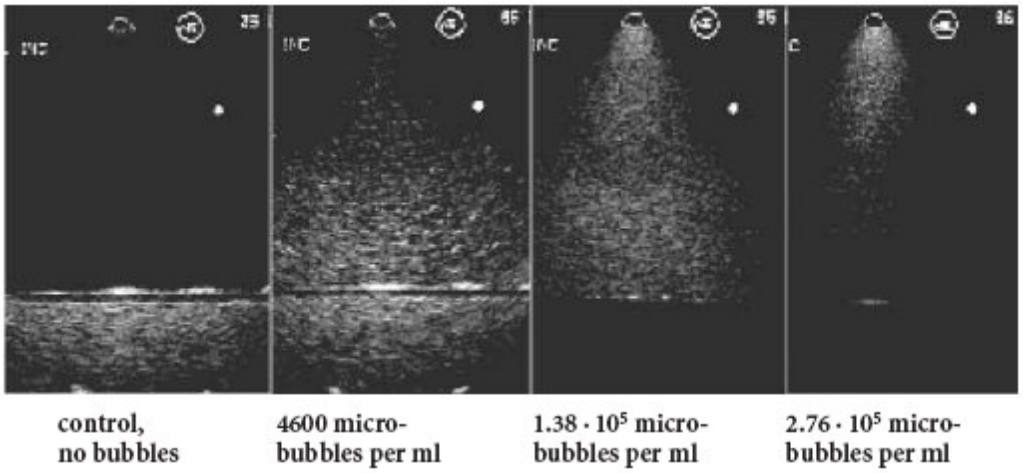

Figure 2-2: Attenuation of US pulse in a saline solution above a tissue phantom with increasing concentrations of MBs. (Recreated from [2])

2.4 Bubble Composition

2.4.1 Stabilization

Henry's law states that:

"At a constant temperature, the amount of a given gas that dissolves in a given type and volume of liquid is directly proportional to the partial pressure of that gas in equilibrium with that liquid" [53]

As such, as the pressure on the gas in a MB increases the rate of dissolution also increases. The pressure exerted on the bubble is determined by the Laplace pressure (Equation 2-6), which relates the pressure difference (ΔP) between the internal ($P_{Internal}$) and the external ($P_{External}$) pressure on a bubble to the interfacial surface tension (σ) (taken here for the following table as the air water surface tension taken as a value of σ_w = 72 mN/m at STP) and the bubble radius (R). One can see that as the radius of a bubble decreases the pressure difference increases. This becomes significant as the bubble size decreases through the micron range (a number of example pressure differentials are given in Table 2-2). When MB radii approach 1 μm it can be seen that the pressure differential becomes equivalent and greater than one atmosphere.

$$\Delta P \equiv P_{Internal} - P_{External} = \frac{2\sigma}{R}$$

Equation 2-6

Bubble Radius, R (μm)	Pressure Difference, ΔP (kPa)
100	**1.44**
20	**7.2**
10	**14.4**
5	**28.8**
1	**144**

Table 2-2: Pressure difference across the interface of air bubbles with varying radii in water. Surface tension of the air-water interface taken as σ_w = 72 mN/m.

In order to be of any use clinically, MBs must not only be able to persist in storage until required but must also persist long enough *in vivo* for an US scan to be conducted after administration into a patient. This second phase also comes with the additional pressure changes from the cardiovascular system; therefore, some method of MB stabilisation is required. Examination of a modified Epstein-Plesset equation (Equation 2-7) gives some indication as to how best to achieve this [54]. This equation relates the rate of change of bubble radius ($\dot{R}$) with the gas concentration of the bulk fluid (C_∞) and the concentration at the fluid gas interface (C_0), the gas diffusion coefficient (D), initial bubble radius (R_0), ambient pressure (P_0) and the interface surface tension (σ). A number of methods to prolong dissolution become evident upon examination of the equation.

$$\dot{R} = \frac{C_0 D}{\rho}\left(\frac{C_\infty}{C_0} - 1 - \frac{2\sigma}{P_0 R_0}\right)\left(\frac{1}{R_0} + \frac{1}{\sqrt{\pi D t}}\right)$$

Equation 2-7

The first method to increase the dissolution time is concerned with the gas in question; again, this can be separated into two components: the gas used and the gas saturation of the system. Firstly, each gas has a given diffusivity coefficient (dependent on temperature and pressure), which typically increases with molecular weight. With this in mind, the vast majority of commercially available MBs tend to use heavy molecular weight gases; for example, sulphur hexafluoride (chemical composition SF_6) as used in SonoVue (Bracco) or octafluoropropane (chemical composition C_3F_8) as found in Optison (GE Healthcare). Some gas properties are included in Table 2-3 [55]. This shows that even with a heavy molecular weight gas, the diffusion times may increase by an order of magnitude; this only prolongs a bubbles' persistence to the 10s of seconds to minutes range.

Recently, it has been suggested that the advantages of using a heavy gas may not be as significant as previously understood [56], [57]. According to Henry's law, it is the partial pressures and not just the absolute pressure that are important in determining dissolution times. With a MB with a heavy molecular weight gas at its core, the bubble therefore has a high partial pressure of the gas used and a low partial pressure outside driving the gas into the solution. Similarly the outside solution has a high partial pressure of oxygen and nitrogen compared to a low internal partial pressure driving gas exchange into the bubble. These changes occur within seconds of the bubble being immersed in a multi-gas environment [56], [57].

Far more important than the type of gas used are the relative concentrations at the MB surface and in the bulk medium. An important caveat to this is that the previous statements are directly applicable to an un-encapsulated MB. With an encapsulated MB there is the additional hindrance to gas transfer imposed by the shell. In this situation, the use of heavy molecular weight gases come with a decreased permeability rate in comparison to air, which can prolong the MB persistence to the range of hours for ideal conditions [55]

Gas	Diffusion Coefficient in water, D (m^2s^{-1})	Permeability through membrane * (ms^{-1})
Air	$2.05x10^{-9}$	$2.86x10^{-5}$
SF_6	$1.2x10^{-9}$	$8.7x10^{-6}$
C_3F_8	$7.45x10^{-10}$	$1.2x10^{-6}$

Table 2-3: Gas properties for commonly used gases in MBs, data taken from [55]**.**

*** Permeability through membrane was defined in the paper as the gas diffusion coefficient across a lipid membrane. Lipid composition as found in the DEFINITY® contrast agent** [58]**.**

The last term on the right hand side of Equation 2-7 is always positive, so one can see that the rate of dissolution is directly related to both the concentration gradient ($\frac{C_\infty}{C_0}$) and the surface tension term ($\frac{2\sigma}{R}$). With regards to the gas concentration gradient, it is apparent that the larger the mismatch between the two concentrations the faster the rate of dissolution. Furthermore, if the system is completely gas saturated i.e. $C_\infty = C_0$ then the MB will still dissolve but the dissolution time is now purely dependent upon the surface tension and the diffusion coefficient of the gas.

This leads onto the second method for increasing the longevity of MBs: encapsulating the MB in a shell. The shell can be made of a number of materials, such as, protein, phospholipids or polymers; the difference between these shell materials will be explored later in this section. The shell provides two important characteristics. Firstly, it reduces the surface tension of the interface, down to a surface tension of zero for a rigid-shelled bubble. As previously explained, the surface tension is one of the main driving factors in the dissolution of MBs. Secondly, the encapsulation material provides a physical barrier that inhibits the passage of the gas across it by decreasing the permeability coefficient (h_g), dissolution time is shown to be inversely proportional to permeability coefficient [55], [59]–[61] as shown in Equation 2-8, where t_{diss} is the dissolution time L_g is the Ostwald gas coefficient, this equation holds true for a gas saturated environment.

$$t_{diss} = \frac{1}{L_g}\left[\frac{P_{atm}R_0}{\gamma}\left(\frac{1}{6}+\frac{D}{4h_gR_0}\right)+\frac{2D}{3h_gR_0}+\frac{1}{3}\right]$$

Equation 2-8

A number of shell materials have been utilised as suitable shell materials for encapsulation of commercial MBs, some of the most common are listed below with their main attributes.

Protein shell

A number of MBs have been developed using a denatured albumin. To manufacture these MBs, a solution of albumin is sonicated in the presence of the gas to be encapsulated. The heat generated in the sonication is typically sufficient to denature the protein and results in a rigid shell of disulfide cross-linked albumin of the order of 15 nm thick [62].

The first commercially available MBs approved for clinical use were protein-shelled MBs called Albunex (GE Healthcare). These MBs were produced in the above method with air as the headspace gas. They had a radii range of approximately 1–7 μm with less than 5% of radius greater than 5 μm and importantly had a shelf life of > 2 years when refrigerated [63]. Furthermore, the use of human serum albumin as the shell material limited bio- and immuno-effects [64].

Subsequent generations of protein-shelled MBs have been developed, with the direct successor to Ablunex being Optison (GE Healthcare). This MB was of a similar formulation but also included the use of octafluoropropane as the gas core material. The combination of heavy molecular weight gas and rigid shell were reported to prolong the persistence time after injection *in vivo* [65]. Albumin-shelled MBs have been used for both targeted imaging [66] and gene delivery [67][68].

Phospholipid/surfactant shell

Lipid and surfactant based MBs were inspired by the observation that the surfactant found on the surface of the alveoli in the lungs can and has to undergo large area expansions whilst remaining an intact layer to facilitate gas transfer [69].

These molecules self-assemble at the interface between the gas and aqueous medium providing a compliant barrier to gas permeation [60], [61]**,** whilst reducing the surface tension of the system [60]. The majority of these molecules are entirely biocompatible and are found throughout organisms as constituent parts of cell membranes [70](this is less so for surfactant-based MBs where the surfactants are largely synthetic in nature [71]). Furthermore the chemical composition of these

molecules renders them ideal for functionalization either for molecular targeting and drug/gene delivery [11], [72], [73]**.** At present a number of commercially available lipid-shelled MBs are approved for clinical use. These include SonoVue (Bracco Diangostics) and Definity (Lantheus Medical Imaging). Interestingly, the first targeted MBs for human trials began recently with a MB designed by Bracco Diagnostics, targeted toward VEGF-R2, a molecular marker for prostate cancer [74].

The main body of work in this thesis is performed using lipid-encapsulated MBs. The properties of the shell will be shown to have a significant effect upon the dynamics and behaviour of MBs and as such, the constituent components of the shell and their attributes will be discussed in detail later in this chapter, in Section 2.4.2.

Polymer Shell

These MBs are comprised of solid cross-linked polymer chains. This shell is often rigid or very nearly rigid, and means that polymer-shelled MBs do not respond as echogenically to an US acoustic wave. In many instances, to get a large acoustic response from these MBs the shell needs to be cracked with high acoustic pressure, then the escaping gas acts as a free gas bubble for a limited time before dissolving [32], [75]**.**

One of the major advantages of polymer-shelled MBs is their persistence both in storage and in the circulation. They have been shown to be readily functionalised, so this long persistence could prove beneficial in aggregating high numbers of the MBs at the intended target site [76]**.**

2.4.2 Shell Morphology

For the purposes of this thesis, only lipid-shelled MBs are utilised, and as such will be the focus in the subsequent sections.

Not only are lipid-shelled MBs some of the most commonly used in current clinical settings, but they also offer a great deal of scope in the redesign and tailoring of their properties to suit specific imaging needs. Consequently, the design and dynamics of lipid MBs is an area of intense research by a number of groups.

Phospholipids, which make up the vast proportion of biological membranes, generally have the same basic structure (see Figure 2-3)[58]. This comprises: a glycerol backbone, 2 long acyl chains of varying lengths and saturations, and a polar head group. These will be discussed in turn to show their effects on the overall behaviour of a MB. The glycerol backbone will not be discussed at it

simply provides the framework on which the other constituent parts are positioned, and is universal to all glycerophospholipids.

The acyl chains and the polar head group behave very differently to each other in solution and highlight one of the reasons that lipids make excellent encapsulation media. The head groups exhibit a slight charge and as such can interact with the hydrogen bonds in water rendering the head groups hydrophilic. In comparison, the long insoluble carbon chains of the acyl groups mean that this portion of the molecule is hydrophobic. This results in an amphiphilic molecule. By nature, these amphiphilic molecules seek to hide their hydrophobic regions from aqueous solution whilst exposing the hydrophilic parts to the solution.

In this way, the molecules self-assemble into vesicles (bi-layers of lipids with the head groups facing outwards towards aqueous solution of both sides) in the presence of only solution, or bubble/micelles (monolayers of lipids) in the presence of a gas or two immiscible fluids. Figure 2-4 shows a schematic representation of how they assemble themselves in the form of MBs. This is a slight simplification of the shells of vesicles and MBs because multilamellar forms can also be produced [77]. Currently there is little control exerted over the shell layering structure during manufacture, so this will not be explored in detail here. However, it is an important factor to remember when discussing the variability between MBs and their response, and will thus be discussed later.

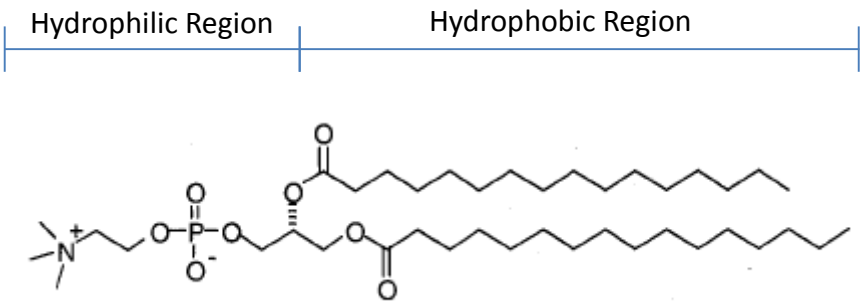

Figure 2-3: Structure of 1,2-dipalmitoyl-sn-glycero-3-phosphocholine (DPPC). A common lipid used in the formulation of MBs. Figure recreated and modified from [58]

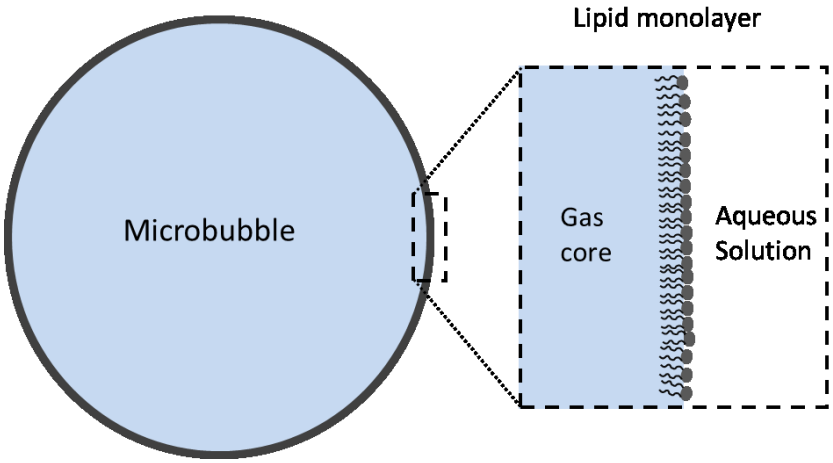

Figure 2-4: Lipid monolayer formation on the surface of MBs. The lipids arrange themselves at the water/gas interface with the head groups facing the solution and the acyl tails pointing towards the gaseous core.

Purely focussing on the monolayer self-assembly as found in MBs, it is important to understand the surface mechanics of these layers. One way to examine these layers is by utilising a Langmuir-Blodgett trough (Langmuir trough for short).

Using a Langmuir trough is a method in which thin films of surfactant can be probed to find pressure area isotherms and hence their surface tension. A known volume of surfactant is injected onto a bed of pure water and the lateral pressure exerted on a plate suspended in the interface gives a measure of the surface pressure. The surface pressure is a function both of the surface tension between the water-air interface, which is known, and the surface tension of the monolayer-air interface.

The review paper [78] provides a comprehensive review of the functionality of Langmuir troughs for further reading. Figure 2-5 provides an example of one of these pressure area isotherms, with several step changes clearly evident in the curve. These step changes occur when the lipid shell changes its phase from a closely packed and ordered state when under compression to an expended or highly disordered and disjointed state when expanded or under tension. These transitions depend on the packing structure of the both the head and tail groups of the lipids.

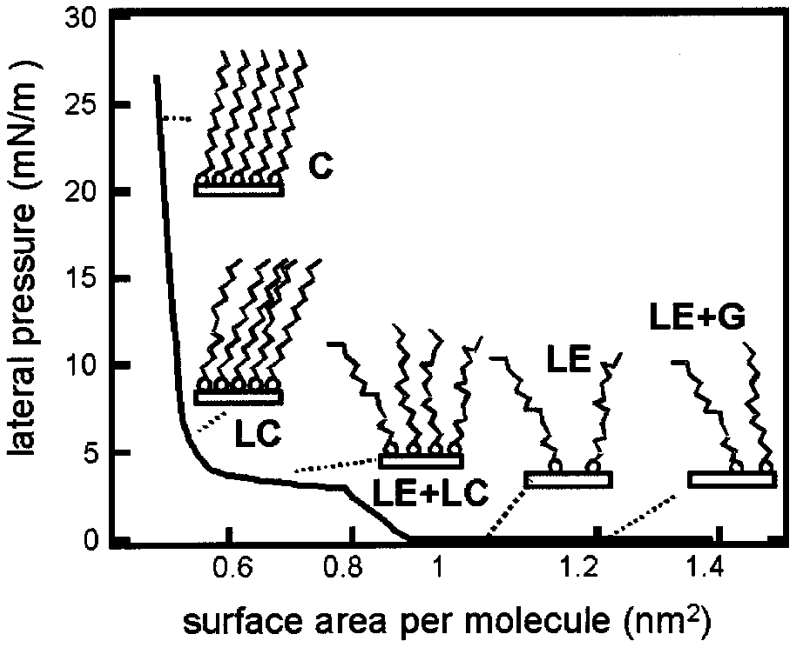

Figure 2-5: Surface pressure isotherm of DPPC. Various phases observed: Condensed (C), Liquid Condensed (LC; also known as the ordered gel phase), Liquid Expanded (LE; also known as the liquid crystalline phase) and Gaseous (G) Figure reproduced from [79]

The choice and composition of the lipid or lipids used can significantly alter the shape of the isotherm and hence the stabilising effect of the encapsulation medium – an expanded or ruptured lipid phase encapsulation provides less resistance to gas permeation than a liquid condensed (LC) or condensed (C) phase [60].

Temperature also plays a significant role in lipid packing and conformity, in fact the transition between the gel-like behaviour of the LC phase and the liquid crystal behaviour of the liquid expanded (LE) phase is more commonly given as a transition or melting temperature (t_m) for standard pressure conditions (101 kPa). A higher temperature means that the acyl chains of the lipid are more energetic and consequently freer to move and rotate. This effectively shifts the curve of Figure 2-5 to the right. The transition temperature for a number of different phospholipids can be seen in Table 2-4 [80]. The choice of lipids used in commercially available contrast agent and indeed those used in the in-house produced MBs for this thesis are such that at body temperature the lipid composition remains below its transition temperature and exist in an LC phase, this corresponds to the left hand side of Figure 2-5.

Understanding the naming of lipids also provides a better understanding of the effects of the composition. The numbers indicate at which of the three positions on the glycerol backbone the subsequent groups occur. Positions 1 and 2 indicate the composition of the acyl groups which are

attached. The two acyl chains can be either the same or different lengths in terms of the number of carbon atoms that these bits of information are given by their trivial or common names. For example "1,2-dipalmitoyl…" indicates that the two carbon chains are of equal length, both with 16 carbons (palmitic being the trivial name for hexadecanoic in the systematic naming system).

With increasing hydrocarbon length there is an increased van der Waals interaction between the chains, which holds them increasingly in place in relation to each other [81]. This means that the energy required to make them disordered is increased, as demonstrated by the first four lipids in Table 2-4. Similarly the saturation state of the carbon chains can also dramatically affect the transition temperature of a lipid [82]–[84].

The acyl chains can either saturated or unsaturated; that is, containing double-bonded carbons. While the single-bonded carbon are free to rotate and move to find the most energetically stable position with neighbouring carbon chains, the same is not true for the double-bonded carbons. The double bond severely inhibits the range of motion that the bond can undergo, and as such, makes close packing of unsaturated acyl chains difficult. The transition temperature for lipids with one or more unsaturated bonds is significantly reduced in comparison to their saturated counterparts.

One must bear in mind that when using MBs in a clinical setting, the MBs will be injected into an organism with a body temperature of approximately 37°C. To prolong the persistence of the MBs *in vivo*, it is desirable to use a lipid or mixture of lipids that have a highly order shell structure at equilibrium. This will minimise surface tension and remove one of the driving factors to dissolution [60]. A highly ordered structure also provides an increased resistance to gas permeation [61], [85], further increasing the MB longevity.

Full name	abbreviation	Carbon chain length : number of double bonds	Transition temperature (°C)
1,2-dilauroyl-sn-glycero-3-phosphocholine	DLPC	12:0	-1 ± 0.8
1,2-dimyristoyl-sn-glycero-3-phosphocholine	DMPC	14:0	23.5 ± 0.4
1,2-dipalmitoyl-sn-glycero-3-phosphocholine	DPPC	16:0	41.4 ± 0.5
1,2-dipalmitoyl-sn-glycero-3-phosphoserine	DPPS	16:0	54
1,2-dipalmitoyl-sn-glycero-3-phosphoethanolamine	DPPE	16:0	63
1,2-distearoyl-sn-glycero-3-phosphocholine	DSPC	18:0	55.1 ± 1.5
1-stearoyl-2-oleoyl-sn-glycero-3-phosphocholine	SOPC	18:0-18:1	6
1,2-dioleoyl-sn-glycero-3-phosphocholine	DOPC	18:1	-19
1,2-dioleoyl-sn-glycero-3-phosphoglycerol	DOPG	18:1	-18

Table 2-4: Transition temperature for a number of common phospholipids.[80]

The head group of the phospholipid is given by the third position in the lipid name. A number of the lipids shown in Table 2-4 have a "–phosphocholine" head group: this is a phospholipid that is ubiquitous within most mammalian membranes [86], and has the structure shown in the hydrophilic section of the lipid in Figure 2-3. As such it is also commonly used for MB encapsulation, one reason being that its transition temperature is above body temperature ensuring a good packing structure.

The head group structures can vary in size and complexity from the very simplest – phosphatidic acid – to large and complex examples, such as Phosphatidylinositol. The head groups all have specific characteristics, such as:

- **Size** – Different sized head groups confer different minimum area per lipids. As such, these also play a part in the packing density and conformity achievable and consequently can affect the transitional temperature in a similar fashion to the acyl chain configuration[80][83]. Examples of this are shown in the entries for DPPC, DPPS and DPPE in Table 2-4.
- **Polarity** – The head groups can be net positive, negative or neutrally charged. This, in turn, also affects how the head groups and hence the lipids pack together and aids the formation of hydrogen bonds further aiding packing [87]. Furthermore, the surface charge can also bring with it biological-effects – it has been shown that negatively charged lipid MBs can have significantly longer retention times in capillary beds [88]. In addition, surface charge can be seen to have an immune response effect resulting in an increased uptake by phagocytes for MBs with a negative charge [89] and can be used for the preferential binding of molecules such as DNA with a positive charge [90].
- **Reactive functional groups** – The different head groups terminate with different functional groups. Not only does this relate to with the previous point about surface charge but it also means that the MB surface can be modified and adapted by the addition of various molecules. This has specific use when tailoring MBs to suit molecular targeting needs by the addition of antibodies or molecules specific to targeted biomarkers [73], [91]. This will be covered in greater detail in Section 2.4.3

The last constituent part of a MB encapsulation is the method by which MB coalescence is prevented. Examination of Equation 2-6 and Table 2-2 shows that it is energetically more favourable for a MB to be of a larger size, as demonstrated by the reduced pressure differential for larger bubbles.

One mechanism through which this can occur is if groups of MBs coalesce to form one large bubble. This is inherently bad for a MB because in a clinical setting it has to be able to pass through the whole circulatory system and is therefore limited by the diameter of the smallest capillaries (≈ 8 μm). Any larger than this and the bubbles will not be able to perfuse the entire system, or, at worst be the cause an embolism or blockage in a vital part of the circulatory system and possibly result in death.

Obviously this is a scenario to be avoided. One method of preventing the MBs from coalescing is by the introduction of buffers: molecules or mechanisms by which it makes the close proximity required for coalescence difficult to achieve.

A buffering method utilised on almost all lipid-shelled MBs typically consists of long polymer units (of the order of 2000–8000 molecular weight) embedded in the surface of the monolayer by way of an acyl chain or lipid 'anchor'. These polymer units extend into the aqueous solution tens of nanometres away from the MB surface and effectively create a boundary layer inhibiting other MBs entering that region [92].

The polymers can either be embedded as standalone chains anchored in the monolayer by a single acyl chain, or, more commonly, the polymer can be covalently attached to the head group of a lipid forming part of the monolayer itself. One of the most common buffers used is (Poly) ethylene glycol (PEG). Figure 2-6 shows a representation of the PEG monomer subunit as well as a schematic representation of how the PEG is situated in the monolayer.

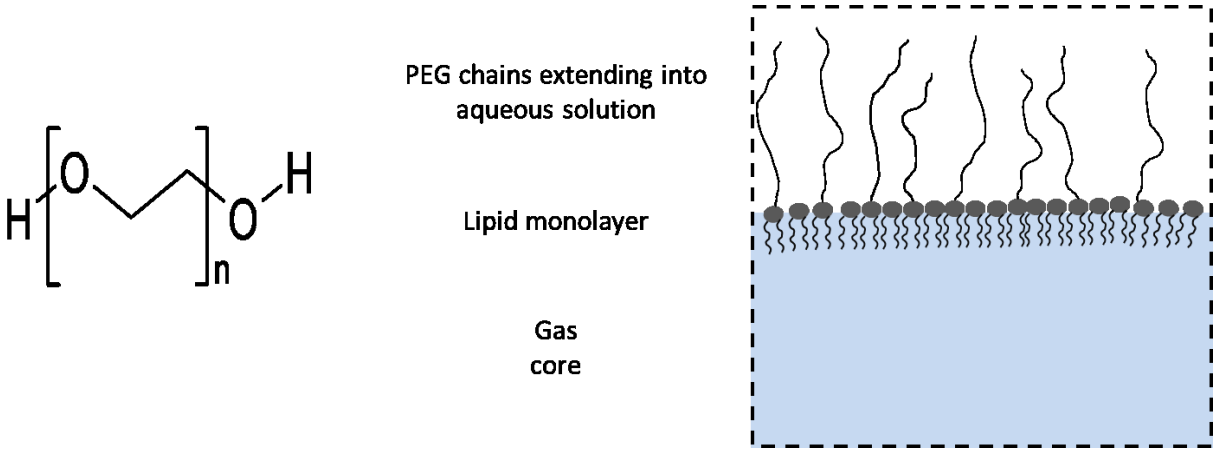

Figure 2-6: PEG monomer unit (left) and a section of a MB surface showing the configuration PEG takes when incorporated into a MB shell

The use of a PEG buffer also has a number of other benefits besides its anti-coalescence properties. The PEG surface has been shown to 'shield' the MB from the body's immune system reducing phagocyte uptake; this results in a longer circulation time before bio-degradation [91].

The PEG chains also allows for targeting ligands to be attached to their ends for specific targeting of the MB to an area of pathology. By attaching the targeting ligands to the end of the PEG rather than directly onto the surface of the MB it means that the targeting ligands have a greater

degree of freedom and the MBs do not have to be in such close proximity to achieve binding with the target site. MB functionalization will be covered further in Section 2.4.3.

The surface tension of the monolayer is linked to the surface pressure (Π) by Equation 2-9 [93]. Because the air-water surface tension (σ_w) can be taken as a constant, the surface tension of the monolayer interface can be visualised as almost the inverse of the surface pressure graph (Figure 2-5). Under high compression, the monolayer surface tension is at a minimum. As the system is expanded, the monolayer relaxes until the molecules lose contact with each other and the monolayer ruptures. At this point the surface tension tends to the surface tension of the air-water interface. The equilibrium position on this curve will dictate the Laplace pressure driving gas diffusion and bubble shrinkage, and is therefore intrinsically linked to the selection of the encapsulation lipids.

$$\Pi = 2\sigma_w - \sigma_m$$

Equation 2-9

The gradient of this curve and the shape and position of any transition regions also play a significant role in MB dynamics. The gradient of the surface pressure curve can be directly linked to the bulk modulus of the monolayer [93] (the two are related by Equation 2-10 where A is the area per molecule). The bulk modulus is typically given in reference to a volumetric change in a material due to a uniform pressure change. Due to the thin nature of the monolayer this can be thought of as a monolayer compressibility modulus or elasticity.

A MB exposed to US will expand and compress according to the pressure variation, and during such volumetric oscillations the area per lipid will change. This area change imposes a changing surface pressure and hence can induce a phase transition. For an oscillating MB, as found during insonation, this can and does have a profound effect on MB dynamics. The effect of variable surface tension will be fully explored in Section 2.5 and also in Chapter 6 when it comes becomes very important to the modelling and simulation of MB dynamics. One should also note that for an insonated MB these changes will be experienced in timescales of the order on microseconds and not at the quasi-static loading states experienced using a Langmuir trough. The effects of compression/rarefaction rate are also discussed in Section 2.5 and Chapter 6.

$$\kappa = -A\left(\frac{\delta\Pi}{\delta A}\right)_T = A\left(\frac{\delta\sigma_m}{\delta A}\right)_T$$

Equation 2-10

The limiting states of lipid compression and expansion cannot be avoided given sufficient amplitude driving pressure. As such, there will always be changes in compressibility of the encapsulation during a compression-rarefaction cycle. It is possible, however, to alter the transition between the two states to remove or smooth out the step changes caused by the transitions from on phase to the next.

As the encapsulation passes through each of the transitions there are points where two phases (and occasionally three phases [84]) exist simultaneously. This does not occur in a uniform way across the surface and instead occurs in discrete regions throughout the surface and provide varying physical properties compared with the single phase. For example, the presence of LC phase domains surrounded by non-crystalline grain boundaries allows for a considerably more elastic response than a pure LC phase.

Above the lipids' transitional temperature the majority of lipids are entirely miscible and homogeneously mix [82].The formation of these domains is dependent upon the species of lipids which make up the shell and is also dependent on the temperature and pressure changes during manufacture and subsequent usage [84].

Figure 2-7 shows the domains formed of a simple two-species MB. The MBs are predominantly made of DSPC (89.9%) with a PEG buffer anchored to the headgroup of the lipid DSPE-PEG2000 (10%), the 2000 refers to the molecular average weight of the molecule. The remaining 0.1% comprised of $DiLC_{18}$, a fluorescent lipophilic dye with acyl chains of equal length to the phospholipids used (C=18). The dye molecule is compatible with both the lipids used and resides just below the head groups [94]. Furthermore, the dye molecule preferentially positions itself in fluid regions, typically existing at the boundaries between solid or compressed regions [84].

Figure 2-7 shows the presence of these grain boundaries both immediately post manufacture (a) and after the MBs have been heated and then cooled in a controlled manner (b).

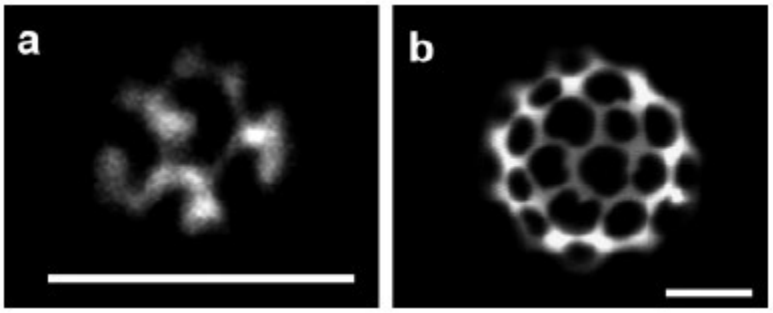

Figure 2-7: Fluorescence images of domain structures present in MBs immediately after manufacture (a) and controlled heating and cooling (b). MBs are formulated from DSPC (89.9%), DSPE-PEG2000 (10%) and $DiIC_{18}$ (0.1%). Image reproduced from [84]

These lipid domains can actually be beneficial in the stabilisation of MBs as they undergo large deformations. As the MBs reach their compression limit in terms of area, the bubble must buckle and fold to account for the volume of lipid and available surface area. The grain boundaries provide ready-made weak points to fold and buckle around, ready to be reincorporated into the expanding shell on the rarefaction phase the pressure cycle [82].

2.4.3 **Functionalization**

Currently there has been a move towards molecular imaging with US [37], [95], [96]. In order to perform this, the MBs have to have a selective preference for a specific region or pathology. It has been shown that capillary transit time can be increased by the selective use of surface charge [88] and that retention and imaging times in organs such as the liver can be increased by the phagocytosis of MBs in macrophages [97]; however, for the selective imaging of a wide range of pathologies, it is best to specifically target a biomarker expressed by that pathology. Such markers that have been selectively targeted can include expressions for inflammation [98], angiogenesis [99], atherosclerosis [100] and thrombosis [101].

The targeting is achieved by conjugating the encapsulation medium of the MB with the partner molecule to the biomarker. Examples of this include functionalising the MB with antibodies targeted to attach to the intracellular adhesion molecules p-selectin [102], [103], e-selectin[72], (ICAM) [10] or vascular cell adhesion molecules (VCAM) [95], which are related to inflammation and immuno-regulation.

How and where these molecules are positioned on the surface of the MB is crucially important in determining the efficacy of the targeting. Typically, the binding molecules will be attached to the end of the PEG buffer [104]. This greatly increases the effective surface area of the MB, making capture and retention at the target site more likely and can also increase the affinity under flow conditions[104]–[106].

One drawback of this approach is that the full exposure of the targeting ligands to the bloodstream – and with that the immune system – leads to an increased immune response to the MBs and less circulation time. A method to reduce the ligand mediated immunogenic response is to partially cover the targeting ligands. To do this, two (or more) lengths of PEG are utilised[64]. The outer, longer layer is not functionalized and acts as described in the manner described in the previous section: acting to sterically stabilize the MBs in solution and to provide a degree of immune response suppression. The targeting ligands are then situated on the shorter length PEG chains. In this way they are hidden or masked from the bloodstream and immune system until the MB comes into contact with a surface, at which time the targeting ligands are exposed [73], [91], [106].

Obviously, this masking of the targeting ligands under a layer of PEG will reduce the MB targeting affinity. One method of increasing this is by the employment of a physical force to manoeuvre the MBs towards a target site and physically press them into the surface to increase binding affinity. This technique has been demonstrated with both magnetic [107] and acoustic forces [108], [109]. The imaging of functionalized MBs will be dealt with in Section 2.7.1.

2.5 Basic Dynamics

The basic dynamics of a MB can be described as the energy balance between the kinetic energy of the fluid surround generated in response to the compression and rarefaction the MB undergoes during an acoustic cycle. This is balanced by the work done on the fluid. The assumptions used in this derivation are that the MB is in an incompressible medium; this holds true provided the MB wall velocity is significantly less than the speed of sound in the medium [110]. Compressibility corrections will be covered in further detail later in this section and Chapter 6 because they can also have an impact on the damping levels experienced by a MB, and so failure to include them can lead to oscillations not being damped as one would expect and consequently amplitude building as a function of number of cycles [111].

The basic energy balance is given below in Equation 2-10. The left hand side of the equation denotes the kinetic energy of the system and the right denotes the pressure difference between the fluid immediately outside of the MB (P_L) and the bulk fluid pressure (P_∞), R is the radius of the MB and the superscript dots referring to the differential with respect to time i.e. radial velocity and acceleration.

$$\rho\left(R\ddot{R} + \frac{3\dot{R}^2}{2}\right) = P_L - P_\infty$$

Equation 2-11

The pressure of the liquid can be determined from the internal pressure of the bubble as given by the Laplace pressure and taking into account the vapour pressure of the gas (P_v) (see Equation 2-12). In the majority of derivations, the vapour pressure is either set to that of water (2.33 kPa) or simply neglected because it is significantly less than the ambient pressure term ($P_\infty \gg P_v$). The internal pressure of the bubble will vary polytropically to a given acoustic driving wave. This results in Equation 2-13, where (γ) is the polytropic index of the gas.

$$P_{internal(static)} = P_\infty + \frac{2\sigma_w}{R_0} - P_v$$

Equation 2-12

$$P_{internal(\text{oscillatory})} = \left(P_\infty + \frac{2\sigma_w}{R_0} - P_v\right)\left(\frac{R_0}{R}\right)^{3\gamma}$$

Equation 2-13

The value of γ is taken as 1 for an isothermal process and can range up to the ratio of specific heats if the expansion and contraction is adiabatic (a value 1.4 for air). The choice of value for the polytropic exponent is determined by the Peclet number (Pe)[112], where (f) is the driving frequency and (D_{th}) is the thermal gas diffusivity (Equation 2-14). If the Peclet number is much greater than 1 ($Pe \gg 1$), then the gas can be considered to behave adiabatically; if, however, the number is close to 1 then the gas behaves isothermally.

Depending on the values examined for the Peclet number, it is possible to get both values ≈ 1 and similarly ≫ 1. To give an example of this consider a 3 µm and a 1 µm radius MB containing C_4F_{10} such as SonoVue (D_{th}= 2 x 10^{-6} m^2/s [111]) insonated at 1 MHz, this gives Peclet numbers of 56.7 and 3.13 respectively, as such there are conflicting reports as to which value of polytropic index is most applicable for modelling modern contrast agents. For example, [113] favours taking the adiabatic approach in contrast to [114], who favours an isothermal approach. If the gas under discussion was air then this could lead to large discrepancies between results. When the gas under consideration is a heavy molecular weight gas, as used in MB manufacture, this is slightly less of an issue, the ratio of specific heats (adiabatic limit) for sulphur hexafluoride as used in SonoVue is 1.07 compared to that of 1.4 for air.

$$Pe = \frac{2\pi R_0^2 f}{D_{th}}$$

Equation 2-14

The pressure of the liquid near the bubble surface is then determined as the gas pressure in the MB minus the instantaneous surface tension, resulting in Equation 2-15.

$$P_L = \left(P_\infty + \frac{2\sigma_w}{R_0} - P_v\right)\left(\frac{R_0}{R}\right)^{3\gamma} - \frac{2\sigma_w}{R}$$

Equation 2-15

Finally the viscous effects of the system also need to be taken into account, as they ensure the continuity of the normal stresses across the MB surface. Taking the viscous term into account, including the acoustic driving pulse and substituting Equation 2-15 into Equation 2-11, the Rayleigh-Plesset (RP) equation, or to give it its full list of contributors, the Rayleigh-Plesset-Noltingk-Neppiras-Poritsky (RPNNP) equation for an un-encapsulated MB, is derived (Equation 2-16). It will simply be referred to as the RP or Rayleigh-Plesset equation for brevity. η is introduced as the dynamic viscosity of the fluid. [54]

$$\rho\left(R\ddot{R} + \frac{3\dot{R}^2}{2}\right) = \left(P_\infty + \frac{2\sigma_w}{R_0} - P_v\right)\left(\frac{R_0}{R}\right)^{3\gamma} - \frac{2\sigma_w}{R} - \frac{4\eta\dot{R}}{R} - P_\infty - P_{ac}$$

Equation 2-16

The damping of MB oscillations has three principle contributions [54]. There is viscous damping, accounted for by the fluid viscosity term in the RP equation above. The next contribution comes from thermal damping or energy lost by the heating of gas and conduction to the surrounding fluid. For linear oscillation regimes, this is accounted for by the correct choice of polytropic exponent; however, for non-linear processes this may not hold true [115], [116], as thermal damping becomes non-linear also. One way of accounting for this without the need of complex damping models has been to increase the effective fluid viscosity [113], but similarly, the term is often deemed much less dominant than viscous damping and is consequently neglected.

The final mechanism of damping is that of radiation damping. To incorporate this into the model, the extended version of the RP equation is required. This extension assumes that the bubble is in a compressible fluid and is of particular relevance when MB wall velocities are small but no longer negligible to that of the fluid speed of sound [112]. Equation 2-17 shows one of the common approaches to include the compressibility effect and is called the Keller-Miksis equation [117], where c is the speed of sound in the medium. Other approaches have also been utilised but will not be examined here due to either an inherent similarity in solution [118] or additionally complex formulation with no real gains in accuracy within the regimes of this study [119].

$$\rho\left(R\ddot{R}+\frac{3\dot{R}^2}{2}\right)=\left(P_\infty+\frac{2\sigma_w}{R_0}-P_v\right)\left(\frac{R_0}{R}\right)^{3\gamma}\left(1-\frac{3\gamma\dot{R}}{c}\right)-\frac{2\sigma_w}{R}-\frac{4\eta\dot{R}}{R}-P_\infty-P_{ac}$$

Equation 2-17

By approximating the MB response to that of a linear oscillator i.e. the radial oscillation is defined as a small excursion (x) from the previous radial position $\mathrm{R}=R_0(1+\mathrm{x})$ this equation can be linearised. The excursion will then follow the basic form of a linear oscillator (Equation 2-18) where ω is the driving angular velocity and the subscript 0 denotes the Eigen values of the system ($\omega_0=2\pi f_0$) where f_0 is the eigenfrequency, f_{res} is the damped resonance frequency and δ is the linear dimensionless damping coefficient, which has constituent parts arising from the fluid viscosity thermal damping and radiation damping.

$$\ddot{x}+\omega_0\delta\dot{x}+\omega_0^2x=P_{ac}\sin(\omega t)$$

Equation 2-18

The eigenfrequency for an un-encapsulated bubble can be found from the Minnaert frequency for a damped oscillator (Equation 2-19 and Equation 2-20) [110], [120].

$$f_0=\frac{1}{2\pi}\sqrt{\frac{1}{\rho R_0^2}\left(3\gamma P_\infty+\frac{2(3\gamma-1)\sigma_w}{R_0}\right)}$$

Equation 2-19

$$f_{res}=f_0\sqrt{1-\frac{\delta^2}{2}}$$

Equation 2-20

2.5.1 First order approximations of shell terms

The basic dynamics of a spherical un-encapsulated bubble can be described using Equation 2-16 or Equation 2-17. The next step in modelling the MB dynamic response is to account for the effect of the encapsulating shell, which, as previously illustrated, brings with it associated changes in elasticity and viscosity. A number of models have been developed that try to characterise MB in terms of shell properties. The Rayleigh-Plesset equation is typically used as a starting point for these modifications, with the differences occurring in factors such as the way the shell is modelled (i.e. finite thickness or infinitesimally thin shells) or the viscoelastic relationships and fluid models. The next section will detail the more prominent models that have been produced as a result of this development building in complexity to the most recent and advanced models.

Principally, there are two approaches to the modelling of MB encapsulation. The first methodology examines the problem from a theoretical view point and derives parameters from first principles. Typically, this will model the encapsulation as a shell with a finite thickness and as such were first more applicable to "thick" shelled MBs i.e. a polymer- or albumin-based shell. Some examples of this can be found in the approaches taken by Church et al. [121] or Hoff et al.[122].

The Church model (Equation 2-21) [121] assumes that the MB pulsates in an infinite incompressible medium; therefore, compressibility corrections are not implemented. The MB has both an internal and external radius (R_1) and (R_2), respectively, with the resting inner radius given as (R_{01}). This shell material is taken as an incompressible medium so the volume of the shell material remains constant. The final radius term is the subscript (e) which refers to the unstrained position of the MB shell and is characteristically different from (R_{01}).

The viscoelastic properties are modelled to follow the Kelvin-Voigt law, which implies Hooke's law with a rate dependant damping for small (linear) oscillations. Essentially, this models the system as a spring mass system with a dashpot for damping. These viscoelastic properties are incorporated by the terms (μ) and (η) corresponding to the shear modulus and viscosity respectively. The subscripts (s) and (l) refer to the shell or liquid properties. P_{G0} is the internal gas pressure of the MB and is equivalent to $P_{internal(static)}$ given by Equation 2-12.

$$\rho_s R_1 \ddot{R}_1 \left[1 + \left(\frac{\rho_l - \rho_s}{\rho_s}\right)\frac{R_1}{R_2}\right] + \rho_s \dot{R}_1^2 \left[\frac{3}{2} + \left(\frac{\rho_l - \rho_s}{\rho_s}\right)\left(\frac{4R_2^3 - R_1^3}{2R_2^3}\right)\frac{R_1}{R_2}\right]$$
$$= P_{G0}\left(\frac{R_{01}}{R1}\right)^{3\gamma} - \frac{2_{\sigma_1}}{R_1} - \frac{2_{\sigma_2}}{R_1} - P_\infty - P_{ac} - \frac{4\eta_l R_1^2 \dot{R}_1}{R_2^3} - \frac{4\mu_s(R_{20}^3 - R_{10}^3)}{R_2^3}\left(1 - \frac{R_{1e}}{R_1}\right)$$
$$- \frac{4\eta_s(R_{20}^3 - R_{10}^3)}{R_2^3}$$

Equation 2-21

The major contributions from this paper showed that the resonance frequency of MBs increased as a function of increasing elastic modulus i.e. stiffer MB have higher resonance frequencies and showed a marked increase over the un-encapsulated MBs. This model also demonstrated that for MBs < 10 μm in radius, the viscous contributions to damping far exceed the losses due to thermal or radiation effects. This last point is just to reiterate that this model is only valid for small oscillations.

Extending this work, Hoff [122] took the approach that the shell thickness (ε) approached the limit of 0 or infinitesimally thin when the thickness was significantly smaller than the resting radius $\varepsilon << R_{01}$. Using this approximation, the Hoff model was given as Equation 2-22. In comparison to Equation 2-16, one can see that the only difference is the inclusion of the shell parameter terms (μ_s) and (η_s,) again denoting the shear modulus and shear viscosity of the shell as before.

It should be noted that with the approximation of Church's model to the first order of expansion, the resulting equation is not as accurate as the more complete Church version; however, it is easier to implement and the relationship back to the original RP equation is more obvious [111].

$$\rho_l\left(R\ddot{R} + \frac{3\dot{R}^2}{2}\right) = P_{G0}\left(\frac{R_0}{R}\right)^{3\gamma} - \frac{2\sigma_w}{R} - \frac{4\eta_l \dot{R}}{R} - P_\infty - P_{ac} - 12\mu_s \frac{\epsilon_0 R_0^2}{R^3}\left(1 - \frac{R_0}{R}\right) - 12\eta_s \frac{\epsilon_0 R_0^2 \dot{R}}{R^3 R}$$

Equation 2-22

The second approach to modelling the effect of encapsulation is to make adaptations to the original PR equation based on experimental observations of MB behaviour. Consequently, it follows that as the control that experimenters have over the various factors in MB characterisation

experiments increases, our ability to detect smaller and smaller phenomena becomes greater, and these adaptations becomes more representative of real MB response.

The first widely accepted attempts of this were conducted by de Jong et al. in their work characterising the properties of Albunex [123], [124]. This model lumped all the damping terms together in one parameter (δ_t). This parameter consisted of all the previously mentioned components of damping for an un-encapsulated MB – viscous (δ_{vis}), thermal (δ_{th}) and radiation (δ_{rad}) – but also included a fourth term for the frictional losses of the shell (δ_{fr}). The frictional damping was then in turn related to a shell friction parameter (S_f). These terms were related together by Equation 2-23 and Equation 2-24.

$$\delta_t = \delta_{vis} + \delta_{th} + \delta_{rad} + \delta_{fr}$$

Equation 2-23

$$\delta_{fr} = \frac{S_f}{4\pi R^3 \rho_l \omega}$$

Equation 2-24

The second parameter introduced was a shell elasticity term (S_p) (the full de Jong model is shown in Equation 2-25). If one then expands this equation to incorporate the damping mechanisms as previously shown – that is: viscous losses included for the surrounding medium, thermal damping accounted for by the correct choice of polytropic exponent fluid and modification of the fluid viscosity if required, radiation damping included using a Keller-Miksis style adaptation, and the shell friction term included separately – then one is left with the following (Equation 2-26). Note that as an additional substitution, the shell elasticity parameter has been related to the shell elasticity modulus (χ) by the relationship $\chi = S_p/2$, and that the shell friction term has been related to the surface viscosity (κ_s) by the function $\kappa_s = S_f/16\pi$. This form of the equation has been widely used for a number of MB characterisation studies and also provides a basis for many of the later advancements.

$$\rho\left(R\ddot{R}+\frac{3}{2}\dot{R}^2\right)==P_{Go}\left(\frac{R_0}{R}\right)^{3\gamma}-\frac{2\sigma_w}{R}-P_0-P_{ac}-\delta_t\omega\rho_l R\dot{R}-2S_p\left(\frac{1}{R_0}-\frac{1}{R}\right)$$

Equation 2-25

$$\rho\left(R\ddot{R}+\frac{3}{2}\dot{R}^2\right)==P_{Go}\left(\frac{R_0}{R}\right)^{3\gamma}\left(1-\frac{3\gamma\dot{R}}{c}\right)-\frac{2\sigma_w}{R}-4\eta\frac{\dot{R}}{R}-P_0-P(t)-4\chi\left(\frac{1}{R_0}-\frac{1}{R}\right)-4\kappa_s\frac{\dot{R}}{R^2}$$

Equation 2-26

The final addition to this section that is important to make a note of is the extension proposed by Chatterjee and Sarkar [125]. This model is almost identical to the de Jong model of Equation 2-26 except for a change in the shell elasticity term. In this model, the elasticity of the shell was related to the density of surfactant molecules on the surface.

As shown in using the Langmuir trough, this surface packing density will vary with area and hence will vary across an acoustic cycle. To relate the change in area to a change in elasticity, Chatterjee and Sarkar related it linearly to a change in effective surface tension. The effective surface tension was therefore given as Equation 2-27, where E^S is the dilatational elasticity and R_E is the unstrained equilibrium radius of the MB. When substituted into the de Jong model it remains exactly the same expect for the elasticity term being changed to the variation shown in Equation 2-28. This method of relating the shell parameters to a changing property led the way onto the non-linear modelling of shell parameters.

$$\sigma=\sigma_w+E^s\frac{(R^2-R_E^2)}{R_E^2}$$

Equation 2-27

$$\frac{2E^s}{R}\left(\frac{R^2}{R_E^2}-1\right)$$

Equation 2-28

2.5.2 **Non-linear shell parameters**

The models described in the previous section reduce the complex bubble morphology and rheology to typically two constant parameters encompassing an elastic term and a viscos term. This approximation can be held valid only for a limited range of oscillations. We have seen in Equation 2-10 and in the Chatterjee-Sarkar model that the compressibility of the monolayer can be directly related to the surface tension. Because this relationship varies with area per molecules and hence MB radius, this value can be expected to change throughout the course of US exposure, something not accounted for by a single constant term.

Furthermore, taking a single value for the elastic or viscos terms neglects any effects that occur at the two extremes of surface tension, that of high compression or alternatively high expansion [126]. Another observation made by a number of groups in the parameterisation of these models with linear shell parameters was that the parameters derived for elasticity and viscosity were dependent upon the initial size of the MB [127], [128]. Intrinsically, this is slightly nonsensical because the properties are inherent to the monolayer and a result of the molecules used and their relative packing density, however, a monotonic change in value with radius as seen in [127] for elasticity in the parameterisation of the Hoff model and in [128] for both the elasticity and viscosity in a linearized version of the Marmottant model [129].

Under high compression there comes a point where the lipid molecules cannot be structured as a locally flat monolayer to reduce the area per lipid any further. At this point the surface tension drops to zero as the layer behaves essentially as a thin solid [47]. If the MB is compressed further it has to deform in a different mode than spherically symmetrical oscillations. Under these conditions, the MB tends to buckle and has been shown to be responsible for a number of observed effects, such as, “compression-only” and subharmonic generation [40], [129], [131]–[133].

Given sufficient energy in this state, MBs can fragment or collapse but modes are not specifically relevant here and will be covered in the later section on MB destruction (Section 2.6.3). Similarly, at the other end of the scale when a MB expands beyond the limits the lipid can overcome with their intermolecular cohesive bonding, the shell will rupture leaving areas on the MB interface. With this, the surface tension of those areas tends to that of the gas/water interface [79]. In both scenarios, the surface tension undergoes rapid changes for small area changes and hence in compressibility modulus.

Marmottant et al. [129] presented a model that attempted to account for these changes in MB elasticity. To do this, the surface tension/area curve was idealised, as shown in Figure 2-8. This discretises the surface tension into three regimes: the buckled, elastic and ruptured regimes.

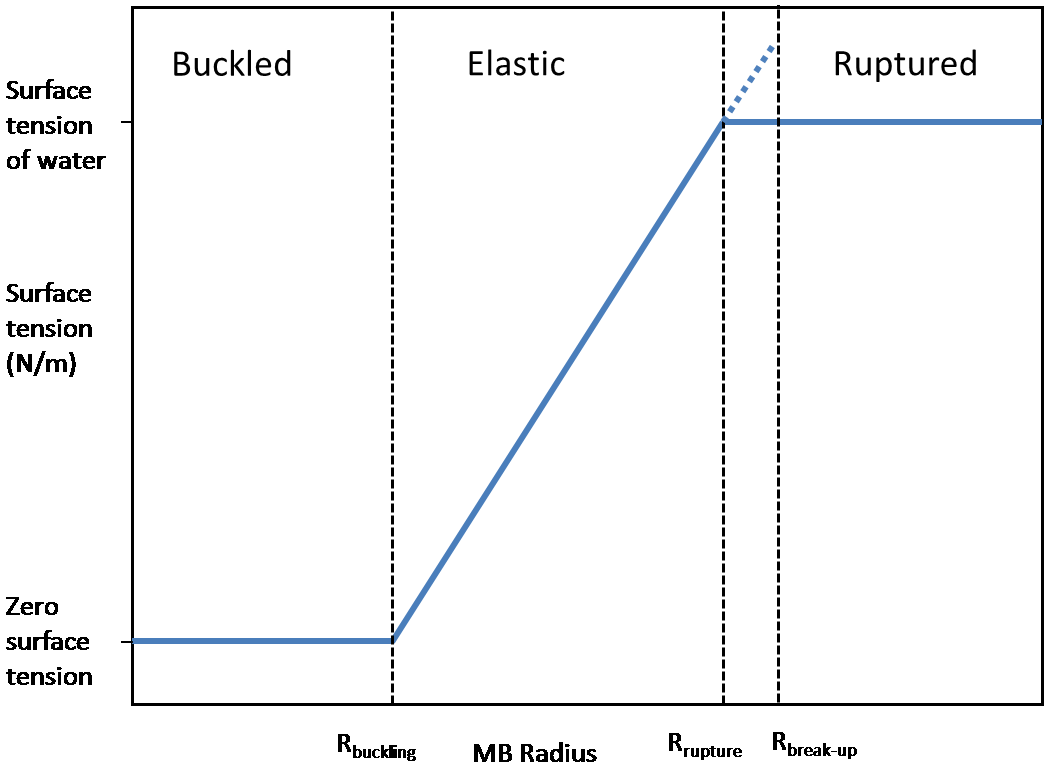

Figure 2-8: Idealised surface tension Vs. area curve as used in [129]

In the numerical model (Equation 2-29), this is accounted for by the term $\sigma(R)$, which is the radius dependent surface tension. The three regimes of surface tension are given by Equation 2-30.

$$\rho\left(R\ddot{R}+\frac{3}{2}\dot{R}^2\right)=\left(P_\infty+\frac{2\sigma_w}{R_0}\right)\left(\frac{R_0}{R}\right)^{3\gamma}\left(1-\frac{3\gamma\dot{R}}{c}\right)-4\eta\frac{\dot{R}}{R}-\frac{2\sigma(R)}{R}-4\kappa_s\frac{\dot{R}}{R}-P_\infty-P(t)$$

Equation 2-29

$$\sigma(R) = \begin{cases} 0 & if\ R \leq R_{buckling} \\ \chi\left(\frac{R^2}{R_{buckling}^2} - 1\right) & if\ R_{buckling} \leq R \leq R_{break-up} \\ \sigma_w & if\ ruptured\ and\ R \geq R_{ruptured} \end{cases}$$

Equation 2-30

This shows that when a MB's radius is decreased below a buckling threshold ($R_{buckling}$), the surface tension terms decreases to zero. Above the threshold set by the break-up radius ($R_{break-up}$), the MB surface tension tends to that of water. These radii limits are set by Equation 2-31 and Equation 2-32.

$$R_{break-up} = R_{buckling}\sqrt{\left(1 + \frac{\sigma_{break-up}}{\chi}\right)}$$

Equation 2-31

$$R_{ruptured} = R_{buckling}\sqrt{\left(1 + \frac{\sigma_{water}}{\chi}\right)}$$

Equation 2-32

The difference in radius between the ruptured and break-up states is included to better match observed experimental results, which see MB seemingly pass the ruptured radius whilst still essentially retaining encapsulation. This has been termed a resistant shell [129]. Between these two states, the MBs are described as acting linearly with respect to radius. According to the simulations produced by Marmottant et al., the MB will only stay in the elastic region for radial variations of the order of 5%. This reinforces the need for a model that can cope with large variations in amplitude for the modelling of MB at even moderate acoustic pressures. As before, if one assumes that the MB remains in the elastic regime (i.e. small oscillations), the elasticity terms reduce to a very close approximation of the de Jong model (Equation 2-26).

Advances have also been made to include terms that exhibit shell properties that vary not with initial radius as has previously been the trend, but rather with rate of radial change. Such materials can exhibit hardening or softening behaviour. Paul et al. [134] proposed two alternative models to simulate the non-linear elasticity. Both models vary the shell elasticity parameter so that

as the MB increases in radius and the constituent shell molecules become more separated, the more the elasticity is reduced, this behaviour is called strain softening.

The first model, termed the quadratic elasticity modulus (QEM), introduces the parameter in a piecewise fashion as the Marmottant model does with the effective surface tension. The elasticity is implemented as the function of two parameters – (E_0^s) the base dilatational elasticity and (E_1^s) the surface tension (σ_0) dependant elasticity. Also, in a mirror of the Marmottant model, once the area expansion reaches a certain point the elasticity is set to zero. The second method proposed is that instead of a piecewise implementation of elasticity; which can cause step changes in elasticity and is not necessarily indicative of reality, should be implemented as a continuous exponential decaying function of amplitude (E_0^s) and decay constant (α^s) which can provide sharp changes in elasticity but without the step change nature evident in the piecewise implementation. Both the Marmottant and Paul models were able to predict fundamental response well, as well as being able to account for non-linear phenomena such as "compression-only" behaviour [133] and also the onset and generation of subharmonics.

It should be noted that although these models all include a non-linear shell elasticity term, they still incorporate the linear version of the shell viscosity as shown in the de Jong/Chatterjee-Sarkar models. A few attempts have also been made to apply a similar non-linear approach to the characterisation of the MB viscosity, the most noticeable being by Doinikov et al. [135]. This model retains a linear elasticity parameter similar to that from de Jong and Sarkar, but relates it to the ratio and models the viscosity as dependent upon the radial velocity – specifically, it models the viscosity as proportional to the ratio $\dot{R}/R$ and is termed shear thinning behaviour, which had previously been suggested in a number of papers [113], [136]. The viscosity was then determined by three constant terms, two viscosity constants (κ_0) and (κ_1) and one normalizing factor (α). This model also had success in modelling some of the non-linear MB behaviour in a similar manner to the variable elasticity models.

2.5.3 Parameterization of models

The use of these increasingly complex and parameter-heavy models brings with it some associated issues; chief amongst these is how one goes about establishing the shell parameters. Table 2-5 briefly compares some of the key models and the parameters that need to be established to implement them.

Model	Elasticity Term	Viscosity Term	Oscillation Range	Parameters required
De Jong	Linear	Linear	Small	χ κ_s
Chatterjee/Sarkar	Linear	Linear	Small	E^s κ_s
Marmottant	Non-Linear	Linear	Large	χ κ_s $R_{break\text{-}up}$ $R_{buckling}$
Paul (Quadratic)	Non-Linear	Linear	Large	κ_s σ_0 E_0^s E_1^s
Paul (Exponential)	Non-Linear	Linear	Large	κ_s σ_0 E_0^s α^s
Doinikov	Linear	Non-Linear	Large	X κ_0 κ_1 α

Table 2-5: Comparison of parameters required and the applicable amplitude range of various MB dynamics models

The Langmuir trough, as described in Section 2.4.2, can provide both the compressibility modulus and viscosity of monolayers of surfactants. Both of which could be used directly in models such as the de Jong model, where those are the two parameters required. The problem with this method is that the Langmuir trough establishes these parameters at quasi-static loading states. The maximum rate of compression or expansion achievable with a Langmuir trough is approximately 400cm^2/min. A MB on the other hand will be experiencing changes in area at a rate approximately 10^5 times greater, even at moderate to low acoustic settings [137]. This is reported to have a dramatic effect on the observed properties and consistently produces values for shell elasticity orders of magnitude larger – values up to 10^2 greater have been quoted, than those used in the models to achieve comparable effects as those seen in experiment [138], [139]. This also provides evidence in support of both strain softening and shear thinning behaviour having an effect in determining the values of shell properties.

Another popular method to parameterise these equations is to limit the oscillations to small amplitudes so that small amplitude approximations can be used to linearize the models. In Equation 2-19, we saw how the RP equation could be linearized to provide a value of the resonance frequency based purely on the initial radius, and fluid/gas properties.

This method can be extended to incorporate some of these shell properties. Van der Meer et al. [113] performs this linearization on the purely elastic version of the Marmottant model (Equation 2-29 with the elastic term set to Equation 2-30 in the region of $R_{buckling} \leq R \leq R_{break-up}$. This linearization yields the following equation for the encapsulated resonance frequency (Equation 2-33), which mirrors the un-encapsulated resonance frequency equation with the addition of the term $4\chi/R_0$, which incorporates the shell elasticity. Similarly, by examining the damping of the system, a linearized version of the shell viscous damping term can be approximated to Equation 2-34.

For the detailed implementation method please refer to [113]. In addition, this linearization can be applied to any of the previously detailed models to derive their characteristic parameters.

$$f_{0\_encapsulated} = \frac{1}{2\pi}\sqrt{\frac{1}{\rho R_0^2}\left(3\gamma P_\infty + \frac{2(3\gamma-1)\sigma_w}{R_0}\right) + \frac{4\chi}{R_0}}$$

Equation 2-33

$$\delta_{shell} = \frac{4\kappa_s}{R_0^3 \rho \omega_0}$$

Equation 2-34

To make use of these relationships one needs to extract the resonance frequency and then work backwards to derive the shell parameters. One of the most common methods to parameterize such a model is by examining the scattering or attenuation characteristics of a population of MBs [123], [134], [140]–[142]. To do this, a bulk suspension of MBs are insonated with a swept range of frequencies and the backscattered signal or attenuation spectrum is recorded. The resonance frequency can then be determined as either the frequency of max scattering or of max attenuation.

There are a few caveats to bear in mind in these experiments. Firstly it is generally the case that the scattering experiments require a higher applied acoustic pressure to get a satisfactory signal to noise ratio than the attenuation. This higher pressure can lead to a disruption of the MBs or the inducement of amplitude oscillations, which would push the response outside the bounds of small oscillations. As such, it is typically attenuation data that is used for MB characterisation.

There are also a number of pressure and frequency dependent effects to bear in mind when dealing with MB response. MBs have been shown to have a pressure dependent resonance frequency [142], [143]. Therefore, using this method to characterize the MB at one pressure does not necessarily mean that those parameters are correct to predict MB response at a different pressure range. One of the reasons for this could be the shear thinning and strain softening behaviour, as described earlier. The higher the pressure the larger the shear and strain rate.

The other important piece of information required is the resting radius (R_0). In this case, where bulk suspensions of MBs are used, this can prove problematic. MB populations will have a mean size that is usually quoted in the manufacturer specifications; For example, SonoVue has a mean radius of approximately 2 μm yet the size distribution quotes that 98% of the MBs are below 8 μm and 99% are sub 15 μm.

A more applicable way to parameterize these models would be to examine the responses from individual MBs. With the earlier advances in MB modelling, there simply were not the experimental techniques available to observe the MBs at this level of detail, and hence the bulk acoustic approaches to MB characterisation. Now, however, there are a number of techniques available to the experimentalist.

The first of these, and the one that really started to reveal some of the complex mechanics of MB responses and interactions was that of the high speed camera. This technique looks at the dynamic response of single MBs with an ultra-fast frame rate (of the order of millions of frames per second) and allows for the radial oscillations of a MB to be directly examined. This technique has revealed a number of previously un-described phenomena. Chief amongst these is the "compression-only" behaviour [133], by which a MB shows very little expansion compared to a high degree of compression, which was attributed to large changes in a MB material properties and was the driving force behind producing non-linear MB models. Some of the other observations that high speed photography has revealed will be discussed in Section 3.2.

The high speed camera offers a number of advantages. The initial radius of the MB can be optically sized to remove any ambiguity. With the initial MB size known, one needs to simply

insonate a single MB at a range of frequencies to determine the frequency of maximum response and hence find the material properties in the same fashion as before. Another advantage is that multiple MBs of various radii can be examined to provide size dependant properties also. This has been implemented by a number of authors on both the Hoff and de Jong (linearized Marmottant) models [127], [144]–[146]. One of the key findings when parameterising these models was the initial radius dependence of the elasticity and viscosity parameters [113], [135], [147], [148].

In addition to high speed photography, one can also observe the radial time curves indirectly by way of light scattering [128], [136]. This technique takes advantage of Mie scattering, which examines the scattered light from small particles, specifically that when a light beam is directed towards a small particle, the light intensity for a given angle of backscatter can be related directly to the particle size. By flowing a very dilute suspension of MBs through the focus of the light whilst insonating the MBs, a high throughput and interrogation of single oscillating MBs can be achieved.

This is the one clear advantage that light scattering has over high speed photography, which by nature is quite a time consuming operation for multiple MBs. Once the radius time curves of the MBs have been extracted, it is then a case of parameterising to the linearized equation as before. Because of the high throughput, many more MBs can be used to form this characterisation.

The above papers parameterized the Hoff, de Jong and Chatterjee/Sarkar models from the same datasets. They concluded that all three models could be parameterized in such a way so as to generate very similar results and that the different parameters of the three models are all related to each other. They too remarked upon the seemingly radius-dependent nature of the shell parameters.

2.5.4 Limitations of models

The main problems and limitations with these models is down to the increasingly complex parameters that are included, what they physically mean in relation to the MB and lastly, how to extract and fit their parameters.

The early models (Hoff, de Jong etc.) had parameters with very real underpinnings – an elastic and viscous term. However, they were obviously vastly simplified and could not replicate some of the complex nonlinear phenomena observed in experiment. To account for this, models such as the Marmottant and later the Paul and Doinikov were developed. These models included non-linear behaviour of the shell properties, but in order to implement them a number of

parameters had to be introduced in a slightly ad hoc fashion. Taking the Marmottant model as an example, in addition to the shell elasticity and viscosity terms, which were fitted using the resonance curve extraction at low acoustic pressure, two additional parameters had to be fitted – the buckling radius and the break-up radius.

In the original paper [129], it states that the MBs at rest in solution will tend to their buckling radius because in this state, the surface tension and hence the Laplace pressure on the MB is at a minimum. It also states that this will occur rapidly in solution in accordance with Equation 2-7. The break-up radius, however, is a far harder parameter to fix. In real terms, the breakup radius occurs when the area expansion undergone by the MB exceeds the maximum area tolerable for the number of lipids in the MB surface. Under Langmuir trough conditions, this rupture point is found at or slightly below zero surface pressure i.e. the surface tension of water (if this value is negative it means that the lipids are exerting an attractive force above the surface tension of water) [149].

Typically though, rupture occurs when the surface tension reaches that of the air water interface (0.072 N/m). Setting the break-up radius to the value of the air-water interface surface tension results in a simulation that does not display compression-only behaviour to the same degree as experiments; in fact, the rupturing of the MB is shown to be one of the determining factor in whether the MB exhibits compression dominated, symmetrical or expansion dominated response.

To achieve the compression-only behaviour observed (in the variable pressure regime, Figure 3.8 of reference [129]), with the pre-fixed values for elasticity, viscosity and buckling radius, it was found that a value for the breakup surface tension of almost twice that of the air-water interface was required, with little discussion on the physical underpinnings of such a result. Going further, when examining individual cases of MB oscillation, particularly when referring to compression-only behaviour [129] or sub-harmonic behaviour [146], values for the break-up surface tension are unfeasibly large so that the MB will never enter a ruptured or expanded state. Values of 1 N/m are used – almost a 14-fold increase on the air-water interfacial values.

This changing of parameters to fit the case that one is studying seems relatively common practice, and does ensure that a good fit with experimental results is achieved. However, the applicability of those parameters for the prediction of new results could be questionable. This holds true for the subsequent models (Paul, Doinikov etc.) also, though they may have the advantage in this situation because all the parameters that require extracting feature in their linearized versions and so can all be fitted simultaneously.

With all these fitting techniques, one issue still remained; that of the radius dependant material properties [113], [127], [128], [135], [136], [147], [148]. Both elasticity and viscosity were seen to vary with oscillation rate/excursion. This suggests that there could be more complex rheological behaviour underpinning the MB shell parameters than is accounted for, even with the more complex models.

As a final point, it has been shown how this parameterization is conducted within the regime for linear oscillations, but then used to model the MB under non-linear conditions. Previously, it was stated in both the cases of using the Langmuir trough data and the seemingly size dependent nature of the MB properties that rate could be a determining factor. The use of linearized properties for a non-linear model could be seen to be an extension of the same point.

2.6 Secondary Dynamics and Acoustic Phenomena

2.6.1 Effect of boundaries

Nearby boundaries have been shown to have a profound effect on the dynamics of MBs and will be found in almost all applications or investigations of MBs. Boundaries can include those found in an experimental setting, such as the surface of a capillary fibre or test cell, as used in most experiments. They can also include those found in a clinical setting, such as blood vessel walls. In fact, in the case of targeted imaging where a MB population is targeted towards a pathology expressed on the endothelium, the presence of the boundary is intrinsic to the situation.

Near a boundary it has been shown that for relatively large radial excursions, MBs do not oscillate in a symmetrical fashion [39], [40], [150]. Figure 2-9 shows some of the effects that being positioned near a boundary has. From above, the MB can be seen to behave almost spherically; from the orthogonal view, however, the shape oscillation can be seen to be highly non-spherical. These kind of oscillations were first predicted by Strasberg [151], and have been shown to enhance the production of subharmonic signals i.e. signals found at half the insonation frequency above a certain threshold pressure [40].

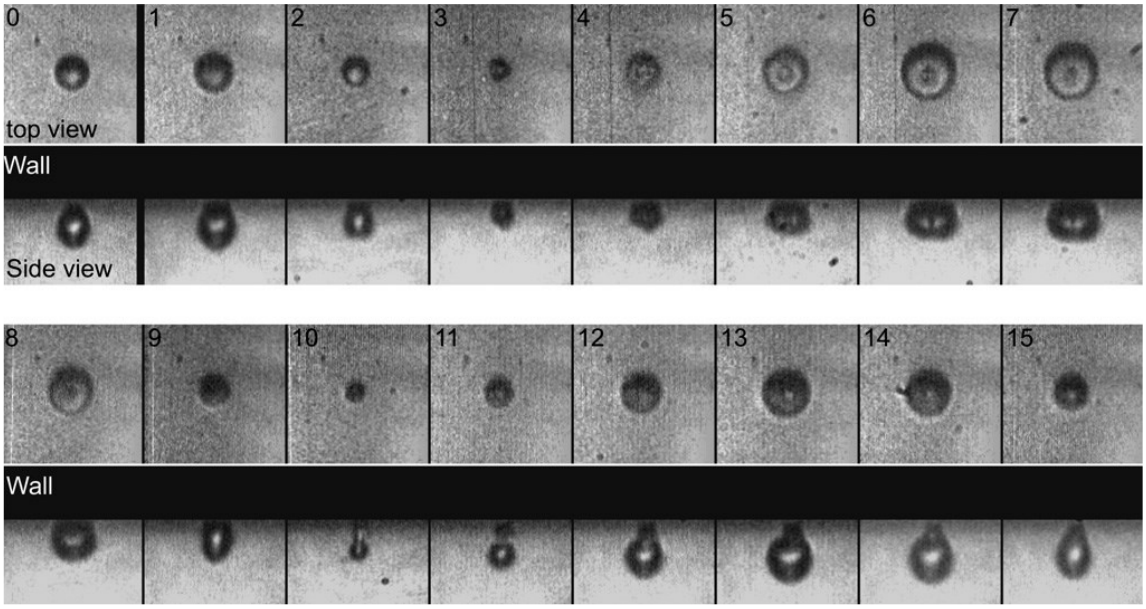

Figure 2-9: High speed camera frames showing MB non-spherical oscillations when in contact with a boundary (images taken from the top and side views). MB radius = 2.3 µm, acoustic pressure = 270 kPa with a centre frequency of 2.25 MHz. Image reproduced from [40]**.**

A number of other boundary-specific phenomena can also be seen in Figure 2-9. Images 5–7 show the presence of a jet directed away from the boundary. These jets occur due to large inertial forces coupled with the asymmetrical MB deformation, resulting in regions of the MB showing high degrees of curvature [152]. The jet's direction, velocity and effect on the MB's persistence have been shown to be highly dependent on the boundary material. The jet tends to be directed towards the interface for hard or rigid boundaries, whereas near a free or soft interface the jet is directed away from the interface [153][154].

The effective stiffness and size of the boundary have been shown to have further effects than just the direction of jets. It has been shown to affect the resonance frequency and relative amplitude of oscillation. Initially, much focus was placed on the response of MBs next to a rigid boundary in the application of underwater explosions. Large free bubbles near a rigid boundary were shown to be directly analogous to a bubble oscillating in phase with a mirror bubble an equal distance on the far side of a boundary [151], [155]. This bubble image method has been shown to be valid in a number of situations[156], [157].

In more recent works, the effect of boundaries on MBs have been shown both numerically and experimentally to decrease natural frequency of oscillation and typically the amplitude as well [41], [42], [158], [159]. Interestingly, [41] showed an increase in the amplitude of response from MBs adjacent to a rigid boundary.

The key difference between this study and the previously mentioned ones is that this study was looking at populations of MBs rather than MBs in isolation. The increase in signal was attributed to bubble aggregation and hence coherent summation of signals. [160][161] also numerically explore the effects of MBs in vessels and examines, not only the stiffness but also the physical dimensions. This was shown to dramatically affect the response of MBs: as stiffness increases, resonance frequency decreases until it approaches that of a rigid tube. This work is supplemented by [162] which shows that resonance frequency also decreases with decreasing vessel diameter, although this is made more complex by the relative size of the MB to vessel, as well as the physical position of the MB in the vessel.

Work on more compliant boundary surfaces, however, has told a different and much more complicated story. Experimental papers have demonstrated a number of effects. [43] showed that there can be a significant reduction in both the amplitude of peak response, while values of up to 50% reduction are quoted and support a previous paper [163], as well as the frequency of max response decreasing by as much as 20% compared to the MBs unconstrained natural frequency.

Reference [164] studied the effect of wall proximity using optical tweezers to examine a range of distances to the boundary and found that both the frequency and the amplitude of maximum response actually behaved in an oscillatory manner, both increasing and decreasing about the value at the boundary. Values varied as much as 30% for the frequency and 110% for the amplitude. This was performed using the same boundary material as [43]. When a very compliant wall was examined – that is, a wall with low stiffness – these oscillatory responses were not evident.

2.6.2 **Acoustic radiation force**

In addition to the oscillatory motion previously described, a MB in an acoustic field will also experience a translation motion along the acoustic field due to an acoustic radiation force. These forces were first outlined by Bjerknes (1906) [165] (the radiation forces are commonly referred to as Bjerknes forces as a result) and are due to the force created by the time averaged pressure gradient acting on a MB.

In a travelling wave situation (i.e. not a standing wave) primary radiation force is shown to act to drive the MB away from the sound source [166] and consequently have been cited as possible mechanisms to the direction of MBs to specific regions and to improve the binding efficiency of targeted MBs, and as such, have been the focus of a number of studies [167]–[169]. [170] optically

examined relatively large MBs at low insonation frequencies and found that factors such as acoustic pressure, pulse length and MB size, specifically in terms of resonance, all demonstrably affected the radiation force experienced. [109] went on to show the potential of acoustic radiation force to move MBs towards target surfaces both *in vitro* and *in vivo*; however, these were conducted without the presence of targeting molecules.

References [108] and [38] expanded upon this work to include the effect of the primary radiation force on adhesion efficiency. They noted that the radiation force increases the MB concentration at target site. Pressures ranging from 22 kPa to 120 kPa were examined, which are relatively low in comparison to some US applications. Up to 60-fold increases in adhesion efficiency were noted for the highest pressures, which could be highly beneficial in molecular imaging applications. The caveat to using an approach such as this to improve binding at a target site is that before using this technique, the user must have a good idea of the position of the pathology in the first place in order to direct the radiation force.

In addition to the primary radiation force, there is also a secondary radiation force (also referred to as the secondary Bjerknes force). This force arises because as a MB oscillates in an acoustic field, it re-radiates an acoustic wave. As this radiated wave interacts with a nearby bubble or boundary, this generates a small force by the same mechanism of the primary radiation force generation. Due to the much smaller pressure re-radiated by the MB and the inverse square law of pressure from a point source, one can see that this force will only act of a very short distance [167], [171].

This secondary radiation force is also subject to size-dependent phenomena, resulting in either an attraction or repulsion force between MBs. [172] shows that MB larger that their resonance size will attract each other. Similarly, if one is larger than the resonance size and one is smaller they will also be attracted; this is due to the relative force difference exerted by each MB, at or near resonance there can actually be a repulsive effect. However, this is found only in specific regions of MB radii and insonation conditions.

Typically, this repulsion is overcome by population effects of multiple MBs and leads to the reversible aggregation of MBs [173]. In their aggregated state, however, the clump of MBs has very different acoustic properties than the individual MBs that it comprises of. Furthermore, the aggregate of MBs could be large enough to pose a risk of embolism *in vivo.* Both these effects have to be considered when using MBs clinically.

Another effect of this secondary force is that MBs are drawn towards a boundary. As previously mentioned, a MB oscillating near a rigid boundary is mathematically equivalent to a MB oscillating in phase with a mirror bubble [151], [155]. This mirror analogy goes as far as to provide its own secondary radiation force attracting the bubble towards each other and hence towards the boundary. This in isolation could prove useful in the adhesion of MBs to target sites, particularly in regions of low flow/shear rates such as capillary beds. However, a problem arises because these MBs are rarely in isolation.

A number of studies have focussed on the effect that multiple bubbles have on each other in adhesion circumstances [105], [171], [174]. These papers examine the effects of secondary radiation force on the adhesion characteristics. Needless to say this is a small force in comparison to primary radiation force; however, it can provide sufficient inter-bubble force to detach the MBs from a targeted surface.

In regions of low vascular flow rate, this does not pose too great a problem; however, if this is coupled with high vascular flow rate it can lead to complete MB removal from the target area. This can be mitigated somewhat by the continued application of a primary radiation force towards the target area, or by the increased affinity of the ligand to target molecule. [174] goes on to discuss how secondary Bjerknes forces could be used to probe the binding force of molecularly targeted MBs, a field of interest which at present is little understood.

2.6.3 Microbubble destruction

There are three principle methods by which MBs are destroyed during use: static diffusion, acoustically driven deflation, and inertial cavitation. The topic of static diffusion was overviewed in Section 2.4.1, giving the reasons for it occurring and the methods by which its effects are mitigated for long MB longevity, both in storage and in use. As such, the remainder of this section will be examining the effects of acoustically driven deflation and inertial cavitation.

Acoustically driven deflation is an increased rate of MB shrinkage due to the changing MB shell conditions brought about by insonation. In section 2.4.1, it was shown that the factors affecting static diffusion were the gas concentrations at the bubble surface and the surface tension of the interface. During insonation, both these parameters will vary with expansion and contraction relevance hence the rate of deflation will also vary with time. This phenomenon has been examined by a number of groups [33], [175], [176] and have shown that the dependence of applied acoustic

pressure, frequency of insonation and size of MB are all contributing factors in determining the magnitude of deflation and hence the MB longevity.

Inertial cavitation occurs when the MB is insonated with a very high acoustic pressure. Under these conditions, the MBs undergo vast volumetric changes, and upon rarefaction, the inertial forces of the fluid overcome the wall's ability to recover and the MB fragments into several smaller MBs [175]. This cavitation behaviour requires a certain pressure level before its onset; this is called the cavitation threshold, and is shown to be dependent on the MB resting radius, applied pressure, transmitted phase and centre frequency [32], [175], [177]–[179]. To a lesser degree MB shell chemistry also plays a role [180]; however, at the types of pressure generally employed (1-2 MPa), the effect of shell chemistry is subtle compared to the previously mentioned factors.

With radial excursions noted in excess of 500% in this regime [175], this can lead to a number of bio-effects [181]. This is especially true if one considers a MB near a boundary at the same time. Wall velocities in the region of several hundred ms^{-1} [178] have been recorded, as has the presence of phenomena such as jetting. Bio-effects include increased vascular permeability [182]–[184], sonoporation [185] as well as cell death in exposed tissue [184]. These effects, if carefully understood and controlled, could prove beneficial when coupled with targeted drug or gene delivery, allowing one to introduce a drug or transfect with genetic material directly into a cell whilst keeping the cell viable [11].

An important point to note when discussing acoustic deflation and fragmentation with regards to lipid MBs is that the damage done to the MB need not be catastrophic for it. The self-assembling nature on the lipids means that if the gas is still available i.e. has not immediately dissolved then the MB can reassemble itself and still retain its sized/composition-dependent properties. This is in comparison to the more rigid (polymer/albumin) shelled MBs, which cannot repair themselves after damage and subsequently dissolve as free gas bubbles. Lipid encapsulated MBs therefore can have a greatly increased persistence after insonation [175].

2.7 Current Imaging Strategies

In fundamental B-mode imaging, where backscattered echoes are received at the fundamental or transmit frequency, MBs offer considerable enhancement over standard tissue returns due to their enhanced echogenicity as a result of their gas core. While this mode can and has been used in situations such as ventricular examinations [186] this method will begin to lose

effectiveness in regions with low blood-to-tissue ratios, due to the relatively low doses of MBs in the image volume. Furthermore, only examining the fundamental returns does not make use of the non-linear signals which MBs produce.

To exploit the harmonic signals generated by MBs, a number of harmonic or non-linear strategies have been developed. Figure 2-10 gives an example of the type of harmonic signals that can be taken advantage of for the development of imaging protocols. Shown are the fundamental response (f_0), sub-harmonic ($f_0/2$), 2nd harmonic ($2f_0$) and an ultra-harmonic ($3f_0/2$). Other harmonics exist further up and down the spectrum; however, in terms of the acoustic regimes discussed in this thesis, these are the most prevalent and as such will be focussed upon.

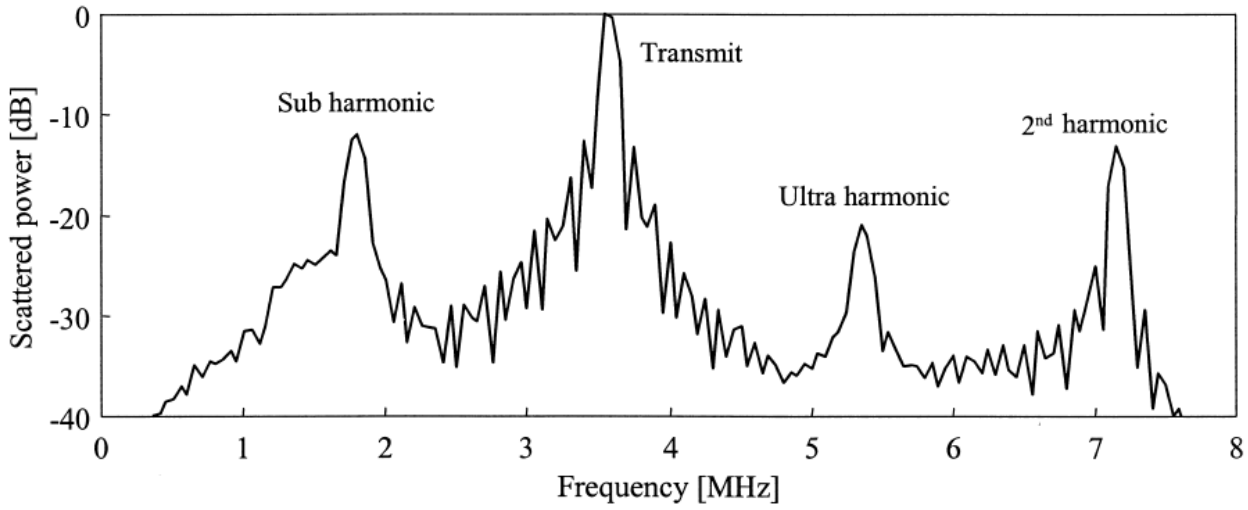

Figure 2-10: Example scattered spectrum of SonoVue. Centre frequency 3.5 MHz, PNP 75 kPa, 40 cycle pulse length. Visible are the fundamental and harmonic responses. Image reproduced from [187]

Harmonic mode imaging transmits at one frequency and then receives at a whole or half integer frequency steps [188]. These harmonic signals are brought about due to changes in the MB response over the course of the acoustic cycle[189].

One of the most prevalent forms of this method is 2nd harmonic imaging, which receives scattered signals at twice the transmit frequency. This method provides a much greater contrast to tissue ratio (CTR) than conventional fundamental imaging and has been used effectively for the enhancement of a number of organs and pathologies such as liver legions [190], myocardial perfusion [191] and tumour perfusion [23].

However, 2nd harmonic imaging does have a number of issues that need to be overcome or accounted for. Typically, in US imaging it is desirable to use relatively short cycle pulses in transmit. These short pulses mean that good spatial resolution can be achieved, but do also mean that the signals have a wide bandwidth. With 2nd harmonic imaging, one needs to ensure that the higher frequency signals received are actually generated by the MBs and not just an artefact of a relatively wide bandwidth fundamental frequency. Therefore, to achieve this longer narrower band, excitation needs to be used, which in turn has a detrimental effect of the spatial resolution achievable [192], [193]. A trade-off therefore has to be reached between contrast and spatial resolution, depending upon the situation the imaging is employed. One method of boosting the contrast signal is to employ higher acoustic pressures; however, this can bring about MB destruction effects.

Pulse inversion (PI) imaging seeks to overcome this issue with 2nd harmonic imaging. Pulse inversion works by sending two pulses in quick succession, the second pulse sent with a phase difference of π radians to the first [192]. Linear scatterers, such as that from tissue in most low powered scanning situations, respond to the pulses in a linear fashion, while non–linear scatterers, such as MBs, respond to the same US pulse in a non-linear manner. By then summing the two received echoes, the linear echoes will cancel each other out, whereas the non-linear echoes will sum to leave a residual signal from the "even" harmonic returns i.e. ½, 2nd, 4th harmonics etc.

This has a number of advantages over simple harmonic imaging. Firstly, because the signal from linear scatterers is cancelled out, it effectively suppresses the signal received from blood and, to a lesser extent, tissue. This leaves a significantly enhanced CTR. Furthermore, PI imaging means that there are no conflicts in transmit and receive frequency overlap, so the whole bandwidth of the transducer can be utilised with wideband insonation. Hence, the spatial resolution problems of harmonic imaging are overcome. In addition, PI imaging offers the advantage that MBs oscillate non-linearly at very low acoustic pressures [188]. This means that non-linear residual echoes can be detected at low insonation pressures, allowing for longer imaging protocols with regards to MB destruction and acoustically driven dissolution.

The main drawbacks in the use of PI imaging are that the attainable frame rate is cut by a factor of two due to two pulses required for each image and that it is very susceptible to motion artefacts, the result of which is an imperfect cancelling of the linear portion of the signal and a false positive non-linear return. Another issue that can arise comes from the propagation of nonlinear signals through tissue [194]. Similarly, the use of amplitude modulation (AM) [195] rather than phase modulation can be used to suppress the linear responses. Using this technique provides the added advantage of preserving some of the odd number harmonics [196]. As a downside to the use

of AM typically will involve at least 3 differing pulses being needed for one image, resulting in a loss in frame rate, as with PI. These two techniques can be used in conjunction with each other, allowing for even better contrast at lower acoustic powers and hence lower MB disruption.

Harmonic, PI and AM imaging have also been applied to improve power Doppler imaging. Doppler imaging is a method by which the frequency shift caused by the motion of scatterers relative to the transducer is detected and spatially tracked. One can display the relative change in frequency, called the Doppler frequency. This provides velocity information about the scatterer and is commonly referred to as colour Doppler. Or, by instead creating an image from the power of the Doppler signal, an image with more sensitivity to low flow and small vessels is produced. This is called power Doppler [197]. Power Doppler can be severely affected by body motion; however, with the application of any of the above mentioned imaging techniques the linear responses from tissue can be supressed and hence the effect of body motion can be reduced.

One version of harmonic imaging that requires special mention is that of sub-harmonic (SH) imaging. SH signals are generated at half the transmission frequency and their generation is frequency, acoustic pressure and cycle length dependent [146], [198], [199]**.** SH signals offer a number of advantages over the other harmonic imaging strategies. SH harmonics are not generated by tissue (apart from in the most extreme acoustic regimes found well outside the bounds of most clinical practice). This means that the image artefacts produced from non-linear propagation are not present in SH imaging. In addition the lower frequency waves are not attenuated as much as the higher harmonic signals, which allows for higher contrast signals from a greater depth penetration.

Working against SH imaging are a few points. Firstly, the low frequency allowing for less attenuation also brings with it a reduction in resolution. One method to retain comparable resolution is to increase the transmit frequency, currently an area of great interest [200]. Another potential issue is the onset threshold for SH generation. This means that a minimum acoustic energy is required before SHs are generated at a detectable level, and could lead to reduced persistence for MBs due to acoustically driven dissolution. Recent papers suggest that in certain situations, SH signals can be detected even at very low acoustic pressures. The appearance of these signals at energy levels below the predicted values is attributed to the properties of the encapsulation medium. Therefore, with careful material selection the required higher pressures can be avoided and persistence increased [201].

MB destruction can also play a useful role in different imaging techniques. The most common of these is that of destruction – reperfusion. In this technique, MBs perfuse the target area and

provide contrast enhancement. The MBs are then disrupted by way of a high acoustic pressure pulse to remove the MBs and hence the contrast enhancement. By then tracking the increase in enhancement with time, one can see how quickly MBs re-perfuse the target tissue and hence the blood perfusion. This has shown particular potential in the field of myocardial perfusion [186]. This technique can also be further optimised by the application of one of the above mentioned imaging modes.

2.7.1 **Functionalization**

Specific issues present themselves when utilising MBs for targeted imaging purposes. One of the purposes of using molecular targeting of specific pathologies is to either detect at an early stage for diagnosis purposes or measure effectiveness of treatment. In both cases the size of expression or relative change in expression will be small. This means that the number of MBs retained at the target site will be low, certainly in comparison to the bolus injection given to the patient. Therefore techniques are required in order to maximise the signal attainable from these MBs adherent to the target site, whilst if possible reducing or rejecting signals from the unbound MBs freely flowing around the vasculature, as well as tissue suppression[37], [38].

The first technique to achieve this is simply that of clearance. Figure 2-11 shows a representation of how the free and adherent MB concentrations vary after injection. The freely circulating MBs are typically cleared from the circulatory system via the lungs and other excretory mechanisms after a period of the order of 10–20 minutes. The targeted MBs on the other hand achieve a lower rate of increase in concentration at the site of interest due to the affinity of the targeting ligand to the biomarker and the probability of the MB being in close enough proximity to achieve adhesion.

Similarly, peak concentration occurs at a later time point and also requires longer to be cleared from the body. This longer clearance time is because once bound to the specific area the MBs do not repeatedly pass through the heart and lungs and the associated pressure regimes that are highly detrimental to a MB's persistence. By delaying the time between injection and imaging, the difference between the two concentrations can be maximised.

Obviously, there is an optimum time point to perform the imaging because even when stationary, the MB will continue to be removed from the system, even if only by static diffusion and dissolution, or uptake by phagocytes. The main drawback to this approach is that the concentration of MBs actually retained at the target site can be very low, depending on binding affinity and blood flow/shear rate, and the concentration will decrease over time. These constraints mean that the imaging of small pathologies can be problematic or lacking in sensitivity [202].

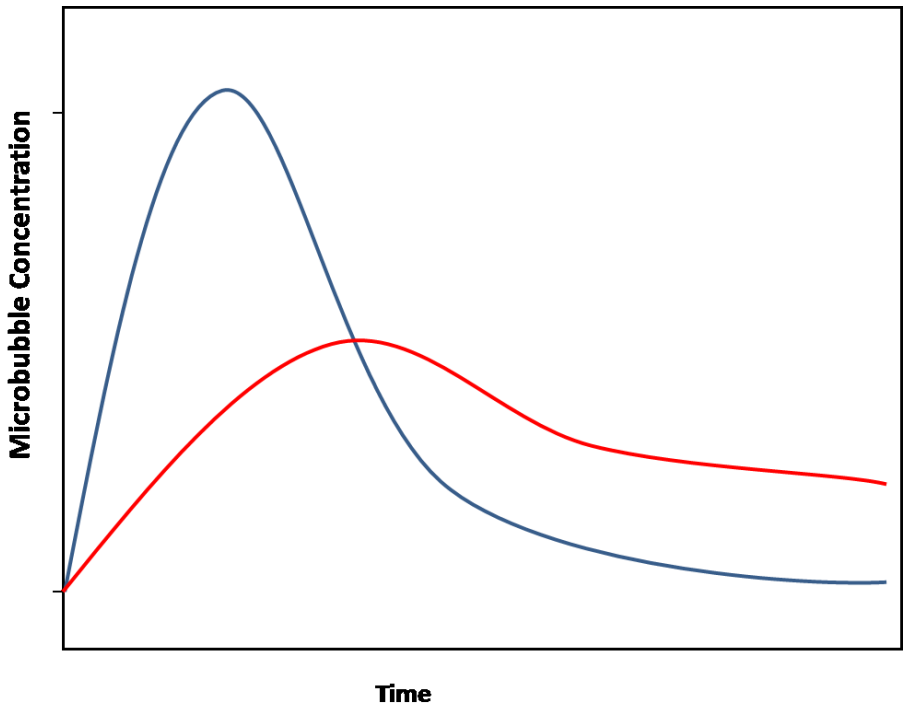

Figure 2-11: Cartoon representation of the accumulation and retention times of targeted MBs. The blue line indicates concentration of freely circulating MBs. The red line indicates the targeted MBs. Timescale of the order of tens of minutes

One possible solution is the use of the primary radiation force to direct MBs towards a target area and then isolate the adherent MBs by way of image subtraction; an approach known as the image-push-image technique [38].

Specifically, this technique uses multiple imaging pulses interspersed with radiation force pulses. Initially a background image is taken that contains both tissue and MB echoes. A regime of low frequency low acoustic pressure radiation force pulses are then utilised to increase the accumulation of MBs at the target site. A second round of images are then taken, consisting of tissue, free MB and bound MB responses. By subtracting the first set of images from the second set, the accumulation of MBs can be detected. Using this technique increases in adherent MB enhancement of 30 dB.

The second way to approach the differentiation issue is by way of filtering. In section 2.7 a variety of methods were shown for the differentiation of tissue response from MB response. To then separate the signals from the adherent MBs from the free flowing MBs, a low pass temporal filter can be applied between successive frames, which effectively removes the contributions of any fast moving MBs[38].

This kind of technique has been applied using a variety of the tissue suppression imaging sequences, such as sub-harmonics [203] and high harmonics, specifically transmit low receive high (TLRH) imaging [204].

2.8 Summary

The response of MBs to US is explored along with the effects that each of the constituent parts of a MB has. Factors such as shell material, internal gas properties, insonation pulse characteristics, local environment conditions – i.e. pressure, gas saturation, as well as local boundary conditions – all play a role in determining the overall dynamics of a MB's response.

By understanding these effects, various imaging strategies have been developed that make use of a MB's non-linear response and thereby increase the applicability and functionality of US. Molecular imaging using US still has a number of obstacles to overcome, namely the differentiation of signals from adherent MBs with respect to the non-adherent MB. Currently this is best achieved by methods that either rely on waiting periods and hence a reduced signal intensity, or by the application of multiple pulse sequences and/or multiple filtering methods, both of which incur time and frame rate penalties. It is postulated that by carefully exploring the effects of the conditions imposed by adhesion and characterising them both experimentally and computationally, new imaging strategies can be formulated that can differentiate adherent from non-adherent MBs.

3 Materials and Methods

3.1 Abstract

This chapter is formed of three distinct sections.

The first section outlines the available techniques for the study and characterisation of MBs under varying experimental conditions remarking on their applicability to this current study. The significant papers which have been generated as a result of their application are also detailed. Continuing from this the experimental techniques chosen for use in this thesis are described including a full rationale behind that choice.

The second section describes the efforts made to produce a testing system capable of performing the required testing. This system was required to be able to acoustically activate individual MBs under a range of boundary conditions and to detect the responses. In conjunction information was required about the size of the MB under examination as one of the key factors in determining their subsequent response. Issues through this development are highlighted along with the steps required to mitigate or control them and the implications that this has on the testing procedure.

The final section of this chapter concerns the validation of the testing rig and testing procedure. This is performed by recreating previously data using a similar experimental setup. Single MBs covering a size range 1 – 6 μm were insonated at frequencies ranging from 2 – 4 MHz, their fundamental and 2nd harmonic scattering was recorded. Good agreement is reached between the data from this chapter and the previously conducted study and general theory. Other parameters thought worthy of interest were also extracted, these included the MB stability and the shape of the MB response. Further issues with the testing rig and procedure are also flagged for later improvement.

Aspects of this work, particularly that of Sections 3.4 and 3.5 was presented at the IPEM, Physics & Technology of Medical Ultrasound conference, 2011. York, UK under the title "*Acoustic Characterisation of Single Ultrasound Contrast Agents: Applications in targeted imaging and therapy.*"

3.2 Evaluation of Microbubble Interrogation Techniques

There are a number of experimental techniques available to the researcher to examine microbubbles. These will be briefly examined along with their associated advantages and disadvantages and important papers which have been generated through their application. On top of which the use of computer modelling is vitally important to the progress of this field however to inform the models experimental parameterisation must be conducted first. The field of computer modelling and its implications will be fully covered in Chapter 6.

There are generally speaking two experimental methods of examining the characteristics of MBs. The first is to examine the properties of bulk populations and infer characteristics through bulk trends and averages, the second is to examine single MBs individually and build up a picture of how a group or population would respond to a given stimuli.

3.2.1 Bulk population approach

By examining the population response one is receiving a signal made up of the summation of the scattering and interference from all the MBs in the insonated region. In the experimental volume there will be a range of MB with differing sizes which will all react differently depending on their size and bubble characteristics. In addition to this there will be significant effects from bubble-bubble interactions [171], [173], [205]

This technique is typically concerned with the scattering and attenuation characteristics of a given pulse through a MB cloud. One of the main advantages of this method it that it's relatively simple and cost effective to implement, typically requiring one transducer for insonation and either another transducer or a hydrophone in the receive function; a typical setup is shown in Figure 3-1

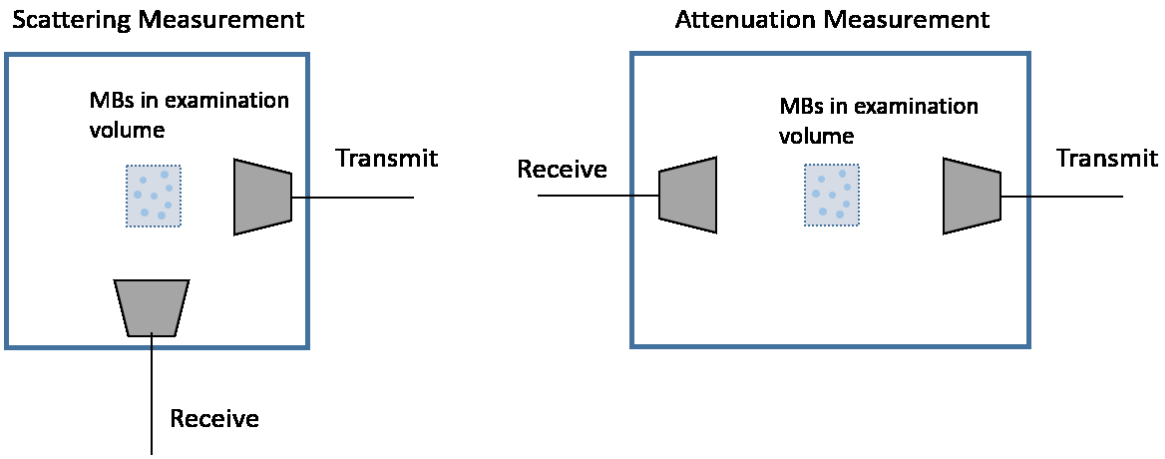

Figure 3-1: Schematic of the typical setup used in bulk scattering (left) and attenuation (right) measurements. Wire ends go to pulse creation and data logging/visualisation equipment (not shown)

Using this kind of set up Tang et al. [143] showed that as the applied pressure is increased the attenuation coefficient of a MB population increases. At 100 kPa the attenuation coefficient is shown to be an order of magnitude higher than the baseline attenuation (at an acoustic pressure of 1 kPa). A similar effect could not be detected for the scattering response of MBs. Emmer et al. [206] extended this work and came to agreement with respect to the pressure dependent attenuation coefficient. Their extension was to remove the larger MBs from the population so the remaining population had a radius < 3 µm. With the contribution from the large MB removed a strong correlation between scattering power and applied pressure.

The attenuation measurements have also been used for the purposes of parameterising some of the MB models as described in Chapter 2. The frequency dependent attenuation spectrum is intrinsically linked to the MB resonance [142]. By then applying one of the linearized models in conjunction with *a priori* knowledge of the MB size distribution one can parameterise the MB shell characteristics (cf. Section 2.5.3 and Equation 2-34 and associated discussion). This technique has been utilised in a number of studies [114], [134], [207]–[209] and has been shown to effectively simulate the approximate response of MBs. This method does have a number of drawbacks however. Using the attenuation characteristics of a whole population of MBs for the fitting of one or two shell parameters means that any variation between MBs is ignored; it will be shown later in this chapter and also subsequent ones that there can be, and generally is a large degree of variation between MBs of different sizes but also between MBs of the same size. This variation is not accounted for in any way by these bulk acoustics. Similarly some specific experimentally observed

phenomena such as “compression-only” behaviour [133] or thresholding effects [179], [206], [210] cannot be replicated with these types of model.

There have been a few notable attempts to examine more detailed situations using bulk population measurements. Doinikov et al. [41] attempted to examine the response of populations of MBs near a rigid boundary and noted that the MBs near the boundary gave a higher level of scattering than those freely floating. In order to achieve this, a very limited population was examined, of the order of 100 MBs in the population and the observed effect was actually attributed to a more coherent summation of responses. The boundary effectively fixed the bubbles in one region and hence produced a higher level of scatter compared to those MBs which were free to circulate.

The applicability of the bulk population examination could be extended if the wide size populations of MBs could be limited then more detailed size specific effects could be examined [211]. The refinement of MB size distributions has typically been achieved by way of exploiting the differential floatation times of different MB sizes [209], [212], [213] however in recent years there has been increasing focus of the generation of monodisperse populations of MBs by way of manufacture in microfluidic devices. These devices have strictly controlled flow rates of shell material and core gas so that tight regulation of MB diameter can be achieved [214]–[216]. The current hurdle to overcome with microfluidic manufacture is the production rate achievable which is currently far behind standard MB generation techniques [217]. Gong et al. [142] utilized microfluidic generation to create populations of MBs with very narrowband size distributions and then examined these populations using the bulk acoustic methods described above. It was noted that in addition to the pressure dependent scattering and attenuation as noted previously there was also a shift in resonance frequency with applied acoustic pressure; as the acoustic pressure was increased the resonance frequency of the MBs was decreased.

3.2.2 **Single bubble approach**

The second method of MB characterisation is that of single MB examination, there are a number of different technologies available for the interrogation of MBs. These range from direct observations, such as high speed photography of the radial dynamics and direct acoustic observation through to indirect methods including atomic force microscopy or light diffraction.

Static analysis can also be achieved on a single bubble basis using atomic force microscopy (AFM). This technique rests a cantilever of know material properties i.e. spring constant, on the surface of a MB. By then varying the force on the lever and measuring its deflection the material properties of the MB can be inferred. Using this technique Chen et al. [218] and Sboros et al. [219], [220] showed that there is an apparent trend of increasing MB stiffness as MB radius increases. In addition Abou-Saleh et al. [221] demonstrated that there is also an increase in stiffness when a protein targeting layer is incorporated into the MB shell, in this case a streptavidin layer. AFM has also been used to quantify the adhesion forces between targeted MBs and their targets. Sboros et al. [220] probed the interactions of an antibody-antigen binding between MBs and cells and found adhesion forces to be consistent with known literature. AFM has shown its potential for the detailed understanding of some MB properties however it does have one major drawback. That is that all testing is performed at static or quasi-static loading conditions. For the purposes of understanding the dynamic response of MBs there are a number of rate dependant effects simply not addressed by this method.

For the dynamic study of MBs one of the most widely utilised techniques has been that of high speed photography. This technique looks at the dynamic response of single microbubbles with ultrafast frame rate cameras (of the order of millions of frames per second). This allows for the radial oscillations of a microbubble to be directly examined allowing for the fitting of data to theoretical models and the shell properties determined. One of the most active research groups in this area is the de Jong group based at the Erasmus MC, Rotterdam. The group developed their own high speed camera called the Brandaris 128 [222]. This camera operates with a frame rate of 25 MHz and is capable of taking 128 consecutive frames. At such a high frame rate the harmonic behaviour of MBs can be optically captured for most clinical frequencies. The highest frequency behaviour able to be captured reliably is given by the Nyquist frequency, for a 25 MHz frame rate the highest frequency behaviour observable will be of the order of 12.5 MHz

Using this system a number of key papers have been generated observing many previously undescribed phenomena. Van der Meer et al. [113] utilized the camera to essentially create a resonance curve for each MB examined in a single run. This was achieved by insonating the MB through a range of frequencies and finding the frequency of maximum response. This peak response was then used to parameterize the linearized form of the Marmottant model (cf. Section 2.5.2). This technique was termed MB spectroscopy and was one of the first papers to show shell parameters that changed with MB radius, specifically this showed that the shell viscosity increased with radius.

Sijl et al. [133] observed “compression-only” behaviour for the first time, noting that it could be represented as a non-linear low frequency modulation of the fundamental scattering. Again by relating this back to the linearized Marmottant model deduced that this effect could be simulated by a changing initial surface tension.

Vos et al. [176] studied the effects on acoustically induced deflation on MB response and noted decrease in MB to repeated insonation. This work was subsequently supported by Thomas et el. [223], [224] who further characterised the disruption of the MB as its size was irreversibly driven through the resonance radius.

The presence of boundaries was initially investigated by Dollet et al. [39], [40]. Non-spherical oscillations were observed near a boundary which increased in magnitude with increasing pressure. Interestingly these studies also use the high-speed camera to view the orthogonal view of the MB. Typically the high speed camera only views the MB from a single view; the top down view typically, these studies however captured both the top and side views and showed there are considerable difference in the modes of oscillation. The effect of boundaries was expanded upon by Garbin et al. [163], [205] who employed optical trapping techniques in conjunction with the high speed camera to control the distance between MB and boundary. It was noted that as the distance to the wall decreases the amplitude of oscillation is significantly reduced. In the same papers the effect of nearby MBs was also examined. The magnitude and phase of the MBs was seen to be affected by both the size of the MB with respect to their resonance frequencies and also the distance between the bubbles. Secondary Bjerknes forces were observed acting to force the MBs closer together. The effect of this was explored in further detail by Garbin et al. [174], [225] who used secondary Bjerknes as a method to unbind adherent MBs from a target surface. With knowledge of the MB sizes and distance between them the magnitude of the secondary Bjerknes force could be quantified and hence the strength of the adhesion bond could be measured.

Sub-harmonic generation has also been an area of interest for high speed camera examination. Sijl et al. [199] examined SH behaviour of MBs at low acoustic pressure and observed that SH generation occurred at pressures far below that predicted by conventional theory, pressures as low as 5 kPa were reported, parameterisation of the linearized Marmottant model could reproduce these effect but the authors state that the values used for some of the model parameters were orders of magnitude away from the typical values and it was simply an effort to see what would be required to produce these effects. Faez et al. [146] examined SH generation at frequencies ranging from 8-12 MHz at a range of acoustic pressures. Approximately 40% the MBs examined exhibited SHs, the range of MBs exhibiting SH was spread over the size range examined. This work

was then extended to the observation of SH *in vivo* [226]. In support of the previous results SH generation was shown to be present in 44% of MBs examined

There are a few drawbacks associated with high speed photography however. Firstly of the "Brandaris" type cameras capable of such high frame rates there are only currently two available, of which one can be used for academic study, as such demand is very high and the group in ownership's output is prolific. Below that level of camera there are many models which can achieve up to 1 MHz frame rates and a multitude in the kHz frame rate bracket. The use of these cameras requires either a reduction in insonation frequency to one far below typical ultrasound use, or, the use of stroboscopic effects to try and fill the dataset; neither of which are ideal for the characterisation of systems which are known to be both rate dependant and subject to change over repeated insonation. In addition the use of high speed camera radial data to inform the parameters used for modelling has a number of issues. Using purely radial information ignores any non-spherical oscillation, oscillations which have been shown to occur at even moderate acoustic conditions when in the presence of a boundary [39], [40].

Laser diffraction has been shown as an indirect method by which MB size information can be obtained and has been used for measuring the size distribution of MB populations. Mie scattering theory shows that the angle light is diffracted from a point source (in this case a MB) can be directly related to the size of the point source [227]. By then incorporating acoustic excitation to the MB as it passes through the laser, time varying size information can be obtained [128], [136]**.** This radial response to an applied ultrasound pulse can then be used in the same manner as the high speed camera obtained radial motion for the parameterisation of theoretical models**.** This technique benefits from being able to have a constant flow of MBs through the laser region (provided the solution is dilute enough to ensure that only single MBs are present in the region at one time), and hence allows for a greatly increased capture rate of data; Data collection rates for high speed photography and single bubble acoustics is far slower in comparison. The use of flow however does mean that situations such as adherence; where the MB is fixed to a target surface and therefore stationary, are not so easily examined without incurring similar timing issues governing the rate of data collection as found in high speed photography or single bubble acoustics.

Single bubble acoustics examines the acoustic responses of single microbubbles in isolation and can be coupled with optical information allowing for microbubble sizing and observations. As a

method of characterising bubble response its resolution is unparalleled due to the significantly faster sample rates achievable with transducers and digital recorders; Sampling rates of the order of GHz are easily achieved meaning that far higher insonation frequencies be used than for high speed photography. There has been a consistent move toward the use of high frequency US for imaging purposes due to the superior resolution achievable [228], similarly the length of the dataset collectable is only limited by available computer memory allowing for longer and complex pulse sequences to be examined than attainable with high speed photography.

Early work on single MBs was typically concerned with the destruction behaviour of MBs. Typically single MB interrogation was achieved with either a tight acoustic focus and a very diluted flow of MBs (e.g Shi et al. [229]) or by utilising even more dilute solutions and clinical scanners (e.g. Guan et al. [230]). These papers developed an understanding of the effect of acoustic amplitude, pulse length, and repetition rates had on MB destruction and also highlighted phenomena such as MB fragmentation. Sboros et al. [231] continued in this vein and also examined the response of single MBs using a very dilute suspension of MBs and a clinical scanner. In this way paper the scattering cross-section of two MB compositions was examined. It was shown that scattering cross-section increased with applied acoustic pressure, furthermore it was shown that MB disruption occurred resulting in the escape of the encapsulated gas to form free MBs. In a continuation of this work Sboros et al. [36] improved the test rig so that a single MB at a time was interrogated using a clinical US scanner. In this way the absolute backscatter from a single MBs was achieved with the ability to differentiate both the fundamental and 2^{nd} harmonic scattering characteristics. In this setup however the sizing of MB for direct comparison with theory was not available

Sijl et al. [232] created a testing rig for the acoustic interrogation of single MBs using single element transducers with the incorporation of a microscope objective to obtain sizing information on the MB. Using this method single MBs were examined at two acoustic pressures, their resulting backscatter was compared to that predicted by theory for unencapsulated and encapsulated MBs. The incorporation of shell parameters improved the fit of this data. Extending this work Sijl et al. [145] then combined the above single acoustics test rig with the Brandaris 128 high speed camera in order to validate both techniques and to evaluate the ability of transforming radial data into a scattered pressure and vice versa. It was found that good agreement could be achieved in the examination of a MBs fundamental response however the acoustic characterisation was more sensitive to 2^{nd} harmonic signal generation while the high speed camera more clearly detected the low frequency component i.e. sub-harmonics, of MB response and also gave a clearer view of “compression-only” type response.

3.3 Rationale behind the experimental approach taken

Given the techniques available and the end goal of understanding the effects that processes such as adhesion plays on it was chosen to focus on the acoustic characterisation of single MBs for the majority of experimental characterisation. The reason for this choice, and for the exclusion of other techniques is given below.

Bulk acoustics have been shown to be good for general characterisation studies however their inability to provide the required detail about specific dynamic situations i.e. MBs next to or adherent to boundaries, means that as a technique it was discounted as an available methodology.

Focussing on single bubble characterisation methods it was important to strike a balance between equipment availability, feasibility and the ease of use/data collection. Access to the Brandaris high speed camera in Rotterdam would have been possible to obtain however would have been severely limited due to its extensive use by the de Jong group in Rotterdam and so was not considered feasible as the main basis of experimental study. Other high speed approaches were available and it was also possible to arrange access to a fast framing camera (Cordin 550 fast-framing camera) via the EPSRC equipment pool. This camera had a maximum frame rate of the order of 2 MHz. Due to the aliasing and the fact that primarily the interesting MB response occurs in the harmonic generation it meant that insonation pulse could have a maximum frequency of approximately 0.5 MHz and as such was not directly relevant to current clinical systems. In terms of resonance radius this means examination of MBs of the order of 12 μm in diameter which is significantly above the mean diameter of all commercially available MBs. The use of this camera was also subject to booking and sharing via other institutions and was problematic to reproducibly setup. With these constraints high speed photography was dismissed unless a very specific experiment or hypothesis could be tested when it would prove feasible to have the time on a high frame rate system.

At the time of study efforts were being made in the group to setup a light scattering test rig similar to the one presented in [128], this setup up was only in the initial stages of development was proving to be more complicated than previously imagined. The use of a flow cytometer as used in [136] was also a possibility however any attempt at such a modification to an existing machine was at a more undeveloped stage that the light scattering test rig. As such both avenues were omitted, at least until the method could be proven to be reproduced in our facilities. At the time of writing these methodologies had largely been neglected in favour of other projects/techniques.

Acoustic characterisation however showed a great deal of potential. The equipment required was readily available, namely sensitive transducers and amplifiers, these had already been incorporated into the groups' bulk acoustic test rig as had previously been used in [67], [143], [194]. The choice of transducer and its bandwidth determined the frequency range and hence MB radii range which was to be interrogated, their relative cheap cost meant that this could be easily changed and optimised if changes in the experimental plan was required. In addition the fact that direct acoustic response data would be collected was seen as advantageous. Any effect observed by techniques such as the high speed photography or laser diffraction are inherently measures of the MB radial change which then have to be converted to a radiated pressure as would actually be received by an ultrasound system (This is covered in detail in Section 6.3 of Chapter 6). This conversion from a radial response to a radiated pressure is based on a number of assumptions i.e. spherical oscillations. These assumptions are known to not necessarily be true for MBs near boundaries and could lead to erroneous pressure responses being predicted or not incorporated in the output. Instead by collecting the acoustic response it means that any observed phenomena is a direct product of the MB response to ultrasound. One must note that the collection of acoustical data means that when one attempts to relate the observed response back to the theoretical models the reverse must be performed, the acoustic data has to be converted to a radial response and as such may experience similar problems, the key difference being that the phenomena has already been found experimentally.

The main components missing for the acoustic interrogation were the ability to optically size MBs before insonation and a method for the confocal focussing of all components. The development of this, the systems implementation and validation will comprise the remainder of this chapter.

3.4 Single Bubble Acoustics Test Rig

3.4.1 Design

For the interrogation of single microbubbles a test rig similar to that described by Sijl et al [232] was designed, built and developed. A schematic of the test rig and peripheral systems can be found in Figure 3-2 and Figure 3-3 below.

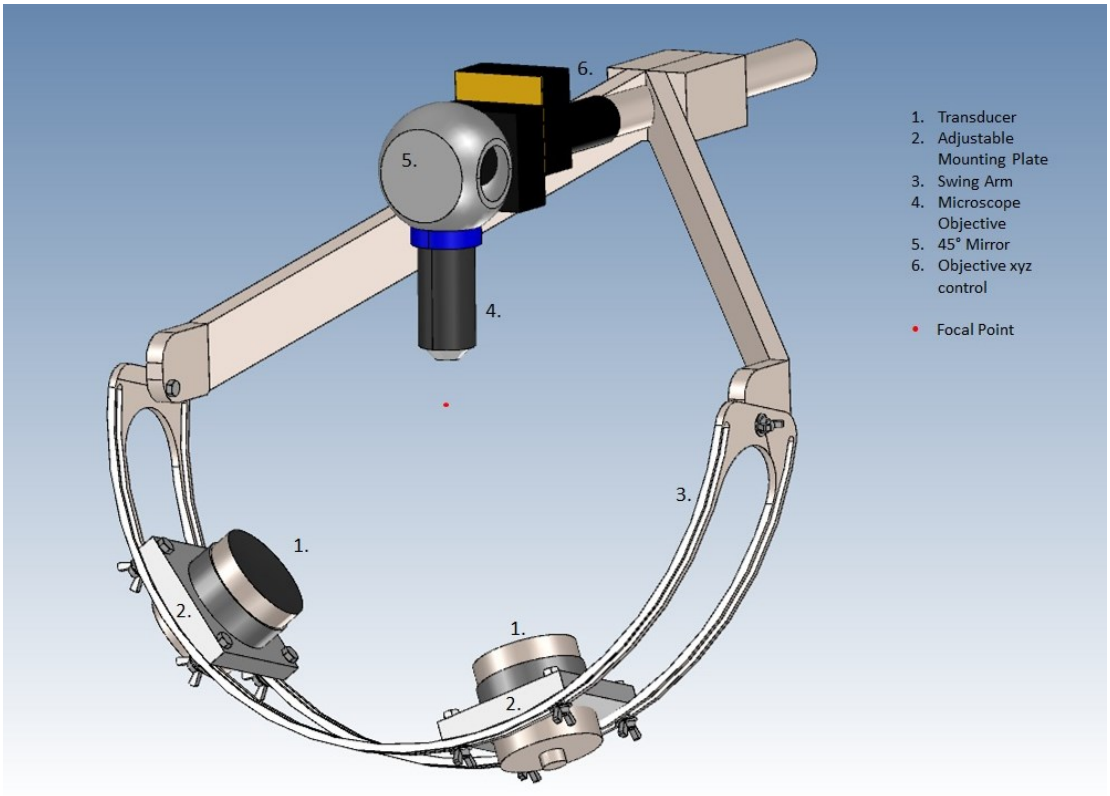

Figure 3-2: Testing Assembly

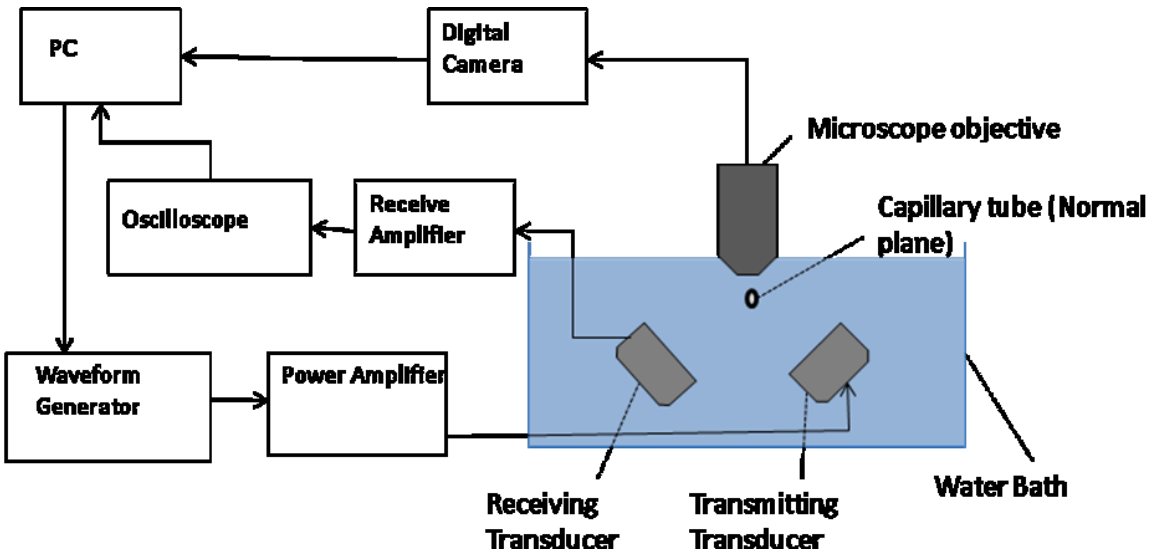

Figure 3-3: Schematic of the test rig and data collection systems

In overview, a pair of matched transducers (Panametrics, V380, 3.5MHz centre frequency, focal length ≈75mm) were focussed to a central point in conjunction with a 40x water immersible objective (LUMPlanFL N 40x W Olympus). The transmitted signal was generated in an arbitrary waveform generator (Sony Tektronix AWG2021) and amplified through a power amplifier (E&I 2100L). The receive signal was then in turn amplified by a pulser/receiver working in the receive mode to perform as an amplifier (Panametrics-NDT 5800) and displayed via a digital oscilloscope (Sony Tektronix TDS7154).

The image from the microscope objective was directed to an off the shelf digital camera (Canon ProShot G5) through a 45° mirror for subsequent offline sizing. The whole system was then controlled via a desktop PC and an in-house developed Matlab Programme (Mathworks, Natwick MA, USA). The capillary fibre (RC55 8/200 Membrana GmbH, Germany) was mounted on a 3-axis translational stage (Newport M-562, CA, USA) which allowed for its placement at the focal point and subsequent translation as required by the experiment.

3.4.2 Transducer Characteristics and Alignment

One of the key factors in the setup of this equipment was to ensure that the focal points of the transducers and optics were confocally aligned. To ensure this was achieved a set procedure was utilised for the alignment of the transducers and optics. One transducer was positioned in a fixed mounting bracket; this was designated the receive transducer and all other equipment was aligned to this. The second transducer, was positioned in an adjustable, spring mount allowing for three dimensional translation of the focal region. To achieve an initial alignment a 500 micron metallic target bead suspended on a 200 micron diameter wire at the focus of the receive transducer. The focus was determined at the position of peak response with the pulser/receiver set up in pulse-echo mode, the time of flight of the pulse gave this position as 78 mm from the transducer surface. With the target bead left *in situ* the second transducer could then be aligned, this involved adjusting the spring mounting plate until the position of the target bead for peak response was coincident with that of the receive transducer. The objective was also mounted on a 3 axis stage allowing for its precise positioning over the target bead.

A number of issues presented themselves with the rudimentary alignment presented above. Any asymmetry in the target bead, for example, surface aberrations or interference by the mounting wire, caused interference in the received signal and meant that trying to compare and match the pulse echo responses from the transducers proved cumbersome. In addition the optical field of view was approximately 200 μm in diameter, as such the use of such a large target bead meant that the optical alignment could be up to ± 300 μm out of alignment with the transducer focus.

It was noticed that in certain situations gas bubbles, typically < 100 μm in diameter, would either spontaneously form on the capillary fibre or could be created by the agitation the water bath. Owing to the gas saturation of the water bath these bubbles could persist for long periods of time. Care had to be taken to ensure that these were not present during the experiments, however, during the setup and alignment phase the isolation of these relatively large bubbles (in comparison to the MB under investigation) not only provided a highly echogenic, symmetrical targets for acoustic focussing but also were smaller than the optical field of view allowing for significantly improved optical alignment. Using this method it was then possible to achieve a much tighter focus with all the components. To verify that the transducers were aligned the transducer positions were altered until the frequency responses to an impulse from both transducers were similar. See Figure 3-4, averaged power spectra results (n=30), transducers driven with an impulse with a peak negative pressure of 100 kPa. The slight changes in the frequency response between the two transducers was

also evident in pulse echo experiments against a solid reflecting target. This indicated that the transducers were not perfectly matched to begin with, however, where corrections for the transducer impulse response are used later in this thesis this slight discrepancy has been accounted for with transducer specific response data.

Calibration data for the transducers can be found in the Appendix 9.1

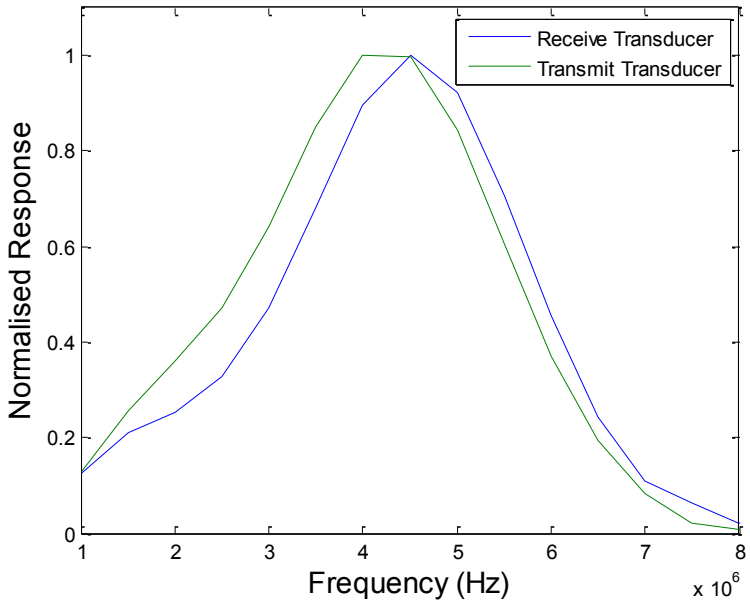

Figure 3-4: Normalised response of both transducers when focussed on a large bubble.

3.4.3 Optical Calibration

Optical calibration was performed using latex sizing beads (1, 3 and 5 µm diameter, Beckman Coulter, CA, USA). The beads were optically imaged and sized based on image intensity to determine their radius. To determine the robustness of the sizing technique multiple images of populations of the three different beads were examined. Edge detection was conducted based on image intensity and the particle size as a number of pixels was determined. This resulted in an average error of 0.1 µm in particle radius and a maximum error of 0.14 µm independent of particle size. This approach is based on Helfield et al. [200]. Final optical calibration was found to be 25 pixels/µm. This was verified before and after each days testing to ensure that the system remained stable throughout experiments.

3.4.4 **Clutter**

During initial testing it was noticed that the nearby presence of supporting equipment could cause interference in the received signal.

To minimise interference created from the supporting equipment the test rig design incorporated ways to alter the position of the transducers relative to each other as well as their orientation to the normal plane of the test section; the swing arm and movable transducer mounts as seen in Figure 3-2. The transducers are mounted in such a way so that the angle in incidence and reflection are not equal (approximately 20 and 45 degrees respectively) furthermore the swing arm is angled so that the transducers were not positioned normally to the test area (approximately 10 degrees from the normal)

Note: The positioning of the transducers so that they were at a slight oblique angle to the capillary fibre produced a component of the primary radiation force along the axial length of the fibre resulting in MB movement when subjected to long exposure times [109], [169], [170]. For the purposes of the work presented here this did not pose a significant problem because the duration of pulses and applied powers were small enough to ensure that MB motion was minimal. For the pulse sequence used the maximum observed MB motion was <15 µm, acoustically this MB displacement will shift the resultant echo in time by approximately 0.2×10^{-9} seconds and can therefore be neglected. One must bear this in mind in the planning of future experiments if significantly longer pulses sequences or increased acoustic power will be utilised.

After minimising the interference from the supporting structures there was still interference present in the received signal. Figure 3-5 provides a visualisation of the form this interference took. The major contributor to this clutter noise were determined to be the presence of the microscope objective in the sound field (Figure 3-5A). As the microbubbles scattered sound in all directions a portion of the scattered wave interacted with the objective and reflected back to the receiving transducer causing an interference with the MB signal. The objective lens used in the experiment had a working distance of 3.3mm which increases the path length for the interfering echoes by ≈ 4.5 mm. For a 2MHz pulse this allows for approximately 6 cycles before interference can be expected.

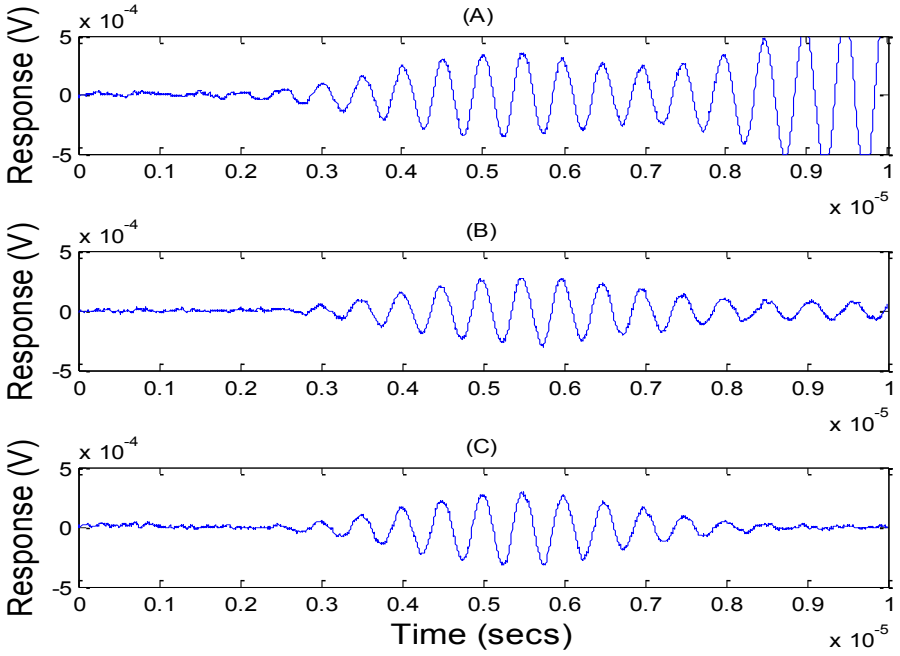

Figure 3-5: Time domain response to the same bubble (A) with the objective in place, (B) close to the free water surface and (C) free from clutter.

To overcome this problem the objective was removed from the acoustic field altogether after taking an image for sizing purposes. While this meant that real-time optical imaging of the bubbles could not be performed it did almost completely resolve the problem of multiple complex reflections.

Figure 3-5B shows the residual interference that remained after the objective had been removed from the field. The cause of this residual wasn't immediately apparent. This was eventually discovered to be reflections from the free water surface interfering in a similar way to the objective. The solution for this was far simpler. By increasing the depth of the capillary fibre the free surface reflections were moved out of the time window occupied by the MB response. Figure 3-5C shows the signal with clutter from the objective and free surface removed.

3.4.5 **Single Microbubble Isolation**

Another key issue that has to be overcome when conducting single bubble acoustics is how to ensure that the detected signal is the emission from just one bubble and not from a number of

bubbles in proximity. The area of acoustic focus was determined to of the order of 2mm in diameter (cf. Appendix 9.1) whereas the optical field of view is of the order of 200μm diameter. Practically what this means is that even though the optical field only contains a single bubble the acoustic field can contain many more. As a result the capillary tube each side of the target bubble has to be optically swept to ensure it is free of bubbles.

In order to achieve the correct spacing between microbubbles, the microbubble solutions had to be heavily diluted. This was typically of the order of 1:10000 although there was a certain degree of variation in this due to the buoyancy of the bubbles and variations in sampling techniques. It has previously been shown that the gas saturation of the solution plays a significant role in microbubble stability and longevity [56], [60], the result being that for all experiments the water bath and dilution medium were required to be left to equilibrate with the atmosphere before experiments could be conducted. Ideally they were left to equilibrate at a lower temperature than the one at which the experiments were to be conducted. That way when the water was brought up to experimental temperature (experiments were conducted at 20°C) it lost the ability to retain as much dissolved gas and one could be certain that the water was gas saturated. As previously alluded to the gas saturation could play a role in the spontaneous formation of bubbles in and around the equipment during experimentation, the presence of these bubbles in the sound field could lead to erroneous results so care had to be taken to ensure that there were none present for each set of data gathering.

When the separation between them is not quite sufficient for confident single bubble imaging it was possible to selectively destroy nearby bubbles leaving the target MB free. By having detailed knowledge of the effective area of acoustic focus is was possible to move the focal region so that the prospective target bubble was outside of the effective radius then by insonating at a high acoustic pressure any microbubbles in the field were destroyed. This would leave the prospective target bubble free from any nearby MBs. It was possible for the high pressure pulse to have a detrimental effect on the target MB as well. A number of studies have shown that even after repeated insonation and size change due to acoustically driven diffusion the newly sized MB will behave in the same manner as a fresh MB at the same size i.e. the history of MB insonation does not affect the subsequent MB response providing a the new resting radius is accounted for [176]. This technique showed potential for greater flexibility in the dilutions used by allowing for slightly under-diluted solutions to be made viable rather than simply discarded.

3.5 Single Bubble Examination of SonoVue® – Test Rig Evaluation

In order to establish the effectiveness and indeed the capabilities of this test rig a simple test case was required. The commercially available contrast agent SonoVue® (Bracco Diagnostics, Inc, Geneva) was used for this study. It is a phospholipid encapsulated microbubble which has been the source of intensive study using a variety of techniques [113], [127], [128], [143], [144], [148] and as such its behaviour is well documented.

The objective of this work is to provide evidence that the test rig functioned as designed and where possible recreating known data. Furthermore, the objective is to explore the possible parameters which can be extracted from the data to be used to direct future experiments. Specifically this will incur examining for changes in scattering properties, both linear and non-linear signal generation as well as determining the MB stability to insonation

3.5.1 Experimental Procedure

Using the experimental set-up as previously described in Section 3.4. The MBs were prepared as per the manufacturers' instructions, a small sample was then removed and diluted with 0.9% NaCl saline solution to achieve the required concentration to ensure that only a single MB was present in the area of acoustic focus.

Once a microbubble was located, isolated and imaged for sizing purposes the microscope objective was removed from the sound field and the US burst was activated. MBs were exposed to a range of pulses in an increasing frequency ramp. The frequency ranged from 2 MHz – 3.5 MHz in 0.25 MHz steps. The power delivered by a sound pulse can be approximated to the mean squared of the time varying amplitude. As the pulse frequency increases the wavelength decreases, therefore, for a set number of cycles the actual power delivered decreases with increasing frequency. To achieve similar power levels delivered across the frequency range it was decided to keep a constant pulse length; a full width half maximum of 3 μs for a Gaussian tapered pulse. In addition to this it was decided to keep all the pulses constant mechanical index (MI) of 0.07. The MI is a commonly used metric used in clinical ultrasound to assess the likelihood of mechanically induced bio-effects (i.e. cavitation) from an US pulse [233]. The MI is formalised in Equation 3-1 where PNP is the peak negative pressure in MPa and F_c is the centre frequency of the pulse in MHz. This MI equates to a

peak negative pressure of approximately 100 kPa at 2 MHz, rising to 130 kPa at 3.5 MHz and was selected sufficiently low so as not to immediately inflict bubble destruction [175], [179], [234].

$$MI = \frac{PNP}{\sqrt{F_c}}$$

Equation 3-1

At each frequency a pulse inversion pair was sent (cf. Section 2.7 for a description of pulse inversion imaging). Briefly this entails, 2 pulses with π radians phase difference between them, neglecting for bubble motion and deflation the summation of these pulses will cancel any linear scattering and return the non-linear residual segment of the signal. A bubble at resonance behaves far more non-linearly to thereby examining for these non-linearities is a good method for resonance determination.

To examine for changes in bubble response over successive pulses the frequency ramp was repeated a number of times (n=4) for each bubble giving a total exposure of 56 pulses per bubble. Tracking how the response changes as a function of pulse number will gives an indication of the MB stability to insonation.

3.5.2 Data Analysis

Data sets for 68 single SonoVue bubbles were recorded covering a bubble radius range from 1.2-5μm. Following an initial examination of the data, 23 datasets were rejected for a variety of reasons; insufficient signal to noise ratio and signal interference due to the presence of large bubbles in proximity being the two main reasons. The 35 remaining datasets were split into individual pulse sequences corrected for gain, windowed using a Hamming window and corrected by the frequency response characteristics of the transducers.

Where data is shown in decibels (dB) this is taken with reference to the noise floor. The noise floor was determined as the frequency dependent power spectrum of the whole experimental test system to a sham exposure (no MBs present) to a pulse of the same characteristics as used in the experiment. This was averaged over 10 repeated exposures (n=10).

3.5.3 **Experimental Results**

Figure 3-6 shows a typical dataset for a single bubble (Radius = 2.3 µm) in both the time and frequency domains. In the frequency domain both the fundamental response (2 MHz) and the bubble's 2nd harmonic response (4 MHz) are visible. By examining and collating the responses from a range of bubble sizes parameters, such as the radius of peak fundamental and 2nd harmonic response as a function of MB can be determined. For the purposes of clarity and ease of understanding the majority of the following results will be shown as a function of a single frequency, it must be recognised however that the acoustic responses are both frequency and size dependant. Where suitable, information is be given to show how the results change as a function of frequency.

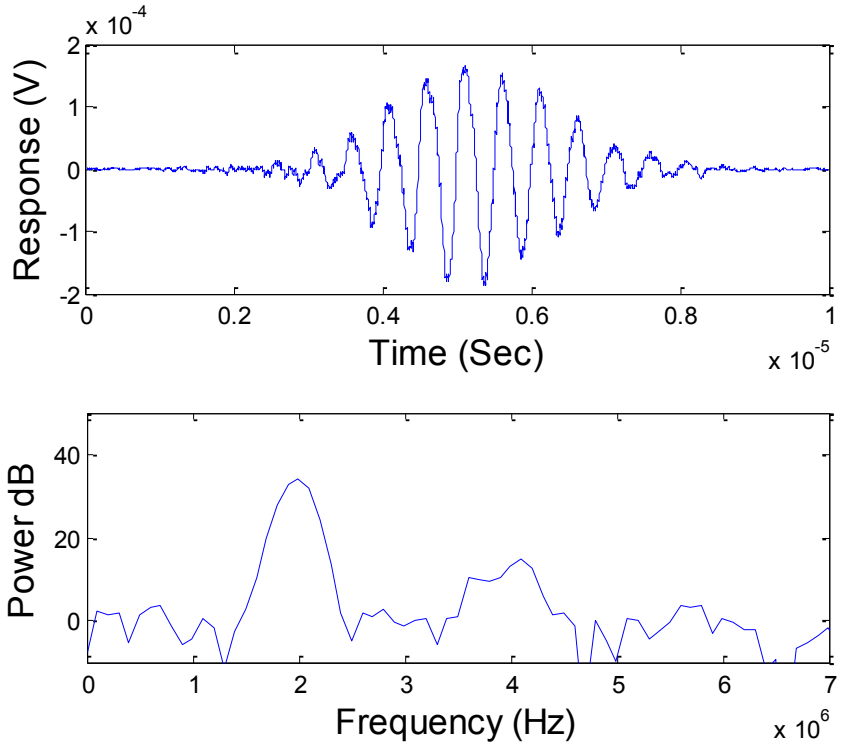

Figure 3-6: Example of the raw time and frequency response data gathered from a MB (R=2.3µm) insonated at 2MHz

3.5.4 Scattering

Figure 3-7 shows the power of the fundamental response of the population of microbubbles at 2MHz. Scattering theory [54] predicts that below the resonance size of the bubble there will be little scattering. When bubble sizes approach the resonance frequency the level of backscatter will increase dramatically, for a microbubble insonated at 2MHz the resonant size is approximately 2µm (cf. Figure 3-10) as demonstrated by the steep gradient in the is region. Above the resonance size the microbubble response is dominated by its size and geometric scattering cross section rather than its resonance response [54].

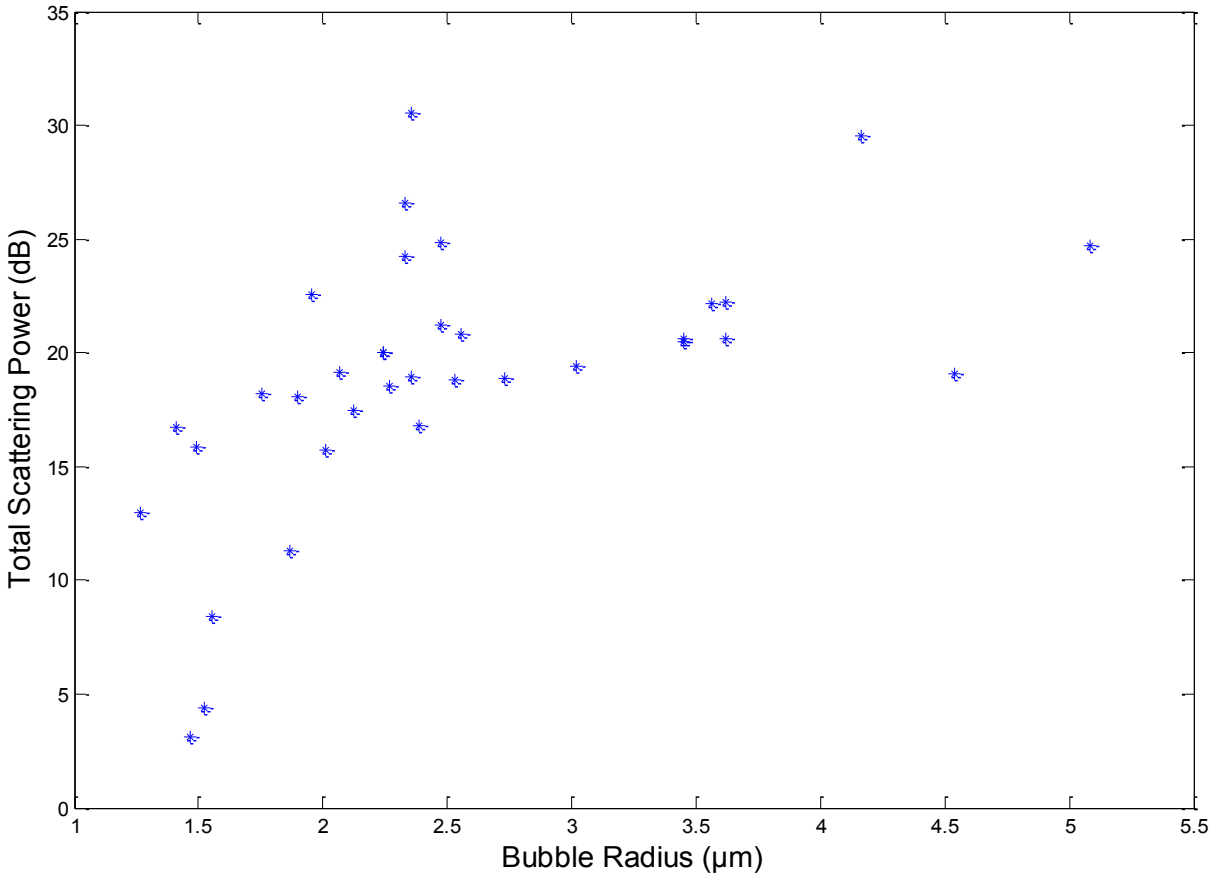

Figure 3-7: Peak scattered power at fundamental frequency. Insonated at 2MHz

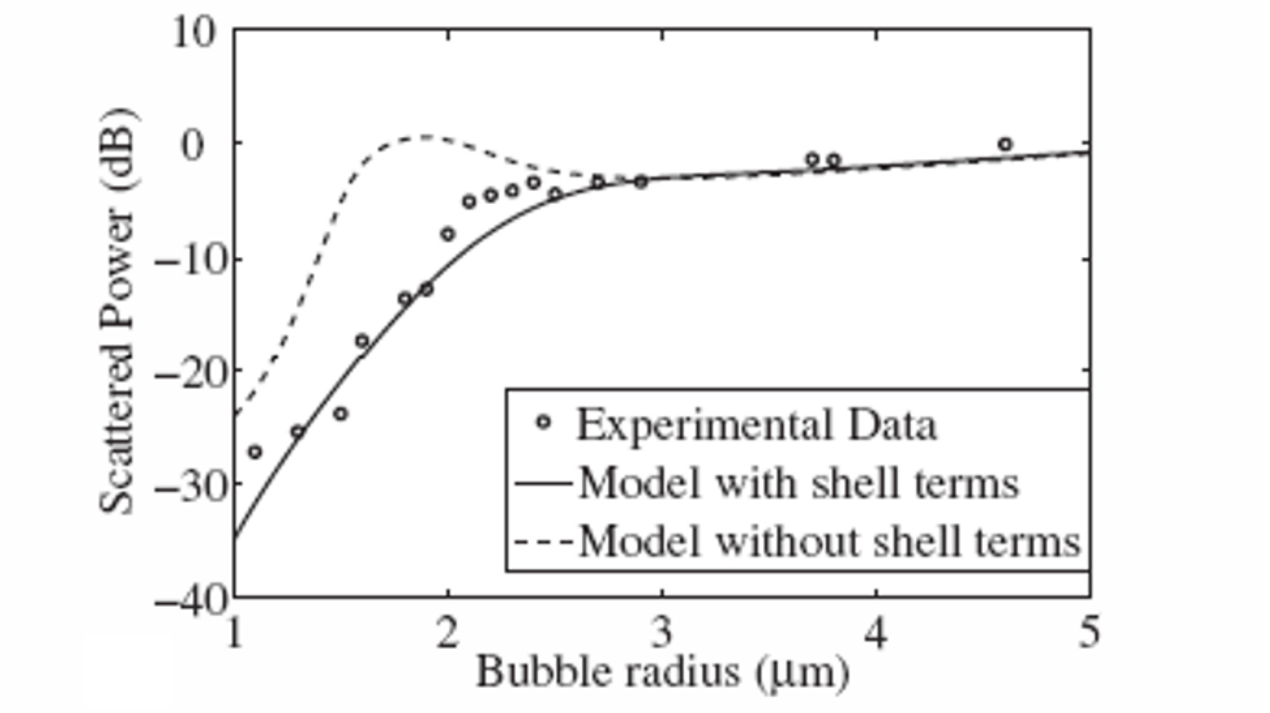

Figure 3-8: Scattering Power of the BR14 contrast agent at 2MHz, 100kPa Peak negative pressure. The difference in the y-axis compared to Figure 3-7 arise because Figure 3-7 is referenced to the noise floor whereas this figure is normalised to the peak response. Figure reproduced from [232]

To compare this data with an equivalent dataset from literature [232] Figure 3-8 expresses the scattering power from the contrast agent BR14 (Bracco Diagnostics, Inc. Geneva) when insonated in a similar testing regime; 2 MHz, 100 kPa PNP, 5 cycle pulse. BR14 is an experimental contrast agent produced by the same manufacturers as SonoVue. It is also a phospholipid encapsulated contrast agent containing perfluorocarbon gas core and for the purposes of this qualitative comparison is taken as analogous. It can be seen that the two trends shown in Figure 3-7 and Figure 3-8 are very similar in dynamic range, with approximately 25dB difference in response from the extremes of minimum to maximum response, similarly the radii of these extremes are seen to be the same. The difference in absolute values for scattering power are due to the reference level taken, the reference level for Figure 3-7 was taken as the noise floor of the system whereas Figure 3-8 used the peak response as the reference value.

Another key point in the qualitative comparison of these datasets is the shape of the curve, in particular the steep increase in scattering power up to a “knee” point of just above 2μm followed by a slower steadier rise when R>2.5μm.

It should also be noted that the spread or variability of data is apparently very different between the datasets i.e. the data published from Sijl et al. looks to be far smoother. This could

simply be an artefact of the data presentation. The data shown in Figure 3-7 is the output from all viable datasets collected with no averaging or smoothing applied. The data in Figure 3-8 in comparison is actually the result of averaging 42 data points, bubbles with a radius within ±0.1µm of each other are averaged (error bars were not included in the publication), to leave 17 data points.

When a MB is excited at its resonance frequency it generates a signal with significantly higher non-linear/harmonic components than a non-resonant MB. Figure 3-9 shows both the second harmonic power (taken as the peak response at twice the driving frequency i.e. receive at 4 MHz when insonated at 2 MHz) and also the pulse inversion residuals for the bubble population, again insonated at 2MHz.

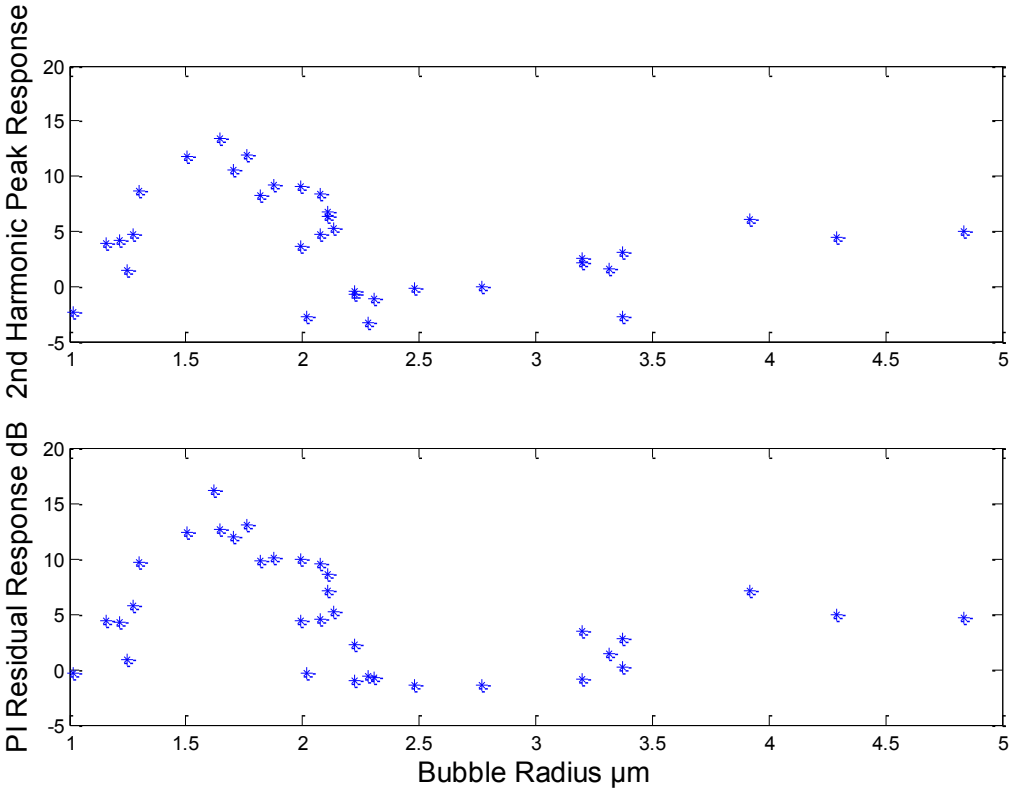

Figure 3-9: Harmonic (top) and Non-linear/Pulse Inversion Residual (bottom) responses of SonoVue at 2MHz.

It can be clearly seen that there is an increased response in both the second harmonic generation and the pulse inversion residuals just below the 2 µm radius mark. Although the two traces are very similar there are a few discrepancies between them, these can be attributed to phenomena such as motion or deflation between the pulse inversion pulses. If this occurs then the linear response for the second of the PI pulses comes from a MB under slightly different conditions.

As such the linear responses do not perfectly cancel out and hence a slightly different non-linear residual is returned [165].

The resonance size can then be extracted as the radius of peak harmonic generation data and compared with those predicted by the literature [144], [147]. Figure 3-10 shows the peak second harmonic generation as a function of the insonation frequency in comparison to the natural frequency of an unencapsulated MB (solid blue line) as given by Equation 3-2, and that of an encapsulated MB (dashed green line) as given by Equation 3-3 with a shell elasticity (χ = 0.54 N/m) [113] Please refer to Section 2.5 for a full explanation of these equations. It can be seen that the experimental results gathered here fall within these two bounds if tending towards the lower bounds of this region. This in itself is not unduly surprising due to the pressure dependent nature of MB resonance [142], at acoustic pressures below 100 kPa MB response has been shown to act in accordance with the models for encapsulated MB, as the acoustic pressure is increased the trend is for more unencapsulated-like behaviour [142]. The error bars are the estimated sizing error in peak resonance radius detection.

$$f_0 = \frac{1}{2\pi}\sqrt{\frac{1}{\rho R_0^2}\left(3\gamma P_\infty + \frac{2(3\gamma-1)\sigma_w}{R_0}\right)}$$

Equation 3-2

$$f_{0\_encapsulated} = \frac{1}{2\pi}\sqrt{\frac{1}{\rho R_0^2}\left(3\gamma P_\infty + \frac{2(3\gamma-1)\sigma_w}{R_0} + \frac{4\chi}{R_0}\right)}$$

Equation 3-3

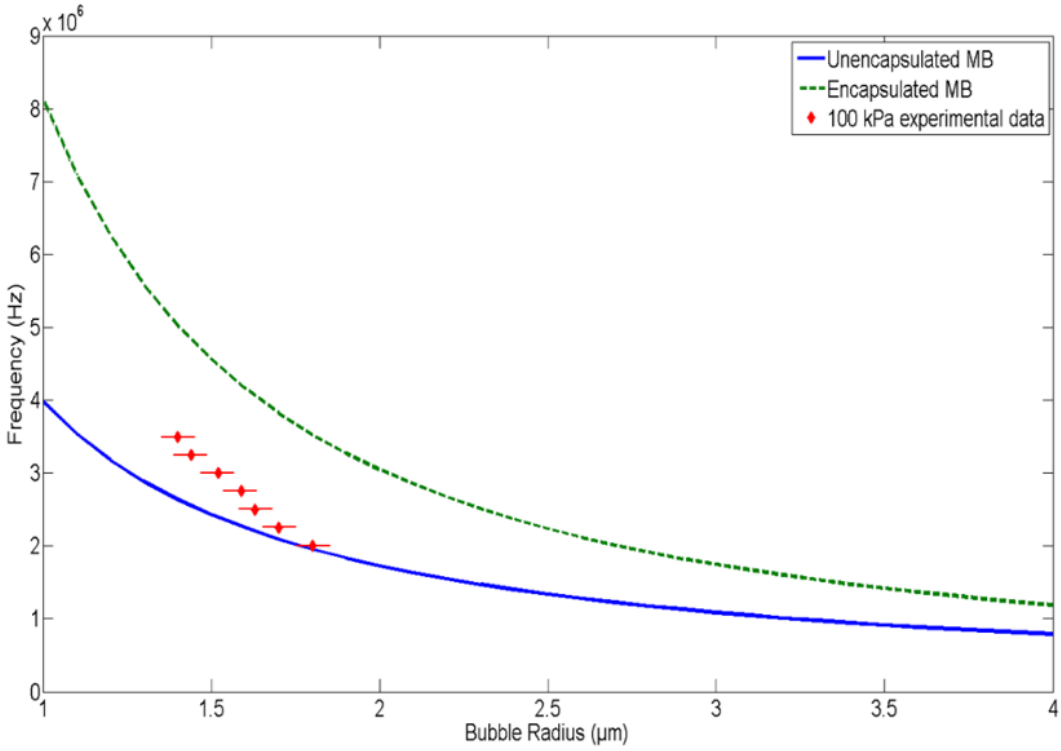

Figure 3-10: The resonant sizes on SonoVue as obtained experimentally from pulse inversion residuals (Red diamonds) and predicted from theory for an unencapsulated MB (Blue solid line, Equation 3-2) and an encapsulated MB with a shell elasticity = 0.54 N/m (Green dashed line, Equation 3-3)

3.5.5 Bubble Stability

Figure 3-11 shows the RMS of the time domain signal for one entire pulse sequence for a number of different bubbles of a similar radius (R_0 = 2.0, 1.9 and 1.8 μm respectively). One whole pulse sequence consists of 4 repeats of a 7 pulse frequency ramp (the two PI pulses are simply averaged in this representation) giving 28 pulses in total, the black dashed lines indicated the end of each repeat. The response is normalised against the peak response. As expected the peak response can be seen to be size/frequency dominated, MBs of this size would be expected to be most acoustically active around the 2 MHz region (cf. Figure 3-10) this is demonstrated by the peak response typically occurring on the first pulse of each repeat and decays away for increased frequency pulses.

The top plot of Figure 3-11 shows this frequency dependant scattering response remaining constant over the 4 repeats of the frequency ramp. One could then infer that this MB is stable or unchanging throughout the sequence. Examination of the middle and bottom plots portrays a

different story. The middle trace shows a response pattern broadly similar to the “stable” MB of the top plot, this difference comes through a decrease in an absolute scattering level and a slight increase in the frequency of max response; this is particularly noticeable for the last repeat. The bottom plot shows a more extreme case of this whereby the amplitude decreases noticeably with each repeat and, in conjunction, the frequency or pulse number of maximum response increases. This would indicate that the repeated insonations are physically changing the MB and hence eliciting a time varying response. One of the most obvious parameters that could be changing is the resting radius of the MB. As the resting radius decreases one would expect an increasing of the resonance frequency (in accordance with Equation 3-3 and Figure 3-10) similarly one would also expect a decrease in the total scattering for a smaller MB. This effect has been noted as acoustically induced deflation [176] and the effect of MB radius and resonance was shown for single MBs [223].

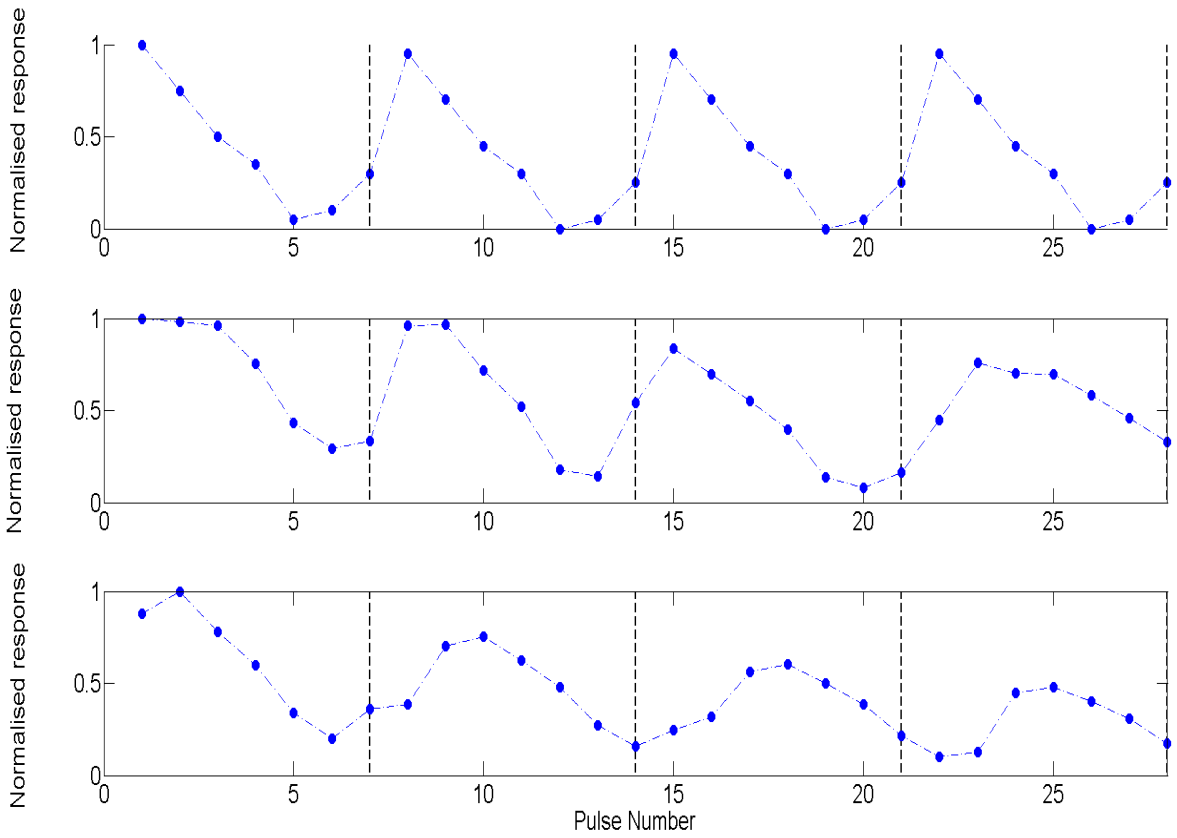

Figure 3-11: RMS data from complete pulse sequence for 3 different microbubbles showing the variation in MB response to repeated insonation. R=2.0 µm (top), R=1.9 µm (middle), R=1.8 µm (bottom)

To evaluate the stability of MBs to repeated insonation a stability parameter was developed, termed the stability index. If one examines the scattering power observed for the same frequency for successive pulse sequence repeats (e.g. to examine the stability at 2 MHz one has to examine pulse numbers 1, 8, 15 and 22 from Figure 3-11. For comparison the scattering power is normalised against the first pulse response) the stability index is then defined as the area under that curve normalised against an ideal constant response. This gives a single value per MB per frequency, a stability index of 1 is equivalent to a MB with no change in response due to successive pulses. An index of less than one shows a decrease in response and a value of greater than one indicates an increase in scattering. When plotted against initial MB radius, the size dependant change in response was obtained.

Figure 3-12 shows the stability index for MBs insonated at 2 MHz. Discrete data points are shown with the markers and the mean trend line (from a moving 5 point average) is shown as the line. One can see that above a radius of approximately 2.5 μm the MBs are relatively stable. Below this radius the MBs are subject to a significant change in response; reductions in signal of up to 35% are indicated. If one compares this figure to that of the second harmonic generation (Figure 3-9) one can see a high degree of correlation between the two indicating that the stability of a MB is intrinsically linked to MB resonance. Another interesting point to note is that although there is an increase in the variation around resonance there are also a number of MBs in this region which show no variation to repeated insonation. This is an indication that within a population there can be varying MB properties for similar sized MBs.

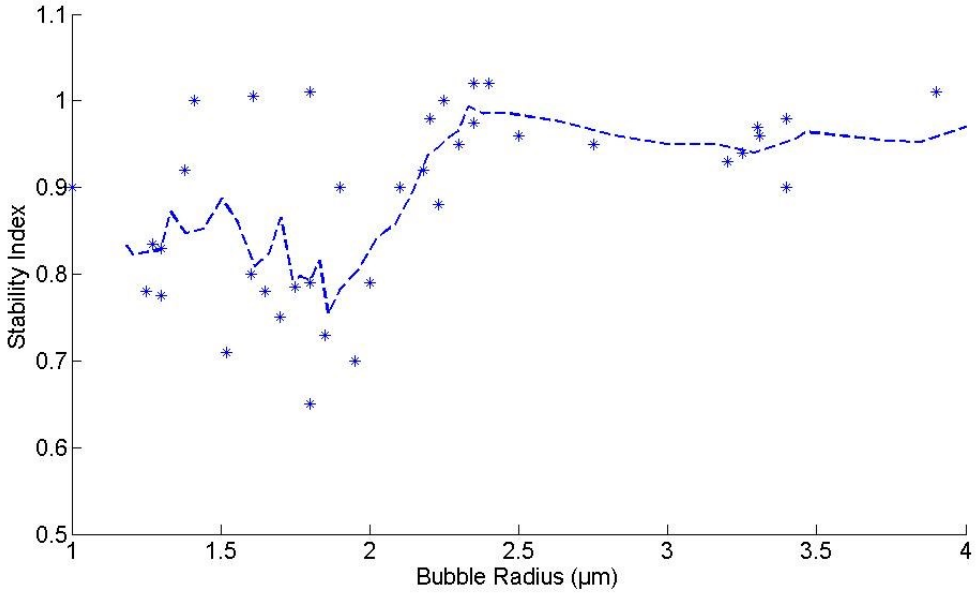

Figure 3-12: Stability Index as a function of MB radius for multiple repeats of a 2 MHz insonation pulse. Data points shown by discrete markers, dashed line indicates the mean trend line as given by a 5 point moving average window.

If the hypothesis that MB stability is a resonance dependent effect is correct then when one explores this at increasing frequencies it would be expected that the range of MBs affected should decrease in radius. In fact, if the stability data for the MBs collected at 3.5 MHz is overlaid on the 2 MHz data (Figure 3-13) one can see that broadly speaking the two datasets overlap each other with no distinct differences. The reason for this is to do with the data collection method and in particular the pulse sequence used. The pulse sequence cycles through the range of frequencies for each repeat, as such any MB with a resonance frequency within the 2 – 3.5 MHz range will be excited at resonance. If one takes this range as the upper and lower limits given by resonance curve for an encapsulated and unencapsulated MB (Figure 3-10); not an unreasonable assumption given the total variability seen between MBs e.g. the variability seen in the fundamental scattering (Figure 3-7), then this encompasses a size range of approximately 1.2 – 2.5 μm. This size range is excited with each repeat of the pulse frequency ramp and consequently is the size range of MB which is observed to experience the most change in response. There is no way to extract the frequency specific stability, this in turn suggests that if one want to extract this information only a single frequency can be examined at a time.

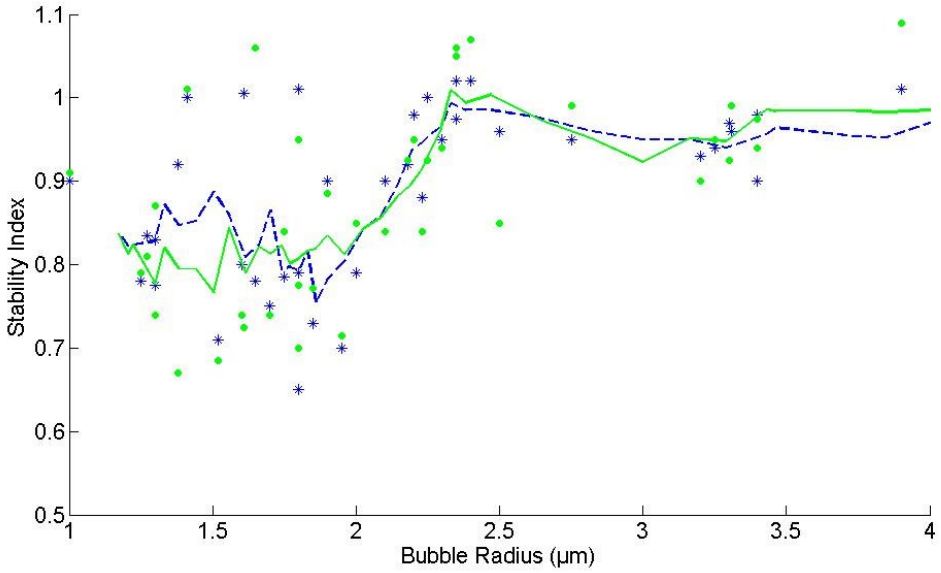

Figure 3-13: Comparison of the stability index as a function of MB radius for insonation at 2 MHz (Blue stars and dashed line) and at 3.5 MHz (Green circles and solid line).

3.5.6 **Bubble Asymmetry**

Another parameter that can be derived from this data is the degree of symmetry that the responses contain. Previous authors [126], [129], [133], [201] have remarked on the radial asymmetry on MB oscillations, so called "compression-only" type behaviour and its importance in the generation of non-linear signals. Figure 3-14 shows the effect of asymmetry on the resulting radiated pressure, this figure was simulated using the Marmottant model [129] as described in Chapter 2, Section 2.5.2. It simulates the response of a 2 μm radius MB to a 10 cycle, 2 MHz, 100 kPa PNP pulse. Scattered pressure is simulated at a distance of 78 mm from the MB mimicking the experimental setup. Shell parameters used were χ=1.01 N/m, κ_s = 5x10^{-8} kg/s, $\sigma_{breakup}$ = 0.13 N/m, $R_{buckling}$= R_0 for the compression dominated curve (Blue dashed) and $R_{buckling}$= 0.5xR_0 for the symmetrical curve (Green line). For a full description of the modelling approach please refer to Chapter 6. As can be seen the compression only radial behaviour correlated well with a similar waveform in the scattered pressure.

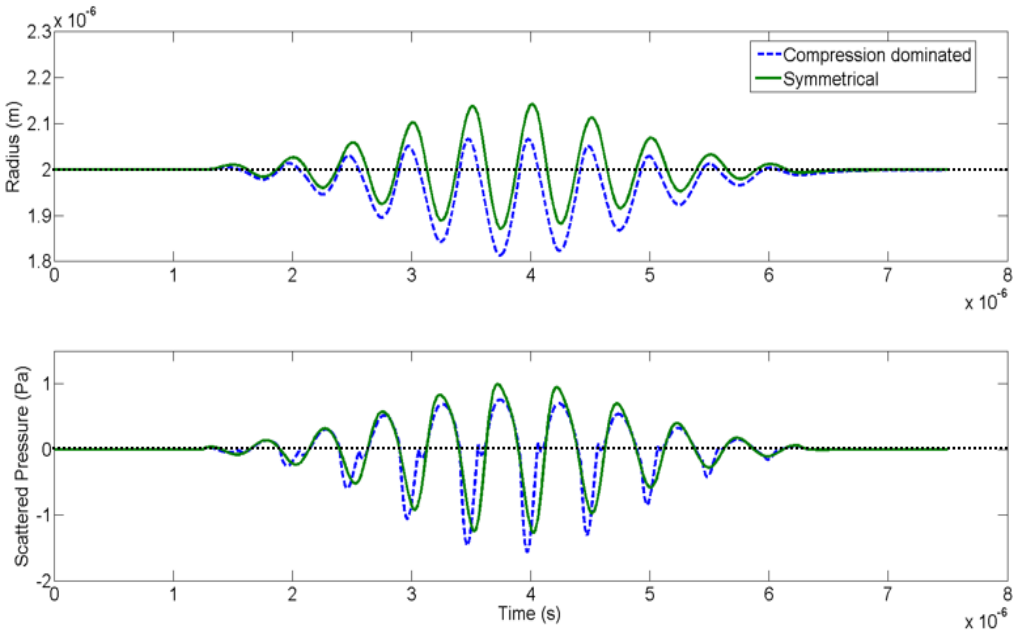

Figure 3-14: Simulated response of a 2 2 µm radius MB to a 10 cycle, 2 MHz, 100 kPa PNP pulse. Scattered pressure is simulated at a distance of 78 mm from the source mimicking the experimental setup. Shell parameters used were χ=1.01 N/m, κ_s = 5x10^{-8} kg/s, $\sigma_{breakup}$ = 0.13 N/m, $R_{buckling}$= R_0 for the compression dominated curve (Blue dashed) and $R_{buckling}$= 0.5xR_0 for the symmetrical curve (Green line).

As a measure of asymmetry the following parameter was extracted (Equation 3-4). Where Asym is the degree of asymmetry and P_{+ve} and P_{-ve} are the peak positive and negative response. This measure gives a parameter which is symmetric about zero, zero being a perfectly symmetrical MB response. It follows that positive and negative values denote a positive or negative skew respectively on the response shape which corresponds to a compression or expansion dominated behaviour respectively.

$$Asym = \frac{P_{+ve} + P_{-ve}}{P_{+ve} + |P_{-ve}|}$$

Equation 3-4

Figure 3-15 below plots this degree of asymmetry value as a function of bubble radius at 2MHz. It can be seen that away from resonance the bubbles tend to behave in a generally symmetrical mode of oscillation with a slight tendency to be slightly expansion dominated. Near resonance it can be seen that the MBs exhibit predominantly compression dominated behaviour.

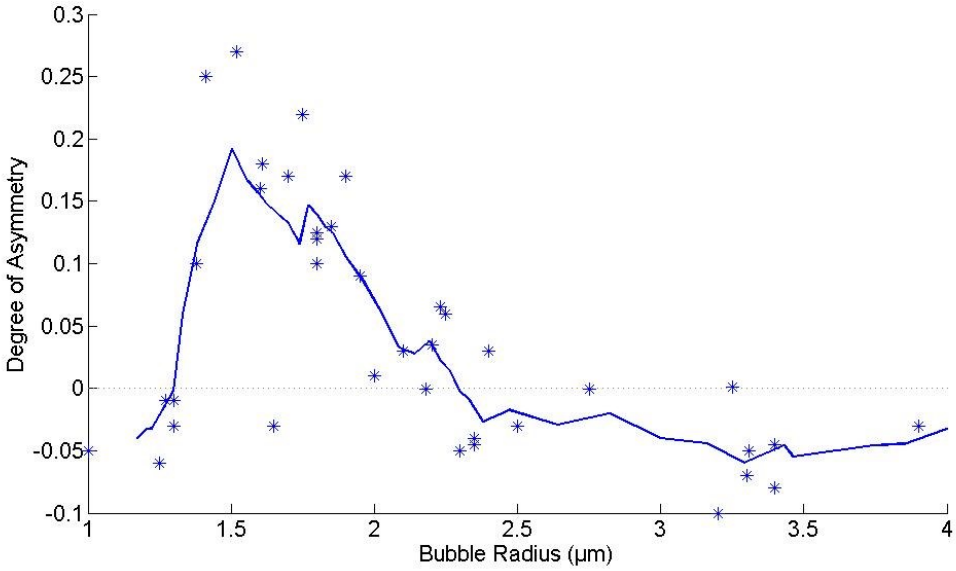

Figure 3-15: Asymmetrical nature of bubble oscillation. A value of 0 indicates symmetrical behaviour, a positive value indicates compression dominated behaviour and a negative value indicates expansion dominated behaviour.

3.6 Summary

In this chapter a method for the acoustic examination of single MBs has been designed and presented. This allows for individual MBs to be insonated, their corresponding scattering response and sizing information to be obtained. The test rig was then validated by the examination of SonoVue, a commercially available contrast agent. By examining a wide size distribution of SonoVue on a bubble by bubble basis it has been demonstrated that MB response characteristics such as the fundamental and 2^{nd} harmonic scattering characteristics can be collected. From these it is possible to infer the onset of MB resonance and compare this with current theory and similar studies from other groups, broad agreement is reached between the output from this study and theory/other studies.

In addition a number of other MB parameters can also be extracted, these include measures of a MB's stability to repeated insonation and measures of a MB's response asymmetry. Understanding the stability of MBs to insonation could have value in the designing MBs, both for designing MBs with prolonged longevity *in vivo* or conversely designing MBs to break or fracture when desired e.g. using MBs as a drug/gene delivery system. The MB response asymmetry can be directly linked to the generation of more highly non-linear signals. Most MB specific imaging techniques (PI, sub-harmonic etc.) make use of these non-linear signal to differentiate the MB from surrounding tissue. By understanding the cause of these non-linearities MBs can be designed to accentuate these properties making detection easier.

This testing validation also served as a method of understand the experimental complexities concerned with a study such as this and exposed a number of methods for improvement. Factors such as precise alignment and experimental equipment interfering with the sound field both led to slight modifications to either the setup or testing procedures. The overlapping of the effect of different frequencies on the stability of MBs means that the pulse sequence has to be redesigned to ensure that all the desired data can be obtained, this may require working at single frequencies at one time which in turn could have an impact on the data collection rates. Lastly the variability of data, even from supposedly similar MBs, was relatively large and may lead to the incorporation of filtering or smoothing to extract trends. It also implies the importance of precise control over all variables where possible.

4 Single Bubble Acoustic Characterisation and Stability Measurement of Adherent Microbubbles*

4.1 Abstract

This chapter examines how the acoustic and stability characteristics of single lipid shelled microbubbles (MBs) change as a result of adherence to a target surface. For individual adherent and non-adherent MBs, the back scattered echo from a narrowband 2 MHz, 90 kPa peak negative pressure interrogation pulse was obtained. These measurements were made in conjunction with an increasing amplitude broadband disruption pulse. It was found that, for the given driving frequency, adherence had little effect on the fundamental response of a MB. Examination of the 2nd harmonic response indicated an increase of the resonance frequency for an adherent MB; Resonance radius increasing of 0.3 µm ± 0.1 µm for an adherent MB. MB stability was seen to be closely related to MB resonance and gave further evidence of a change in the resonance frequency due to adherence. Similarly the envelope of the time domain data also showed a strong correlation with resonance; exhibiting a compression dominated response near resonance conditions.

* Adapted from [44] *Single Bubble Acoustic Characterisation and Stability Measurement of Adherent Microbubbles,* accepted for publication in Ultrasound in Medicine and Biology 2013 May; 39(5):903-14

This work was also presented at The IEEE International Ultrasonics Symposium, 2011. Orlando, FL under the title "*Single Bubble Acoustic Characterisation and Stability Measurement of Adherent Microbubbles* **"**

Further aspects were also presented at The 17th European Symposium on Ultrasound Contrast Imaging, 2012. Rotterdam, NL under the title "*Size dependant asymmetrical microbubble response***"**

4.2 Introduction

Targeted microbubbles (MBs) have shown potential in allowing the use of ultrasound in a variety of new applications [37], [235], [236]. By functionalising the shell of the MBs to target specific markers expressed in the endothelium the contrast agent can be used to highlight areas of interest [237] and have been used, *in vivo,* to image inflammation [97], [98], angiogenesis, atherosclerosis [100], thrombosis [101]. Currently, targeted contrast agents for the molecular imaging of prostate cancer are undergoing initial human trials [74]. Their use as targeted drug delivery vehicles is also under investigation [12]. These targeting ligands (be they antibodies, proteins, peptides, etc. dependent upon the pathology to be targeted) are situated on the surface architecture of the MB, either on the shell itself or more commonly at the end of a spacer, typically a (poly) Ethylene Glycol (PEG) spacer (see e.g. [106]). By this attachment the MB is brought to within tens of nanometres of the vasculature wall which, in turn, has been shown to affect the dynamic response of a microbubble to ultrasound [43], [160], [162], [163], [225], [238], [239]. One of the main challenges associated with the use of targeted microbubbles for molecular imaging is how the signals from the attached microbubbles are differentiated from those of the free flowing/unattached microbubbles.

The first approach typically used is that of clearance imaging. Unbound MBs are typically cleared from the circulatory system in approximately 10 minutes leaving the bound MBs for imaging [98]. The main disadvantage with this technique it that the while some MBs are retained at the target site this number too decreases throughout the clearance period. Ideally imaging should be performed at the time point of maximal MB retention and has directed many approaches to focus upon image processing techniques to achieve this differentiation. Due to their compressible nature, microbubbles generate substantially more scattering than tissue and in particular generate more harmonic signal; either higher or sub-harmonics, even at low acoustic pressures [201], [240]. Such features allow microbubbles to be distinguished from tissue by image subtraction or examination of the harmonic signals generated. The differentiation between attached and unattached bubbles is then conducted by temporal filtering. An attached bubble will appear as a stationary scatterer whereas an unattached bubble will appear as a moving scatterer, therefore stationary bubbles can be detected by applying a low pass filter to remove bubbles in motion. Several authors have successfully demonstrated variations of this technique *in vitro* [38], [203], [241], however, *in vivo* a number of further complications such as body/tissue movement make these techniques more difficult to employ successfully. A more efficient and selective imaging strategy could be developed

if the signals generated by attached microbubbles showed unique acoustic characteristics which could then be specifically identified. In order to do this the acoustic characteristics of microbubbles under a variety of conditions must be precisely determined so that specific imaging protocols can be devised. It is known that the local conditions can have a significant impact on MB response. Increasing values of wall rigidity decrease MB resonance frequency. In the cases where an elastic wall is modelled this can have the effect of increasing or decreasing the resonance frequency depending on the specific material properties of both the wall and the surrounding medium. In most physiologically analogous situations this has been shown to increase MB resonance frequency [42], [160], [239]. Patil et al. [159] conducted a 3D finite element examination of a MB adherent to a rigid wall in comparison with a free, unconstrained MB. In addition to showing many of the shape fluctuations as seen in high speed imaging experiments [39], [40] the model also predicted a shift in resonance frequency as a result of adherence; having the effect of lowering the resonance frequency and suppressing some of the second harmonic signal generation. These observations have been supplemented by a high speed imaging study [43], however, acoustic verification of these results has not yet been presented. Furthermore, microbubble destruction thresholds and unstable mode oscillations have also been shown to be affected by the presence and characteristics of nearby boundaries, however, the presence and effects of binding on MB stability is not fully understood. Couture et al. [203] have demonstrated that there is also a difference in the dissolution time of adherent MBs in comparison to non-adherent MBs after ultrasound is applied. Adherent MBs were shown to dissolve at a significantly faster rate than their non-adherent counterparts. This could provide a differentiation technique based on the disruption of MBs. However, this would require high temporal resolution to be achieved.

Any difference, for example changes to resonance frequency, detected between adherent and non-adherent MB acoustic signatures is expected to be subtle and size dependant. As such, bulk acoustic measurements; where scattering and attenuation measurements are performed on bulk suspensions of MBs, are unlikely to elucidate the important details. Consequently, in this work, the acoustics characteristics of single MBs in varying conditions will be investigated. The acoustic characterisation of individual microbubbles has been implemented by a number of authors [36], [176], [231], [242], [243] and have highlighted phenomena including acoustically induced deflation, compression and expansion only behaviour, and changes in bubble stability when confined in small vessels. The objective of this study is to perform an acoustic investigation of the effect that binding a MB to a surface has in comparison to an unbound microbubble in otherwise similar conditions i.e. near a boundary yet unattached. Specific attention will be given to both the resonance characteristics of the MBs as well as changes in bubble response to repeated insonation.

4.3 Methods

4.3.1 Experimental setup

The equipment, as shown in Figure 4-1, consisted of a pair of matched transducers (V380, Panametrics, Olympus Industrial, UK) (4 MHz centre frequency, -6dB bandwidth 86%, focal length 75 mm, diameter 25mm) focussed to a central point in conjunction with a 40x water immersible objective (LUMPlanFL N40xW Olympus Medical, UK). Positioned at the focus was a 200 µm diameter capillary fibre (RC55 8/200 Membrana GmbH, Germany) through which the microbubble suspension was flowed. Sham experiments, conducted without the presence of MBs, showed that the fibre did not scatter sound at a level detectable using the current set-up and was therefore considered both acoustically and optically transparent. The fibre was mounted on a 3-axis translational stage (Newport M-562, CA, USA) for accurate positioning. Note; that to minimise acoustic interference, particular care must be taken over the alignment of the transducers and optics. The transducers were positioned approximately 10 degrees off axis from the objective; similarly the angles between the two transducers were unequal (positioned approximately 20 and 45 degrees from the normal for the receive and transmit transducers respectively) to minimise direct reflections.

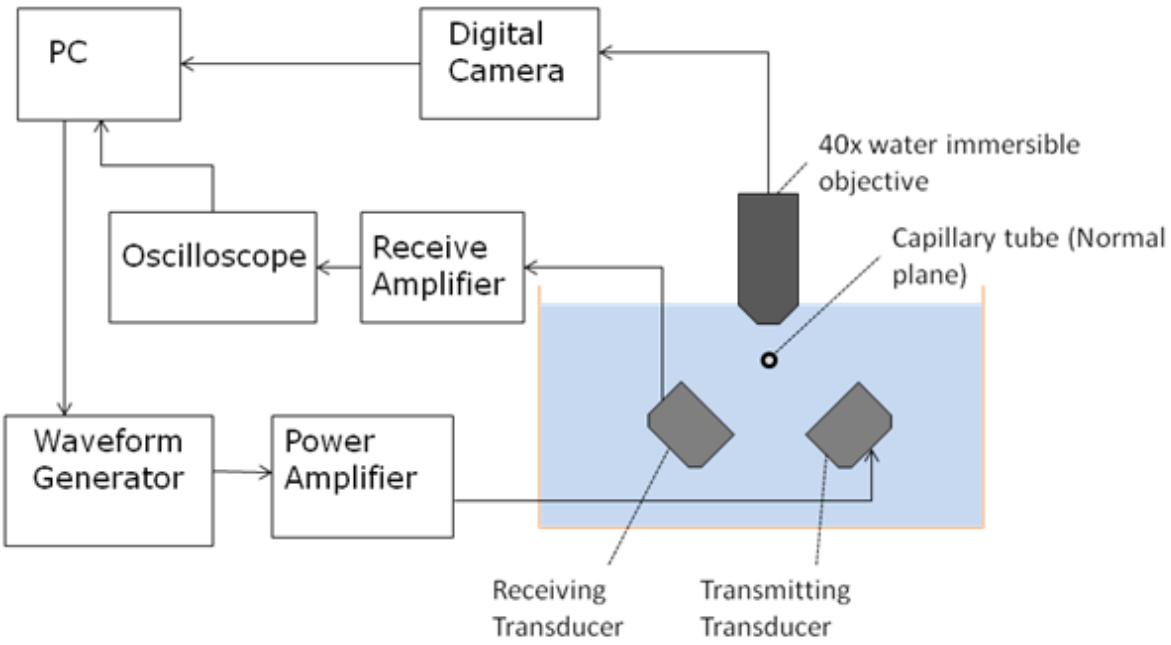

Figure 4-1: Schematic of the Experimental Setup.

The transmitted signal was generated in an arbitrary waveform generator (Sony Tektronix AWG2021) and amplified through a power amplifier (2100L, E&I, NY, USA). The scattered signal was amplified by a pulser/receiver operated in receive mode (Panametrics-NDT 5800) and displayed via a digital oscilloscope (Sony Tektronix TDS7154). The image from the objective was directed to a digital camera (Canon ProShot G5) through a 45° mirror and focussing lens for subsequent sizing. Optical calibration was performed as described in 3.4.3. Final optical calibration was found to be 20 pixels/μm. The whole system was controlled via a desktop PC and an in-house developed MATLAB Programme (Mathworks, Cambridge UK). The gas saturation of the solution has been shown to affect the MB stability and the reproducibility of measurements [56]. In accordance with these findings, filtered, gas equilibrated water was utilised for all experiments. The water is filtered via reverse osmosis (euRO 20, Triple Red Ltd, Bucks. UK) and is considered de-ionized. All experiments were performed at 20^{o}C.

4.3.2 Microbubble and Capillary Fibre Preparation

In house MBs were utilised for this study, these MBs have been developed over a number of years by members of the research group. The use of these allowed for the direct specification of MBs to our needs, specifically it allowed for the functionalization of MBs with our chosen molecular probe and the production of similar un-functionalized MBs for control purposes. The production and characterisation of the MBs are presented by Sennoga et al. [244]. Microbubbles were prepared by sonication (Misonix Sonicator 3000, settings 21kHz 165W; 30s) of an octofluoropropane-saturated aqueous suspension of distearoyl-phosphatidylcholine (DSPC), distearoyl-phosphatidylethanolamine-PEG2000-biotin (DSPE-PEG2000-Biotin) and poly(ethyleglycol)-monostearate (PEG40-stearate). Non-targeted microbubbles (control) were prepared similarly, substituting DSPE-PEG2000-Biotin with methoxy-poly(ethyleglycol)2000 distearoyl-phosphatidylethanolamine (DSPE-mPEG2000). Microbubble size distribution and concentration were measured to have a mean size diameter of 2.4 (±0.4) μm and a number concentration of 1.2×10^{9} microbubbles/mL using optical microscopy [245].

In order to conduct these experiments it was vital to ensure that only a single bubble was present at the acoustic focus (Please refer to Appendix 9.1 for the transducer calibration). To achieve this, the MB solution was diluted by approximately 1:100,000 with some variation introduced due to bubble buoyancy, sampling errors and variations in initial concentration of the MB solution. The transducer focal region was measured to be approximately 2.4 mm in diameter. The capillary fibre

was checked optically to a distance of >1.5 mm either side of the target bubble to verify that no other bubbles were present.

Upon introduction the MBs rise to the upper inner surface of the capillary fibre, as stated in the introduction brings with it some profound changes in bubble response. Because this will affect both the adherent and non-adherent MBs this was deemed acceptable and favourable, allowing direct comparison of bound and unbound bubble without any changes in local conditions or geometry.

Capillary fibres were cleaned with sterilised PBS (Sigma-Aldrich Ltd. Dorset, UK) and flooded with unlabelled Streptavidin (Invitrogen Life Technologies Ltd, UK) solution at a concentration of 0.25 mg/ml, before incubation over night at 4°C.

This method of targeted MB generation, tube preparation and MB adhesion was successfully employed by Loughran et al. [105] , the same materials and equipment was used for this study.

4.3.3 Acoustic Pulse Characteristics

Accurate transducer alignment was essential to the success of this investigation. The setup and calibration of the transducers was conducted as described in Section 3.4.2.

Each MB was insonated with a pulse sequence split into two distinct phases. Phase One (Figure 4-2 (a)) consisted of five, 2 MHz, 10 cycle pulses at a peak negative pressure (PNP) at the focus of 90 kPa. Phase Two (Figure 4-2(b)) consisted of alternating two cycle, 3.5 MHz centre frequency broadband pulses and the same 2 MHz narrowband pulse as in Phase One for 10 repeats (20 pulses in total) After each repeat the broadband pulse amplitude was increased in increments of approximately 45 kPa from 50-450 kPa PNP. All pulses are sent at a pulse repetition frequency (PRF) of 100 Hz. MBs were exposed to a total of 25 pulses and the whole pulse sequence lasted 0.25 seconds.

The rationale behind this pulse sequence was twofold; the first narrowband pulse will give the bubble's acoustic behaviour at the bubble size imaged by optical microscope. The repeated pulses will then show how the bubble responds to repeated exposure. It is understood that MB stability is significantly affected by resonance [175]; it was intended that the first five pulses should provide detailed information on the acoustic and stability characteristics of MBs at or near resonance for a given narrowband excitation. Because the size distribution of bubbles examined is

dependent on their initial size distribution and longevity after extreme dilution, the technique is biased towards larger bubbles. For bubbles with radii away from that of the resonance size it has been shown that little disruption occurs [176]. Therefore in an effort to maximise the data obtainable from MBs away from resonance, broadband pulses of increasing amplitude were employed.

For this study all the interrogation insonations were conducted at a single frequency, this was a direct consequence of the frequency overlap observed when examining MB stability in the previous chapter (Section 3.5.5). This did mean that the data collected was somewhat restricted in nature and would not allow for later spectroscopy techniques as described by Van der Meer et al. [113] for MB modelling, however, the gains in resolution due to the limiting of variables was deemed worthwhile. Methods of using this data for modelling will be discussed in Chapter 6

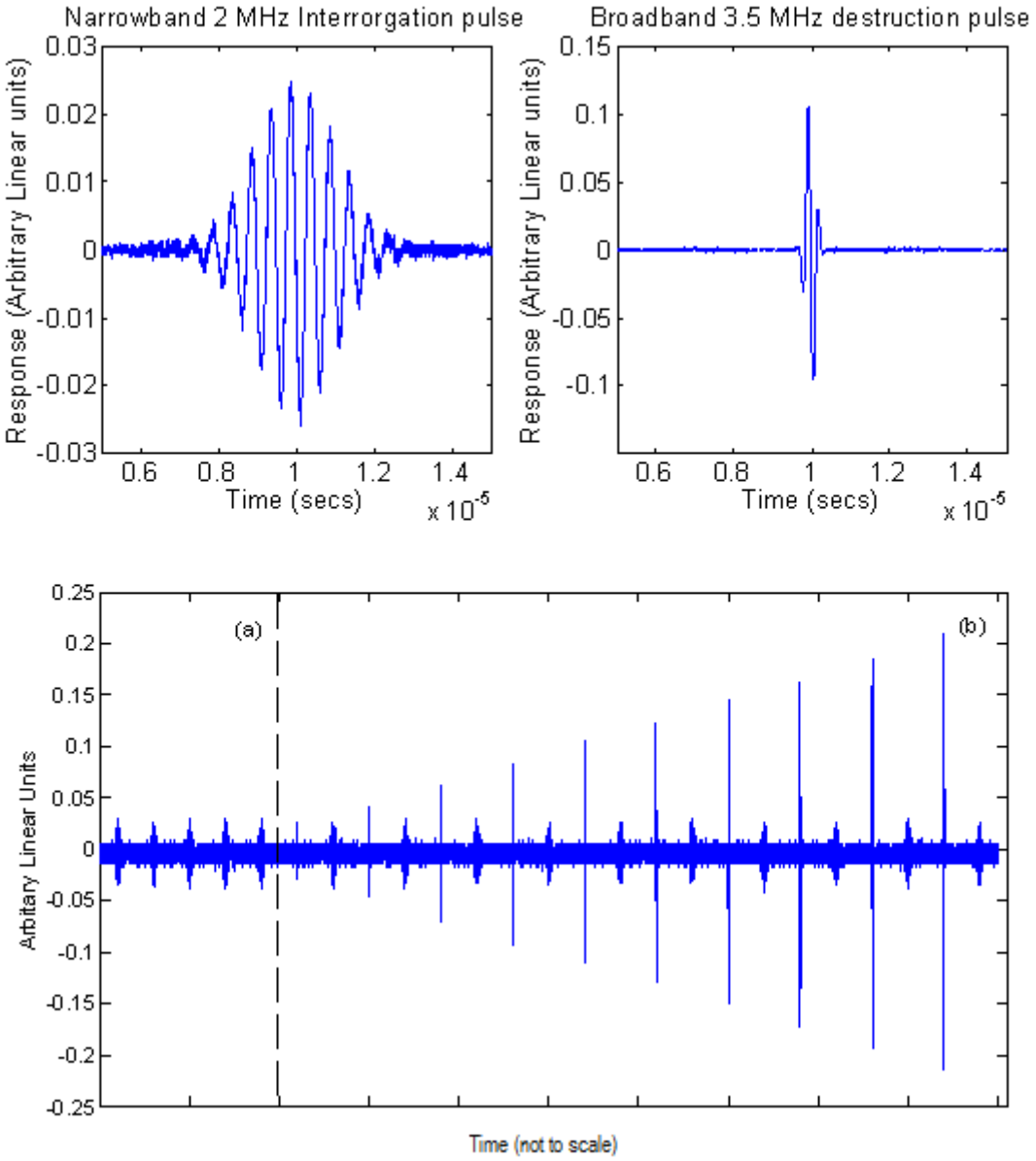

Figure 4-2: Pulse definition. 2 MHz, 10 cycle interrogation pulse (Top Left), 3.5 MHz, 2 cycle destruction pulse (Top Right). Full pulse sequence (bottom); first 5 interrogation pulses (a). Ramp of destruction pulses interleaved with interrogation pulses (b)

4.3.4 Data Analysis

The data for each bubble was split into single pulses, corrected for amplifier gain, zero offset and windowed using a hamming window. The data was then corrected for the frequency response characteristics of the transducer (cf. Appendix 9.1).

Figure 4-3 shows both the time and frequency domain responses recorded for 2 adherent microbubbles of different sizes. The left hand panels show the response of a MB near resonance Note: for a 2 MHz insonation pulse the resonance radius for a lipid encapsulated bubble is predicted

to be around 1.8 μm [144], [147], this near resonance response is clearly demonstrated by the strong second harmonic component in the frequency spectrum. The panels on the right show the response of a bubble which is above the resonance size for a 2 MHz insonation pulse. Fundamental scattering can be seen to be increased and the generation of the 2nd harmonic signal is diminished. In the results that follow scattering power is defined as the total area under the frequency spectrum curve normalised by the noise floor of the system. The noise floor was determined as the frequency dependent power spectrum of the whole experimental test system to a sham exposure (no MBs present) to a pulse of the same characteristics as used in the experiment. This was averaged over 10 repeated exposures (n=10). Similarly the scattering power of the separate harmonics were taken as the band-pass area 0.5 MHz either side of the peak frequency (see Equation 4-1 where f_{high} and f_{low} refer to the upper and lowers bounds of the frequency range examined. This corresponds to the centre frequency of examination ±0.5 MHz.). By tracking the changes in scattering power of the various harmonics as a function of bubble size, a detailed picture of MB acoustic characteristics can be determined.

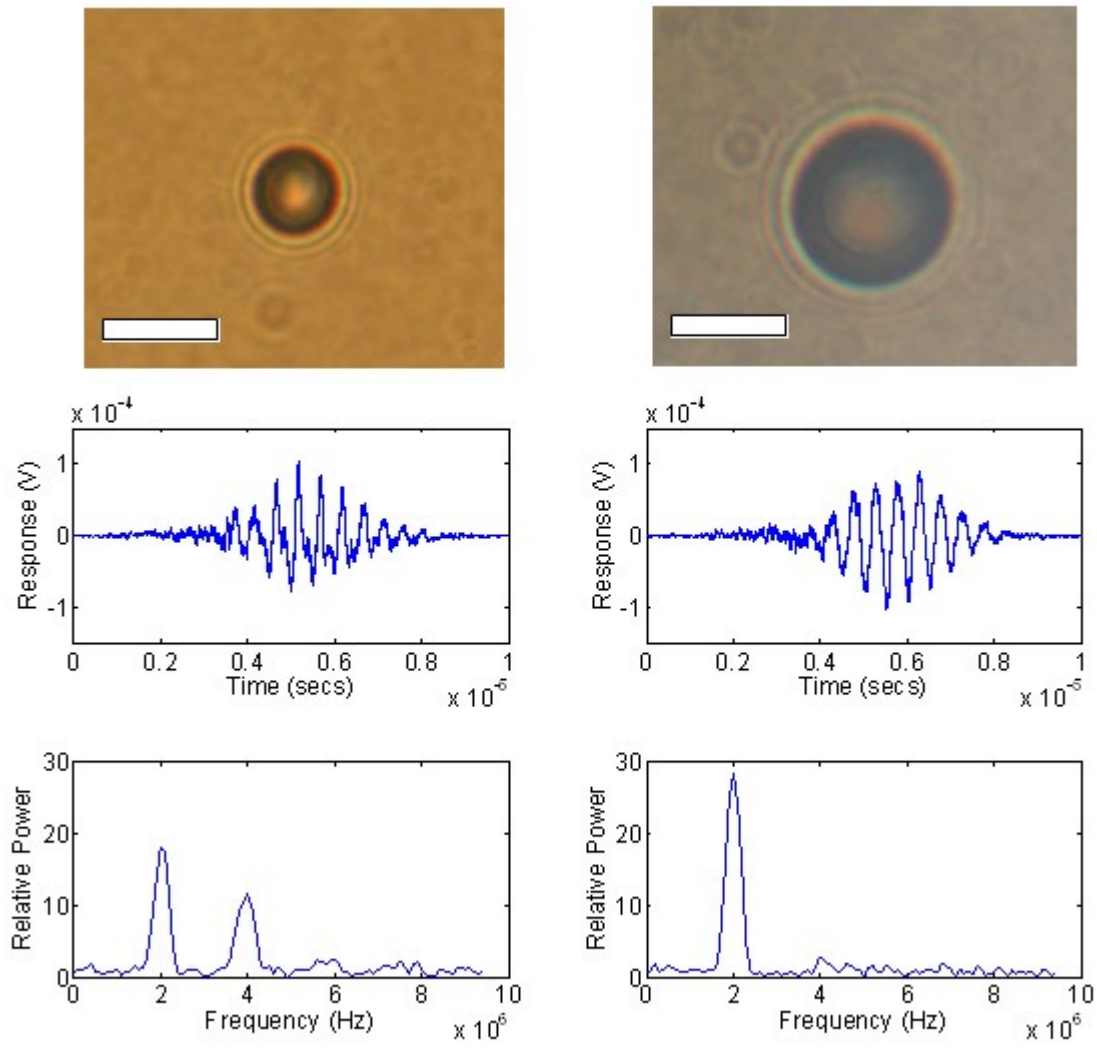

Figure 4-3: Typical acoustic responses for MBs at resonance (left) away from resonance (right). Top panes show sizing photos, middle panes and bottom panes show the bubble response in the time and frequency domains respectively. Scale bar = 5µm.

$$Scattering\ Power\ (dB) = 20\log_{10}\left[\frac{\sum_{f_{low}}^{f_{high}} signal\ amplitude\ spectrum\ (f)}{\sum_{f_{low}}^{f_{high}} noise\ amplitude\ spectrum\ (f)}\right]$$

Equation 4-1

To evaluate the change in bubble response to repeated insonation the total scattering power was tracked as a function of interrogation pulse number. Figure 4-4 shows the normalised scattered power against pulse number for three bubbles undergoing different changes in response. Scattered power is normalised against the response from the first pulse. Three distinct modes of MB

response are visible. The green trace shows a MB which does not alter in response power over the entire pulse sequence as demonstrated by a normalised power remaining at ≈1. The blue trace shows a MB which undergoes a reduction in scattering response immediately after the first insonation pulse. The red trace shows a MB that does not exhibit a change until after the first 5 interrogation pulses. With reference to Figure 4-2 this indicates that the increasing ramp of broadband disruption pulses is responsible for the change in response. To parameterise this change in response, the area under each response curve was found and normalised against a constant response of 1 i.e. the response of a MB exhibiting no change. This gives a single value per MB, a value of 1 is equivalent to a MB with no change in response. A value of less than one shows a decrease in response. When plotted against initial MB radius, the size dependant change in response was obtained. This parameter will henceforth be referred to as the stability index.

This method was deemed an improvement upon the previous chapter's standard deviation method of stability measurement. The use of the standard deviation was susceptible to errors when extremes of MB response were examined. For example if one considers a MB which is nearly total disrupted after the first pulse, measuring the standard deviation of all the pulses will produce an low standard deviation (all pulses after the first would be approximately the same i.e. ≈ 0) and hence the outcome would be a stable MB. This method of normalised area under the curve accounts for this and all other modes of MB disruption.

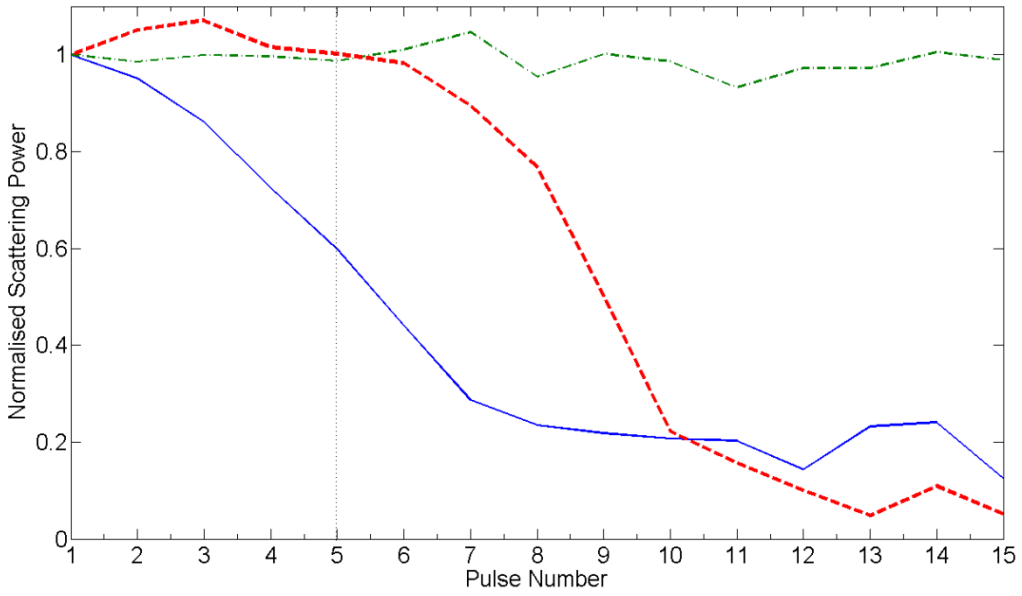

Figure 4-4: Normalised total scattering as a function of interrogation pulse number to show bubble response as a function of pulse repetition. The green line shows a bubble with no change in response over the pulse sequence. The blue line shows a bubble exhibiting a change in response subsequent to the first insonation. The red line shows a bubble exhibiting a change in response as the destructive broadband pulses are applied (post pulse 5).

Figure 4-5 shows the time domain traces from two adherent MBs. The top trace is from a near resonant bubble (R_0=1.8 µm) and exhibits a distinctly non-symmetrical response profile (the peak positive response ≈ 1.5 times the peak negative response). This is in comparison to the response on the bottom trace from a much larger bubble (R_0=3.1 µm) which exhibits a much more symmetrical response. To extract some information from this data the degree of asymmetry was established as Equation 4-2. Where P_{+ve} and P_{-ve} denote the peak positive and negative time domain response values respectively. The output of this is a parameter which is symmetrical about 0 between 1 and -1. A positive values indicates a positive response dominated oscillation and vice versa. This formulation is an improvement on the parameter used previously in Chapter 3 and was implemented to remove the possibility of erroneous solutions due to extremes of MB response.

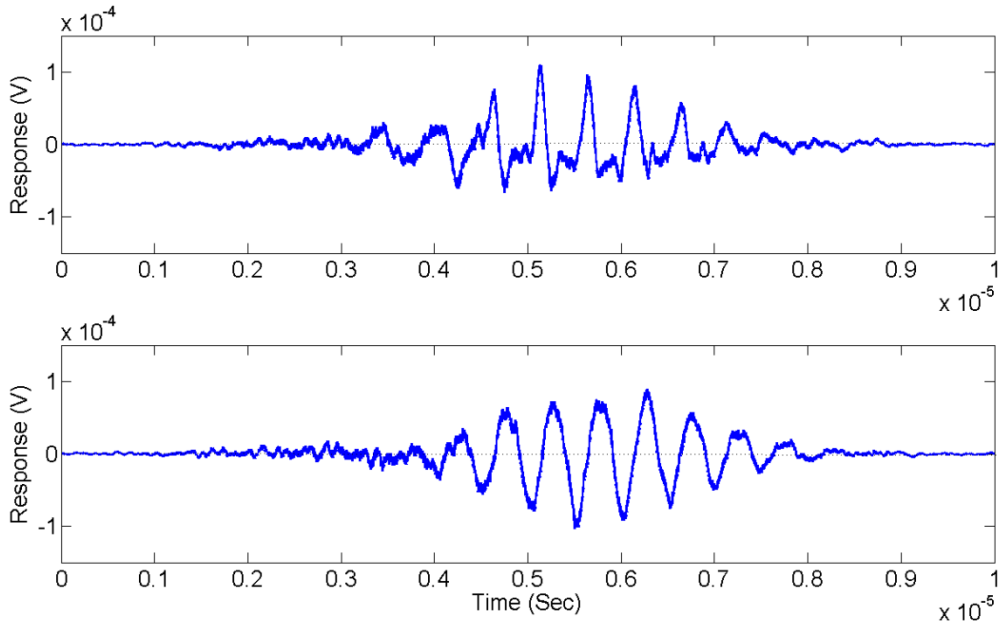

Figure 4-5: Examples of the differences observed in response asymmetry. Top: MB radius = 1.8 µm, degree of asymmetry = 0.2, Bottom: MB radius = 2.45, degree of asymmetry = -0.04.

$$Asym = \frac{P_{+ve} + P_{-ve}}{P_{+ve} + |P_{-ve}|}$$

Equation 4-2

4.4 Experimental Results

4.4.1 Data Smoothing

Individual data points were subject to a large degree of variation, the cause of which will be discussed later. In order to extract trends within the data the mean and standard deviation of a five point moving window was calculated for each data. Note: End data points were subject to smaller widow sizes i.e. first and last data points used a 3 point window, second and penultimate points used a 4 point window. On subsequent figures employing this windowing, mean data is displayed as a line with shaded regions representing the standard deviation of the mean. Raw data is displayed as discrete points.

To show the statistical significance between the comparison trends the data is binned into 0.2 μm bins (conservatively above the maximum sizing error). This results in bins ranging in size up to 12 data sets per bin depending upon the spread of MB sizes interrogated. The data is then tested using a two tailed unpaired t-test to determine if the two sets of data are significantly different. The significance level is set to $P>0.05$ and the regions of significant difference are highlighted in the relevant figures. Due to the nature of the experiment and the number of samples which make up each bin, the power (i.e. the confidence that the t-test will provide a positive rather than false positive result.) has also been calculated. This was performed using the software package Statmate (Graphpad Software, CA, USA.)

4.4.2 Scattered acoustic power

The following data presents the results from all four experimental conditions tested: 1) Untargeted MBs, uncoated capillary fibre (UTUC) 2) Untargeted MBs, Coated capillary fibre (UTC) 3) Targeted MBs, uncoated fibre (TUC) and 4) Targeted MBs, Coated fibre (TC). The number of data points for each of the test cases were; TC n=41, UTUC n=44, TUC n=49, and UTC n=45. By comparison of these cases the effect that the functionalization of both the bubbles and the capillary fibre has on MB dynamic response can be elucidated. For display purposes each case is shown individually then for comparative analysis the mean trend lines are superimposed on each other.

Figure 4-6 shows the fundamental scattering results. In general good agreement can be observed between all testing regimes, especially through the resonance region where the greatest

variation was anticipated (P>0.05 for the entire range radius). Following this, Figure 4-7 displays the 2nd harmonic scattering data. Good agreement is observed between the three non-adherent cases (i.e. UTUC, TUC and UTC P>0.05) both in terms of resonance radii and scattering power. The slightly lower peak values for the UTUC case could be explained by the limited number of data points within this region (please refer to the top left of Figure 4-6). The adherent MBs are statistically different (P<0.05) from the all three non-adherent cases in the radius range 1.8 - 2.0 µm.

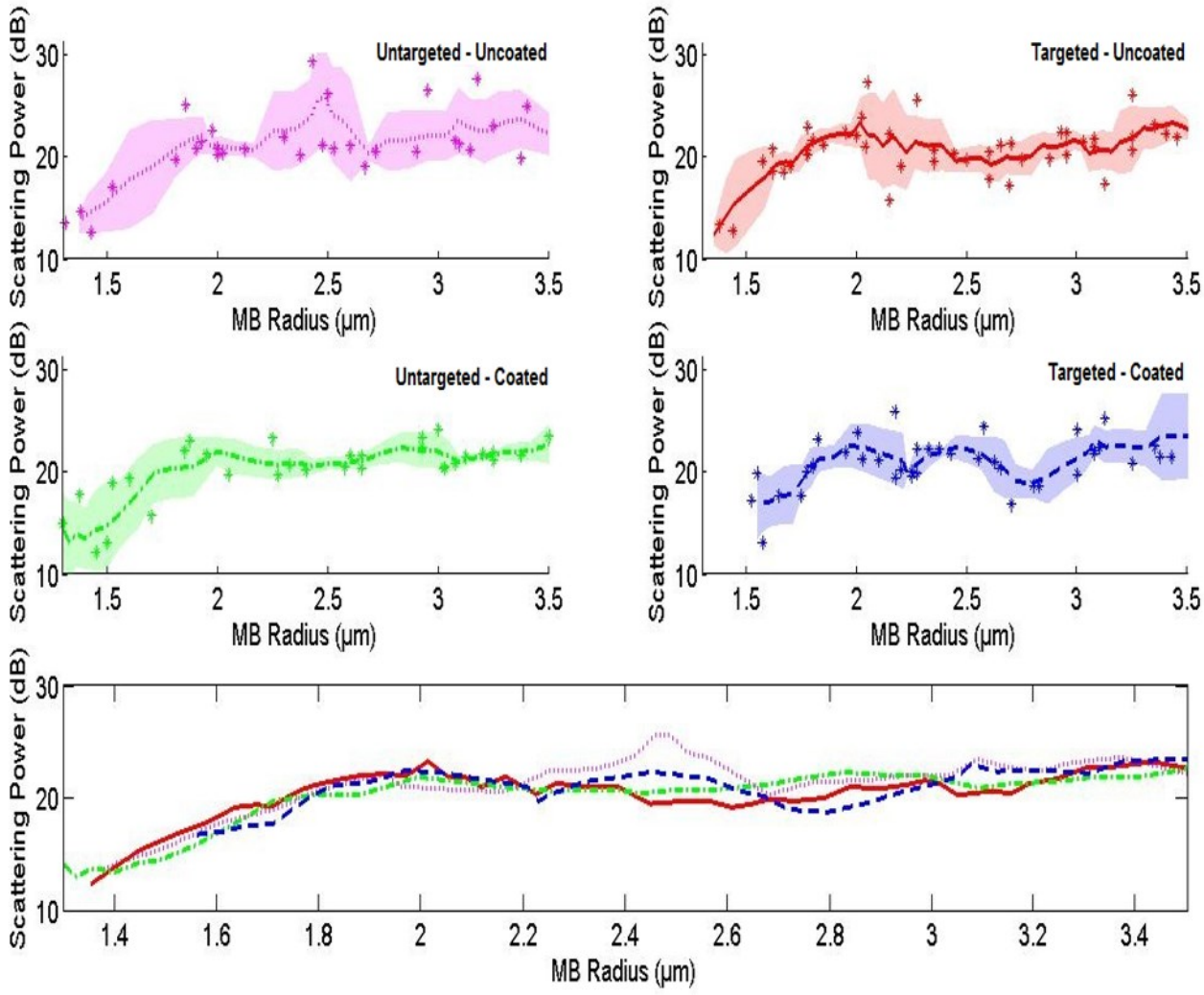

Figure 4-6: Fundamental scattering as a function of bubble radius for the 4 testing regimes. The 3 non-adherent or control cases of: Untargeted – Uncoated (Top left), Targeted – Uncoated (Top right), Untargeted – Coated (Middle left). And the adherent or Targeted – Coated (Middle right) regime. Mean trend lines superimposed to show comparison (Bottom). P>0.05 for the entire radius range.

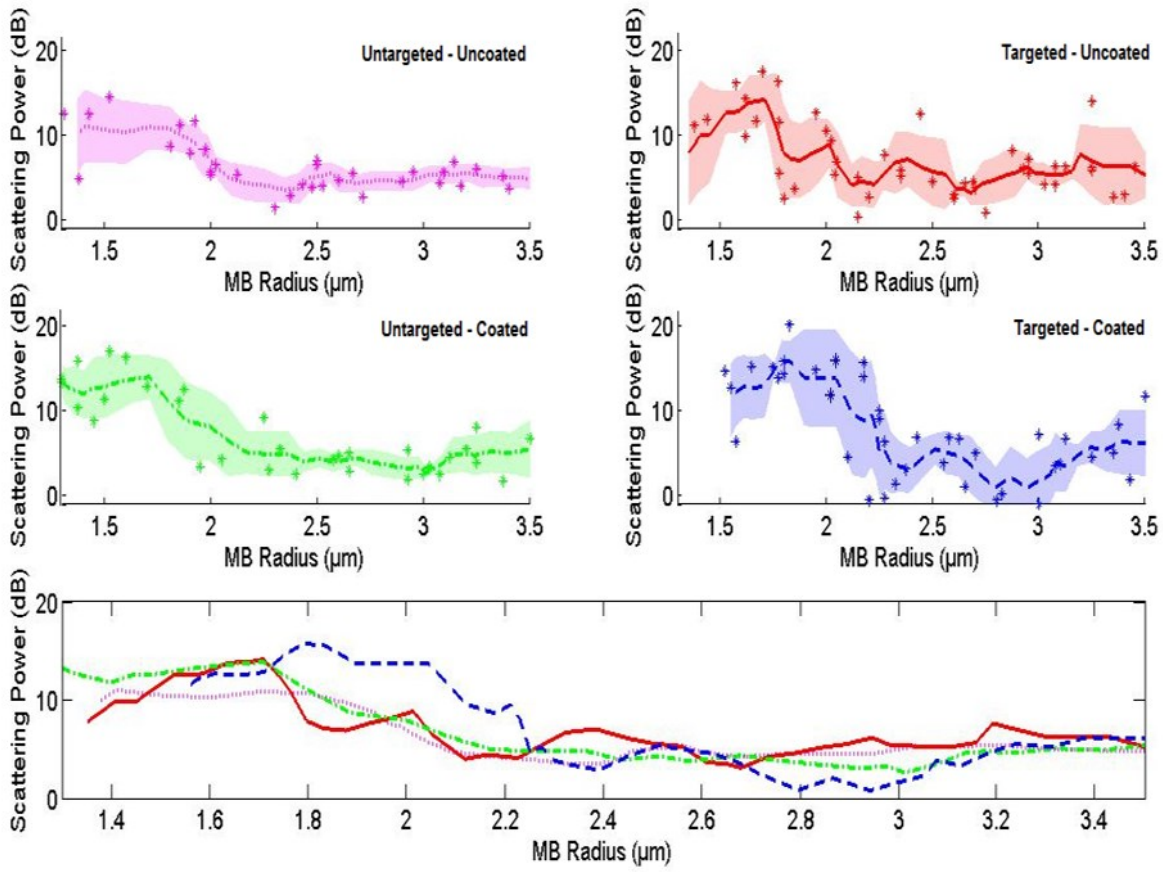

Figure 4-7: 2nd Harmonic scattering as a function of bubble radius for the 4 testing regimes. The 3 non-adherent or control cases of: Untargeted – Uncoated (Top left), Targeted – Uncoated (Top right), Untargeted – Coated (Middle left). And the adherent or Targeted – Coated (Middle right) regime. Mean trend lines superimposed to show comparison (Bottom). All three non-adherent regimes have a $P>0.05$ throughout the radius range examined. The adherent case differs ($P<0.05$) from the non-adherent cases in the radius range 1.8-2.0 μm (Power=35%).

To establish the radii associated with peak 2nd harmonic generation the data was fitted with a polynomial curve. Figure 4-8 shows this curve fitting for the adherent MBs. The radius at which maximum 2nd harmonic generation occurs is indicated by the solid line (R=1.86 μm). To provide confidence bounds for this peak the mean residual was subtracted from the peak 2nd harmonic scattering power, this provided a range of MB radii from 1.75 – 1.97 μm. This data has been collated for all testing regimes in Table 4-1.

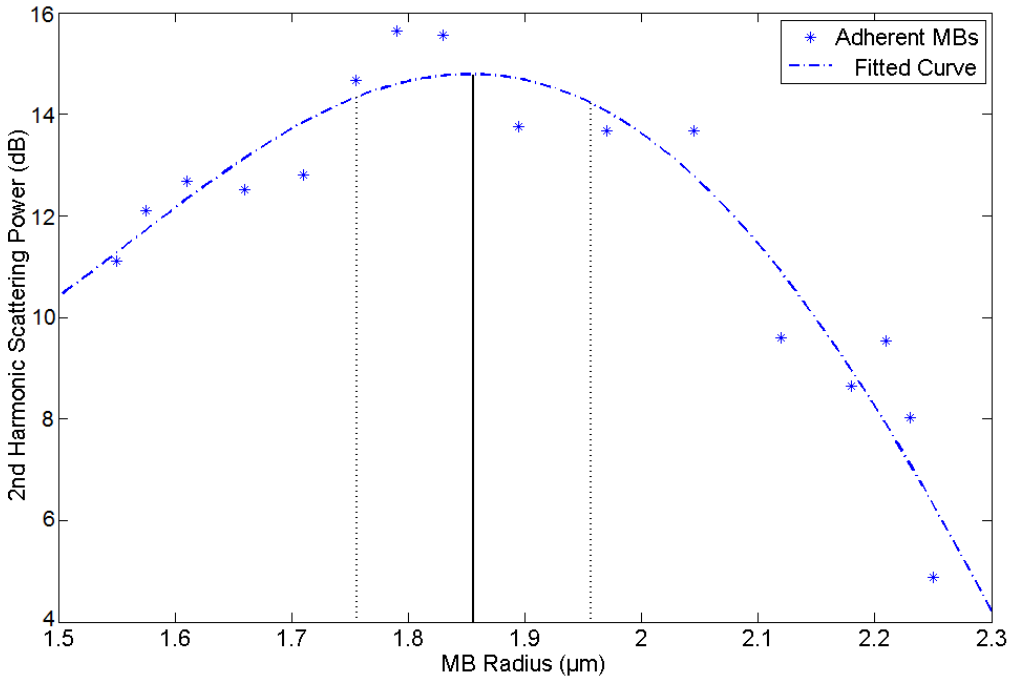

Figure 4-8: Example of curve fitting to the 2nd Harmonic scattering data of adherent MBs for resonance detection. Curve maximum occurs at R = 1.86 μm indicated by the solid black line, dashed lines show the confidence interval for peak detection.

Testing Regime	Resonance Radius (μm)	Confidence Interval (±μm)
Untargeted – Uncoated	1.59	0.11
Targeted – Uncoated	1.60	0.09
Untargeted – Coated	1.60	0.10
Targeted - Coated	1.86	0.11

Table 4-1: Resonance radii as derived from curve fitting to 2nd harmonic generation.

Given the similarity between the three unbound cases, the following sections consist of comparisons between the adherent (TC) and the non-adherent (TUC) MBs to identify difference between otherwise identical bubbles with or without target receptors.

Figure 4-9 shows the MB scattering power as a function of MB radius for: Fundamental scattering (top) and 2nd harmonic scattering (bottom). The fundamental scattering can be seen to be at a minimum below the resonance radius. Through the resonance radius for a 2 MHz insonation pulse (≈1.8 μm based on current theory for phospholipid shelled MBs [144], [147]) there is an

increase in the fundamental scattering until a radius ≈2 µm where upon the rate of increase levels out. This trend is consistent in both the adherent MBs as well as the non-adherent MBs. There is no statistical difference between the trends.

The 2nd harmonic scattering power shows a maximum around where one would expect the resonance radius to occur. Peak maxima were extracted (Table 4-1) and showed an adherent MB resonance radius of 1.86 µm in comparison with and a non-adherent resonance radius of 1.60 µm, the two datasets have been shown to be statistically different in the range 1.8 – 2.0 µm ($p<0.05$). It should be noted that the power of the statistics in this region was only 35% indicating low confidence in this p value due to the sample size and observed variation. The implications of this will be discussed in Section 4.5. Away from resonance effects (>2.5 µm) the response characteristics between the two bubble types are in agreement with diminished 2nd harmonic generation.

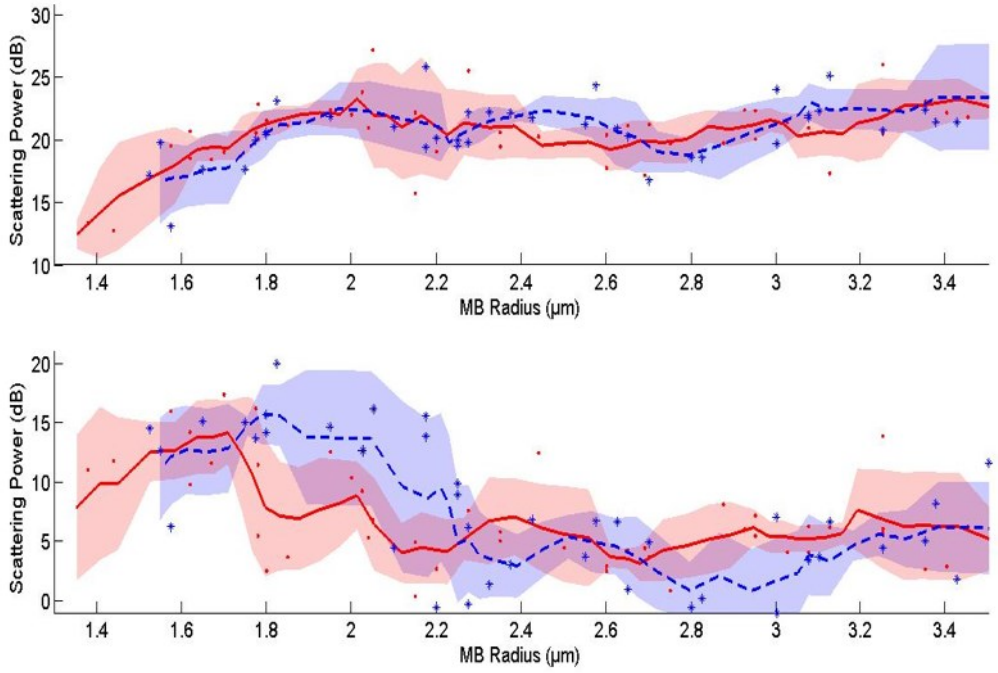

Figure 4-9: Scattering power as a function of MB radius for: Fundamental scattering (top) and 2nd harmonic scattering (bottom). Comparison between adherent MBs (Blue dashed line) and non-adherent (Targeted MBs in an Uncoated capillary fibre, Red solid line).

4.4.3 MB response to repeated insonation

Figure 4-10(top) shows the bubble stability index after the first 5 insonation pulses. A stability index of 1 refers to a bubble whose response is invariant with repeated insonation. A stability index less than 1 indicates that the MB response decreases with subsequent insonations. A number of bubbles can also be seen to have a stability index of greater than 1 indicating an increase in acoustic response to successive insonations, the possible reasons for this is expanded upon in the discussion.

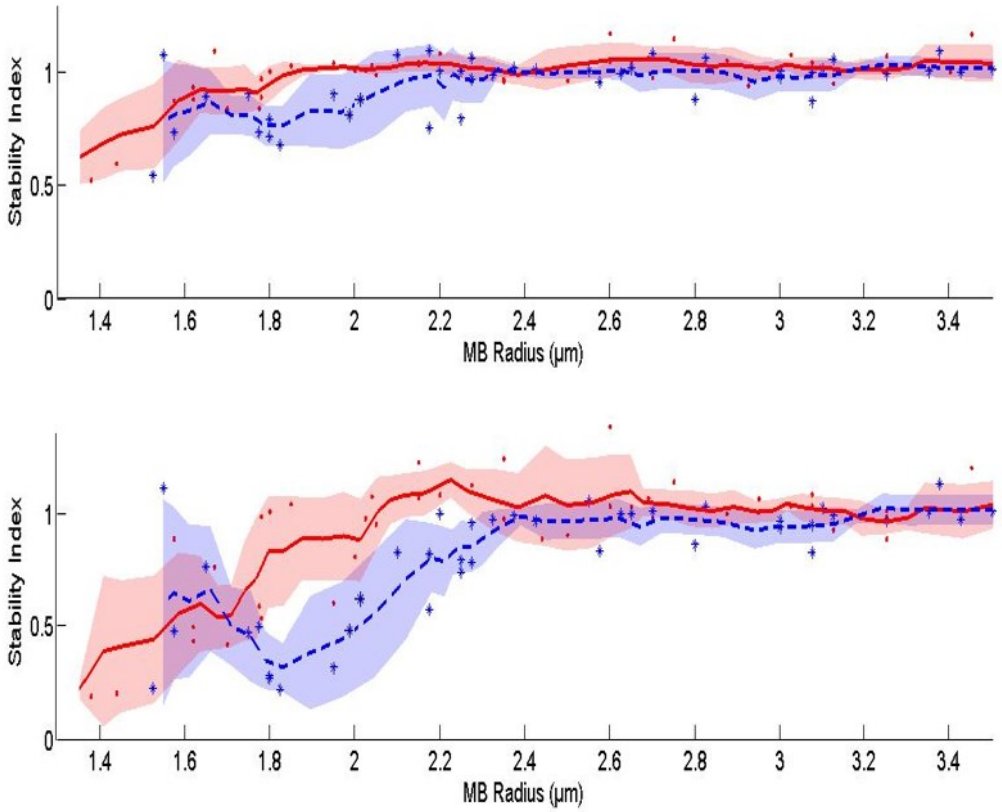

Figure 4-10: Stability index for the first 5 pulses of pulse sequence (top). Comparison between adherent MBs (Blue dashed line) and non-adherent MBs (Red solid line). P<0.05 in the radius range 1.8-2.0 µm (Statistical power= 75%). Stability index after exposure to the whole pulse sequence (bottom). Comparison between adherent MBs (Blue dashed line) and non-adherent MBs (Red solid line). P<0.05 in the radius range 1.8-2.4 µm (Average statistical power for range = 72%).

MBs near the peak second harmonic generation as seen by Figure 4-9 for both adherent and non-adherent MBs are subject to the most disruption. Upon exposure to the first 5 interrogation pulses non-adherent MBs first experience a decrease in response at radii ≈< 1.8 µm. This is in

comparison to adherent microbubbles which experience this response at a larger initial radius ≈< 2.2 μm. P<0.05 in the range 1.8 – 2.0 μm, this statistical significance was reached with a power of 75%. The size below which the MB response is seen to decrease will be called the disruption threshold. As with the 2nd harmonic generation, for MB of radius greater than 2.5 μm the MBs can be seen to be essentially invariant with pulse repetition for both adherent and non-adherent MBs (P>0.05). Figure 4-10 (bottom) shows the stability index after the bubble has been exposed to the whole pulse sequence i.e. insonated with both the interrogation pulses as well as the increasing pressure ramp of broadband insonation. Broadly speaking it shows the same trend as the top of Figure 4-10, showing the size dependence on the stability index. One can also observe that the MB disruption threshold for both MB cases has increased, from approximately 1.8 to 2.0 μm for non-adherent MBs and from 2.2 to 2.4 μm for adherent MBs. Furthermore, the levels of disruption experienced in both cases are dramatically increased and it follows that the curves are significantly different over a wider range, P<0.05 in the range 1.8 – 2.4 μm, this was achieved with a statistical power averaging 72% across the range. Peak predictive confidence was observed in the size range of 2.0 to 2.2 μm with a confidence level of 80%.

4.4.4 **Response Asymmetry**

Figure 4-11 displays the degree of asymmetry as a function of MB radius. A degree of asymmetry of zero corresponds to a perfectly symmetrically oscillating MB, a positive degree of asymmetry indicates that the transducer response is skewed to a positive side and vice versa for a negative degree of asymmetry. Due to the transducers used and the data collection systems a positively skewed dataset is related to the compression phase of the MB oscillation and likewise a negative skew indicates an expansion dominated effect.

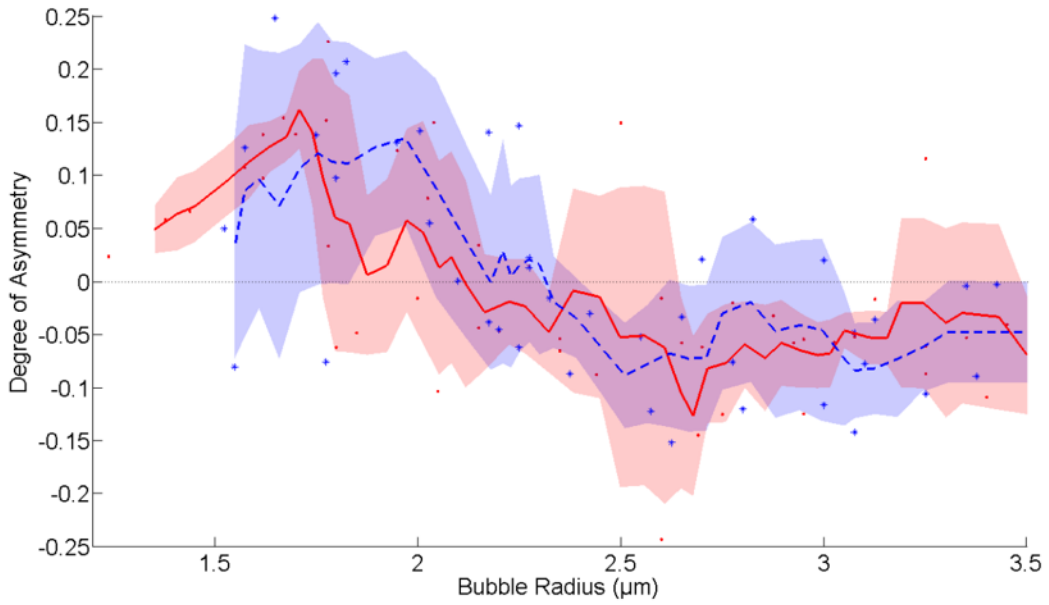

Figure 4-11: Degree of asymmetry as a function of MB radius for adherent (Blue dashed line) and non-adherent MBs (Red solid line). P>0.05 for the whole size range

Examination of Figure 4-11 shows that when the MBs are excited above their resonance size their response is typically slightly expansion dominated. As the MB size approaches the resonance radius the expansion dominated effect changes polarity and becomes a compression dominated effect. In comparison to both the 2nd harmonic scattering and MB stability there is no statistical difference between the adherent and non-adherent cases (P>0.05 for the entire range of MB examined). There is the suggestion of the radius difference as previously observed between the cases however the degree of asymmetry is shown to be subject to very high variations in magnitude, for example, examination of the data around the 1.7 – 1.8 µm for the adherent MBs shows both expansion dominated behaviour and compression dominated behaviour in close proximity.

4.5 Discussion

4.5.1 Experimental errors and variability

The data presented shows a large degree of variability even for similar sized bubbles, the cause of which may be attributed to several factors. While bubble response is strongly dictated by initial bubble radius the bubble's structural properties have also been shown to have a significant effects, specifically initial surface tension resulting in differences in both amplitude and shape of oscillation i.e. compression/expansion only behaviour, bubble destruction and fragmentation etc. [129], [132]. A factor which could help improve the quality of the data shown and indeed any inferences made would be through the gathering of more datasets. This would allow for trend-lines to be plotted with greater confidence and the resultant statistics to carry more weight.

During insonation the MBs are all exposed to a primary radiation force resulting in bubble motion. Given a sufficiently large motion this could move the MB out of the focal region of the transducers given rise to misleading results. To certify that this would not be an issue a number of bubbles were insonated with the full pulse as described earlier but with the microscope objective still in place to directly observe bubble motion. The maximum bubble motion was observed to be of the order of <10 μm.

Another possible source of error comes from the presence of nearby bubbles in the acoustic field. While this is minimised by the optical verification that the capillary fibre is clear either side of the target bubble only the upper surface of the fibre is scanned for time efficiency purposes and the fact that any MBs should rise through buoyancy. Therefore it doesn't mitigate against bubbles being entrained elsewhere on or in the fibre either trapped by particulate matter or forming because the whole system is immersed in gas saturated water. Typically any large bubbles of this kind were detectable from the magnitude and shape of the response and discounted however for smaller bubbles these responses could easily be overlooked leading to skewed data.

4.5.2 Scattered acoustic response

All the bubbles examined, both adherent and non-adherent, displayed similar fundamental response to the 2 MHz insonation pulse indicating that under these conditions the presence of binding does not significantly alter a MB's fundamental response. Examination of the 2nd harmonic

scattering does exhibit a difference however (Figure 4-9). The shift in resonance radius between the two cases; 1.86 µm for the adherent MB compared with 1.60 µm for the non-adherent MB, indicates an increase in resonance frequency for the adherent MBs, It should be noted that although the peak fitting shows a difference between the adherent and non-adherent resonance frequencies the statistical power behind this only indicates a 35% chance that this is a true positive result, additional support for this supposition however occurs via the stability data in the following section where the confidence is far greater. The difference between the resonance radii of the adherent (TC) in comparison to the three non-adherent MB cases indicates that it is adhesion which causes the shift in resonance radius (and therefore frequency) and not simply an artefact of the functionalization of either the capillary fibre or the MB, this is in agreement with the finding shown in [43]. While the contribution of the second harmonic can be seen to have quite a dramatic effect on the level of total scattering, especially around resonance, it does not provide sufficient difference to clearly delineate the adherent from the non-adherent MBs on its own. This in itself is important when trying to implement differentiation protocols in more complex scenarios, implying that detailed frequency content is required rather than just total backscatter in the differentiation of adherent and free MBs.

Comparing these results to the findings of both Patil et al. [159] and Overvelde et al. [43] a number of differences present themselves. All three studies (this present study, Casey et el., included) show differences in the acoustic characteristics for adherent MBs however the way this difference is demonstrated is different in each case. The Overvelde study would appear to be most comparable to this present study i.e. similar frequency ranges, bubble type and applied pressures. By insonating both adherent and non-adherent MBs of similar size (Radius ≈ 2.1 µm) through a range of frequencies and recording their oscillations via a high speed camera the frequency of maximum response was found. It was found that adhesion reduced the normalised frequency of maximum response by 30%. The normalised response is the experimentally obtained resonance frequency divided by the resonance frequency of an unencapsulated MB of similar size. By applying the same normalisation to this current study the change in resonance size equated to an increase in normalised resonance frequency of 19%.

Given the large discrepancies between the findings of this study and the Overvelde study for seemingly similar acoustic conditions one must then assume that there is a difference in other experimental conditions or in the way results are analysed which causes this discrepancy.

There are a number of factors which could influence the MB response in these studies. For example, any differences in MB shell chemistry effectively change the MB visco-elastic properties between the two studies. This has the effect of modifying the shape and position of the resonance

frequency curve. In addition it has been previously postulated that both shell elasticity and viscosity have a size dependant nature [128], [136], [219] further skewing the resonance frequency curves. As an aside to shell chemistry the binding mechanisms used in the two studies are also different. A Biotin/Streptavidin ligand pair in this (Casey et al.) study compared to a fluroscein/anti-fluroscein anti-body binding mechanism if the Overvelde study. The rationale for utilising Biotin/Streptavidin was that its high binding affinity ($k_a \approx 10^{15}$ /M) would maximise any differences between an adherent and non-adherent MBs. In contrast fluroscein/anti-fluroscein has a much lower binding affinity ($k_a \approx 10^{10}$ /M) which could also account for some of the observed differences. The contribution of binding affinity to MB acoustic behaviour has not been explored and will be a focus of a future investigation.

The local MB is confining conditions are also known to have a dramatic impact on the resulting bubble dynamics, [41], [158], [160], [162], [239] have shown that wall stiffness can either increase or decrease the resonance frequency of a MB positioned near it. Helfield et al. [246] explored the effects of adhesion using far higher transmit frequencies but noted that either an increase or decrease in resonance frequency could be observed depending on the transmit frequency. Rigid boundaries having been shown the effect of decreasing the resonance frequency [41] whereas compliant boundaries have to opposite effect [42], [158]. Furthermore, the relative size of the vessel compared to the MB has also been shown to enhance this change in resonance frequency. In this study the MBs are confined in a 200 µm cellulose capillary fibre compared to the Overvelde study which utilised the Opticell™ culture dishes (polystyrene membranes with 2 mm of clearance). Not only are materials different and hence the material properties and effects on MB dynamic characteristics but also because the capillary fibre is much closer in size to the MBs a number of size dependant effects become more pronounced.

As a final cause of the discrepancies one must also examine what it is that the studies are actually gathering as their datasets. This present study is examining the scattered pressure and specifically the 2nd harmonic signal generation as an indicator or resonance. In comparison the Overvelde study is examining the radial oscillations and specifically the maximum radial excursion. By nature this is predominately a measure of the fundamental MB response. As a further complication, this data is obtained via a high-speed camera limited to a single orthogonal view. As previously stated a MB near a boundary can experience significant asymmetry in oscillation [39], [40]. While it has been demonstrated that it is possible to derive the pressure-time trace from the radius-time curve by assuming purely radial oscillation it was shown in the same study in situations such as these the acoustic recording of MB response was more sensitive to changes in the higher harmonics than high speed camera observations however did not record low frequency effects as

well [145]. One caveat to all of this is that if the difference in experimental setup between this present study and the Overvelde study cause significant discrepancies between the obtained results it might be that in a more complex in vivo situation where far less experimental control can be exerted that any observable differences are diminished if observable at all.

4.5.3 MB response to repeated insonation

Figure 4-10 indicates that resonance plays an important role in the stability and longevity of MBs. This stands to reason when one considers that a bubble at resonance will experience the widest fluctuations in size as well as shape deformations. This is supported by Guidi et al. [176], [242] who utilised a high speed camera approach to show that phospholipid shelled MBs undergo acoustically induced deflation after repeated insonation and that this is exacerbated near resonance. The shift in resonance size shown in the 2nd harmonic scattering is also clearly evident in both parts of the figure by the shift in disruption threshold to larger MBs for adherent MBs. Unlike the 2nd harmonic generation however there is no distinct disruption peak associated with the resonance frequency however due to the greater difference between the adherent and non-adherent stability indices far greater confidence can be placed in the statistical significance that there is indeed a difference brought about by adhesion. The stability index indicates that bubbles smaller than the resonance radius undergo severe disruption even at the relatively low acoustic pressure (specifically the small radii MBs of Figure 4-10), the caveat to this is that this can only be said to be true for these specific experimental conditions. It may be that given larger MBs and a lower driving frequency the bubbles smaller than the resonance radius may be robust enough to survive.

The employment of the broadband destructive pulse activated a wider size distribution of MBs as demonstrated by the increase in disruption threshold for both adherent and non-adherent MBs alike. In future however, it may be useful to consider utilising either a broader band or lower centre frequency transmitting transducer for the activation a more diverse size population of the MBs. With the current set up one can see that the majority of MBs interrogated are still above the size range affected by the ultrasound in both the 2nd harmonic and stability index data.

A number of MBs show that there has been an increase in the total scattering to successive pulse (a stability index >1). As already described, MBs are known to exhibit acoustically induced deflation in response to ultrasound [176]. By this mechanism if a MB with radius initially above the resonance radius was insonated each successive pulse could deflate the MB, driving its radius

towards the resonance size. In this case, and with reference to Figure 4-9 one can see that for little change in fundamental scattering as the MB approaches resonance the 2nd harmonic contribution to total scattering would result in an increase in total scattering and hence a value >1 for the stability index.

4.5.4 Response asymmetry

The description of MB radial response asymmetry has been the focus of a number of studies since the observation of "compression-only" behaviour by Sijl et al. [133] however there has been little emphasis placed on what this radially asymmetry means in terms of the scattered pressure. Radial asymmetry has be attributed to sharp changes in the MB shell rheological behaviour i.e. sharp changes in elasticity. This was modelled effectively by the Marmottant model as a MB resting in its buckled state. Any oscillation from this median position would either incur a sharp increase in elasticity if the MB expands or zero elasticity upon compression (cf. Section 2.5.2 for the basic description of the variable elasticity and Section 6.4.2 for its subsequent implementation into modelling). This is typically attributed to a pressure dependent effect with no correlation is inferred between compression-only and resonance. If one considers that through resonance the MB shell is undergoing extremes in oscillation due to the rapidly increasing fundamental response and peak 2nd harmonic response. These extremes in oscillation could drive the MB response towards the elasticity transitions in a similar way to increasing the acoustic pressure. Similarly if the MB stability is most affected near resonance one could reasonably expect this to alter the shell properties towards the buckled shell state and hence increase asymmetry. Pressure response asymmetry could therefore be used as a novel method of detecting MB resonance.

4.5.5 Directions for future investigation

The shift in acoustic frequency detected could have potential for the development of novel imaging strategies for the differentiation of adherent MBs. At present the detected shift in resonance frequency is very small and subject to variation between MBs (even of similar size). In most bulk or non-single bubble techniques these subtle differences will be masked by the response from the polydisperse MB population. Currently there is significant effort developing methods for the production of monodisperse populations of MBs [211], [214], [215]. With tightly controlled MB physical characteristics (i.e. radius, shell composition), not only will the variability between MBs of similar sizes be reduced but the MB radius can be tailored to the specific imaging parameters and

make maximum use of any resonance frequency shift. In addition one of the immediate methods that could be implemented to improve of the results would be via the collection of increased sized datasets, this would allow for far greater confidence to be placed in the inferred trends and statistics.

The examination of sub-harmonics (SHs) rather than higher harmonics may also have potential. SHs are produced at half the insonation frequency and have been shown to be at a maximum when a MB is driven at twice its resonance frequency [198]. If the shift in resonance observed here is also evident in the SH response of MBs this would effectively result in difference in resonance radius being exaggerated twofold allowing for easier differentiation. The generation of SH is still not fully understood with figures quoting only approximately 40% of MBs in a given population will actually generate SH.

4.6 Summary

The acoustic setup for detailed interrogation of single microbubbles under controlled conditions is presented. The adherence of MBs to a capillary fibre wall via a Biotin-Strepavidin bond can be seen to increase the MB resonance frequency by shifting the radius of peak generation of 2^{nd} harmonic signals. The fundamental scattering properties of the MBs are seen to be unchanged by the presence of adhesion. It should be noted that in its present state these differences are difficult to detect reliably in vitro so there are still significant issues to be faced before this could be applied in vivo.

Microbubble stability is observed to be heavily dependent upon the resonance properties, with resonance bubbles being significantly more susceptible to disruption than MBs situated above their resonance radius. The change in resonance frequency shown by the 2^{nd} harmonic generation is also highlighted by the bubble disruption.

Pressure response asymmetry has been shown to be linked with the resonance radius of the MB and could provide a non-direct method for determining the onset of MB resonance.

5 Sub-Harmonic Characterisation of Adherent Microbubbles

5.1 Abstract

This chapter continues the acoustic characterisation of the MBs as used in Chapter 4 however this extends to examine the sub-harmonic component of the MB response. In order to achieve this a number of changes had to be made to the testing rig and protocol. Adherent and non-adherent MBs were insonated with a 2 MHz, 200 kPa PNP 10 cycle pulse and their scattering response was collected focussing on the 0.5 – 1.5 MHz range where SH were expected to be generated. SH were detected for all testing cases within a narrow frequency and MB radius range. This range corresponded well with current theory for the prediction of conditions for SH onset. There was a high degree of variability seen in the acoustic responses for all testing regimes and it was not possible to differentiate the adherent response from the non-adherent responses under these conditions.

This work was presented at The IEEE International Ultrasonics Symposium, 2012. Dresden, Germany. Under the title "*Sub-Harmonic Characterisation of Single Adherent Microbubles* **"**

In addition aspects of the work were also presented at the Microbubble Symposium: Fabrication, Characterisation and Translational Applications, 2012. Leeds, UK. Under the title *"Single Bubble Sub-harmonic Characterisation of Lipid Shelled Microbubbles: Effect of Functionalization and Adherence."*

5.2 Introduction

MBs have been proven to have extensive applications in ultrasound imaging; their acoustic properties mean that they produce significantly higher levels of scattering than the surrounding medium. Furthermore, the scattering is highly non-linear. When the received MB signal is compared to the response from tissue it results in a dramatically increased contrast to tissue ratio CTR. The non-linear response; particularly the higher order modes of response, has led to a number of imaging strategies specifically utilising this, such as, pulse inversion or amplitude modulation (cf. Section 2.7)**.** One of the disadvantages of using these higher order response modes is that artefacts can arise from nonlinear propagation of these non-linear signals within the tissue [194], consequently an area of active research has been into the sub-harmonic response of microbubbles.

Sub-harmonics are the signals received at half the transmit frequency ($f_0/2$) and have the benefit of not being subject to non-linear propagation through tissue at typical applied acoustic pressures [194]. In this way many of the artefacts observed in higher harmonic imaging are circumvented. The lower frequencies involved mean that there is a reduction in axial resolution compared to higher frequencies however they also mean that greater depth penetration can be achieved due to the decreased attenuation at lower frequencies [210]

Higher harmonic signals are generated for MB across the broad range of MB radii, frequency and incident pressure conditions as a continuous process [247]. Conversely sub-harmonics have been predicted to have a minimum threshold pressure before onset [198], [210]. For free gas bubbles this onset pressure is shown to be at minimum when the MB is insonated at twice its resonance frequency, when this is applied to MB with a encapsulating material this minimum is seen to change in relation to the rheological properties of the encapsulation medium i.e. its dilatational viscosity and elasticity. This effect has been demonstrated both experimentally and in simulation [134]. It should also be noted that depending upon the theoretical model used the frequency and pressure required for this onset can vary [198], [199].

Following from the previous chapter which examined the fundamental and 2nd harmonic response as a function of shell modifications for targeting and adherence, this chapter seeks to explore the effect that functionalization and adherence has on the sub-harmonic part of the MBs scattered signal. Previously it was noted that the adherence of MBs in these specific experimental conditions has the effect of effectively increasing the resonance frequency of a given MB. This was displayed by a shift in MB radius of the peak generation of the 2nd harmonic signal content. The size shift noted was of the order of 0.3 µm and consequently close to the limit of detectability with the

current setup. The peak generation of SH signal is predicted to occur when the MB is insonated near or at half its resonance frequency, if this is instead thought of in terms of resonance size it means that peak SH generation is expected when the bubble radius is twice the resonance radius for the insonation frequency. If the resonance shift due to adherence detected in the 2nd harmonic signal of Chapter 4 is also detected in SH signals, this could lead to a twofold increase in the observed size difference between adherent and non-adherent resonance radii and could prove a more reliable method for the differentiation of signals from adherent MBs.

5.3 Methods

5.3.1 Experimental Setup

The experimental setup is similar to the one previously described in Chapters 3 and 4. The principle difference being the centre frequency and bandwidth of the receive transducer. For this study the receive transducer had a centre frequency of 1 MHz and a -6 dB bandwidth between 0.5 – 1.5 MHz. The full reasoning for this will be covered in section 5.3.3, briefly it was to allow for detection of a SH signal at 1 MHz for a 2 MHz insonation pulse similar to the one utilised in Chapter 4. The experimental setup was as follows.

Two focussed transducers (the transmit transducer was the 3.5 MHz centre frequency transducer as used in Chapters 3 and 4 and the receive transducer as described above) were confocally aligned with the field of view of a 40x water immersible objective (LUMPlanFL N 40x W Olympus). These three components focussed on a 200 µm diameter capillary fibre (RC55 8/200 Membrana GmbH, Germany) through which the microbubble suspension a 200 µm diameter capillary fibre (RC55 8/200 Membrana GmbH, Germany) in which the microbubbles were interrogated.

The transmitted signal was generated in an arbitrary waveform generator (Sony Tektronix AWG2021) and amplified through a power amplifier (2100L, E&I, NY, USA). The scattered signal was amplified by a pulser/receiver operated in receive mode (Panametrics-NDT 5800) and displayed via a digital oscilloscope (Sony Tektronix TDS7154). The image from the objective was directed to a digital camera (Canon ProShot G5) through a 45° mirror and focussing lens for subsequent sizing.

5.3.2 Microbubble Preparation and Tube Preparation

The MBs and capillary fibres were prepared in exactly the same fashion as previously (cf. 4.3.2).

Microbubbles were prepared by the sonication (Misonix Sonicator 3000, settings 21kHz 165W; 30s) of an octofluoropropane-saturated aqueous suspension of distearoyl-phosphatidylcholine (DSPC), distearoyl-phosphatidylethanolamine-PEG2000-biotin (DSPE-PEG2000-Biotin) and poly(ethyleglycol)-monostearate (PEG40-stearate). Non-targeted microbubbles (control)

were prepared similarly, substituting DSPE-PEG2000-Biotin with methoxy-poly(ethyleglycol)2000 distearoyl-phosphatidylethanolamine (DSPE-mPEG2000). Microbubble size distribution and concentration were measured to have a mean size diameter of 2.4 (±0.4) μm and a number concentration of 1.2×10^9 microbubbles/mL using optical microscopy [245].

Capillary fibres were cleaned with sterilised PBS (Sigma-Aldrich Ltd. Dorset, UK) and flooded with unlabelled Streptavidin (Invitrogen Life Technologies Ltd, UK) solution at a concentration of 0.25 mg/ml, before incubation over night at 4°C. The tubes were flushed with saline and then ready to use. Tubes were changed regularly throughout each testing day to negate any degradation. This method of targeted MB generation, tube preparation and MB adhesion was successfully employed by Loughran et al. [105] , the same materials and equipment was used for this study.

5.3.3 **Acoustic Pulse Definition**

Ideally the pulse used to excite the MBs in this experiment would be similar if not exactly the same as used in the previous chapter to facilitate the comparison between the data and aid the inference of any conclusions made. For example, it is known that MBs have both frequency and pressure dependant response characteristics so if these parameters are changed one could reasonably expect some aspects of the MB behaviour to be different. This however was impinged upon by the nature of the experiment and the conditions this imposed/required.

The first issue was that by keeping the transmit frequency consistent with the chapter 4 (2 MHZ) it means that the sub-harmonic signals, by definition, are expected at $f_0/2$ or in this case 1 MHz. This necessitated the replacement of the receive transducer to the one described above. This transducer was of the order of 50% less sensitive than the transducers previously used but was significantly more sensitive than the 3.5 MHz centre frequency transducer in the 1 MHz region (see Figure 5-1 for a comparison of the relative bandwidths and sensitivity of the transducers used in this study, the transducers were used in pulse echo mode targeted at a plane reflector and excited the same voltage impulse, data is normalised to the peak response obtained). Given the bandwidth of the 3.5 MHz transducer one option would have been to transmit at 4 MHz and receive at 2 MHz using the exactly the same set up as Chapter 4. The problem with this arrangement would have been the MB size at which SH would be expected to occur. Using these frequencies the resonant radius of the MBs would have been < 1 μm. These small MB were known to be very unstable at such high dilutions and consequently very difficult to isolate, this is illustrated by the lack of datasets below 1 μm in both Chapters 3 and 4, this was not because those results would not have been of interest it

was simply a fact that no MBs of that size were observed for long enough to allow for characterisation. It was deemed favourable to keep the transmit frequency at 2 MHz thereby increasing the bubble radius where one expected the majority of SH generation to occur and thereby increase the data collection rate by having a more stable /easily isolated MB.

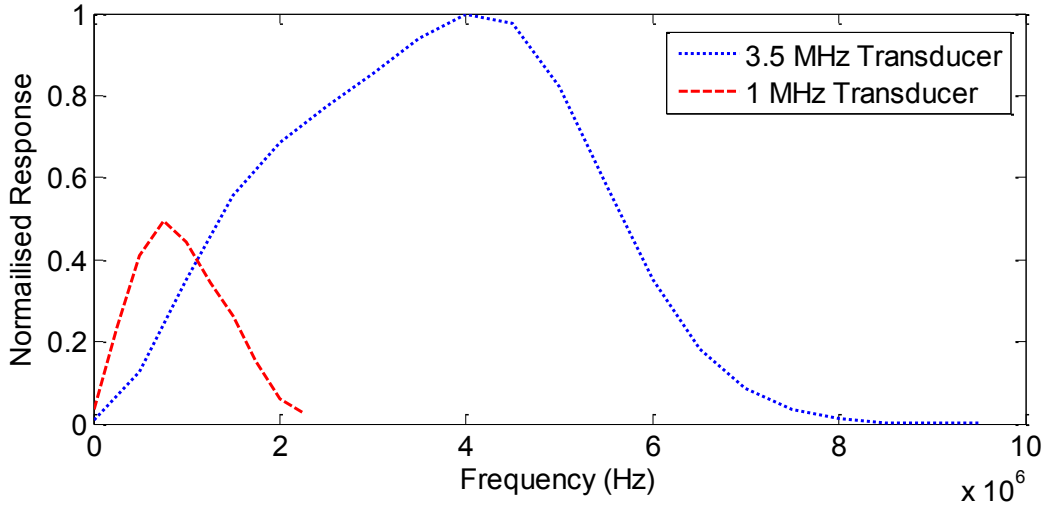

Figure 5-1: Relative Frequency Response Curves of the Two Transducers used in this Experiment

The generation of SH signals has been shown to be open to a large degree of variability depending of the pressures applied (both acoustic and ambient) [201], [248], [249], the formulation and shell composition of MB used [200] and even open to quite a large degree of variation for MBs of the same size from the same population [146], [226]**.** Therefore it was decided that a preliminary study was required to get a broad understanding of the MBs SH behaviour and to use that to inform decisions such as applied acoustic pressure and pulse sequence.

This preliminary study used the setup as described above and insonated a dilute suspensions of MBs (Approximately $1x10^6$ MB/ml.) with a 2 MHz 10 cycle pulse of increasing peak negative pressure from 50 kPa to 300 kPa at the focus (verified using a 1 mm diameter needle hydrophone (HPM1/1 Precision Acoustics, Dorset UK)). Once MBs were positioned in the focal region they were exposed to 10 repeats of the above pulse before the focal region was moved to a new set of MBs; this was performed multiple times (n=10) for each frequency of excitation. The use of the dilute suspension rather than single MBs not only greatly increased the data collection rate but also gave a much higher chance that at least one of the MBs in the focal region generated a SH response

however this was achieved at the expense of knowledge the precise size make-up of the MBs under examination. By recording insonations from multiple populations a broad understanding independent of MB size could be achieved. By tracking the SH signal intensity as a function of applied pressure a baseline pressure for further experiments was established, it should also be noted that the use of MB populations rather than single MBs will also artificially increase the reflected signal strength. These results are displayed below in Figure 5-2. The data shown at each pressure value consists of the mean SH response and associated standard deviation taken over 10 insonations of the same bubble population for N number of bubble populations. Also shown is the absolute peak SH response.

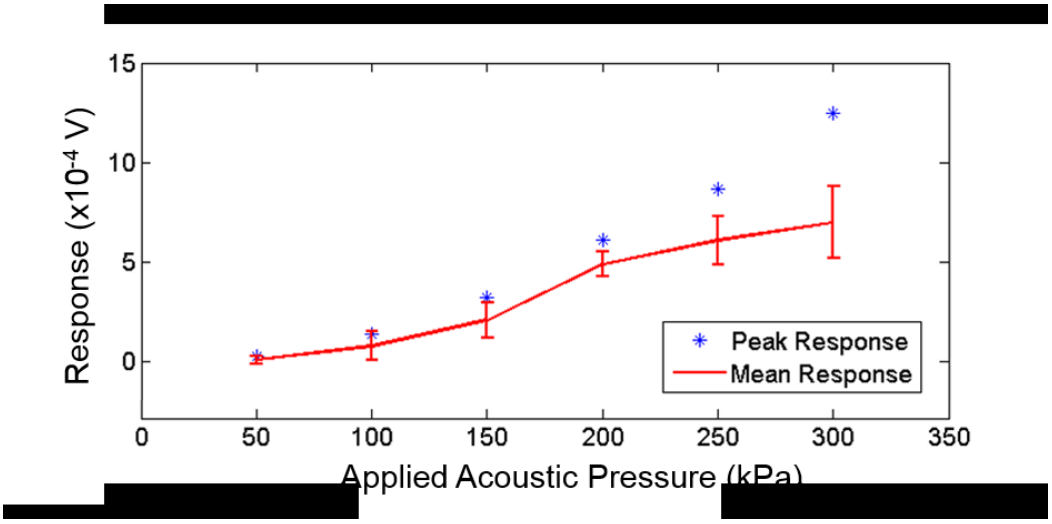

Figure 5-2: Peak and mean SH response for small populations of MBs as a function of applied acoustic pressure.

Examination of the peak SH signal indicates the SH are generated across the pressure range tested; albeit at very low levels for the lowest applied pressures. This is in broad agreement with previous studies which all show experimentally with that SH can be generated at low acoustic pressures; Using high speed photography SH signals have been detected at insonation pressures as low as 5 – 10 kPa [132], [199] however using acoustic methods this value increases to approximately 50 kPa for SH onset [201]. It must be noted that although SH signals are detectable at the low acoustic pressures, 50 and 100 kPa, they are almost indistinguishable from the noise floor of the system. Examination of the mean SH signal shows that using this setup it is only above an applied pressure of 150 kPa that a consistently observable SH signal is detected. Between 150 kPa and 200 kPa one can see that both the peak and mean SH signal intensity increases and becomes more consistent as demonstrated by the decreasing standard deviation. Above 200 kPa it can be seen that although the peak SH signal is still increasing the mean signal doesn't continue its rate of increase

and indeed increases in its standard deviation. This could be due to MB destruction through the course of one pulse sequence due to the increased acoustic pressure and is therefore a regime which should be avoided.

As with the main experiment in Chapter 4 the pulse sequence which the MBs were exposed to was split into two sections, Figure 5-3. The first section (Figure 5-3a) consisted of 5 interrogation pulses; centre frequency of 2 MHz, 10 cycles and a PNP at the focus of 200 kPa. The second section of the pulse sequence (Figure 5-3b) used the same interleaved interrogation pulses as before, this time however interspersed with a sequence of increasing cycle length pulses. These pulses increased in cycle length from 2 to 9 cycles at a PNP of 200 kPa. All pulses were sent at a PRF of 4 kHz

The rationale behind this sequence was as follows. The first pulse gives a bubble response with precisely known initial conditions, the following 4 pulses of the first section allow for the acoustic monitoring of the MB stability to repeated insonation. It was also expected that a similar MB stability profile would emerge in accordance with the findings of Chapter 4, Figure 4-10. That is, that MBs near or below their resonance size would experience a marked decrease in signal response to successive insonations. The interleaved pulses were incorporated on anecdotal evidence that the SH generation could be linked to pulse length.4

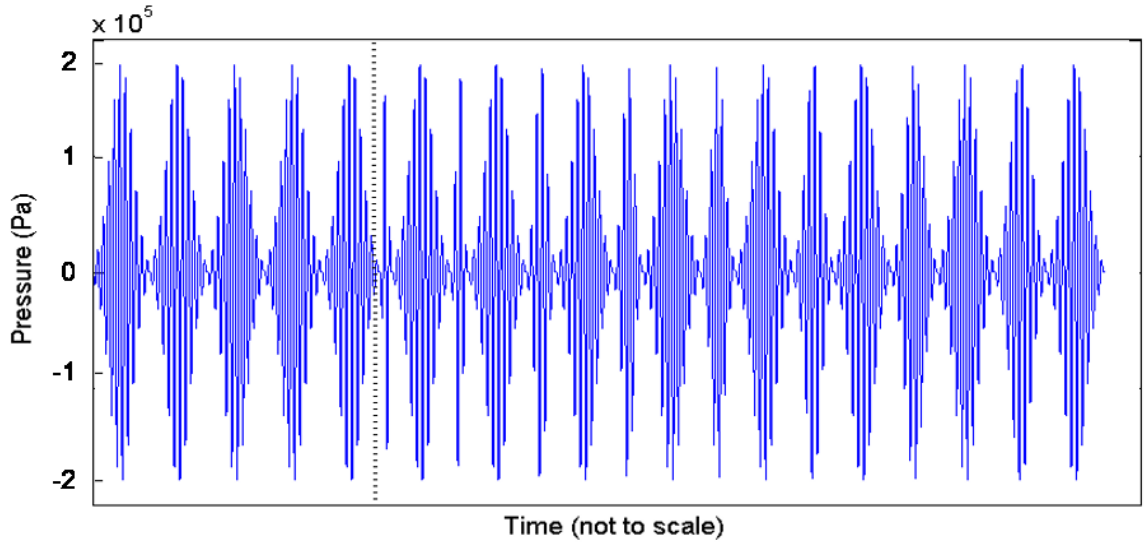

Figure 5-3: Pulse sequence used for SH characterisation. The first 5 pulses are the identical 2 MHz, 10 cycle, 200 kPa PNP pulses. The second half consists of the same pulse as above interleaved with a ramp of increasing pulse length pulses (PNP 200 kPa) from 2 cycles to 9 cycles. Total number of pulses in sequence = 21.

5.3.4 **Data Analysis**

The data for each bubble was split into single pulses, corrected for amplifier gain, zero offset and windowed using a hamming window. The data was then corrected for the frequency response characteristics of the transducer. Where scattering powers are shown in dBs the reference was taken as the noise floor of the system established by the average response of the system (n=10) to a sham exposure, all other experimental conditions were the same as in the full experiment except for the presence of MBs.

As previously remarked upon in Sections 3 and 4, there was a great deal of variation between individual datasets, even in the case of MBs of a similar size. To smooth this data for the ease of displaying trends a 5 point moving average was applied in both the recorded data (y direction) and sizing data (x direction). From this the mean and Standard deviation were extracted. In the following figures employing this windowing, mean data is displayed as a line with shaded regions representing the Standard deviation of the mean. Raw data is displayed as discrete points.

The statistical significance between the comparison trends the data is shown as a p value. This p-value refers to the difference between the datasets in 0.2 μm width bins. The significance level is set to $P>0.05$ and the regions of significant difference are highlighted in the relevant figures.

For a fuller description of both the moving window average and the determination of statistical significance please refer to Section 4.3.4.

From the previous experiments it has been clear that if valid conclusions are to be reached using this single bubble technique a large dataset is required. Consequently a great deal more time was spent ensuring not only that the data was acquired in sufficient volume but also, due to the size dependant nature of the results, that this dataset was sufficiently distributed across the range of sizes to be examined.

5.4 Experimental Results

5.4.1 Scattered Acoustic Power

Figure 5-4 displays the scattering signal received about the 1 MHz frequency band, this was taken as the area under the frequency spectrum from 0.8 – 1.4 MHz; this frequency range encompassed all SH signals observed. The top 4 plots shown the scattering from each of the four test cases examined: Untargeted MBs in an uncoated capillary fibre (UTUC) shown in purple (n=119), targeted MBs in an uncoated capillary fibre (TUC) shown in red (=96), untargeted MBs in a coated capillary fibre (UTC) shown in green (n=91) and targeted MBs in a coated capillary fibre (TC) shown in blue (n=109). The bottom plot displays the mean trend lines superimposed upon one another to show the relative similarities/differences.

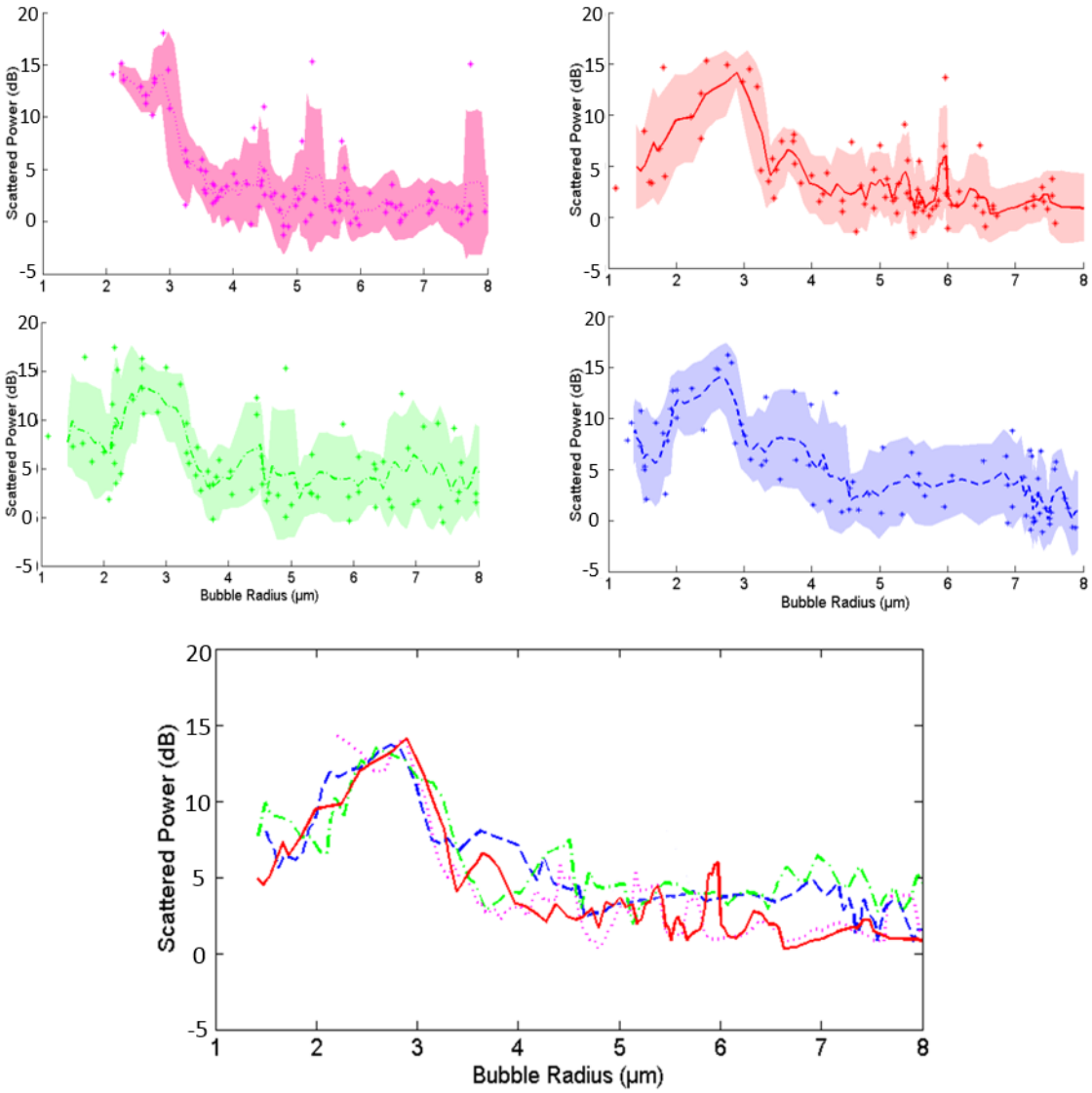

Figure 5-4: Sub-Harmonic scattering as a function of MB radius. Top four plots show the mean trend lines, Standard deviation and the raw data points for: UTUC (top left), TUC(top right), UTC (bottom left) and TC (bottom right). The final plot (bottom middle) shows the mean trend lines superimposed on each other.

The general trend for all four follows the same pattern. SH generation can be seen to reach a peak at a MB radius between 2-3 µm. After this maximum the SH generation can be seen to decline until the noise floor of the system was reached. Individual curves shown some variation from each other but this can be attributed to the highly variable signal from MB of similar size but this is typically due to one or two outliers and their compound effect on the moving average, these are clearly seen in both

Using the peak extraction method detailed in section 4.3.4 the radii of peak SH signal generation were determined and can be found in Table 5-1.

Testing Regime	Peak Sub-Harmonic Generation Radius (μm)	Confidence Interval (±μm)
Untargeted – Uncoated	2.7	0.3
Targeted – Uncoated	2.9	0.1
Untargeted – Coated	2.8	0.1
Targeted - Coated	2.9	0.1

Table 5-1: Radii of peak sub-harmonic signal generation

Evidently there is little to separate the curves, both in terms of their peak generation given in the table above but also in the comparison of the curves away from the peak. Indeed when the statistical analysis was performed p values of > 0.05 were achieved for the entire radius range examined.

A more detailed examination of the individual responses is presented in Figure 5-5. These plots show the frequency power spectrum as a surface plot for all MB sizes and covering the full frequency range examined. The right hand side of all four of the surface plots (f = 2 MHz) show a strong response in the fundamental mode. Due to the bandwidth of the 1 MHz transducer this has been included more for display purposes rather than for any analytical study, its serves as a visual aid to highlight the position of any subsequent SH emissions (cf. Section 5.5.1 for further explanation). SH responses are visible in all for experimental cases predominantly occurring in a discrete MB size range from 2 – 3 μm through the frequency ranges of 0.8 – 1.4 MHz. Similarly in all 4 cases a lower amplitude band of SH can be seen for all MB sizes in the 1.2 -1.4 MHz range.

For completeness and to give the number of MB datasets which make up these surface plots the number of MB for each bin size of Figure 5-5 are displayed in Figure 5-6. For the regions of zero MBs the surface plots were created via linear interpolation.

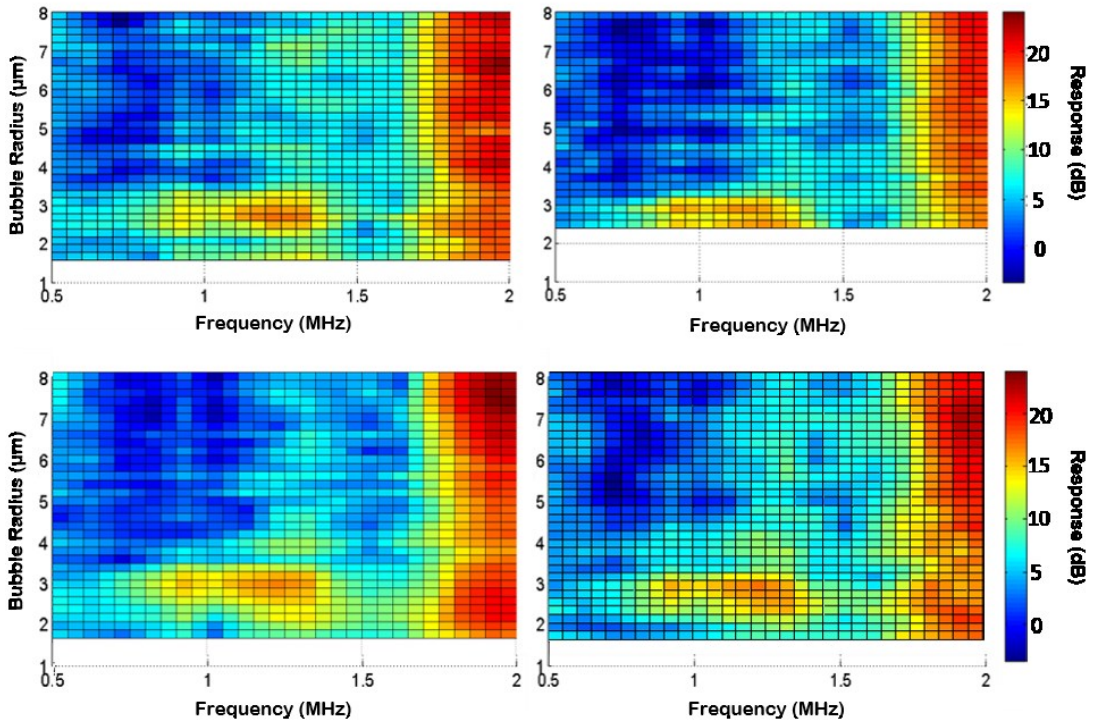

Figure 5-5: Surface plot showing the full spectrum of frequencies and bubble radii examined. TUC (top left), UTUC(top right), UTC (bottom left) and TC (bottom right).

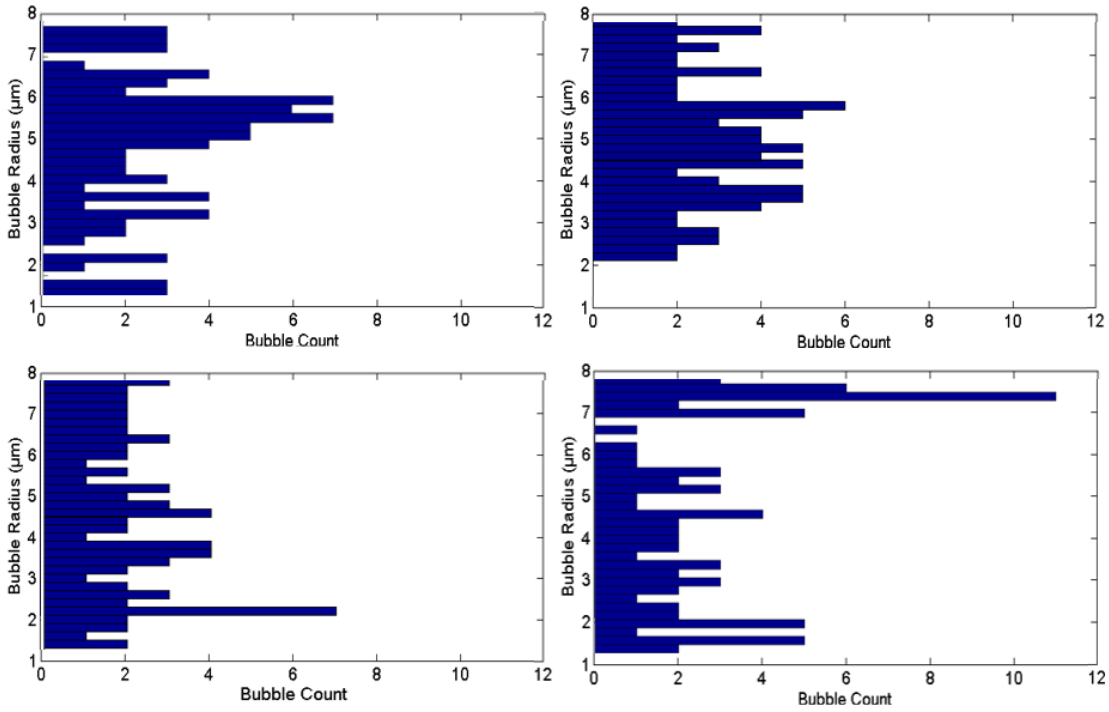

Figure 5-6: Histogram plots showing number of MBs used to create the surface plots shown Figure 5-5

.

5.5 Discussion

5.5.1 Challenges with this study

Ideally this study would have been conducted in such a way to allow for seamless comparison and integration with the results from previous experimental chapter (Chapter 4) and hence provide a more detailed characterisation of the MBs and the effects of adhesion. To achieve this one would have to keep the experimental parameters i.e. pulse characteristics, MB conditions etc. as close as possible if not identical to those used previously. Due to the restrictions imposed by the nature study itself and the equipment required this was not entirely feasible.

Keeping the transmit frequency the same (2 MHz) meant that the transducer previously used as a receiver would not have had the required bandwidth to detect the SH (expected at half the transmit frequency). The new transducer sourced for these experiments which had the required bandwidth. During the preliminary testing phase it was noted that an increased pressure driving pulse had to be utilised to achieve a reproducible SH signal. This increase in pressure meant that some unavoidable changes in MB dynamics would be expected to occur. Changes such as pressure dependent resonance frequency [142], [250] acting to lower the resonance frequency of the MBs. There was no readily available method to quantify this change with the current setup. The 1 MHz centre frequency receive transducer's bandwidth (cf. Figure 5-1) meant that capturing the fundamental response was at the very limit of the detectable frequency range and even though it was detectable the reliability of this data for anything but a qualitative check that it was present would have been ineffectual.

In terms of SH emission specifically, the increase in acoustic pressure could actually have benefitted the experiment. It has been shown that the onset of SH signal generation has a threshold associated with it [210]. Depending on the type of model used to describe the system this onset can be as low as 6 kPa with some validation using high speed photography [132], [199]. A more common consensus reached regarding the onset of SH is that although SH may be produced at these low pressure there is a significant increase of the generation of SHs at pressures > 150 kPa. Increases of the order of 20 – 40 dB are quoted in this growth region, this range of values is more consistent with acoustic characterisation studies [134], [251]. A possible reason why this wasn't observed in this thesis is that this growth region has been observed to occur at pressures as high as 300 – 400 kPa depending upon MB formulation and ambient conditions **[**198**]**.

5.5.2 **Scattered Acoustic Power**

SH signals were detected in all the MB testing cases (both adherent and control cases). The intensity of the SH signal was highest in all cases in a size region of approximately 2.2 – 3.4 μm in radius and in the frequency range of 0.8 – 1.4 MHz. This was true for all the testing cases. The fact that SH signal were present in discrete size and frequency ranges was expected and consistent with previous experimental results [134], [199], [200]. According to general theory the peak generation of SH signal should occur when a MB is insonated at twice its resonance frequency [210], [252] however the caveat to this is that threshold was originally determined for unencapsulated MBs and only holds true for encapsulated MBs when small amplitude oscillations are considered and simple Newtonian models used for the shell material (This has no separate elasticity term but uses an increased surface tension term instead, For an example see Chatterjee et al. [125]), this is also broadly consistent when viscoelastic models with constant elasticity/viscosity terms are considered i.e. de Jong shell terms [198] (Figure 5-7 (left)). When one examines the excitation threshold as predicted by a model using a more realistic rheological model for the shell parameters i.e. one that incorporates non-linear elasticity or viscosity (cf. Section 2.5.2 Page 60), the distinct peak SH onset at twice the resonance frequency becomes a more diffuse onset frequency which encompasses frequencies from below the resonance frequency to twice the resonance frequency as found for the unencapsulated MB (Figure 5-7 (right)).

Figure 5-7 (figure reproduced from [198]) shows the simulated pressure required for SH onset as a function of frequency for a 3 μm radius MB (these trends vary for different sized MBs however these curves are broadly indicative of the likely response). The left panel shows this function for a MB modelled using the de Jong model and illustrates the minimum pressure required for SH onset occurring when the MB is insonated at twice the resonance frequency (solid line), as the MB expands the surface tension increases by placing an upper limit on the effective surface tension term when this value reaches the surface tension of water (0.072 N/m) the onset pressure is reduced for lower frequencies (dashed line). The insert shows how the surface tension varies with radius and the effective upper limit applied. The right hand panel shows the effect of incorporating shell parameters as given by the Marmottant model (Shell parameters used χ = 0.53 N/m, κ_s = 1.2×10^{-8} Ns/m. Details not given for the specific values of buckling radius or breakup surface tension however they are both incorporated in the modelling). The use of the Marmottant model means that the frequency of SH onset moves from the distinct peak at twice the resonance frequency to actually occur somewhere in the range of $f_{res} \leq$ frequency of $SH_{onset} \leq 2f_{res.}$ The position of these curves is subject to variation depending on the shell parameters used.

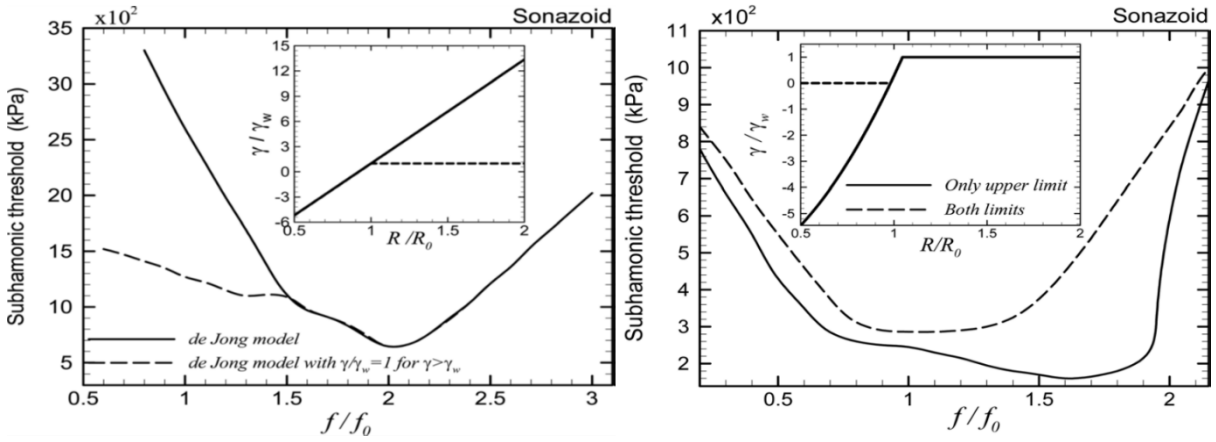

Figure 5-7: Examples of the variation in SH onset threshold using different rheological models for the MB shell parameters. Left: Using the de Jong shell formulation (cf. Equation 2-25 page 59) (solid line) and the effect of including an upper limit on MB surface tension (dashed line). Right: Using the Marmottant formulation, dashed line shows the effect of both buckling and rupture while the solid line only incorporates rupture. Insets on both panes show the effective surface tension as a function of radial excursion. Figure reproduced from [198]

For this experimental study where the insonation frequency is fixed and the MB size range is varied, Figure 5-7 implies that one would expect the peak SH generation to occur anywhere the resonance radius and a MB twice the resonance radius. In accordance with the resonance radii determined in Chapter 4 (cf. Table 4-1, page 129) one would expect the peak SH to feature within the size range of approximately 1.6 – 3.2 µm for a non-adherent MB and 1.8 – 3.6 µm for an adherent MB. This is diffuse region is demonstrated by the experimental data however any differentiation between the two test cases was not evident. Similarly the fact that the frequency of SH generation is observed occur over a distributed band of frequencies (0.8 – 1.4 MHz) as opposed to simply half the insonation frequency is a result of the onset threshold occurring not a $f/f_0 = 2$ but at a range of values from 0.75 – 2.1 depending on the shell model used (Figure 5-7).

The rationale behind examination of the SH signals was to try and accentuate the difference found in radii of peak 2nd harmonic generation found in Chapter 4. When one compares the SH scattering of non-adherent MBs to that of the adherent MBs there was no statistically significant difference observed between the two cases as shown in Figure 5-4, $p > 0.05$ for the entire radius range examined. To extend this comparison and compare the whole frequency/size range of the experiment Figure 5-8. Good cancellation of the fundamental scattering and the primary region of SH scattering can be seen. The remaining area of the plot would indicate that the larger adherent MBs generate higher intensity SHs than their non-adherent MBs. When one examines this result in conjunction with the variability in SH signal generation shown by the spread to raw data points in

Figure 5-4 one has to conclude that this difference is indistinguishable from the variation naturally present in the results and as such would not be a good indicator in vivo.

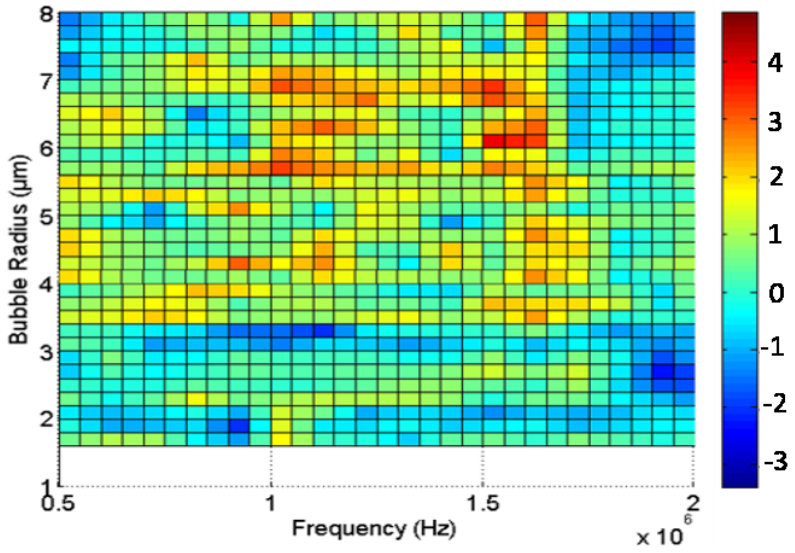

Figure 5-8: Residual scattering found by subtracting the TUC scattering plot Figure 5-5 top left) from the TC scattering plot (Figure 5-5, bottom right). Gives a measure of the difference between the adherent and non-adherent SH scattering

5.5.3 Errors and Improvements

The signal generation for all frequency ranges examined (SH emissions in this chapter and the fundamental/2nd harmonic in the preceding chapter, even from like MBs and was highlighted as an area that would continue to obscure subtle changes in MB response. In an effort to counteract this variation a significantly higher number of datasets was collected for each MB test case; typically ≈ 100 MBs for each case for this chapter in comparison to ≈ 45 MBs in Chapter 4. What became evident however was that the variability seemed to be inherent to the MBs rather than to the testing procedure. One must also note the caveat that in addition to this SH generation has been observed to be more variable in nature so there could be two effects compounding here. In either case what is required is significantly tighter control over the MBs that are under examination. Without precise control over the shell characteristics the results obtained will always be subject to high degrees of variation. This will be expanded upon in Chapter 7.

The replacement of the receive transducer was not ideal and impacted the study in a number of ways. The increase in applied pressure could have changed the basic MB dynamics in terms of resonance frequency but then also gave a higher probability of detectable SH being

generated so was not overly detrimental. The main issue with the changing of the transducer was that reliable fundamental and higher harmonic scattering data could not be obtained, without this data the SH signals were difficult to interpret in terms of overall MB response (e.g. the comparison with pulse asymmetry could have proven very beneficial). At the time of the conduction of the study attempts were being made to create a protection circuit for the transmit transducer. The protection circuit would have allowed for high amplitude pulses to be transmitted by the transducer and then low amplitude signals received by the same transducer operating in pulse-echo mode to be passed to the receive amplifier and oscilloscope without the danger of the high amplitude signals being passed to the sensitive receive equipment and possibly damaging them. This circuit was functional for relatively high signal to noise applications such as bulk acoustics however was not fit for purpose in the low signal situation of single bubble acoustics and hence had to be omitted.

One other enhancement to the experiment could have been to alter the envelope of the insonation pulse. Biagi et al. [253] demonstrated that the shape of the envelope of the driving pulse can dramatically accentuate the level of SH generated; sharp changes in pulse shape provide greatest enhancement, enhancements of up to 30 dB are quoted. The conclusion being that sharp or abrupt changes in insonation dramatically increase the activation of the non-linear oscillation modes of the MB. This was not incorporated in the current setup in order to remain a close as possible to the excitation pulse used in Chapter 4.

5.6 Summary

In this chapter the test rig used in Chapters 3 and 4 is modified to allow for the examination of SH signals when using a similar excitation pulse to that used previously. The generation of SHs was examined as a function of MB modification for targeted imaging purposes and the effect of adhesion was also studied

MBs were insonated with a 2 MHz, 200 kPa pulse. SH signals were detected in approximately 48% of MBs examined irrespective of test case. SH signals were seen to be generated predominantly in a discrete MB size region (2.2 – 3.4 μm) and frequency range (0.8 – 1.4 MHz). This area of SH generation corresponded will with theory predicting frequency and pressure required for the onset of SHs.

A high degree of variability was observed in the SH response making differentiation of the adherent and non-adherent test cases impossible. This also indicates that control of MB properties will be key in the differentiation of these cases in the future.

6 Computational Modelling

6.1 Abstract

This chapter examines the theoretical models used to model and predict MB behaviour, focussing on those models which are most widely used in MB characterisation studies to allow for comparison between the data. In addition models which are directly applicable to the current experimental scenario are examined i.e. single MBs near a compliant boundary.

Using the single MB data gathered in the proceeding chapters these models are parameterised using a new comprehensive fitting approach. The resulting parameters are discussed in terms of the currently held consensus and also to validate some of the current theories concerning the rate dependent nature of some of the MB material properties. Shell elasticity is seen to decrease with increasing strain in so called "strain-softening" behaviour. Shell viscosity is likewise seen to decrease as a function of dilatational strain rate with "shear-thinning" behaviour. MB buckling and rupture are seen to be resonance dependent although again variability in data makes some inferences less concrete. The found model parameters are used to recreate the experimental data to demonstrate the suitability of both the model and the subsequently determined parameter values, this is conducted well for the fundamental and 2^{nd} harmonic data although there were a number of issuers regarding the recreation of the SH datasets. The parameters derived for adherent and non-adherent MBs are compared and only minor differences can be observed between them, again emphasis is placed upon the variability of the datasets in conjunction with only a small difference expected between the adherent and non-adherent test cases.

6.2 Introduction

Accurate modelling of MB response is important for predicting the likely scattering response to various US insonation and experimental conditions. This knowledge plays a vital role in all aspects of MB research; from the tailoring of shell material properties to accentuate certain scattering properties, to the design of imaging and pulse characteristics to best exploit the predicted response.

A number of models exist to parameterize and predict MB dynamic behaviour. The majority of these models are based on the Rayleigh-Plesset type equation and were introduced in Chapter 2. As explained these models have been extended to include a number of experimentally observed phenomena and the effects of boundary conditions. At some stage in each of these models some experimentally derived parameters are required. One of the key issues with using any of these models is how the experimentally derived parameters are fitted to the model and the effect that any simplifications or assumptions used in the fitting process have on the model's ability to be used as a predictive tool.

The following chapter will parameterise a number of the standard models used to for the description of MB behaviour. These models will represent a progression from the simpler linear forms of the RP style equations (the linearized Marmottant model for small amplitude oscillations) through to models which better account for the increasingly nonlinear MB behaviour (Full Marmottnat model with non-linear elasticity to account for large deformations and buckling)and finally models which also incorporate the effects of boundaries. A full description of all the models used will follow in Section 6.3. To parameterise these models the experimental data from Chapter 4 will be used. The extracted parameters are then examined both to provide a physical underpinning of the observed effects but also attempt to provide evidence from a theoretical standpoint as to the differences observed between the adherent and non-adherent MBs.

In order to produce results which are comparable with previously published parameterisation studies on lipid MBs only the most prevalent shell models will be examined. The non-linear Marmottant model [129] Equation 6-1 and in particular it's linearized form [113] Equation 6-4 have provided the theoretical description of MB shell behaviour in a wide range on studies ranging from bulk acoustic studies looking at the attenuation and scattering from large populations of polydisperse MBs [134], to single bubble characterisation using either high speed cameras [113][144] light scattering techniques [128], [136].

6.3 Description of Models

To describe the MB rheological behaviour the derivations originating from the Marmottant model [129] were utilised. As previously stated, these bubble models have been extensively used for the characterisation of MB properties using a number of experimental techniques. The basic models used in this chapter are described below.

6.3.1 Nonlinear Marmottant model

The Marmottant model was introduced in Section 2.5.2. Briefly, to account for large variations in radial oscillation this model introduces a variable surface tension which changes with radius, the rationale behind this being that the surface tension of a lipid encapsulated MB derives from the surface packing structure of the lipids arranged upon it. As the MB undergoes radial oscillations the surface area varies and for a given number of lipids on the surface their packing structure must alter accordingly. This variation results in a radius dependent surface tension term shown diagrammatically in Figure 6-1 and similarly in Equation 6-1. By utilising this expression for surface tension the model is able to account for MB phenomena at the more extreme acoustic conditions such as buckling; when the surface tension from the shell tends to zero indicating the highest packing order, and shell rupture; when the surface tension tends to that of the air water interface. Through manipulation of these parameters it has been used to characterise processes such as compression only behaviour [133] and can be made to produce SH signals for certain regimes [199].

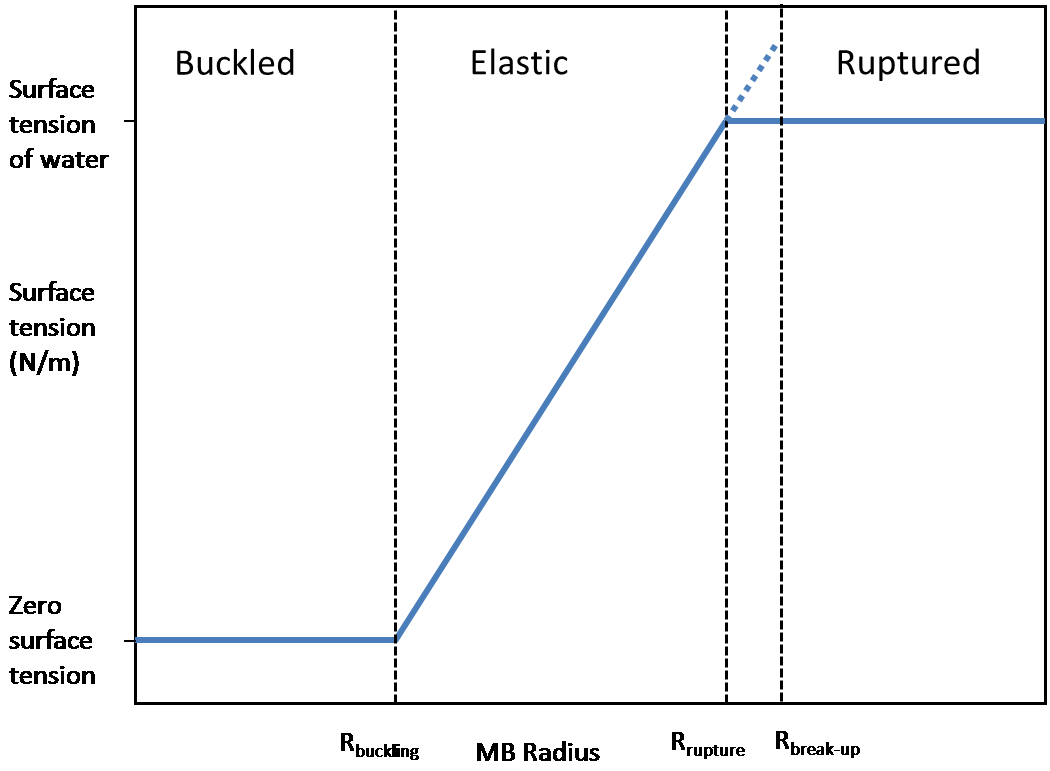

Figure 6-1: Idealised surface tension Vs. area curve as used in [129]

$$\rho\left(R\ddot{R}+\frac{3}{2}\dot{R}^2\right)=\left(P_\infty+\frac{2\sigma(R_0)}{R_0}\right)\left(\frac{R_0}{R}\right)^{3\gamma}\left(1-\frac{3\gamma\dot{R}}{c}\right)-4\eta\frac{\dot{R}}{R}-\frac{2\sigma(R)}{R}-4\kappa_s\frac{\dot{R}}{R}-P_\infty-P(t)$$

$$\sigma(R)=\begin{cases}0 & if\ R\leq R_{buckling}\\ \chi\left(\dfrac{R^2}{R_{buckling}^2}-1\right) & if\ R_{buckling}\leq R\leq R_{break-up}\\ \sigma_w & if\ ruptured\ and\ R\geq R_{ruptured}\end{cases}$$

Equation 6-1

In order to use this model as a predictive tool a number of physical parameters have to be explicitly fitted to controlled experimental data. In the Marmottant model there are four such parameters: the shell elasticity (χ), shell viscosity (κ_s), buckling radius ($R_{buckling}$) and the break-up radius ($R_{break-up}$), more rigorously the break-up radius is set by the parameterisation of the surface

tension of break-up ($\sigma_{break-up}$) Equation 6-2. This can be visualised as the end of the dashed line in Figure 6-1. After break-up the MB shell is said to be ruptured and the surface tension tends to that of water.

$$R_{break-up} = R_{buckling}\sqrt{\left(1+\frac{\sigma_{break-up}}{\chi}\right)}$$

$$R_{ruptured} = R_{buckling}\sqrt{\left(1+\frac{\sigma_{water}}{\chi}\right)}$$

Equation 6-2

6.3.2 Linearized form

Given the number of parameters to fit in the full Marmottant model it is common practice to use the assumption that at low acoustic pressures the radial amplitude of the MB oscillations will remain small. This allows for the simplification of the variable surface tension term by way of a first order Taylor expansion as shown in Equation 6-3.

$$\sigma(R) \approx \sigma_w + 2\chi\left(\frac{R}{R_0}-1\right) \qquad for\ |R-R_0| \ll R_0$$

Equation 6-3

In the regime of small oscillations the variable elasticity term can be replaced with Equation 6-3 to give the governing equation below (Equation 6-4). This will be referred to as the linearized Marmottant or de Jong model – technically this is not quite the same as the original de Jong model (Equation 2-26, Section 2.5.1) however with a few term substitutions they are essentially analogous.

$$\rho\left(R\ddot{R}+\frac{3}{2}\dot{R}^2\right) = = P_{Go}\left(\frac{R_0}{R}\right)^{3\gamma}\left(1-\frac{3\gamma\dot{R}}{c}\right) - \frac{2\sigma_w}{R} - 4\eta\frac{\dot{R}}{R} - P_0 - P(t) - 4\chi\left(\frac{1}{R_0}-\frac{1}{R}\right) - 4\kappa_s\frac{\dot{R}}{R^2}$$

Equation 6-4

There is one important caveat to the use of the linearized form and that is that the range of values for which this small amplitude assumption are valid covers only a very small range of acoustic pressures. An example of this can be demonstrated by the application of some typically given values for the MB parameters to Equation 6-2 (parameters used: $\chi = 0.51$ N/m, $\sigma_{break-up} = 0.13\ N/m$, $R_{buckling} = 2$ µm, $\sigma_{water} = 0.072\ N/m$. Values taken from [129]) this gives an elastic range between the buckling and ruptured states of approximately 5% ($2 \leq R \leq 2.14\ \mu m$), one must also note that this is peak to peak radial oscillation range. To achieve this experimentally it would require an applied acoustic pressure somewhere of the order of <20 kPa. Figure 6-2 displays this graphically as a plot of the normalized peak to peak radial amplitude for a 2.05 µm radius MB subjected to increasing amplitude acoustic pulses. The model is parameterized with the above characteristics. The normalized amplitude is simply the peak to peak radial amplitude divided by the resting radius (Equation 6-5). It can be seen that for small amplitudes (20 kPa) the two models do indeed give the same linear response (the range of $2 \leq R \leq 2.14\ \mu m$ corresponds to a normalized peak to peak amplitude of 0.07 which occurs at approximately 20 kPa.

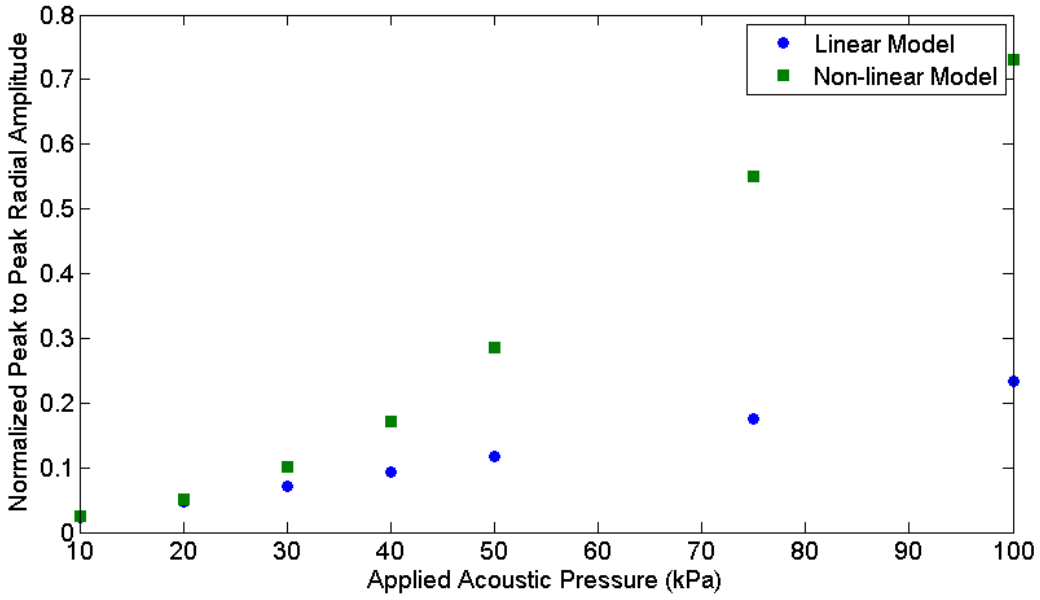

Figure 6-2: Normalized peak to peak amplitude as a function of applied acoustic pressure for the linearized (Blue circles) and fully non-linear (Green squares) Marmottant models. Model Parameters χ = 0.51 N/m, $\kappa_s = 7.2 \times 10^{-9}$, $\sigma_{breakup}$ = 0.13 N/m, $R_{Buckling}$ = 2 µm, σ_{water} = 0.072 N/m, R_0 = 2.05 µm

$$Normalized\ Amplitude = \frac{(R_{max} - R_{min})}{R_0}$$

Equation 6-5

After this pressure the two models are seen to diverge, this occurs because the elasticity term in the non-linear model gives significantly lower estimates of the shell elasticity compared to the linear model; values ranging from zero in the buckled state to the surface tension of water when past the break-up radius, the linearized model on the other hand always has a contribution from the surface tension of water with an additional shell modifier on top. This can be seen by comparing the terms of elasticity terms from the linearized Marmottant model (terms used shown in Equation 6-6) and the non-linear Marmottant model (terms used shown in Equation 6-7, where $\sigma(R)$ is as previously given in Equation 6-1). Even in the region of congruity between the models the linearized form always overestimates the contribution of the surface tension due to inclusion of the water surface tension term, its overall effect however is not pronounced enough at these low acoustic pressure levels to cause divergence. To show this divergence Figure 6-3 shows the contributions from the elasticity/surface tension terms for both models at 3 acoustic pressures 20 kPa, 50 kPa and 100kPa. The overestimation of the term by the linearized form is self-evident as well as the degree on nonlinearity which is introduced at higher pressures. It is this change in surface elasticity which allows the non-linear Marmottant model to exhibit asymmetric non-linear phenomena i.e. "compression-only" behaviour.

$$Linearised\ Elasticity\ terms = \frac{2\sigma_w}{R} + 4\chi\left(\frac{1}{R_0} - \frac{1}{R}\right)$$

Equation 6-6

$$Nonlinear\ Elasticity\ term = \frac{2\sigma(R)}{R}$$

Equation 6-7

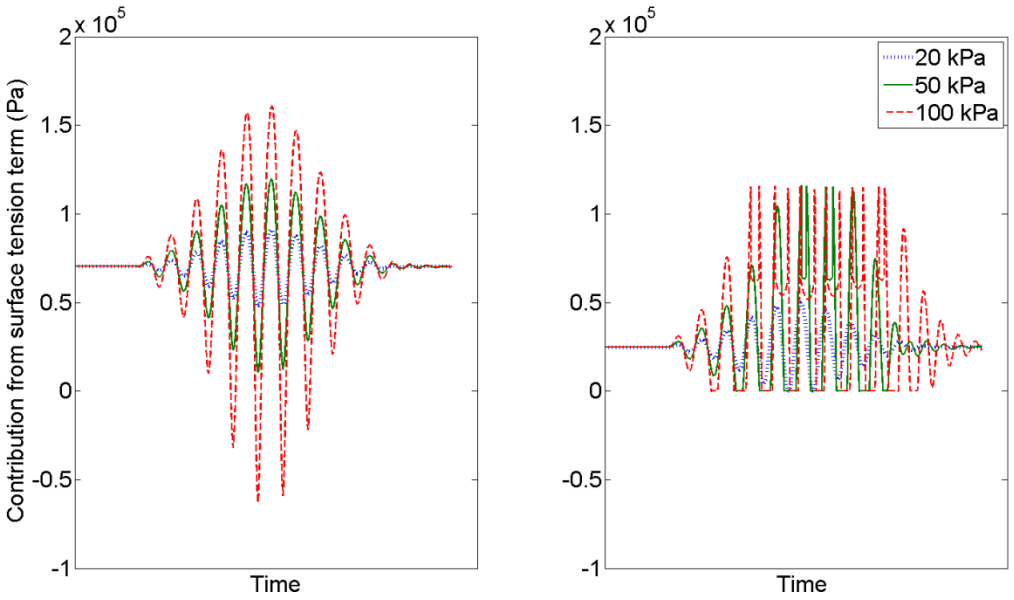

Figure 6-3: Comparison of the contribution from the term $\sigma(R)$ for both the linearized (left) and non-linear (right) Marmottant models for increasing acoustic pressure. Model parameters are consistent with those shown in Figure 6-2.

In order to compare the outputs from these models to the experimental data the radial behaviour needs to be converted into radiated pressure. The scattered pressure is dominated by the contribution from the MBs volumetric change in response to the incident acoustic field, specifically the second order differential of the volumetric changes [145]. This is formalised by Equation 6-8 where the scattered pressure ($P_{scattered}$) is a function of time (t) and the radial distance from the MB to the transducer surface (r). The term r/c indicates the lag in the received signal due to the time of flight from MB to transducer. V is the volume of the MB. This derivation assumes that only a single MB is oscillating, that the bubble motion remains spherical throughout its oscillations and does not move or translate during US exposure. Whether these assumptions remain valid for the course of the experiments covered in this thesis will be explored later in this chapter.

$$P_{scattered}\left(r, t-\frac{r}{c}\right)=\frac{\rho}{4\pi r}\frac{\partial^2}{\partial t^2}V(t)=\frac{\rho}{r}\left[R(t)^2\ddot{R}(t)+2R(t)\dot{R}(t)^2\right]$$

Equation 6-8

6.3.3 **Effect of boundaries**

Due to the way in which the previous chapter's experiments were conducted the MBs are always oscillating in the presence of a boundary by way of buoyantly resting against the upper surface of the capillary fibre. The effect of nearby boundaries on MB dynamics has been an active area of study. Not only is this to try and effectively model experimental outcomes for studies such as this but also to predict the response *in vivo.* In a large proportion of *in vivo* imaging situations the MBs will be in the small scale vasculature. This is especially true in the case of targeted imaging where a MB will be brought into contact with the endothelium, the change in response from the MB due to the boundary properties could be used differentiate those MBs adherently bound to the endothelium compared to those freely circulating. Furthermore different pathologies have different material properties associated with them, e.g. liver fibrosis [254], tumours [255] and lesions [26]

As previously stated in Section 2.6.1 (Page 69) many of the attempts to model bubbles near boundaries have focussed on violent collapse of relatively large bubbles near rigid boundaries in maritime or underwater explosion situations. With this as a starting point many of the models for describing MB dynamics have also focussed on the boundary as being a rigid barrier [41]. For biological purposes and indeed for studies such as this, the effect of an elastic or compliant wall is more relevant. This kind of problem has been approached from a finite element standpoint [160], [161] and more recently in the form of a modified Rayleigh-Plesset style equation [42], [158], [256].

The following modified Rayleigh-Plesset equation was proposed by Doinikov et al. [158] to simulate the acoustic interactions that occur due to a MB oscillating near an elastic boundary of finite thickness with a fluid medium either side of the boundary (Figure 6-4). The model accounts for the physical properties of the fluid; subscripts 1 and 3 refer to the near and far side of the boundary respectively. The wall is treated as an elastic solid material and as such has a density (ρ), bulk modulus (K), shear modulus (μ), and Poisson's ratio (ν) and the MB oscillates at a distance (d) from the wall.

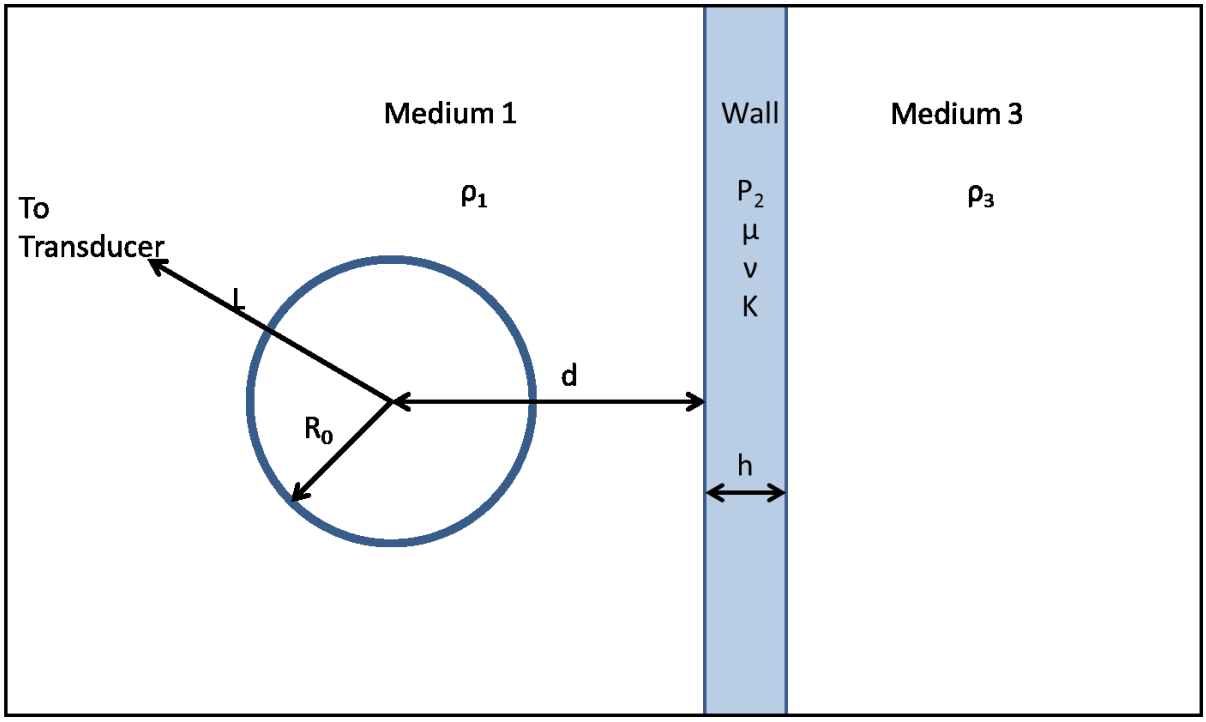

Figure 6-4: Description of the physical situation modelled by the Doinikov model for MB response near a finite elastic wall. Figure recreated from [158]

The full derivation of the governing equation is given by Doinikov et al. [158] and the equation is below as Equation 6-9, henceforward this model will be referred to as the Doinikov elastic wall model. The equation presented is actually a later variation developed by the same group and has been included in preference to the original equation due to a more easily applicable formulation for the liquid compressibility corrections [256].

It can be seen that the right hand side of the equation follows that standard formulation of many of the previously reported RP style equations, the term S is used to denote the shell material model i.e. Marmottant, de Jong formulation. Specifically these shell parameters are given in the linearized form in the latest paper [256] however the non-linear version of shell parameters is interchangeable as per Equation 6-1 and Equation 6-4 i.e. the linear form is simply the non-linear formulation approximated using the small amplitude oscillation assumption (Equation 6-3). The left hand side of the equation can be seen to be heavily modified by the fluid medium properties and the parameter (β). This parameter is defined by Equation 6-10 and accounts for the mechanical properties of the wall.

$$R\ddot{R}\left[1-\left(\frac{\rho_1-\beta}{\rho_1+\beta}\right)\frac{R}{2d}-\left(\frac{\beta-\rho_3}{\beta+\rho_3}\right)\frac{R}{2(d+h)}+\left(\frac{\rho_1-\beta}{\rho_1+\beta}\right)\left(\frac{\beta-\rho_3}{\beta+\rho_3}\right)\frac{R}{2h}\right]$$
$$+\frac{3}{2}\dot{R}^2\left[1-\left(\frac{\rho_1-\beta}{\rho_1+\beta}\right)\frac{2R}{3d}-\left(\frac{\beta-\rho_3}{\beta+\rho_3}\right)\frac{2R}{3(d+h)}+\left(\frac{\rho_1-\beta}{\rho_1+\beta}\right)\left(\frac{\beta-\rho_3}{\beta+\rho_3}\right)\frac{2R}{3h}\right]$$
$$=\frac{1}{\rho_1}\left[\left(P_0+\frac{2\sigma}{R_0}\right)\left(\frac{R_0}{R}\right)^{3\gamma}\left(1-\frac{3\gamma\dot{r}}{c}\right)-\frac{2\sigma}{R}-4\eta\frac{\dot{R}}{R}-P_0-P(t)-S\right]$$

Equation 6-9

$$\beta=\rho_2\frac{3K-2\mu}{3K+4\mu}=\rho_2\frac{\upsilon}{1-\upsilon}$$

Equation 6-10

To illustrate the effect that changing wall parameters and altering the distance of the MB to the wall has on the MB response Figure 6-5 below displays one of the figures from the original Doinikov et al. [158] paper. This shows the normalized peak response from a MB as a function of applied frequency for a MB in 3 positioning scenarios: In an unbounded medium i.e. away from a boundary, at the interface of an elastic boundary; the material properties used here are consistent with an Opticell chamber as used in a number of MB interrogation studies [133], [163], [199], and finally for MB adjacent to a rigid boundary. The model parameters used in this simulation were as follows: R_0 = 2.45 μm, P_0 = 101.3 kPa, ρ_1 = ρ_3 = 1000 kg/m^3, ρ_2 = 1060 kg/m^3, η = 0.001 Pa.s, σ = 0.0072 N/m, c = 1500 m/s, γ = 1.095, K = 3.75 GPa, μ = 1.34 GPa (these wall parameters equate to a Poisson's ratio of ≈ 0.37), h = 75 μm. The linearized form of the Marmottant model was used for shell properties with χ = 0.51 N/m and κ_s=0.72 x 10^{-8} kg/s. the MB was simulated in response to a swept frequency range from 0.05 – 3 MHz at a peak negative acoustic pressure of 200 kPa. It can be seen that the proximity to the wall brings into play the physical properties of the wall. This can have effects on both the amplitude of oscillation as well as the resonance frequency. A rigid boundary has the effect of reducing the natural frequency of the bubble while slightly accentuating the peak magnitude of response. An elastic boundary is shown to have the opposite effect and increases the resonance frequency of the MB whilst slightly damping the magnitude of oscillation. These are in broad agreement with results found by other authors [163]. One should note at this point that these effects are specific for the chosen wall parameters, the term "elastic boundary" could encompass a wide range of material properties. It will be shown later in the next section (Section 6.3.4) that the varying of the wall parameters can lead to either an increase or decrease in MB resonance frequency with respect to the no-boundary condition.

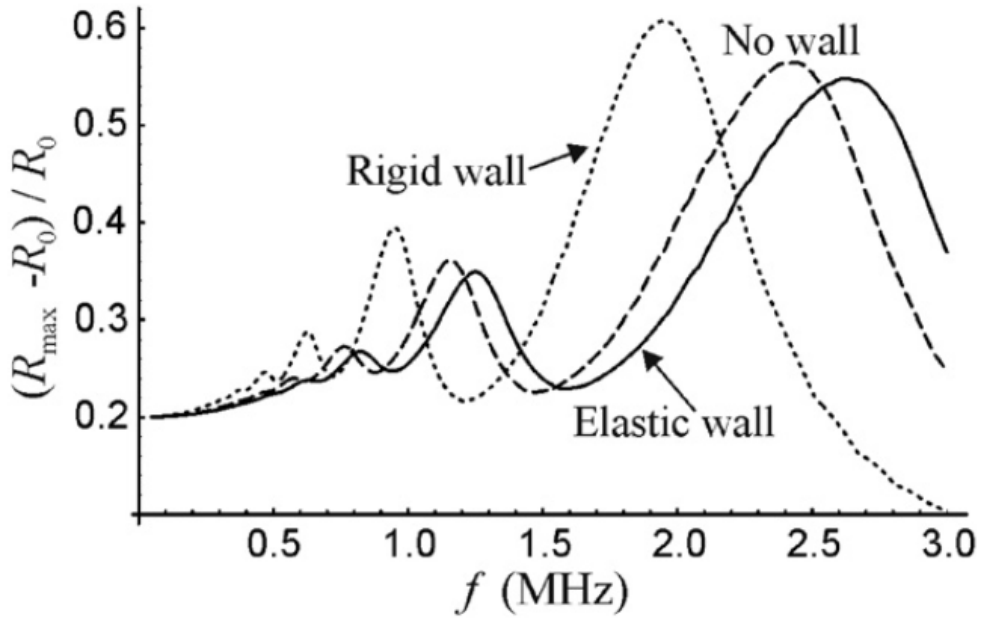

Figure 6-5: Effect of boundary properties on the radial response of MBs. MB of radius 2.45 μm simulated under an 8 cycle 200kPa. De Jong model used for shell parameter Figure reproduced from [158]

The presence and properties of the boundary also have an effect on the scattered pressure resulting in a modified form of Equation 6-8. This modified for is shown below Equation 6-11 [256] where the transducer positioned at a distance to the MB (L) which is much greater than the distance between the MB and wall (d) and wall thickness (h) (cf. Figure 6-4).

$$P_{scattered}(L \gg d, h) = \frac{\rho_1}{L}\left[R(t)^2\ddot{R}(t) + 2R(t)\dot{R}(t)^2\right]\frac{4\beta\rho_3}{(\rho_1 + \beta)(\beta + \rho_3)}$$

Equation 6-11

6.3.4 Description of modelling approach

For their seeming complexity the above models essentially reduce to second order differential equations. These equations can then be solved numerically given the boundary conditions and system/bubble parameters.

To achieve this, a programme was custom written in MatLab (MathWorks, Cambridge UK). This script allowed for the manipulation of all key parameters within the model. Figure 6-6 shows a selection of screenshots from the model setup phase. In this one can choose which theoretical model will be applied; currently there are four variations of the models for shell parameters and boundary situations available; both the linearized or non-linear Marmottant shell model either with or without a nearby boundary. The simulation constants are then defined, these include: the acoustic pulse characteristics; the transducer properties, the two transducers used in the experimental sections of this thesis are programmed in, these are used to correct for frequency response and calibration of the system; wall properties if the model requires them; and finally material constants for the experimental conditions. The default settings are shown, if modelling data is shown without specifying otherwise then these are the model constants taken. The final input dialogue box is for the definition of the model variables under examination. For the parameterization process it is required that a range of values for these properties be explored. Shown below are a number of ways in which this can be implemented, the inputs follow the standard MatLab scripting conventions. Values separated by colons indicate a range of values, for example, in the bubble radius tab the value 1:0.1:3 indicates a range of MB radii from 1 – 3 μm in 0.1 μm steps. The second option is to input discrete values; this is achieved by separating the values with a space. Single values are also permitted. Further changes can be made to all other parameters however not at this top level of user interaction.

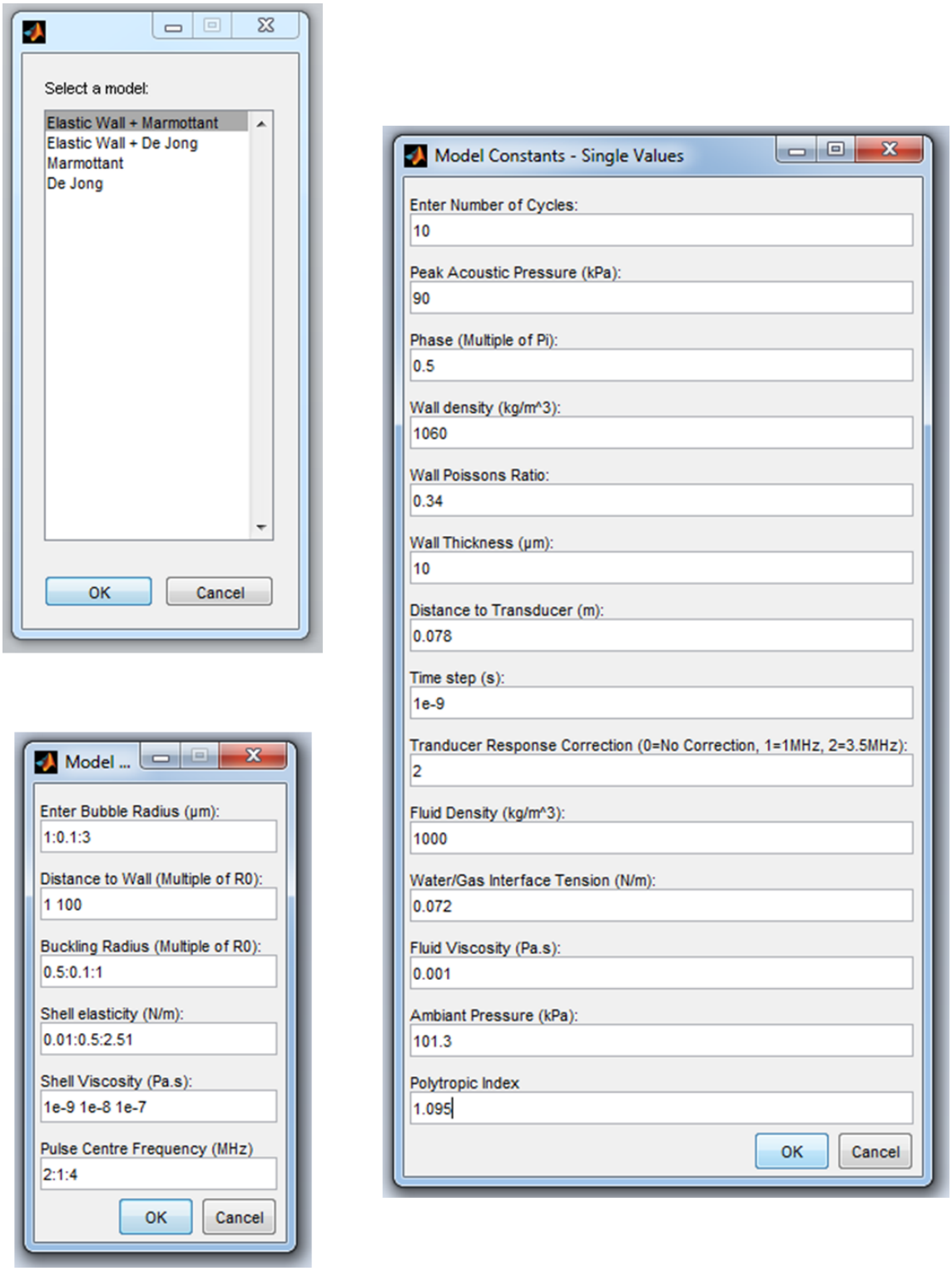

Figure 6-6: Screenshot from the initialization of the simulation programme. Model type (top left), model constants (right) and model variables (bottom left) can all be entered. Values seen in the model constants box are the typical default values used in the following simulation unless otherwise specified.

Once the simulation constants and variables have been defined they are passed through to the solver. The script used an in house developed solver based on a 4th order Runge-Kutta method to determine the MB radial position at incremental time steps. The method is briefly outlined below. Y is the vector containing the MB radius (r) and first time differential (dr) of the radius at a given time point (n), (dt) is the time step of the simulation.

$$Y_{n+1} = Y_n + \frac{1}{6}(k1 + 2 * k2 + 2 * k3 + k4)$$

Equation 6-12

$$k1 = dt * F(t_n, Y_n)$$

$$k2 = dt * F\left(t_n + \frac{dt}{2}, Y_n + \frac{k1}{2}\right)$$

$$k3 = dt * F\left(t_n + \frac{dt}{2}, Y_n + \frac{k2}{2}\right)$$

$$k4 = dt * F(t_n + dt, Y_n + k3)$$

Equation 6-13

F is given as the setup of the ordinary differential equation returning the vector (r) of the first ($\dot{r}$) and second ($\ddot{r}$) time differentials of the MB radius at time n given by Equation 6-14, the need for the vector form of the output is to account for the second order nature of the problem. The following is an example using the linearized Marmottant model simply for demonstration; as can be seen it is simply the rearranged form of Equation 6-4 to make the radial acceleration the subject. The full MatLab code can be found in the appendix to this thesis, Section 9.2.

$$\ddot{r} = \frac{1}{r}\left\{\left[\frac{1}{\rho}\left(P_0 + \frac{2\sigma_w}{R_0}\right).\left(\frac{r}{R_0}\right)^{-3\gamma}\left(1 - \frac{3\gamma\dot{r}}{c}\right) - \frac{2\sigma_w}{r} - 4\eta\frac{\dot{r}}{r} - P_0 - P(t) - 4\chi\left(\frac{1}{R_0} - \frac{1}{r}\right) - 4\kappa_s\frac{\dot{r}}{r^2}\right] - \frac{3}{2}\dot{r}^2\right\}$$

$$\mathrm{r} = [\dot{r};\ \ddot{r}]$$

Equation 6-14

To ensure that the model behaves as described in the original paper and to show the effect of varying wall properties a number of plots using similar parameters to above were produced. As seen in Equation 6-10 the wall properties are included in the model by way of the parameter β which relates the material density with a non-dimensional ratio based on the material mechanical properties (in this code it is specifically implemented using the Poisson's ratio variation as displayed in Equation 6-10). As such one of the most effective methods to examine the effect of wall properties is to simply change the material density. Figure 6-7 shows the effect of increasing the wall density. A value of 1000 kg/m^3 is approximately equal to the wall density value used by Doinikov et al. in the original formulation, following this the comparison of the green trace with that of the "no wall" trace (black dashed line) should replicate the "No Wall"/"Elastic Wall" example given in Figure 6-5 which it does with reasonable accuracy. It can also be seen that the most extreme case, that of ρ_2 = 8000 kg/m^3 (approximately equivalent to a steel wall) the figure approaches the trace of the rigid wall. There are differences in the amplitude and position of this comparison but in the original paper the rigid wall curve was produced using a different model which assumes an infinitely thick wall whereas this current plot assuming a thin, stiff yet elastic wall and as such discrepancies should be expected, the fact that the trend is moving in the correct direction is in agreement with the published data provides some validation that this implementation is performing as required.

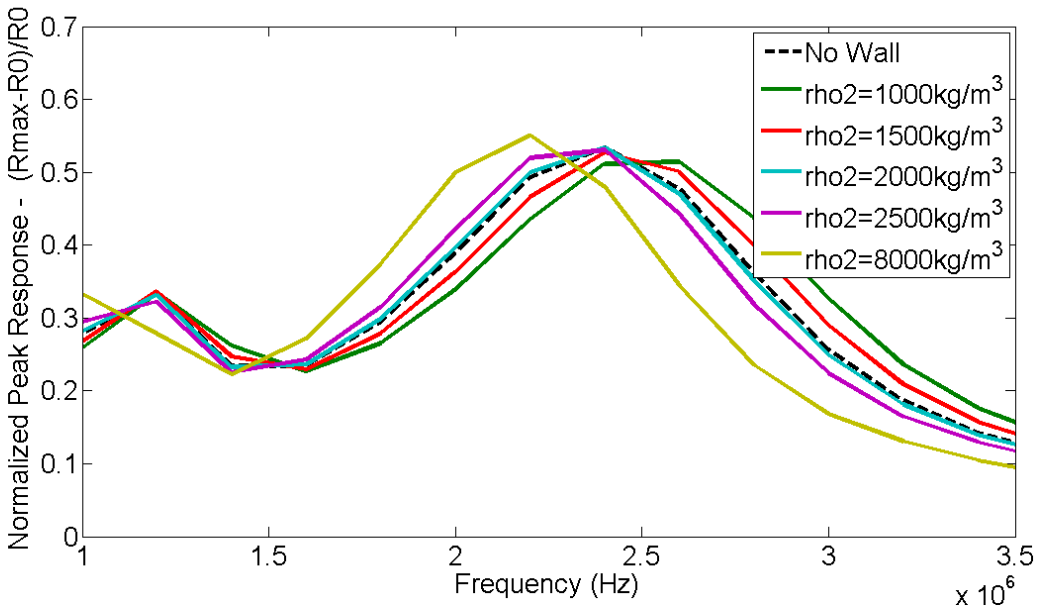

Figure 6-7: Simulated effect of wall properties MB response. MBs are simulated in contact with boundary.

Figure 6-8 shows the effect of increasing the distance between the MB and the wall. All distances are measured in terms of MB radius. These curves relate to the wall properties ρ_2 = 1000

kg/m^3, h = 10 µm (note: thinner wall properties used than the Doinikov paper however this was consistent with the experimental wall used in the previous experimental chapters), ν = 0.37. It can be seen that the largest variation in response modification occurs between the MB being directly adjacent to the wall and one radius away from the wall. The effect of the wall can be seen to drop off in intensity with increasing distance. After a distance of 5 radii the effect drops to a value approximately equal to that of the free MB.

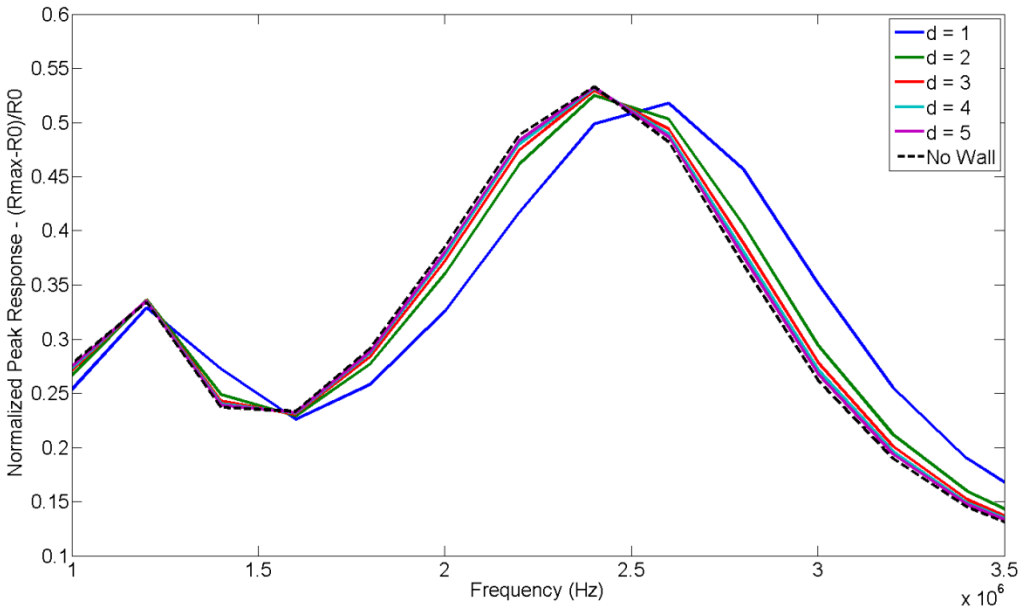

Figure 6-8: Simulated effect of distance to boundary on MB response. Distance values are given in terms of multiples of MB radius, d=1 positions the centre of the MB 1 radius away i.e. MB resting against wall. Wall density =1000 kg/m^3

6.3.5 Parameter fitting procedure

As previously explained (cf. Section 2.5.3 Page 64) the standard approach to the parameterization of these models is by the extraction of an experimental resonance frequency and using that in conjunction with the linearized resonance frequency for an encapsulated MB shown (Equation 6-15).

$$f_{0\_encapsulated} = \frac{1}{2\pi}\sqrt{\frac{1}{\rho R_0^2}\left(3\gamma P_\infty + \frac{2(3\gamma-1)\sigma_w}{R_0} + \frac{4\chi}{R_0}\right)}$$

$$f_{res} = f_0\sqrt{1-\frac{\delta^2}{2}}$$

$$\delta = \delta_{rad} + \delta_{vis} + \delta_{shell}$$

Equation 6-15

This implementation was not suitable for the type of data gathered experimentally in Chapter 4 for a number of reasons. Firstly, the data gathered was all collected at a single frequency (2MHz). The reason for this was so that acoustic tracking of MB stability could reliably be achieved, negating the need for optical verification of MB size and integrity between pulses which was impractical with the experimental implementation. Because of this it means that only a single resonance peak can be extracted from the whole dataset, which, in turn would lead to very low confidence in the derived parameters. In addition to this the applied acoustic pressure was 90 kPa for the data gathered on the fundamental and second harmonic response (Chapter 4) means that in both these cases one would expect the oscillation of the MBs to become larger than the limit of validity for the linearized form of the Marmottant equation (cf. Figure 6-2 and Figure 6-3 and associated discussion). The incorporation of the non-linear model brings with it the additional parameters for buckling and breakup radius, neither of which are accounted for in Equation 6-15 and would require some *ad-hoc* adjustment or secondary fitting. Furthermore simply by examination of the spread and variability of the data gathered in Chapter 4 it would seem to make little sense in trying to evaluate an entire size distribution of MBs in terms of one or two distinct parameters, certainly while trying to elucidate fine differences between situations i.e. adherent/non-adherent MBs. It was decided that it would be more beneficial to discover the how these parameters varied on a bubble by bubble basis.

To achieve this, simulations were run to explore the full range of MB parameter space. The limits of parameters were selected as the extremes of MB parameters as found in previous papers (typical values quoted in previous papers cf. [113], [129]. The ranges of values used are shown in Table 6-1**.** Because the range of parameters which require fitting is multi-variable this

results in a very large multi-dimensional matrix containing all permutations of variable. For example in the case of the Doinikov elastic wall model with shell parameters taken from the non-linear Marmottant model form the resulting simulation data takes the form of a 8 dimensional array; the 6 parameters below plus one for insonating frequency (kept constant for these simulations) and one dimension for the time varying radial output. Other model parameters are as per the default settings shown in Figure 6-6. Figure 6-9 shows the input pulse used in both the experimental work of Chapter 4 and the following parameterisation work.

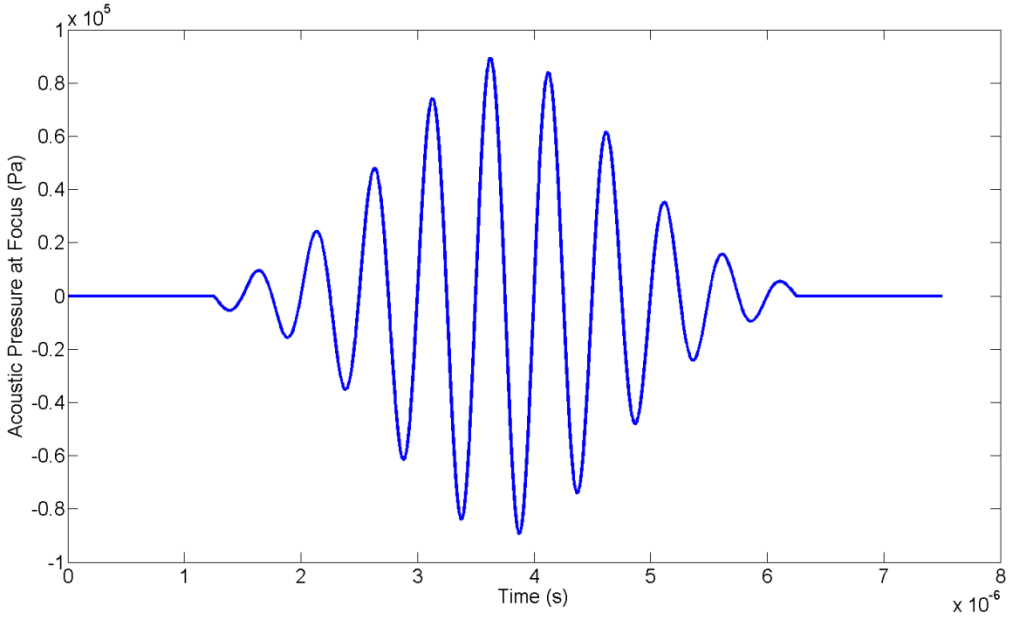

Figure 6-9: Simulated input pulse for model parameterization. Signal characteristics: 2 MHz centre frequency 10 cycle Gaussian windowed pulse with a peak negative pressure of 90 kPa. Signal is the same pulse used in the experimental work

It should be noted that the MB radius range only extends as far as 3 µm. Initial fitting studies showed that away from resonance the fitting was far more susceptible to variation because the MB simply acting a forced linear oscillator away from resonance and non-unique solutions to the parameter fitting were found. It was decided therefore to limit the size range for fitting in an attempt to decrease the computational time required for both the simulations and subsequent fitting, this will be expanded upon later in this chapter in Section 6.4.4.

Parameter	Range
MB Radius	1.5 – 3 μm
Shell Elasticity	0.01 – 2.51 N/m
Shell Viscosity	$1x10^{9}$ – $5x10^{7}$ Kg/s
Buckling Radius	0.5 – 1*
Break-up Surface Tension	0.072 – 1 N/m
Distance to Wall	1 -10*

Table 6-1: Range of shell parameters used in the fitting process. * indicates values in terms of initial MB radius

To determine the best fit parameters the following procedure was undertaken. The experimental time domain data was corrected for the transducer response properties and windowed using a Hann window. Similarly the simulated data was filtered to remove signal content from outside of the experimental transducer bandwidth (fourth order Butterworth filter with a pass band of 1 – 7 MHz was applied). The experimental data was then cross correlated with the simulated data to match the waveforms in time. This is performed for every MB in the size range compared against every permutation of model parameters in the simulated dataset, this resulted in two multidimensional matrices of equal size (the size being the length of time domain signal and the other dimensions accounting for number of, and range of model variables examined as given in Table 6-1). The parameters of best fit were determined by the comparison of these two matrices and the extraction the minimum standard difference STD (given by Equation 6-16 and as described by Tu et al. [128]) where (t) is the time point of the sample, (R) is the instantaneous radius at time (t), exp and sim refer to the experimental or simulated data respectively and N is the number of samples. Figure 6-10 shows and example of the experimental data compared with the fitted experimental data for two different MBs. The top plot shows a MB near resonance (R_0 = 1.7 μm) and demonstrates how the harmonic content manifests itself in the time domain signal; best fit parameters found as the minimum STD were: χ = 0.51 N/m, κ_s = $1x10^{-8}$ kg/s, $\sigma_{breakup}$ = 0.5 N/m, $R_{Buckling} = R_0$. The bottom plot shows a the response from a MB far above resonance (R_0 = 3 μm), as can be seen there is little harmonic signal evident and the response is characteristic of a forced linear oscillator; best fit parameters found as the minimum STD were: χ = 0.01 N/m, κ_s = $5x10^{-7}$ kg/s, $\sigma_{breakup}$ = 0.13 N/m, $R_{Buckling} = R_0$.

$$STD = \frac{\sqrt{\sum_{i=t_{start}}^{t_{end}} \left(R_{exp,i} - R_{sim,i}\right)^2}}{N}$$

Equation 6-16

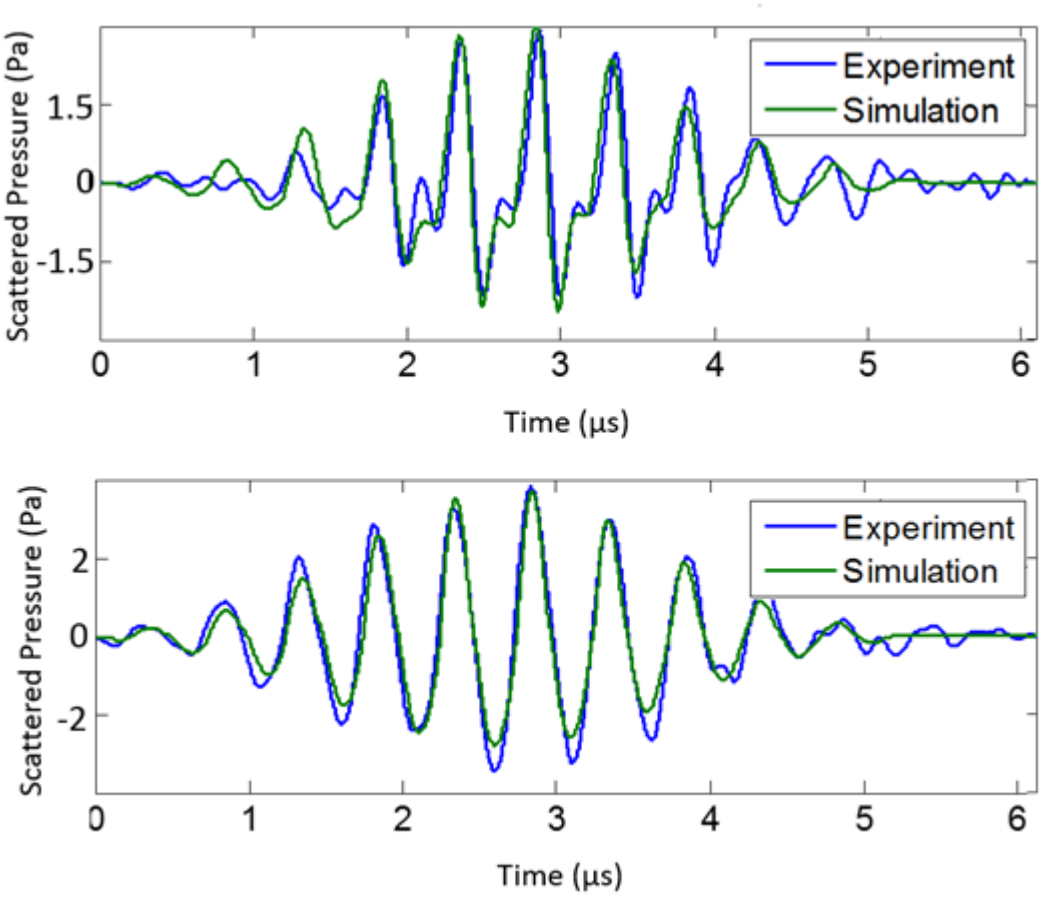

Figure 6-10: Example of parameter fitting using the non-linear Marmottant model without the presence of a boundary. Top plot: MB near the resonance size (R_0 = 1.7 μm), best fit parameters: χ = 0.51 N/m, κ_s = 1x10^{-8}, $\sigma_{breakup}$ = 0.5 N/m, $R_{Buckling}$ = R_0. Bottom plot: MB above resonance (R_0 = 3 μm), best fit parameters: χ = 0.01 N/m, κ_s = 5x10^{-7}, $\sigma_{breakup}$ = 0.13 N/m, $R_{Buckling}$ = R_0.

The fitting process was conducted for 3 variations of the model; the two formulations of MB shell parameters without wall effects present and then finally the non-linear shell model in conjunction with the elastic wall model. Using the linearized form of the equation is generally simpler to implement, when performing a fitting process such as this; which can be computationally expensive, the simple models are often useful for validation purposes. The extension from the linearized form into the model which includes non-linear terms serves as a check to ensure that the models and the fitting process are performing as expected. With the linearized and non-linear fitting

completed the process of fitting the data to the more complex model incorporating wall effects could then proceed with a better understanding of the factors involved.

Due to the lack of statistical significance between the three experimental control cases (Untargeted-Uncoated, Targeted-Uncoated and Untargeted-Coated) noted in Chapter 4 these datasets were joined together to for one large dataset for fitting. Once baseline parameters for a non-adherent MB had been found the effect that adhesion plays on these parameters would then be explored. This will be discussed in Section 6.5.

6.4 Parameterisation of Models

6.4.1 Linearized Marmottant model

In this section the established parameters from using the linearized shell model are presented. The parameters derived for each bubble individually and plotted as a function of MB resting radius. Using this linearized form without the presence of a boundary there are only two parameters to determine, elasticity and viscosity. The fitted parameters as a function of MB size can be seen below. Figure 6-11 shows the shell elasticity and Figure 6-12 showing the derived viscosity using the STD of absolute difference.

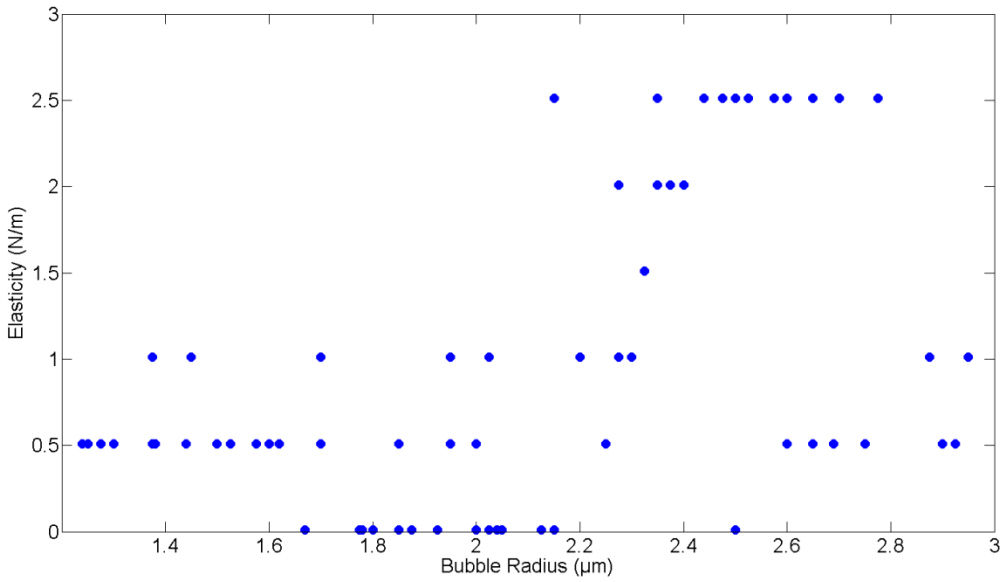

Figure 6-11: Shell elasticity fitted using the linearized shell model. Parameter extracted as the best fit using the minimum STD method.

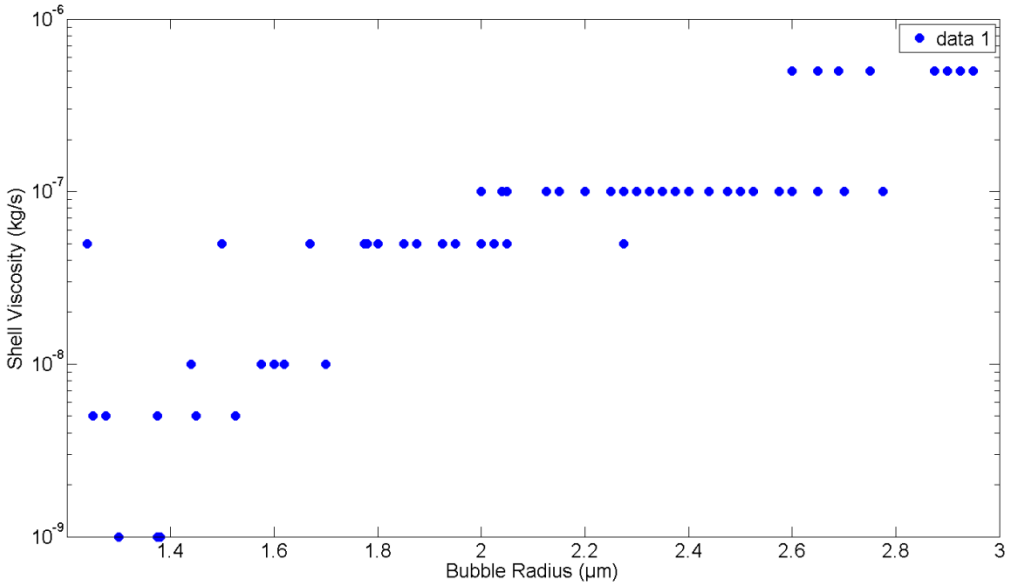

Figure 6-12: Shell viscosity fitted using the linearized shell model. Parameter extracted as the best fit using the minimum STD method.

The shell elasticity (Figure 6-11) can be seen to have a modal value of 0.51 N/m, this value is typically used in a wide range of studies where only a single value is presented for the parameterisation of lipid MBs, in addition to this 75% of the MBs exhibit an elasticity value of between 0.01 – 1.01 N/m. For the viscosity there is no clear average value however instead the viscosity is seen to exponentially increase with increasing MB radius (Note: This is not a linear trend due to the semi-log nature of the graph plotted.). Similarly the range of values arrived upon for shell viscosity correlate well with previous estimates; both the shell elasticity and viscosity broadly correspond with data previously reported [126], [128], [136] in terms of magnitude and distribution. This would indicate that the values arrived upon in this fitting process were not simply an artefact of the range of values chosen in the initial simulation setup. As reported in previous studies parameterising the linearized Marmottant model [67], [82], [83], [90], [91], [102], [103], one can observe that both the elasticity and viscosity have been seen to increase with increasing MB radius and could in turn be an artefact of rate dependent effects such as the so-called "strain-softening/hardening" or "shear-thinning" behaviour. This increase in parameter value with increasing MB radius is directly observable in both the above figures (The elasticity trend is a weak positive correlation) provides some validation that the modelling and parameterising technique used in this study are appropriate and functioning as intended, at least in relation to other studies using

similar models.. Whether or not this confirms the rate dependant nature of MB parameters will be explored when discussing the more complex parameterisation to follow (Section 6.4.4).

6.4.2 Non-linear Marmottant model

For the non-linear parameterisation there were 2 addition parameters to fit, the elasticity and viscosity as before but also terms for the buckling radius of the MB the surface tension at breakup. These last two terms have the units of multiples of R_0 and N/m respectively.

As before the experimental MB data was correlated with the full parameter range of simulated data for the same sized MB. The extracted parameters are displayed below.

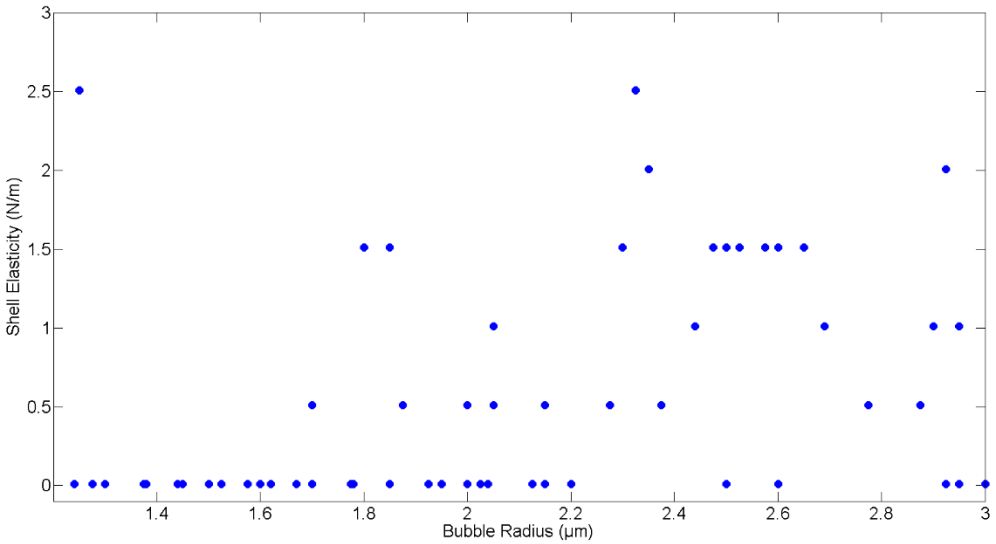

Figure 6-13: Shell elasticity fitted using the non-linear shell model. Parameter extracted as the best fit using the minimum STD method.

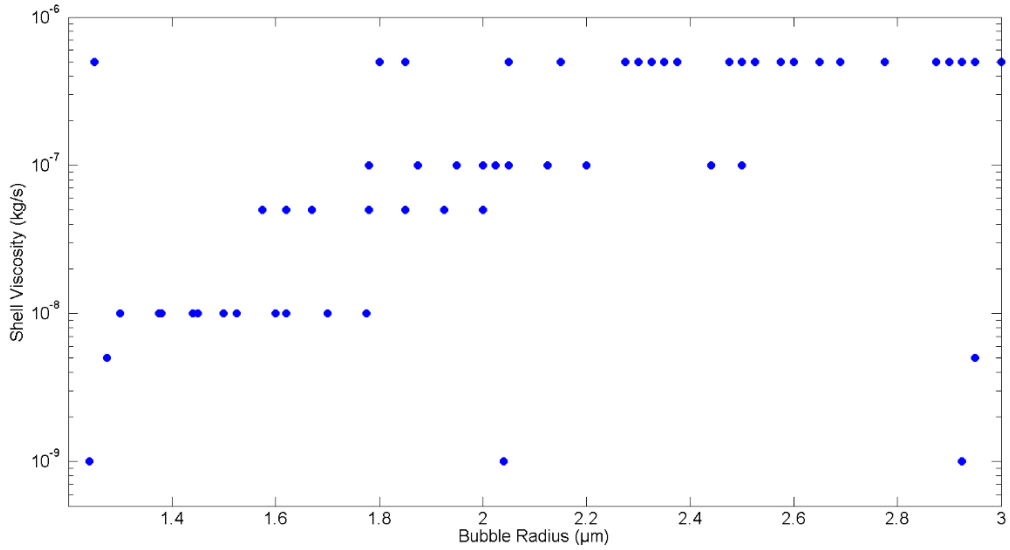

Figure 6-14: Shell viscosity fitted using the non-linear shell model. Parameter extracted as the best fit using the minimum STD method.

In comparison to the parameters deduced from the linearized form of the shell model the data shown above in Figure 6-13 and Figure 6-14 shows similar trends of the shell elasticity and viscosity respectively. The elasticity plot displays the same trend of slight increasing shell elasticity with increasing MB radius however as before the data is subject to an even higher degree of variation than seen in the linearized model, this is particularly true at the high MB radii. The viscosity shows a very similar trend to that presented in Figure 6-12 with viscosity rising as a function of MB radius.

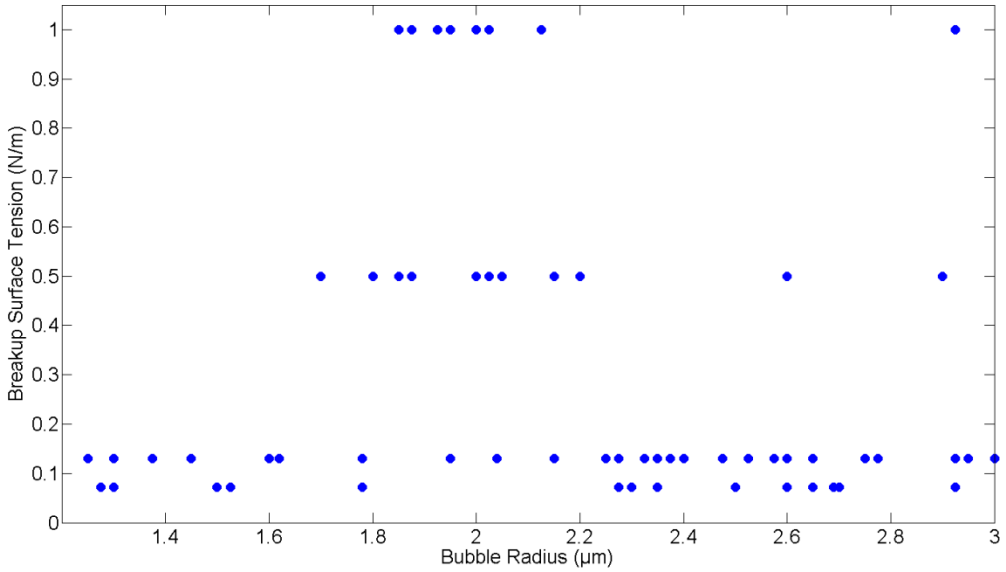

Figure 6-15: Breakup surface tension fitted using the non-linear shell model. Parameter extracted as the best fit using the minimum STD method.

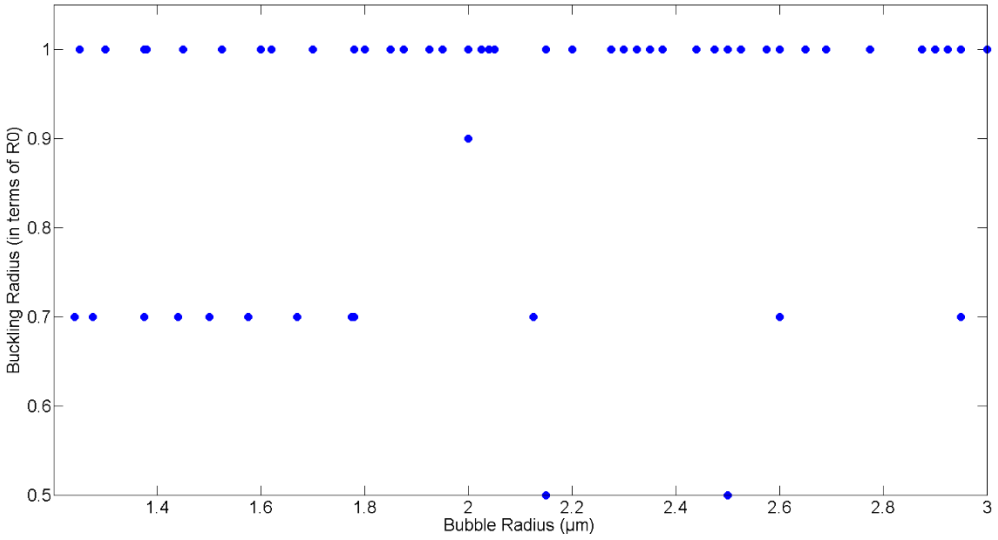

Figure 6-16: Buckling radius fitted using the non-linear shell model. Parameter extracted as the best fit using the minimum STD method.

The break up surface tension is shown to consistently be in the range of 0.072 N/m; the surface tension of water, to 0.13 N/m; a commonly quoted value for break-up surface tension from previous papers. This value hold true across the range of MB radii examined except for the region from approximately 1.6 – 2.2 μm during this region where the break-up surface tension is seen to dramatically increase. Such an increase has been suggested in previous papers (e.g. Marmottant et al [129]) where it was termed "resisent shell" and was used when parameterising for phenomena

such as “compression-only” behaviour. Subsequent to that paper the use of a “resistent shell” has also been used when attempting to fit the model to other highly non-linear phenomena such as subharmonics.

A similar effect is seen when one examines the buckling radius. Throughout the majority of the MB radius range the buckling radius is determined to be 1; that is the buckling radius is equal to the initial radius. Through the radii range of $R < 1.8$ μm the buckling radius is seen to reduce to a minimun value of approximately 0.7 of the resting radius however this only occurs for approximately half the MBs under investigation.

When one compares this size range to the range of MB the exhibit resonance dependant behaviour; observable in the second harmonic scattering power, MB stability index and degree of asymmetry as seen in Chapter 4 one can see very good correlation. Whether or not this effect is actually a direct representation of the physical changes present in the MBs during this regime or if it is simply the way the model can best represent the observed phenomena is yet to be seen.

6.4.3 **Doinikov elastic wall model**

To examine the role the wall plays in modifying MB response the last parameterisation includes the wall effect as described by the Doinikov elastic wall model. Due to the apparent success of the non-linear shell fitting in producing coherent results and the inherent issues regarding using the linearized form of shell model it was decided to only apply the non-linear shell properties here. In addition to the 4 parameters to fit from the non-linear Marmottant model there is now the additional term to account for the distance from the MB to the boundary. Boundary material properties are taken from the equipment manufacturer. Wall density = 1060 kg/m^3 and Poisson’s ratio = 0.37.

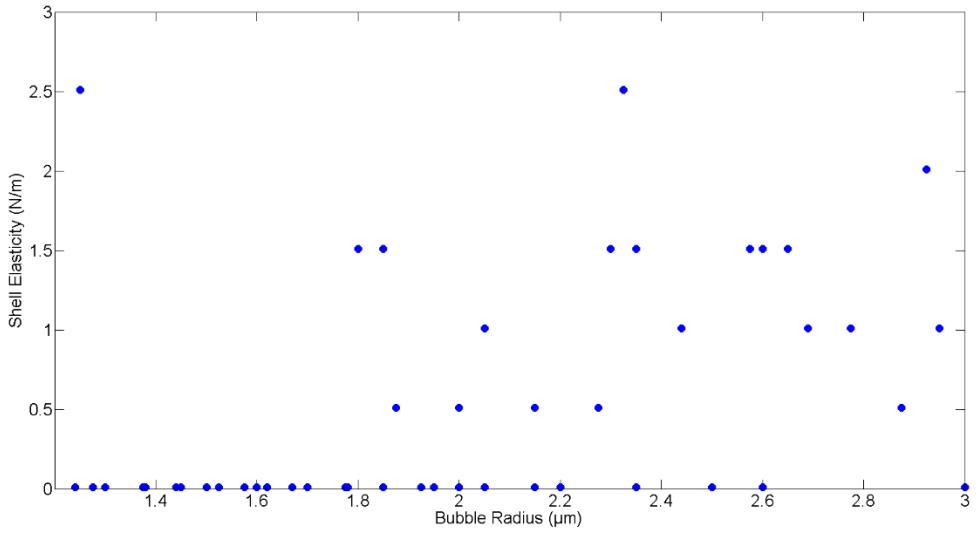

Figure 6-17: Shell elasticity fitted using Doinikov elastic wall model with the non-linear shell parameters. Parameter extracted as the best fit using the minimum STD method.

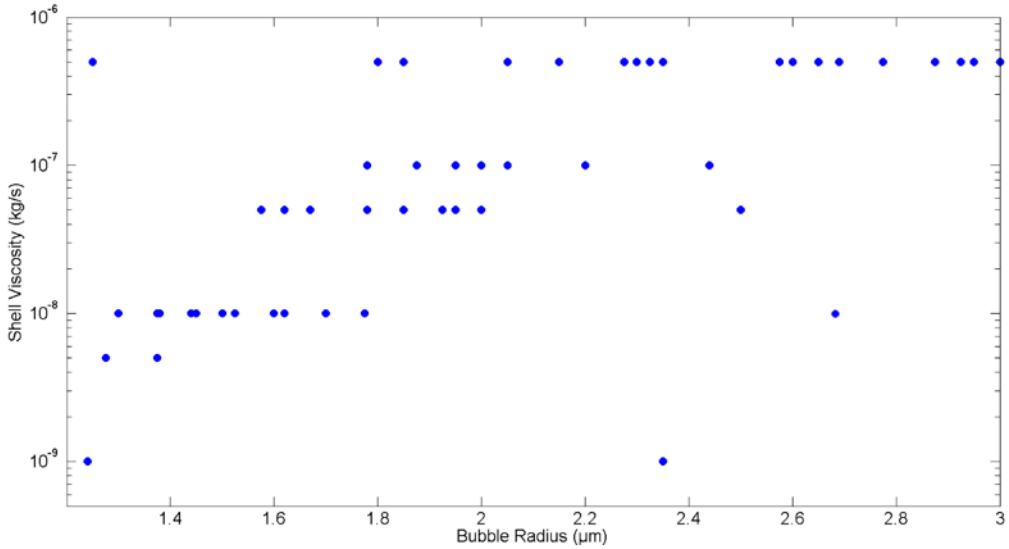

Figure 6-18: Shell viscosity fitted using Doinikov elastic wall model with the non-linear shell parameters. Parameter extracted as the best fit using the minimum STD method.

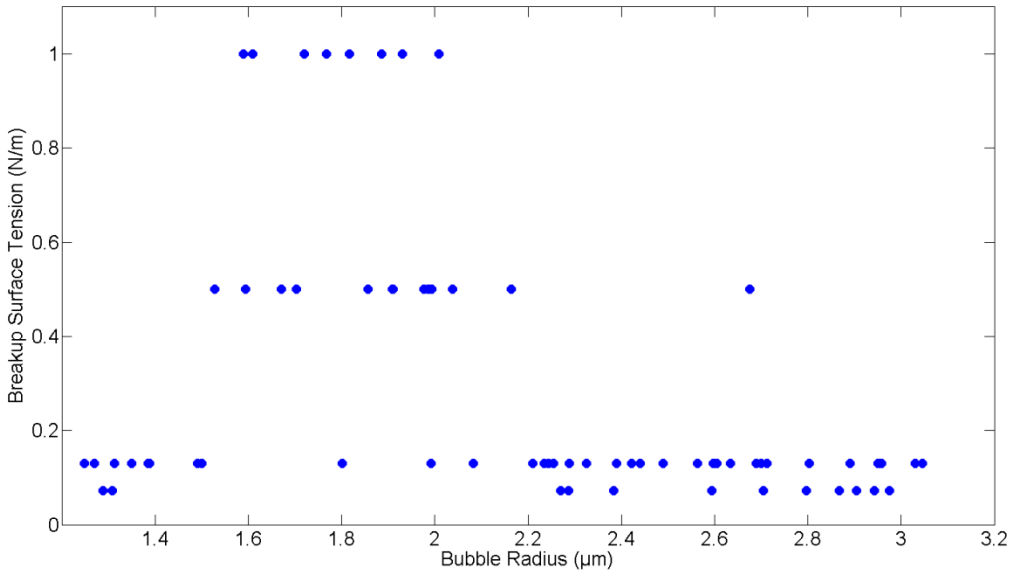

Figure 6-19: Break-up surface tension fitted using Doinikov elastic wall model with the non-linear shell parameters. Parameter extracted as the best fit using the minimum STD method.

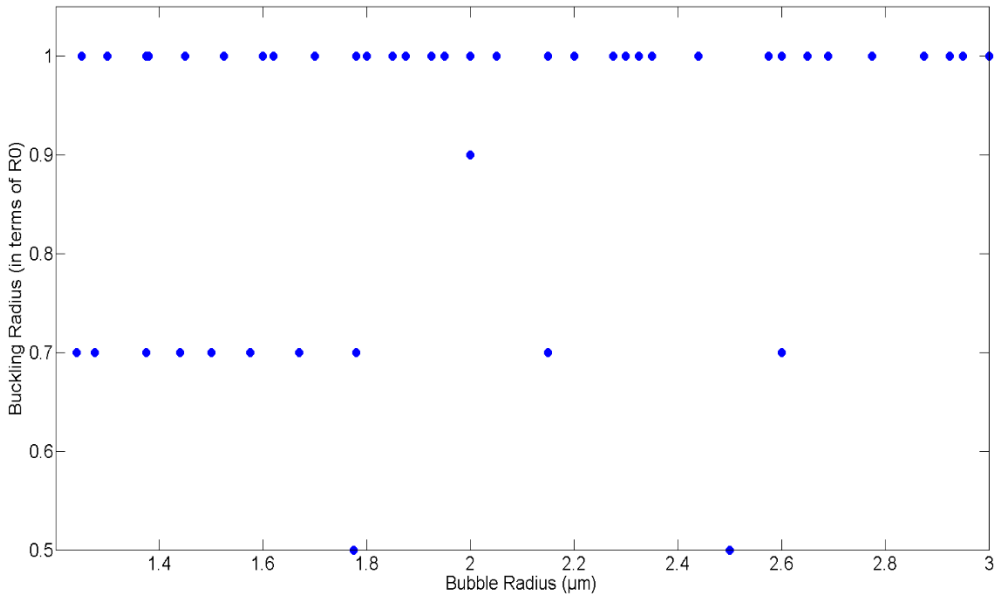

Figure 6-20: Buckling radius fitted using Doinikov elastic wall model with the non-linear shell parameters. Parameter extracted as the best fit using the minimum STD method.

The parameters extracted using the Doinikov wall model in addition to the non-linear Marmottant shell parameters follow a very similar trend to those observed from the Marmottant model in isolation. The shell elasticity term displays the characteristic increasing trend in magnitude and variation with MB radius. The viscosity similarly exhibits size dependent behaviour increasing with MB radius. Similarly both the buckling radius and breakup surface tension exhibit the same size

dependent behaviour as noted previously. In addition to the above parameters there is the additional parameter to fit regarding the radial distance to the boundary at which the MB oscillates at, this is shown in Figure 6-21: Distance to boundary fitted using Doinikov elastic wall model with the non-linear shell parameters. Parameter extracted as the best fit using the minimum STD method. Throughout the majority of the size range examined the wall distance is best fitted at a value of 1 i.e. the centre of the MB to the wall is equal to the radius so the MB is resting against the boundary. The only exception to this is when considering MBs of small radii where it appears that the MBs act as is at a much greater distance. At a distance of 5 radii the MB behaviour approaches that of a free MB (cf. Figure 6-5).

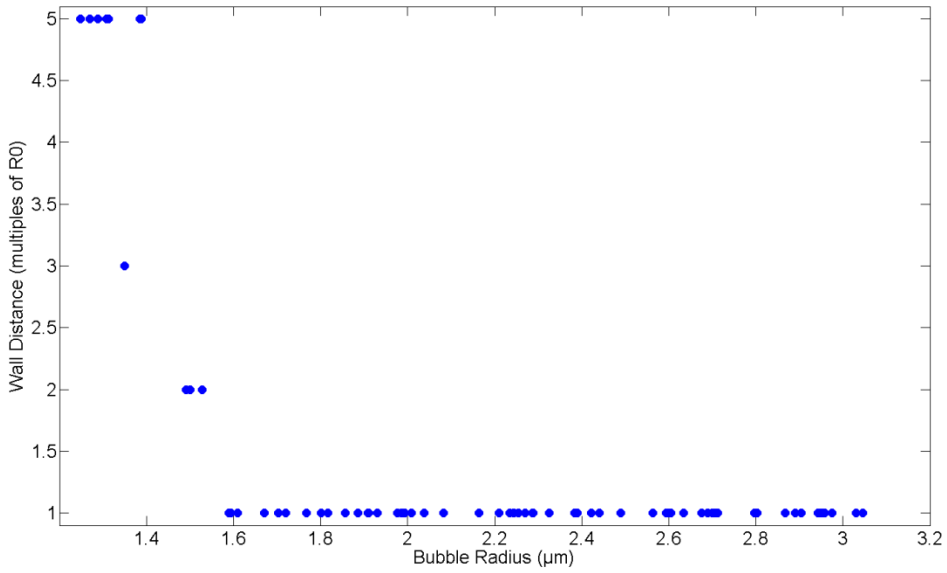

Figure 6-21: Distance to boundary fitted using Doinikov elastic wall model with the non-linear shell parameters. Parameter extracted as the best fit using the minimum STD method.

When one compares these wall modified extracted parameters to the previous values given by the Non-linear Marmottant model in isolation it becomes apparent that in this situation the boundary only alters the fitting process very marginally. If one considers that the boundary in this experimental situation is of the order of 10 μm thick and with a density close to that of water it is not surprising that the effect it has is small.

6.4.4 **Discussion of fitting process**

One of the main concerns with fitting data to a model with so many discrete variables is that the model can be made to describe any behaviour given enough parameter space. What is required is a method to test the uniqueness of the solution found. To do this one must examine the interdependency of the variables. To visualise this for more than 2 parameters is difficult however if one fixes some of the variables then such interdependency can be readily achieved. In previous studies the two parameters most heavily examined have been the shell elasticity and viscosity; as such these are the two parameters which will be focussed upon.

The following surface plots (Figure 6-22 and Figure 6-23) show the variation in fitting accuracy against the full range of shell elasticity and viscosity. The fitting accuracy has been normalised to the best fitting case, a value of 1 being the best fit. The other parameters from the simulation ($R_{Buckling}$, $\sigma_{Break\text{-}up}$, and d) have all been fixed. Because the values found for buckling radius and surface tension at breakup have been shown to vary as the MB radius approaches the resonance radius this interdependency examination has been carried out at two distinct sizes; a MB near resonance (R_0 = 1.8 μm) and a MB well above resonance (R_0 = 2.9 μm). For these cases the values chosen for buckling radius and breakup surface tension were $R_{Buckling}$ = 0.8, $\sigma_{Break\text{-}up}$ = 1 and $R_{Buckling}$ = 1, $\sigma_{Break\text{-}up}$ = 0.13 for at resonance and above resonance cases respectively. In order to create a finer view of the variation of fitting with parameter value additional simulations were performed with a much finer parameter spacing that used in the bulk of the fitting to fill the parameter space. For limited examples this provides an excellent way of providing more detail however it does come at the expense of computational power and time, hence it would have been impractical to incorporate into the full fitting procedure.

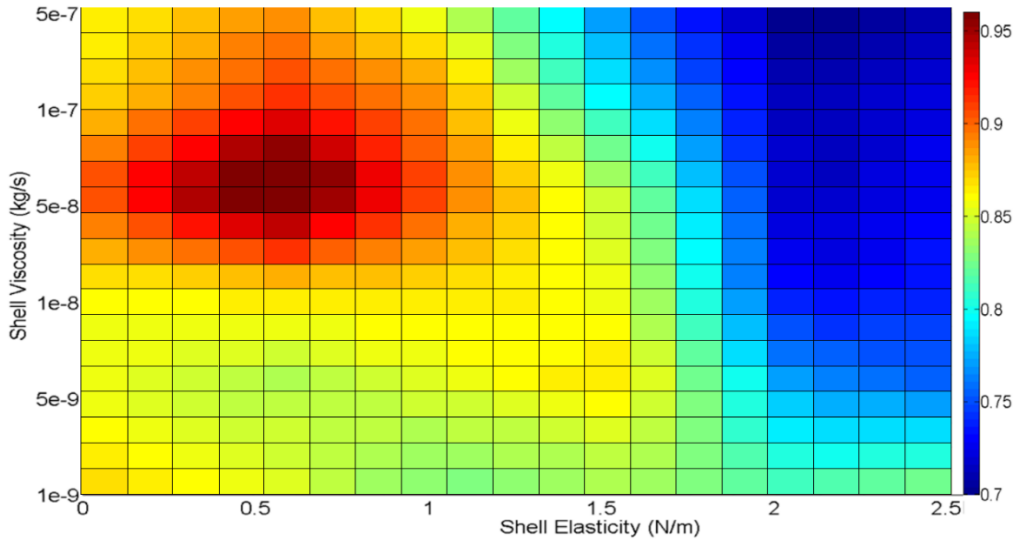

Figure 6-22: Surface plot show the depency of fitting accuracy as a function of MB shell elasticity and viscosity for a MB near resonance (R_0 = 1.8 µm)

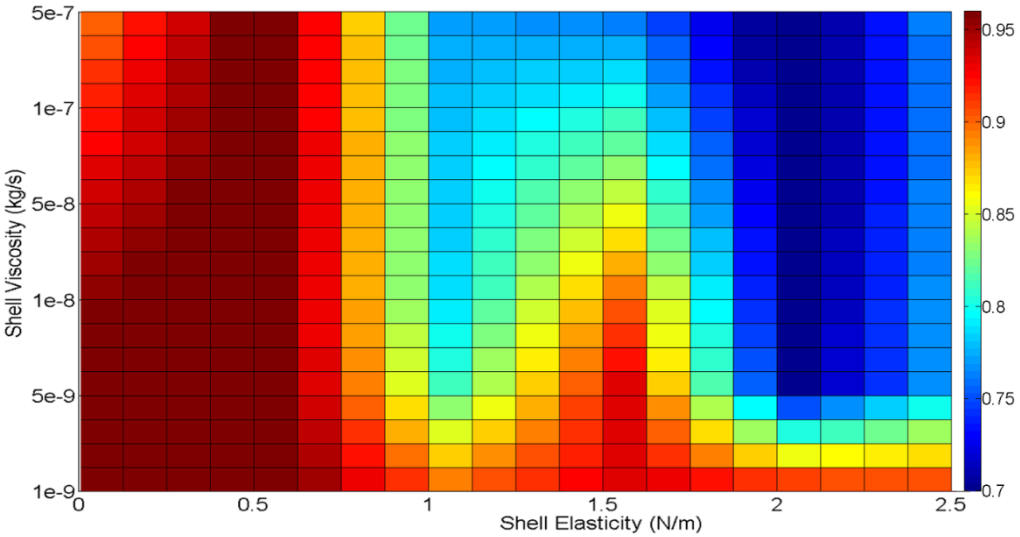

Figure 6-23: Surface plot show the depency of fitting accuracy as a function of MB shell elasticity and viscosity for a MB above resonance (R_0 = 2.9 µm)

Examining a MB near resonance (Figure 6-22) one can see that the fitting process does converge on a solution which is narrow in distribution, that is there is only a single peak region being generated with a drop-off in accuracy for all other values of elasticity and viscosity. The same cannot be said of the above resonance case, in this example there is a region of shell parameters for which the fitting is equally good. This region extends for all viscosities when an elasticity of 0.5 N/m is selected. There is also evidence of a secondary peak to fitting occurring at the point of shell elasticity = 1.5 N/m. This supports the view that for larger MBs their behaviour is generally dominated by the

MB size with shell effects a secondary consideration, whereas for smaller MBs the shell plays a critical role in defining MB dynamics [146]

In this scenario this implies that for the best fitting MBs should be excited at or near their resonance. This intuitively makes sense because it in in this region that the MB behaves most non-linearly and consequently there is more data to fit to i.e. more harmonic information which is unique to that particular excitation. Above resonance all these MBs simply behave as a forced oscillator for which the only real output that changes and can be fitted to is the amplitude variation. This indicates that a multi-frequency approach to parameterization would lead to improved parameter fitting as a larger proportion of MBs could be excited at their resonance frequency.

The fact that relatively large regions of the elasticity/viscosity surface show quite high values of fitting could be a reason why good fitting of data is quoted in previous studies where only a single, size independent, value has been given for these parameters. This is particularly true for the above resonance case, typical values given in these single value studies tend be occur around the 0.5 N/m mark and as such good fitting can be achieved for the whole range of viscosities.

With the fact that fitting accuracy reduces significantly away from resonance if one examines the ranges of values obtained for the shell elasticity and viscosity but limits the field of view to that concerning resonance (with reference to Figure 4-7, Page 128, this resonance affected region is estimated as $R < 2.3$ μm). Using the data extracted from the Marmottant model as an example (Figure 6-13 and Figure 6-14 page 185) we see that shell elasticity and viscosity compare well with previous findings (Li et al. [126]) These findings were obtained by fitting the Marmottant model to SonoVue using light scattering data, during this fitting the break-up surface tension was set to 1 N/m using the “resistant shell” as previously described and no mention is made of the buckling radius. There are a few discrepancies in terms of the range of these parameters between this thesis and Li et al. however in previous work by the same group it was noted that up to an order of magnitude difference in viscosity and twice the range of values for elasticity were found between MBs of different compositions. (Definity and SonoVue compared in [136] using light scattering data)

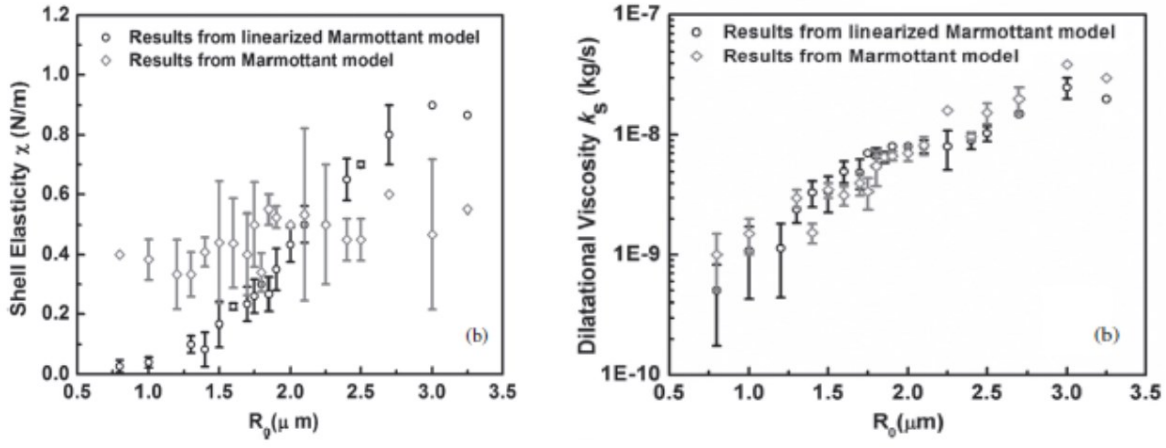

Figure 6-24: Fitted shell parameters for shell elasticity and viscosity from Li et al. [126]

There is still the question to ask as to whether it is reasonable, or indeed justified to say that a shell material property can exhibit such wildly different properties depending on its size.

A number of sources have postulated that both the elasticity and viscosity are in fact rate dependent effects rather than MB size dependent [67], [82], [83], [90], [91], [102], [103]. Specifically it expected that the elasticity is subject to either a strain-softening [135] or hardening [226] behaviour and the viscosity to exhibit shear-thinning behaviour [113]. To examine if this was true using this experimental data the shell elasticity was plotted against the maximum strain (R_{max} – R_0)/R_0 and the viscosity was plotted as a function of dilatation shear rate $\left(\frac{\dot{R}}{R}\right)_{max}$, this can be approximated as shown in Equation 6-17 as derived in [113].

$$\left(\frac{\dot{R}}{R}\right)_{max} \approx 2\pi f_0 \left(\frac{\Delta R_{max}}{R_0}\right)$$

Equation 6-17

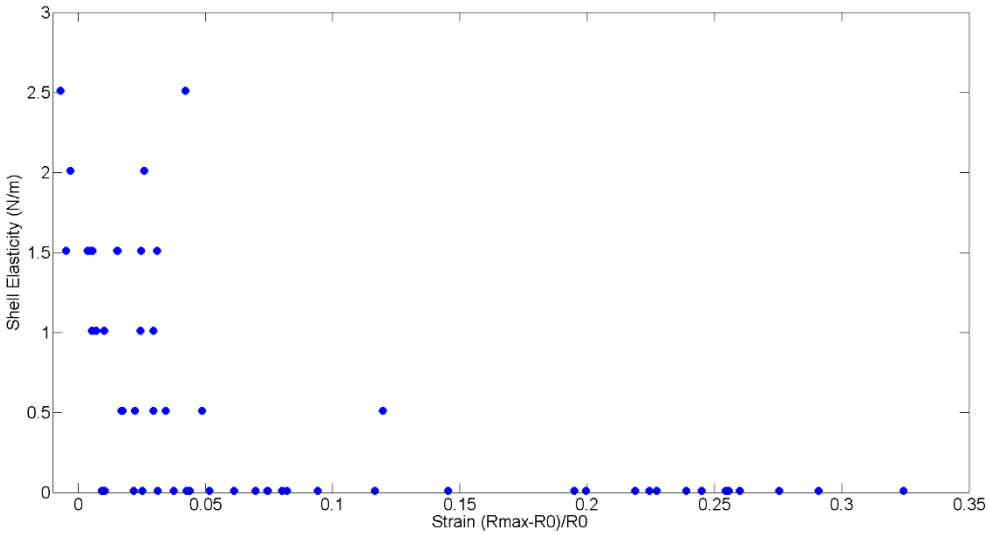

Figure 6-25: Shell elasticity as a function of maximum strain, data fitted to the Doinikov elastic wall model using non-linear Marmottant shell parameters.

Figure 6-25 shows the shell elasticity as a function of strain. It was previously suggested that the perceived radius dependent shell properties we not in fact radius dependent but that this was actually an artefact produced from a strain dependency. Specifically it was expected that the elasticity shows a "strain softening" effect; whereby as the maximum strain is increased the elasticity effectively decreased. This is attributed to a decrease in the coherence and associated forces between the molecules of the encapsulation at these higher strains [89]. This is supported by the above fitting showing a good between shell elasticity and maximum strain.

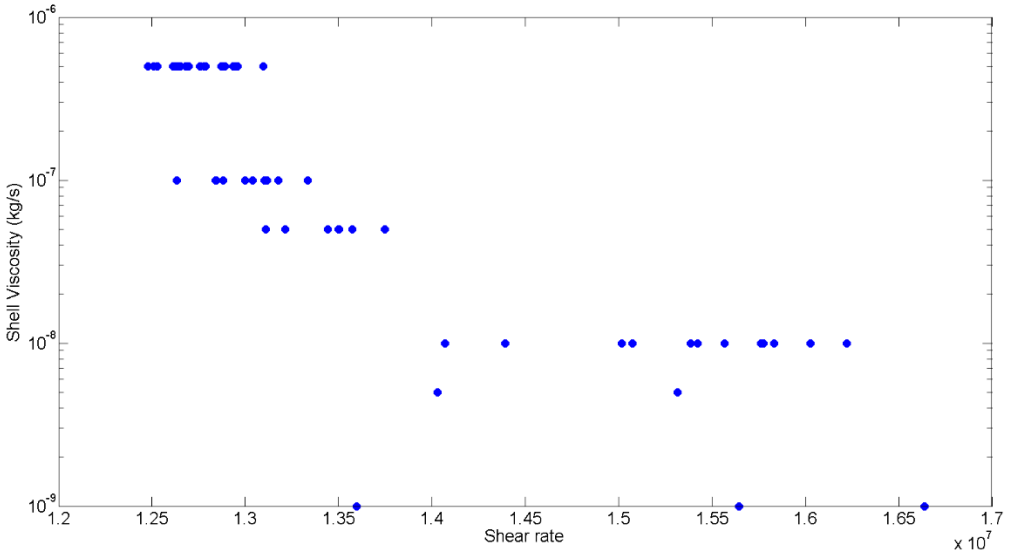

Figure 6-26: Shell viscosity as a function of shear rate, data fitted to the Doinikov elastic wall model using non-linear Marmottant shell parameters.

The viscosity strain rate dependence or "shear thinning" behaviour is presented in Figure 6-26. Shear thinning behaviour was introduced as a possible reason for the observance of a radius dependant viscosity. Because viscosity is a material property it should be specific to the material and not a function of its dimensions. It also implies that as the shear rate increases the viscosity and hence the damping it contributes to is diminished. This is supported by the above findings.

The other possible avenue to try to explain the seemingly size dependent nature of the shell material properties is that the simplifications regarding the rheological behaviour of the shell are simply not accurate enough. Introducing more non-linear parameters for the elasticity and viscosity based on the actual behaviour of the material rather than in an ad hoc fashion in the case of the Marmottant model could be the key to providing better modelling capability. An example of this newer model is given by Li et al. [126] and is termed the NSEV model (Nonlinear shell elasticity and viscosity). This model has been shown to produce values for the shell elasticity and viscosity which remain largely constant independent of MB radius which intuitively seems more applicable as a material property.

Using the derived size varying MB parameters it is then possible to try to recreate the original experimental data. Figure 6-27 shows the simulated response of a range of MB radii to a 90 kPa PNP, 2 MHz, 10 cycle pulse as used in Chapter 4. By viewing the MB response along the 2 MHz and 4 MHz lines respectively one can recreate the fundamental and 2nd harmonic response graphs found in Chapter 4. The scattering data from Chapter 4 is recreated as a surface plot (Figure 6-28) Both in

terms of amplitude, position and shape these curves bear a high degree of similarity showing that the model can faithfully represent this data.

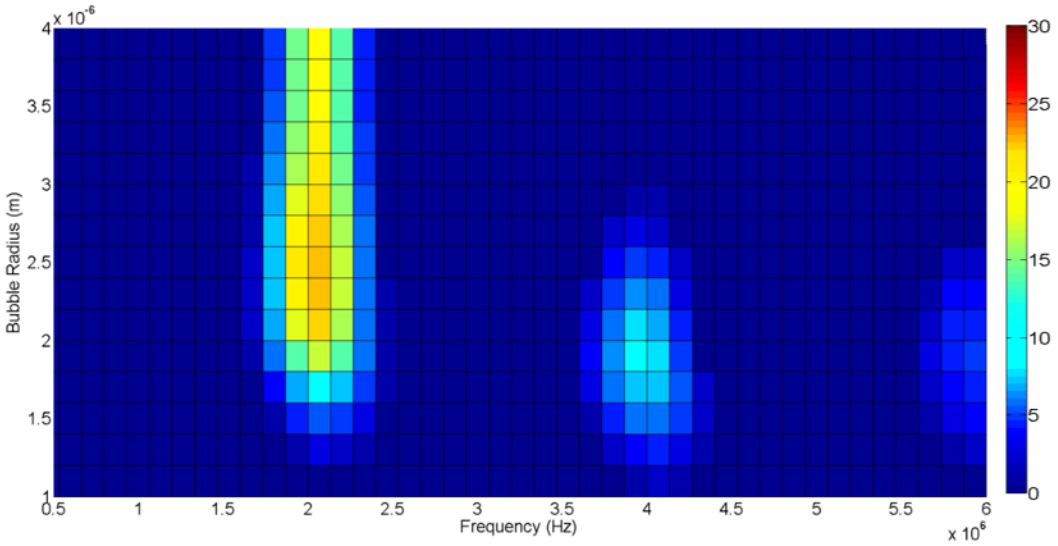

Figure 6-27: Surface plot of the calculated scattered power in response to a 90 kPa PNP, 2 MHz centre frequency pulse as used in Chapter 4

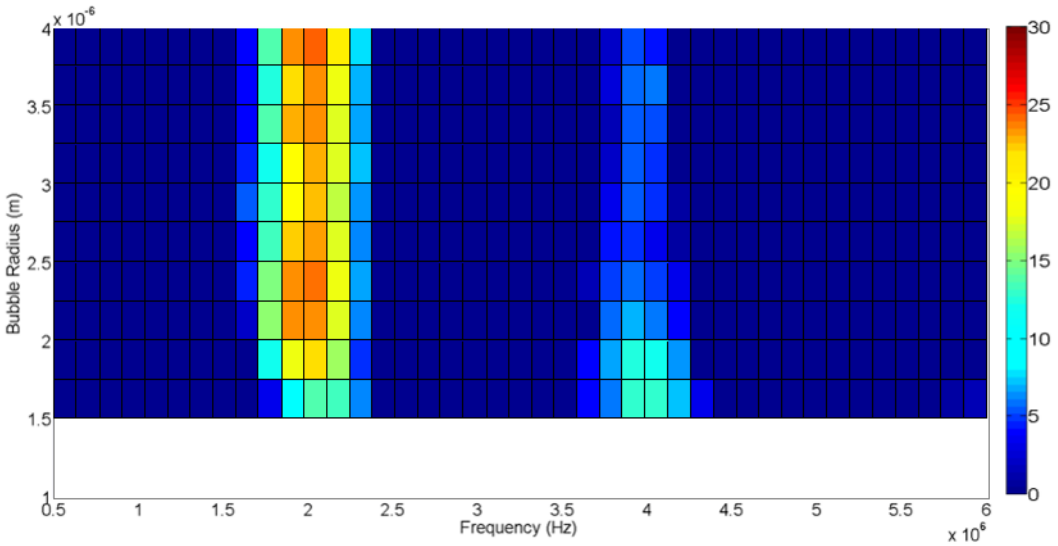

Figure 6-28: Surface plot of the experimental scattered power spectrum. Data taken from the TUC case in Chapter 4. MBs insonated using a 90 kPa PNP, 2 MHz centre frequency pulse.

Figure 6-29 displays the same power spectrum surface plot but this time in response to the 200 kPa PNP pulse used in Chapter 5. As expected the scattering power levels for the fundamental and second harmonic are enhanced. Conspicuous by its absence however is any trace of sub-harmonic generation. The reasons for this are not fully understood however there are a number of possibilities as to why this may be. Firstly there is the question of applied pressure. SH have been

shown to have threshold levels before their onset [198], [210]. The latter of these papers investigates the SH response of a number of non-linear shell models to explore their differences. Using the Marmottant model with single value shell parameters of χ=0.53 N/m, $\kappa_s = 1.2\text{x}10^{-8}$, $R_{buckling} = R_0$ and $R_{break\text{-}up} = 1.5R_{buckling}$ (this equates to a surface tension at break-up of approximately 0.66 N/m), they note that for a 2 MHz insonation pulse the SH threshold pressure is of the order of 350 kPa and then has a scattered pressure some 40 dB below the fundamental response, These parameters fall within the bounds established by the proceeding fitting (Section 6.4.3) and as such one could expect similar results.

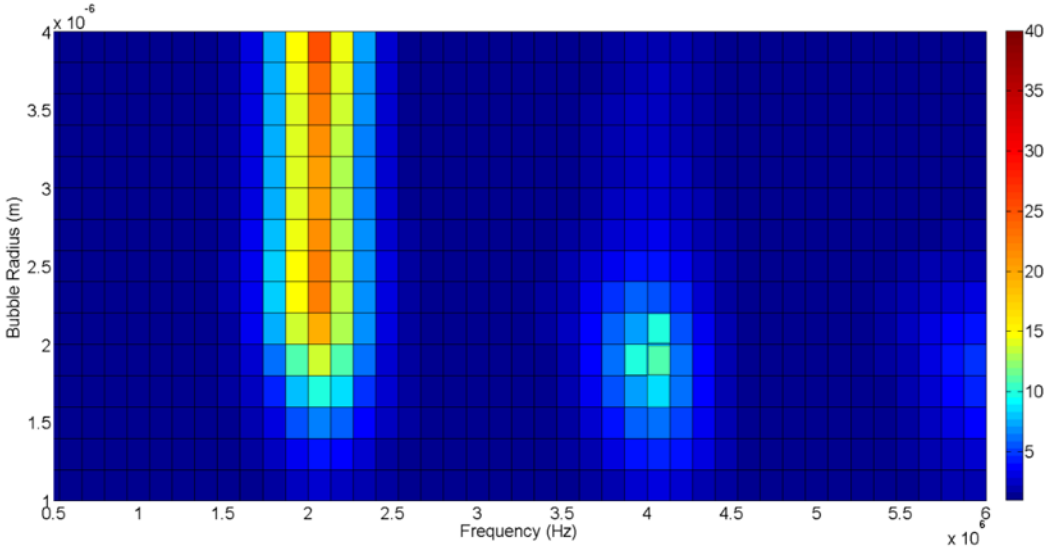

Figure 6-29: Surface plot of the calculated scattered power in response to a 200 kPa PNP, 2MHz centre frequency pulse as used in Chapter 5

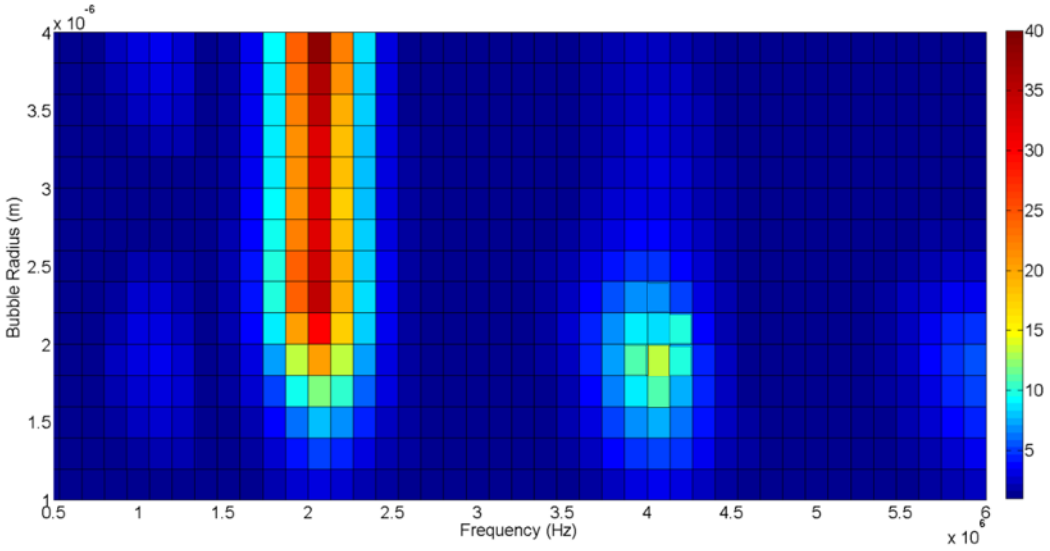

Figure 6-30: Surface plot of the calculated scattered power in response to a 400 kPa PNP, 2MHz centre frequency pulse appearance of SH signals present in the 1 MHz region.

To attempt to replicate similar a similar response using the parameters derived in Section 6.4.3 an acoustic pressure of 400 kPa was applied, the resulting plot can be seen in Figure 6-30: Surface plot of the calculated scattered power in response to a 400 kPa PNP, 2MHz centre frequency pulse appearance of SH signals present in the 1 MHz region The onset of SH signal can be detected in the 1 – 1.5 MHz frequency band however at significantly reduced power levels in comparison to the fundamental and 2nd harmonic.

One must also point out at this time that the parameters derived earlier in the chapter were for a 90 kPa pulse and not a 200 or even 400 kPa pulse. As previously stated the driving pressure is known to alter characteristics such as the resonance frequency and will also play a role in defining the maximum strain rate, both of which one would expect to alter the MB properties so the use of the 90 kPa derived properties may not be ideal in this situation for predicting the onset of SHs.

The fitting of parameters to the SH data produced in Chapter 5 proved highly problematic. Due to the nature of the transducers used in the experiment itself there was very little receive bandwidth available (approximately 0.25 – 1.75 MHz) for the collection of signals from outside the predicted SH range. This effectively meant that the SH signals of around 1 MHz were received in isolation without a strong fundamental signal to gauge amplitudes against or to be used in the fitting process. As observed in Section 5.4.1 Page 150 the SH signal itself was subject to a high degree of variability, even for similar MBs. As such the validity of attempting to fit parameters to it are questionable especially with the additional issue of having no other frequency component to compare it to.

6.5 Changing Parameters as a Function of Microbubble Adhesion

With reasonably good confidence in the fitting of the non-adherent MBs, certainly for the fundamental and 2nd harmonic responses attention was now focussed the effect that adherence plays on the derived parameters. Below the figures show a direct comparison between the parameters extracted for the non-adherent MBs (Blue circles) and the adherent Mb (Red triangles).

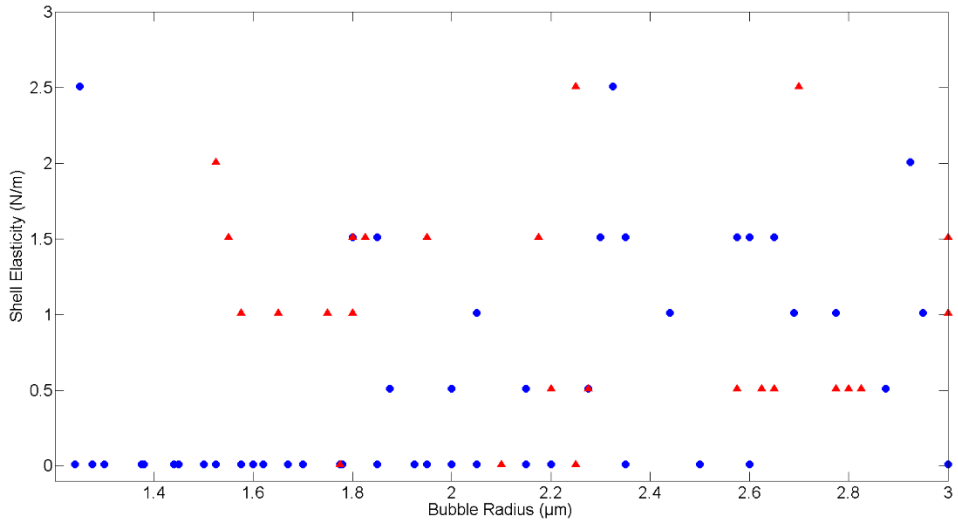

Figure 6-31: Comparaison of the fitted shell elasticity for non-adherent MBs (Blue circles) and the adherent Mb (Red triangles) using the Doinikov elastic wall model and non-linear shell parameters. P>0.05 for all size ranges except for 1.6 1.8 µm where p<0.05.

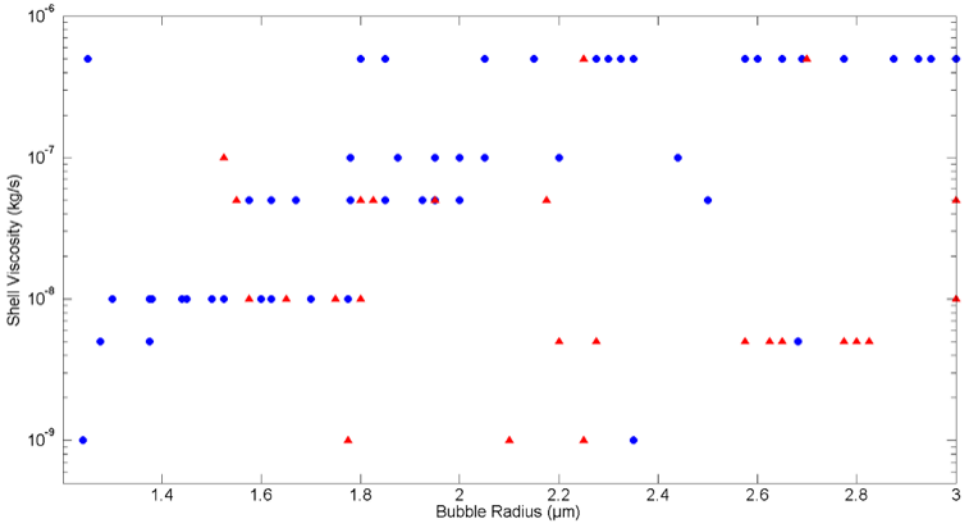

Figure 6-32: Comparaison of the fitted shell viscosity for non-adherent MBs (Blue circles) and the adherent Mb (Red triangles) using the Doinikov elastic wall model and non-linear shell parameters. P>0.05 for all size ranges

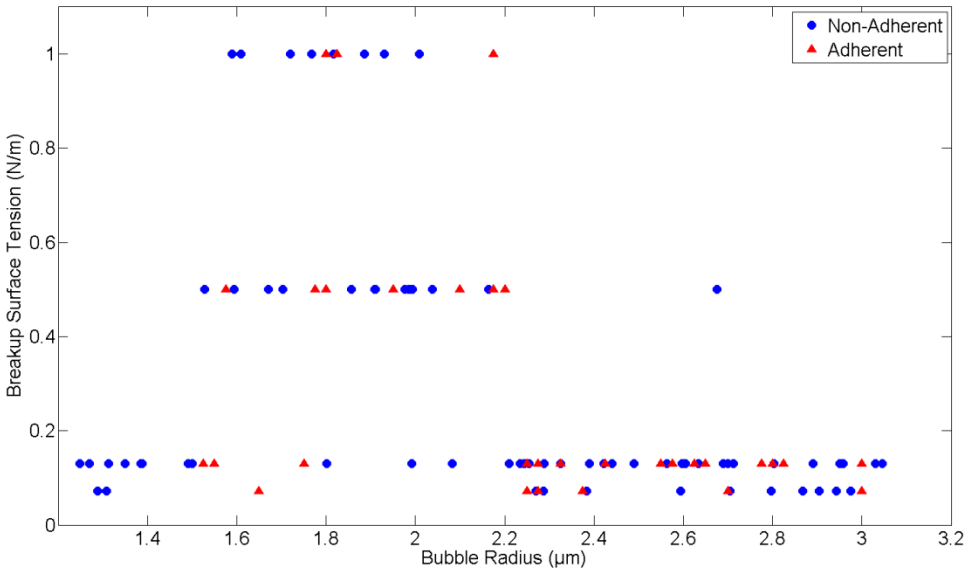

Figure 6-33: Comparaison of the fitted breakup surface tension for non-adherent MBs (Blue circles) and the adherent Mb (Red triangles) using the Doinikov elastic wall model and non-linear shell parameters. P>0.05 for all size ranges

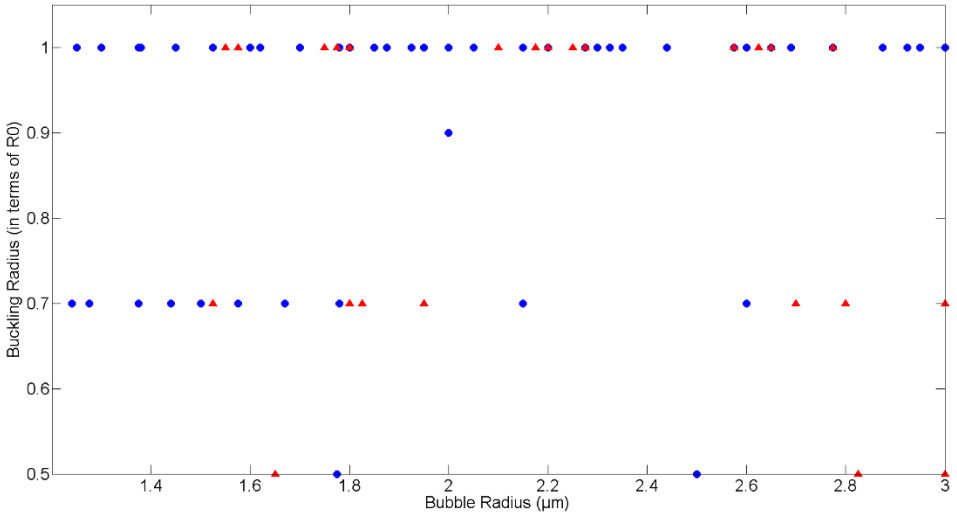

Figure 6-34: Comparaison of the fitted buckling radius for non-adherent MBs (Blue circles) and the adherent Mb (Red triangles) using the Doinikov elastic wall model and non-linear shell parameters. P>0.05 for all size ranges

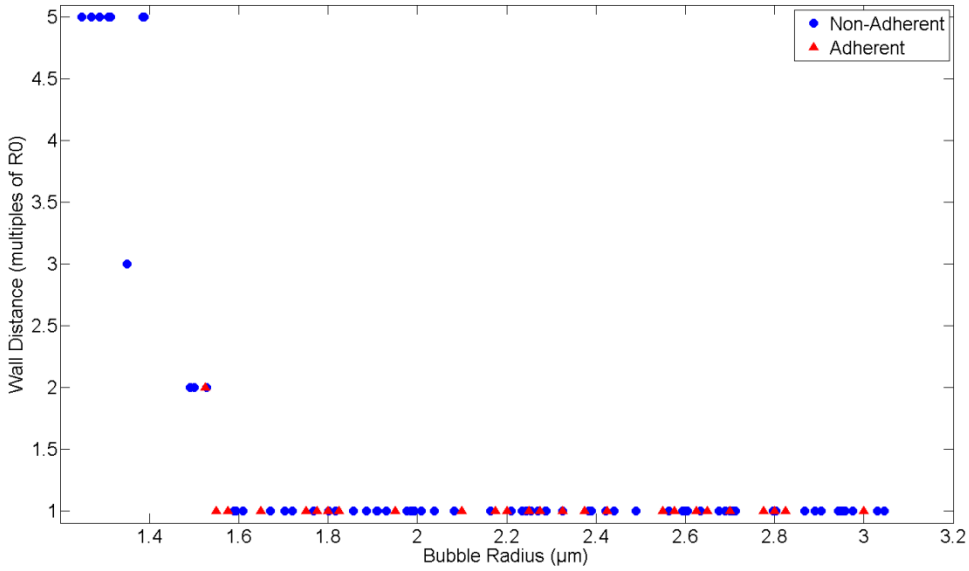

Figure 6-35: Comparaison of the fitted wall distance for non-adherent MBs (Blue circles) and the adherent Mb (Red triangles) using the Doinikov elastic wall model and non-linear shell parameters. P>0.05 for all size ranges

As can be seen from the fitted parameters above that for the vast majority of the parameter space there is no appreciable difference between the parameters extracted from the adherent MBs compared with their non-adherent counterparts. This was confirmed by the conduction of statistical analysis as described in Section 4.3.4. Briefly, the data was separated into bins of 0.2 μm width and an unpaired t-test was applied. For the range of MB radii shown all the tests returned with a p value > 0.05 indicating that the values given by the adherent and non-adherent cases for all parameters were statistically equivalent.

There are a number of possible explanations for this. When one considers the overall response observed in Chapter 4 there are a few confounding factors which make the results from this fitting to be expected. Although there is a measurable difference between the adherent and non-adherent cases, it only manifests itself in specific ways; that of 2nd harmonic peak generation and stability over time. There was no measurable acoustic difference in the fundamental scattering of the MB or in the degree of asymmetry. One could argue that the fundamental response would be the most critical in the fitting process. Similarly the degree of variation observed in the acoustic responses could mean that any subtle change which exists in the MB response is far outweighed by the variation seen between MBs.

There is one caveat to this and that is in the range of 1.6 – 1.8 μm of the shell elasticity plot (Figure 6-31) where there was a statistical difference shown between the datasets (P<0.05). This

could provide evidence to suggest that adhesion can play a role in the modification of MB shell parameters, indeed this observed difference does correlate with the observed shift in peak 2nd harmonic generation seen in Chapter 4, however as a note of caution the issue of noise/variability does cast suspicion over the validity of the result. Once again a method to reduce the variability of the responses is required before this observation can be confirmed.

6.6 Summary

A number of models of increasing complexity for the description of both the MB rheological behaviour and surrounding environment have been implemented successfully in the form of numerical simulations. These models were parameterised by a new method which exhaustively simulated the whole parameter space and then explored each permutation of model parameters to find a best fit scenario. This is in contrast to the typically approach which makes a number of assumptions, such as small amplitude oscillations, to reduce the number of variables required but does so at the expense of the model accuracy and applicability. To the authors knowledge this approach has not been conducted previously and could provide a method for the more specific parameterisation of theoretical models.

The parameters converged on using this fitting approach converge well with previously reported values. Interestingly this approach provided clear insight into the size dependant nature of some of these parameters. Specifically it showed that the shell elasticity increases with MB radius, or, to examine this in a different light, that the shell elasticity decreases with increasing maximum strain. This is an effect called strain softening and has be suggested as a source of shell non-linearity and as a method to avoid a sized dependent material property. Similarly, the size/strain rate dependant viscosity (shear-thinning) manifested itself showing that the dilatational viscosity decreases with increasing shear rate.

Other important observations regarding the model parameters include the buckling radius and breakup shell surface tension seeming to have a resonance dependence. Both parameters are seen undergo wide fluctuations in the resonance size region whilst remaining constant in the remainder of the size range examined.

Examination of the interdependence of these parameters showed that the solution converged upon was indeed a unique solution showing a definite peak in fitting accuracy. This peak was accentuated by performing the fitting process at or near the resonance frequency of the MB. With the current experimental data this was a slight drawback due to the single frequency utilised in experiments however it was somewhat mitigated against by the sheer volume of data available. In the future a multi-frequency analysis could help to improve fitting accuracy; this wasn't an option with the current experimental set up. The interdependency examination also showed that if one of the selected parameters is correct then it is possible to achieve a satisfactory degree of fitting with a wide range of values for the other shell parameter. This could explain how single values are used with some degree of success for situations where the parameter values could be expected to vary as

a function of size/rate. Using the derived parameters it was possible to faithfully recreate the scattering power spectrum as observed in experiment. The recreation of SH data proved problematic with the current values for model parameters however SH signals could be generated with significantly increased acoustic pressure.

Model parameters were also extracted from experimental data for adherent MBs. In comparison to the non-adherent control case there was very little difference observable in the model parameters. Once of the major contributing factor to this could be the variability between MBs resulting is variable response effects for seemingly similar MBs. To examine the difference between the MBs in this situation in greater detail it is suggested that far greater control over the MB manufacture needs to be exerted to reduce the variability. A possible method for this is the generation of MBs through microfluidic devices [214], [257].

7 Discussion and conclusions

7.1 Overview

Molecular imaging offers huge potential in medicine for applications in early diagnosis of a variety of pathologies, targeted gene/drug delivery as well as drug discovery. Irrespective of the imaging modality used molecular imaging poses a number of challenges that need to be addressed. Issues such as binding affinity, specificity, how one discretizes the target signal from the background signal, safety and ultimately the cost and time taken are all key factors. Imaging techniques such as PET or MRI can reduce the impact of binding affinity and discretization of the target signal by using very small quantities of highly specific imaging probes; the use of small quantities of imaging probe also reduces the safety concerns which accompany the contrast agents available for those technologies, however, this is all achieved with a prohibitively high cost in terms of both monetary and time considerations and as such cannot be utilised to the full potential promised by the field. Contrast enhanced ultrasound as a molecular imaging strategy has a number of benefits in terms of the cost, time taken and practicality however the one of the major drawbacks to its implementation is how one differentiates the smaller intensity signal produced from the adherent MBs, which is effectively masked by the far more substantial response generated by the greater numbers of non-adherent MBs flowing in the vasculature. Current approaches either make use of the differential in clearance time between adherent and non-adherent MBs for imaging or make use of a number of techniques to enhance the numbers of MBs at the target site and then apply an array of filtering processes to remove the unwanted signal. Both these approaches increase the length of time and complexity for a scan and as such negate some of the benefits of using US that made it attractive in the first place (cf. Section 2.7, page 74).

It has been shown that boundary affects can significantly alter the response of MB dynamics and hence scattered acoustic signal (cf. Section 2.6.1, page 69). Furthermore, recent papers have alluded to changes in MB response [43] or material properties [258] as a consequence of adherence. The remit of this thesis was therefore to examine if an acoustic difference could be observed between adherent and non-adherent MBs and if that difference could be exploited to inform the development of a real-time imaging strategy for US molecular imaging.

To achieve this goal it was decided to focus on developing a better understanding of the fundamental dynamics of a MB under adherent conditions and how that differs from its non-adherent counterpart. This was first conducted experimentally to determine if under well-defined

conditions a change in acoustic response could indeed be detected. The second approach was to then apply theoretical models to the observed responses to attempt to understand the physics of the situation, and, if possible discover ways for the enhancement or accentuation of any differences.

The remainder of this chapter will discuss the key findings from this thesis and explore the avenues that present themselves for possible extensions and implications of this work. Finally, the principle conclusion to this thesis is presented.

7.2 Key Discussions

One of the driving factors in the conduction of this research was that if any differentiation of MB behaviour arose as a function of MB adherence to a target surface had to be detectable acoustically. While there were a number of studies indicating the effect that boundaries, and possibly adhesion, had on MB radial dynamics it would not mean anything unless those differences in radial response manifested themselves at a detectable level in the scattered response. This was the main motivation for the conduction of single MB acoustics. If it wasn't possible to differentiate adherent from non-adherent MBs at the most controlled level then it would be highly unlikely to be attainable in the more diverse in vivo clinical settings.

To achieve this goal a testing rig and procedure was developed for the examination of single MBs under controlled conditions of either adherence to a thin elastic boundary or simply in proximity to a nearby thin elastic boundary. This case represents the situation which would be the most difficult to differentiate between adherent and non-adherent MBs and as such a good first examination point.

7.2.1 Resonance shift due to adherence

Chapter 4 examined the effects of adhesion on the fundamental and 2nd harmonic scattering properties. It was observed that there was a shift in the radius of peak second harmonic generation between the adherent and non-adherent MBs. Using the 2nd harmonic generation as an indicator of resonance it was inferred that the presence of adhesion has indeed resulted in a detectable acoustic difference although the confidence level in this result is low (statistical power of 35%). This difference corresponded to an increase in the resonance frequency of approximately 19% when normalised against the natural frequency of an unencapsulated MB of the same size. In terms of resonance radius this equated to a difference in MB diameter of approximately 0.5 µm (cf. Section 4.4.2 Page 126). In addition to the evidence of an acoustic difference in resonance due to adhesion from the 2nd harmonic there was also support in the form of stability data. The stability of a MB to repeated insonation is known to be strongly affected by resonance and is one of the driving forces in acoustically driven diffusion. As such, one would expect a MB at resonance to exhibit the most disruption to successive pulses, if the resonance shift suggested by the second harmonic was indeed a true effect one would expect to see a difference in the onset of MB disruption as a function of radius. This is exactly what was observed, MBs of a statistically significantly larger radius were seen

to be disrupted (cf. Section 4.4.3 Page 131, statistical power approximately 70%). This shift in disruption threshold corresponded well with the 2nd harmonic peak shift.

With reasonable confidence that the observed shift in resonance was a true effect it was then considered how best to accentuate that difference to allow for easier visualization and detection. As it was the observed shift in resonance was to the low end of the system's capability to detect effectively. It was hoped that by examination of the SH component of the scattered signal this difference could the accentuated. Classical theory [210], [252] predicts that the onset of SH generation requires an onset pressure and that this pressure is at minimum when a MB is insonated at twice its resonance frequency. In regards to the methodology of the experimental technique used here where a single frequency of excitation was used (cf. Section 4.3.3 Page 119) it was hoped that the peak SH at twice the resonance frequency would manifest itself as a 2 times radius difference in peak SH generation. This was not the case. SH signal generation was observed for both adherent and non-adherent cases. Instead of occurring in separated discrete regions with an increased size difference between the radii of peak signal generation, the SHs appeared in both cases to be located; both in terms of frequency and MB radius, about the same region (cf. Section 5.4.1 Page 150). Additionally this region appeared to be neither at the resonance size nor at twice the resonance size as was expected, instead occurring in a diffuse size range between the two.

The error of this expectation due to the incorrect application of classical theory for unencapsulated MBs being applied for the more complex case of encapsulated MBs. The addition of the encapsulation can be seen to spread out the frequency at which SH generation onset occurs. In fact using a MB model which correctly accounts for the non-linear behaviour of a MB shell this onset frequency is observed to become a broad peak effectively encompassing both the resonance frequency up to twice the resonance frequency (cf. Figure 5-7 Page 156), taking into account the variability seen in the SH responses this correlated well with the observed experimental data, however, it did not provide the enhancement of the resonance frequency difference hoped for as a function of adhesion. While there were a number of hypotheses which could explain the difference in response to try and elucidate the differences with a greater physical underpinning computational modelling was turned to.

7.2.2 **Modelling and parameter fitting**

The parameterization of the theoretical models can have large implications on the quality of the data that they are capable of outputting. The increased complexity of many of the current models for MB response come with an increasing number of parameters which require experimental data to be fitted to extract the value of the model parameter. The typical approach to fitting this type of model is to assume that the MB response is limited to small amplitude oscillations which allows for the MB response to be linearized. This reduces the parameters that require fitting to essentially two variables which are purely dependant on an experimentally extracted resonance frequency (cf. Section 2.5.3 Page 64). For models which required values for more variables e.g. the non-linear Marmottant model, these additional parameters tended to be fitted in an ad hoc fashion after the initial linearized fitting. Chapter 6 set out to improve on this fitting technique. By creating simulation data which covered the entire known parameter space of all the variables which required fitting and then finding the parameters of best fit multiple single MB datasets it was hoped that a more accurate fitting could be achieved and that it would also be more sensitive to subtle variations in parameter. The downside to this type of approach is that it is very expensive in terms of computing power and run time.

One of the goals of this section was to observe the effect that the increasing complexity of model had on the extracted model parameters when using the new method for parameter fitting. To do understand this a set of commonly used MB models which follow a natural progression in complexity were examined (cf. Section 6.3 Page 162). The simplest of these models has 2 parameters to fit; a shell elasticity and shell viscosity (this model is analogous to many of the models currently used when small amplitude oscillations are assumed), the next level of complexity introduced non-linearity into the shell elasticity in the form of an upper and lower threshold for a sharp change in elasticity to simulate a MB at the extremes of an oscillation. The last model examined brought in an extra variable which represented the effect of a nearby elastic boundary. This model was also the most applicable in terms of trying to match the experimental data from Chapters 4 and 5 and hence the ultimate goal of the modelling section was to examine the effect of adhesion in terms of the parameters derived from this model, to the authors knowledge this is the first attempt at parameterising this model with single MB acoustic data. The parameters extracted for all three model variations showed general good agreement with previously reported examples and also successfully observed hypothesised rate dependent shell effects such as strain-softening elasticity and shear-thinning viscosity. For the more complex two models there appeared to be strong links between the buckling radius and breakup surface tension with MB resonance which are

not typically accounted for in previous characterisation studies. Both these parameters are shown to strongly affect the non-linear behaviour of the MB.

Evaluating the interdependence of the fitted parameters suggested that unique solutions to the parameter fitting were more likely to be achieved when the data being used comes from a MB near resonance. This could be attributed to the presence of more harmonic content in the signal which provides more data to fit to. It also suggests that for this type of characterisation a multi-frequency examination should be undertaken to collect more data of MBs at their resonance frequency however with the testing rig and procedure in its current form this was not a viable option (cf. Section 3.5.5. Page 106). Away from the resonance region the variability in derived parameters is significantly increased and consequently would not give a robust estimate of the MB properties.

Comparison of the adherent to non-adherent fitted parameters showed a large degree of overlap in parameter values. Given that the fundamental response was broadly similar (cf. Section 4.4.2 Page 126) and that as mentioned in the preceding paragraph that it is only at resonance that one can expect tight fitting of the parameters this is not unduly surprising. There was one stand out region where statistical difference was achieved and that was in the shell elasticity at the point that resonance was seen to move in the 2^{nd} harmonic data. At this point the adherent MBs were shown to have an elevated elasticity. An increase in elasticity is known to have to effect of increasing the resonance frequency however a caveat must be inserted here that due to the high variability in the received responses not too much confidence should be put in this result until the issue of variability between MBs can be resolved.

7.3 Future Directions

7.3.1 Signal variability

The main factor which made these experiments and subsequent fitting difficult to achieve was that of signal variability. Throughout the entire experimental phase of this thesis, even with extremely conservative methods of MB isolation and consistency in experimental calibration and methods, the amount of variation observed in the received signals meant that heavy data smoothing data to be applied to extract trend lines. To give an example of the variation observed between similar sized MBs in all three experimental chapter instances can be found with >10 dB of scattering power can be seen for nearly identical sized MBs (cf. Figure 3-7 Page 102, Figure 4-6 Page 127 and Figure 5-4 Page 151 for examples of this). The fact that it was present in Chapter 3 which utilised commercially available MBs suggests that there is something about the MB manufacture in general which leads to this variability. SonoVue (as used in Chapter 3) and the in house produced MBs used in the remainder of the experimental work are produced by the agitation of a solution containing the shell material in the presence of the encapsulated gas. A recent study [258] used fluorescence lifetime imaging as a probe to track the shell viscosity in situ in individual MBs generated by this technique. This study showed that not only is there significant variation in the shell thicknesses between MBs but also extreme heterogeneity in the viscosity values between MBs but also between different areas of the same MB. One could reasonably expect that the shell elasticity could follow a similar pattern, in fact there is already data to suggest that is the case by the formation of domain structures of different lipid phases [84].

It has been quoted from a number of authors that increased sensitivity for molecular imaging could be obtained by limiting the size distribution of MBs which are used [211], [212]. To that end a number of groups have recently been focussing on the development of monodisperse populations of MBs via their manufacture on microfluidic devices [214]–[216], [257]. Using such methods one of the key variables in predicting MB would become controllable and more importantly easily tailored to suit the imaging need. Microfluidics have also been shown to create much more consistent shell thicknesses with a consistent amount of encapsulation medium present on each MB. One would assume that this would also control the range of possible values that parameters such as shell elasticity and viscosity could have in the population at large. Indeed if precise enough control could be taken over these parameters then one could also hope that control could also be exerted over parameters such as the buckling radius and breakup surface tension, both of which are known to be functions of the lipid packing on the MB surface. The current issue with microfluidics is the

attainable production rate meaning that only low numbers on MB can be produced. For single bubble imaging this is not an issue and therefore should be an area of focus for future single MB characterisation studies.

7.3.2 **Experimental testing**

One of the pieces of information which would have been useful to have during the course of experiments would have been the MB radius between pulses, this would have greatly aided the stability characterisation and would have allowed for parameter fitting to be reliably conducted for every pulse in the pulse sequence. In the current setup this was not possible due to the issue with interference (cf. Section 3.4.4 Page 96). If the rig could be redesigned so that clutter was not an issue then inter pulse imagery could be a viable option. In addition if this were achieved then multiple frequency excitation could also be used on each MB greatly increasing the available data to be used in subsequent fitting. Such an increase in the available datasets would also increase the statistical power placed behind any conclusions drawn as was shown to be an issue in Section 4.4.2 (page 126)

There is obviously also a lot of scope for exploration in terms of the current parameter space. This present study has not attempted to experimentally investigate the effects of changing parameters such as the boundary material properties; this could be useful in the validation of the Doinikov elastic wall model and be of significant importance when the characterisation is applied to in vivo situation. Similarly the current binding mechanism is essentially one of the strongest binding affinities available for purposes such as this. Real binding mechanisms would a) not typically have such high affinities or binding strengths and b) would contain multiple ligand – receptor pairs for complementary binding. Both of these could have an effect on any observed response. All these suggestions however would be of little use if control over the variability of MBs cannot be achieved.

7.3.3 **Modelling and Simulation**

The modelling technique of fitting the entire parameter space to the response from individual MBs was seen to be effective in the convergence to model parameters similar to those of previously reported findings where differing modelling and fitting techniques were employed. With increases in computing power the expense and time required to perform this fitting, will continue to decrease which will allow for the handling of much larger datasets and more finely spaced parameters to be fitted. Furthermore the use of increasingly realistic models, i.e. models which better map the rheological behaviour of the MB encapsulation, will inevitably require more powerful computing. If this is coupled with the ability to control MB variability then this technique should prove valuable in detecting very subtle changes in MB response and shell characteristics.

The models used in this thesis are currently some of the most widely used, however, they are not the most complex of those available and as such do not account for all the types of rheological shell behaviour expected. As a consequence not only do these models, when parameterised, exhibit material properties that are size dependant but the range of extracted values can cover orders of magnitude, for example the dilatational viscosity as shown in this thesis and previously in literature [128], [136]. The use of some of the more advanced models i.e. ones that incorporate heavily non-linear shell parameters for both elasticity and viscosity can overcome some of these issues and make allowances for strain softening and shear thinning behaviour [126], [134], [135] and hence could provide deeper insights into the MB dynamics. Again however, without much tighter control over the MB properties in the first place to achieve less variable experimental datasets there would be little point in attempting this.

7.4 Conclusion

This thesis has explored the effects of adhesion on the dynamics acoustic response of MBs. The effect of functionalization of MB for targeting purposes was seen not to affect MB response in the regimes examined. Adhesion was seen to subtly increase the resonance frequency of the MB, this was only observed weakly in the 2nd harmonic frequency range but with far greater confidence in the resonance dependant stability of MB. This observed difference suggests that adhesion plays a small role in determining MB dynamics, by understanding and maximising the differences caused by adhesion it could prove possible to develop imaging strategies to discretize adherent MBs from their non-adherent counterparts based on their acoustic content, the caveat to this is that at the magnitude observed in this thesis this would not be possible. Significant improvements would have to be made for there to be any viability in this for use as an imaging strategy.

A new method for the parameterisation of theoretical models was presented, this method was able to parameterise the shell behaviour in a manner consistent with current thought and also display hypothesised behaviour such as rate dependent shell parameters. The modelling of the effect of adherence also suggested that shell elasticity may increase in the region of resonance for adherent MBs bringing about the observed increase in resonance frequency however due to the noise and variability of the experimental data this is not confirmed.

8 References

[1] a S. K. Dzik-Jurasz, “Molecular imaging in vivo: an introduction,” *Br. J. Radiol.*, vol. 76, no. suppl_2, pp. S98–S109, Dec. 2003.

[2] T. Quillard and P. Libby, “Molecular imaging of atherosclerosis for improving diagnostic and therapeutic development.,” *Circ. Res.*, vol. 111, no. 2, pp. 231–44, Jul. 2012.

[3] M. F. Kircher, H. Hricak, and S. M. Larson, “Molecular imaging for personalized cancer care.,” *Mol. Oncol.*, vol. 6, no. 2, pp. 182–95, Apr. 2012.

[4] L. Fass, “Imaging and cancer: a review.,” *Mol. Oncol.*, vol. 2, no. 2, pp. 115–52, Aug. 2008.

[5] Q. Meng and Z. Li, “Molecular imaging probes for diagnosis and therapy evaluation of breast cancer.,” *Int. J. Biomed. Imaging*, vol. 2013, p. 230487, Jan. 2013.

[6] A. Nordberg, “Molecular imaging in Alzheimer’s disease: new perspectives on biomarkers for early diagnosis and drug development.,” *Alzheimers. Res. Ther.*, vol. 3, no. 6, p. 34, Jan. 2011.

[7] M. O’Donnell, E. R. McVeigh, H. W. Strauss, A. Tanaka, B. E. Bouma, G. J. Tearney, M. A. Guttman, and E. V Garcia, “Multimodality cardiovascular molecular imaging technology.,” *J. Nucl. Med.*, vol. 51 Suppl 1, no. Supplement_1, p. 38S–50S, May 2010.

[8] N. Tahara, A. Tahara, A. Honda, Y. Nitta, N. Kodama, S.-I. Yamagishi, and T. Imaizumi, “Molecular imaging of vascular inflammation.,” *Curr. Pharm. Des.*, Jun. 2013.

[9] W. Cai and X. Chen, “Multimodality molecular imaging of tumor angiogenesis.,” *J. Nucl. Med.*, vol. 49 Suppl 2, no. Suppl_2, p. 113S–28S, Jun. 2008.

[10] F. S. Villanueva, R. J. Jankowski, S. Klibanov, M. L. Pina, S. M. Alber, S. C. Watkins, G. H. Brandenburger, and W. R. Wagner, “Microbubbles targeted to intercellular adhesion molecule-1 bind to activated coronary artery endothelial cells.,” *Circulation*, vol. 98, no. 1, pp. 1–5, Jul. 1998.

[11] K. Ferrara, R. Pollard, and M. Borden, “Ultrasound microbubble contrast agents: fundamentals and application to gene and drug delivery.,” *Annu. Rev. Biomed. Eng.*, vol. 9, pp. 415–47, Jan. 2007.

[12] W. G. Pitt, G. a Husseini, and B. J. Staples, “Ultrasonic drug delivery--a general review.,” *Expert Opin. Drug Deliv.*, vol. 1, no. 1, pp. 37–56, Nov. 2004.

[13] N. Delhi, “Review Article A Review on Basic Concept of Drug Targeting and Drug Carrier System drug targeting,” vol. 2, no. 1, pp. 130–136, 2013.

[14] G. Bao, S. Mitragotri, and S. Tong, “Multifunctional nanoparticles for drug delivery and molecular imaging.,” *Annu. Rev. Biomed. Eng.*, vol. 15, pp. 253–82, Jan. 2013.

[15] S. Bhaskar, F. Tian, T. Stoeger, W. Kreyling, J. M. de la Fuente, V. Grazú, P. Borm, G. Estrada, V. Ntziachristos, and D. Razansky, “Multifunctional Nanocarriers for diagnostics, drug delivery

and targeted treatment across blood-brain barrier: perspectives on tracking and neuroimaging.," *Part. Fibre Toxicol.*, vol. 7, p. 3, Jan. 2010.

[16] J. K. Willmann, N. van Bruggen, L. M. Dinkelborg, and S. S. Gambhir, "Molecular imaging in drug development.," *Nat. Rev. Drug Discov.*, vol. 7, no. 7, pp. 591–607, Jul. 2008.

[17] B.-C. Ahn, "Applications of molecular imaging in drug discovery and development process.," *Curr. Pharm. Biotechnol.*, vol. 12, no. 4, pp. 459–68, Apr. 2011.

[18] R. Weissleder, "Molecular Imaging 1," 2000.

[19] M. a Pysz, S. S. Gambhir, and J. K. Willmann, "Molecular imaging: current status and emerging strategies.," *Clin. Radiol.*, vol. 65, no. 7, pp. 500–16, Jul. 2010.

[20] M. E. Phelps, "Positron emission tomography provides molecular imaging of biological processes.," *Proc. Natl. Acad. Sci. U. S. A.*, vol. 97, no. 16, pp. 9226–33, Aug. 2000.

[21] P. M. Matthews, E. A. Rabiner, J. Passchier, and R. N. Gunn, "Positron emission tomography molecular imaging for drug development.," *Br. J. Clin. Pharmacol.*, vol. 73, no. 2, pp. 175–86, Mar. 2012.

[22] W. Moses, "Fundamental Limits of Spatial Resolution in PET," *Nucl Instrum Methods Phys*, vol. 21, no. supplement 1, 2011.

[23] J. U. Harrer, L. Mayfrank, M. Mull, and C. Klötzsch, "Second harmonic imaging: a new ultrasound technique to assess human brain tumour perfusion.," *J. Neurol. Neurosurg. Psychiatry*, vol. 74, no. 3, pp. 333–8, Mar. 2003.

[24] T. R. Porter and F. Xie, "Myocardial perfusion imaging with contrast ultrasound.," *JACC. Cardiovasc. Imaging*, vol. 3, no. 2, pp. 176–87, Mar. 2010.

[25] N. Frulio and H. Trillaud, "Ultrasound elastography in liver.," *Diagn. Interv. Imaging*, vol. 94, no. 5, pp. 515–34, May 2013.

[26] I. A. Gheonea, Z. Stoica, and S. Bondari, "Differential diagnosis of breast lesions using ultrasound elastography.," *Indian J. Radiol. Imaging*, vol. 21, no. 4, pp. 301–5, Oct. 2011.

[27] W.-J. Moon, S. L. Jung, J. H. Lee, D. G. Na, J.-H. Baek, Y. H. Lee, J. Kim, H. S. Kim, J. S. Byun, and D. H. Lee, "Benign and malignant thyroid nodules: US differentiation--multicenter retrospective study.," *Radiology*, vol. 247, no. 3, pp. 762–70, Jun. 2008.

[28] M. Mitterberger, W. Horninger, F. Aigner, G. M. Pinggera, I. Steppan, P. Rehder, and F. Frauscher, "Ultrasound of the prostate.," *Cancer Imaging*, vol. 10, pp. 40–8, Jan. 2010.

[29] P. Rausch, K. Nowels, and R. B. . J. Jeffrey, "Ultrasonographically guided thyroid biopsy: a review with emphasis on technique," *J. Ultrasound Med.*, vol. 20, no. 1, pp. 79–85, Jan. 2001.

[30] R. Gramiak, P. M. Shah, and D. H. Kramer, "Ultrasound cardiography: contrast studies in anatomy and function.," *Radiology*, vol. 92, no. 5, pp. 939–48, Apr. 1969.

[31] A. L. Klibanov, *Contrast Agents II*, vol. 222. Berlin, Heidelberg: Springer Berlin Heidelberg, 2002, pp. 73 – 106.

[32] S. H. Bloch, R. E. Short, K. W. Ferrara, and E. R. Wisner, "The effect of size on the acoustic response of polymer-shelled contrast agents.," *Ultrasound Med. Biol.*, vol. 31, no. 3, pp. 439–44, Mar. 2005.

[33] M. a Borden, D. E. Kruse, C. F. Caskey, S. Zhao, P. a Dayton, and K. W. Ferrara, "Influence of lipid shell physicochemical properties on ultrasound-induced microbubble destruction.," *IEEE Trans. Ultrason. Ferroelectr. Freq. Control*, vol. 52, no. 11, pp. 1992–2002, Nov. 2005.

[34] M. J. Hasik, D. H. Kim, L. E. Howle, D. Needham, and D. P. Prush, "Evaluation of synthetic phospholipid ultrasound contrast agents," *Ultrasonics*, vol. 40, no. 9, pp. 973–982, Nov. 2002.

[35] A. L. Klibanov, "Microbubble Contrast Agents," vol. 41, no. 3, pp. 354–362, 2006.

[36] V. Sboros, S. D. Pye, C. a Macdonald, J. Gomatam, C. M. Moran, and W. N. McDicken, "Absolute measurement of ultrasonic backscatter from single microbubbles.," *Ultrasound Med. Biol.*, vol. 31, no. 8, pp. 1063–72, Aug. 2005.

[37] J. R. Lindner, "Molecular imaging with contrast ultrasound and targeted microbubbles.," *J. Nucl. Cardiol.*, vol. 11, no. 2, pp. 215–21, 2004.

[38] S. Zhao, D. E. Kruse, K. W. Ferrara, and P. a Dayton, "Selective imaging of adherent targeted ultrasound contrast agents.," *Phys. Med. Biol.*, vol. 52, no. 8, pp. 2055–72, Apr. 2007.

[39] B. Dollet, S. M. van der Meer, V. Garbin, N. de Jong, D. Lohse, and M. Versluis, "Nonspherical oscillations of ultrasound contrast agent microbubbles.," *Ultrasound Med. Biol.*, vol. 34, no. 9, pp. 1465–73, Sep. 2008.

[40] H. J. Vos, B. Dollet, M. Versluis, and N. de Jong, "Nonspherical shape oscillations of coated microbubbles in contact with a wall.," *Ultrasound Med. Biol.*, vol. 37, no. 6, pp. 935–48, Jun. 2011.

[41] A. A. Doinikov, S. Zhao, and P. A. Dayton, "Modeling of the acoustic response from contrast agent microbubbles near a rigid wall," *Ultrasonics*, vol. 49, no. 2, pp. 195–201, 2009.

[42] A. a Doinikov, L. Aired, and A. Bouakaz, "Dynamics of a contrast agent microbubble attached to an elastic wall.," *IEEE Trans. Med. Imaging*, vol. 31, no. 3, pp. 654–62, Mar. 2012.

[43] M. Overvelde, V. Garbin, B. Dollet, N. de Jong, D. Lohse, and M. Versluis, "Dynamics of coated microbubbles adherent to a wall.," *Ultrasound Med. Biol.*, vol. 37, no. 9, pp. 1500–8, Sep. 2011.

[44] J. Casey, C. Sennoga, H. Mulvana, J. V Hajnal, M.-X. Tang, and R. J. Eckersley, "Single Bubble Acoustic Characterization and Stability Measurement of Adherent Microbubbles," *Ultrasound Med. Biol.*, vol. 39, no. 5, pp. 903–914, 2013.

[45] H. Azhari, *Basics of Biomedical Ultrasound for Engineers*. Hoboken, NJ, USA: John Wiley & Sons, Inc., 2010.

[46] B. Ihnatsenka and A. P. Boezaart, “Ultrasound: Basic understanding and learning the language.,” *Int. J. Shoulder Surg.*, vol. 4, no. 3, pp. 55–62, Jul. 2010.

[47] a. Ng and J. Swanevelder, “Resolution in ultrasound imaging,” *Contin. Educ. Anaesthesia, Crit. Care Pain*, vol. 11, no. 5, pp. 186–192, Aug. 2011.

[48] T. D. Mast, “Empirical relationships between acoustic parameters in human soft tissues,” vol. 7853, no. November 2000, pp. 37–42, 2013.

[49] S. A. Goss, R. L. Johnston, and F. Dunn, “Comprehensive compilation of empirical ultrasonic properties tissues Hueter which MHz , of loss,” *J. Acoust. Soc. Am.*, vol. 64, no. 2, 1978.

[50] L. Jakevi and A. Dem, “Ultrasound attenuation dependence on air temperature in closed chambers,” vol. 63, no. 1, pp. 18–22, 2008.

[51] P. A. Dayton and T. O. Matsunaga, “Ultrasound-mediated therapies using oil and perfluorocarbon-filled nanodroplets,” *Drug Dev. Res.*, vol. 67, no. 1, pp. 42–46, Jan. 2006.

[52] P. S. Sheeran, S. Luois, P. a Dayton, and T. O. Matsunaga, “Formulation and acoustic studies of a new phase-shift agent for diagnostic and therapeutic ultrasound.,” *Langmuir*, vol. 27, no. 17, pp. 10412–20, Sep. 2011.

[53] R. Battino and H. L. Clever, “The Solubility of Gases in Liquids,” *Chem. Rev.*, vol. 66, no. 4, pp. 395–463, Aug. 1966.

[54] T. G. Leighton, *The Acoustic Bubble*. Academic Press, 1997, p. 613.

[55] K. Sarkar, A. Katiyar, and P. Jain, “Growth and dissolution of an encapsulated contrast microbubble: effects of encapsulation permeability.,” *Ultrasound Med. Biol.*, vol. 35, no. 8, pp. 1385–96, Aug. 2009.

[56] H. Mulvana, E. Stride, M.-X. Tang, J. V Hajnal, and R. J. Eckersley, “The influence of gas saturation on microbubble stability.,” *Ultrasound Med. Biol.*, vol. 38, no. 6, pp. 1097–100, Jun. 2012.

[57] J. J. Kwan and M. A. Borden, “Microbubble dissolution in a multigas environment.,” *Langmuir*, vol. 26, no. 9, pp. 6542–8, May 2010.

[58] Lantheus Medical Imaging, *Definity Data for Clinicians*, no. 2. 2001, pp. 2–4.

[59] A. Katiyar and K. Sarkar, “Stability analysis of an encapsulated microbubble against gas diffusion.,” *J. Colloid Interface Sci.*, vol. 343, no. 1, pp. 42–7, Mar. 2010.

[60] P. B. Duncan and D. Needham, “Test of the Epstein-Plesset model for gas microparticle dissolution in aqueous media: effect of surface tension and gas undersaturation in solution.,” *Langmuir*, vol. 20, no. 7, pp. 2567–78, Mar. 2004.

[61] M. A. Borden and M. L. Longo, “Oxygen Permeability of Fully Condensed Lipid Monolayers,” *J. Phys. Chem. B*, vol. 108, no. 19, pp. 6009–6016, May 2004.

[62] H. Hellebust, C. Christiansen, and T. Skotland, “Biochemical characterization of air-filled albumin microspheres.,” *Biotechnol. Appl. Biochem.*, vol. 18 (Pt 3), pp. 227–37, Dec. 1993.

[63] C. Christiansen, H. Kryvi, P. C. Sontum, and T. Skotland, “Physical and biochemical characterization of Albunex, a new ultrasound contrast agent consisting of air-filled albumin microspheres suspended in a solution of human albumin.,” *Biotechnol. Appl. Biochem.*, vol. 19 (Pt 3), pp. 307–20, Jun. 1994.

[64] C. C. Chen, “Engineering Microbubbles with the Buried-Ligand Architecture for Targeted Ultrasound Molecular Imaging,” 2011.

[65] S. Podell, C. Burrascano, M. Gaal, B. Golec, J. Maniquis, and P. Mehlhaff, “Physical and biochemical stability of Optison, an injectable ultrasound contrast agent.,” *Biotechnol. Appl. Biochem.*, vol. 30 (Pt 3), pp. 213–23, Dec. 1999.

[66] G. Korpanty, P. A. Grayburn, R. V Shohet, and R. A. Brekken, “Targeting vascular endothelium with avidin microbubbles.,” *Ultrasound Med. Biol.*, vol. 31, no. 9, pp. 1279–83, Sep. 2005.

[67] R. J. Browning, H. Mulvana, M.-X. Tang, J. V Hajnal, D. J. Wells, and R. J. Eckersley, “Effect of albumin and dextrose concentration on ultrasound and microbubble mediated gene transfection in vivo.,” *Ultrasound Med. Biol.*, vol. 38, no. 6, pp. 1067–77, Jun. 2012.

[68] P. A. Frenkel, S. Chen, T. Thai, R. V Shohet, and P. A. Grayburn, “DNA-loaded albumin microbubbles enhance ultrasound-mediated transfection in vitro.,” *Ultrasound Med. Biol.*, vol. 28, no. 6, pp. 817–22, Jun. 2002.

[69] N. H. Notter and Z. Wang, “Pulmonary Surfactant: Physical Chemistry, Physiology and Replacement: Reviews in Chemical Engineering,” *Reviews in Chemical Engineering*, 1997. [Online]. Available: http://www.degruyter.com/view/j/revce.1997.13.4/revce.1997.13.4.1/revce.1997.13.4.1.xml. [Accessed: 15-Aug-2013].

[70] a a Spector and M. a Yorek, “Membrane lipid composition and cellular function.,” *J. Lipid Res.*, vol. 26, no. 9, pp. 1015–35, Sep. 1985.

[71] S. Singhal, C. C. Moser, and M. A. Wheatley, “Surfactant-stabilized microbubbles as ultrasound contrast agents: stability study of Span 60 and Tween 80 mixtures using a Langmuir trough,” *Langmuir*, vol. 9, no. 9, pp. 2426–2429, Sep. 1993.

[72] A. H. Myrset, H. B. Fjerdingstad, R. Bendiksen, B. E. Arbo, R. M. Bjerke, J. H. Johansen, M. A. Kulseth, and R. Skurtveit, “Design and characterization of targeted ultrasound microbubbles for diagnostic use.,” *Ultrasound Med. Biol.*, vol. 37, no. 1, pp. 136–50, Jan. 2011.

[73] D. H. Kim, A. L. Klibanov, and D. Needham, “The Influence of Tiered Layers of Surface-Grafted Poly(ethylene glycol) on Receptor−Ligand-Mediated Adhesion between Phospholipid Monolayer-Stabilized Microbubbles and Coated Glass Beads,” *Langmuir*, vol. 16, no. 6, pp. 2808–2817, Mar. 2000.

[74] H. Wijkstra, M. Smeenge, J. Rosette, S. Pochon, I. Tardy-Cantalupi, and F. Tranquart, “Targeted microbubble prostate cancer imaging with BR55,” *17th Eur. Symp. Ultrasound Contrast Imaging*, 2012.

[75] S. H. Bloch, M. Wan, P. A. Dayton, and K. W. Ferrara, “Optical observation of lipid- and polymer-shelled ultrasound microbubble contrast agents,” *Appl. Phys. Lett.*, vol. 84, no. 4, p. 631, Jan. 2004.

[76] F. Cavalieri, A. El Hamassi, E. Chiessi, and G. Paradossi, “Stable polymeric microballoons as multifunctional device for biomedical uses: synthesis and characterization.,” *Langmuir*, vol. 21, no. 19, pp. 8758–64, Sep. 2005.

[77] S. Kim, R. E. Jacobs, and S. H. White, “Preparation of multilamellar vesicles of defined size-distribution by solvent-spherule evaporation,” *Biochim. Biophys. Acta - Biomembr.*, vol. 812, no. 3, pp. 793–801, 1985.

[78] F. Grunfeld, “A modular multifunctional Langmuir–Blodgett trough,” *Rev. Sci. Instrum.*, vol. 64, no. 2, p. 548, Feb. 1993.

[79] V. Knecht, M. Müller, M. Bonn, S.-J. Marrink, and A. E. Mark, “Simulation studies of pore and domain formation in a phospholipid monolayer.,” *J. Chem. Phys.*, vol. 122, no. 2, p. 024704, Jan. 2005.

[80] S. Lee, D. H. Kim, and D. Needham, “Equilibrium and Dynamic Interfacial Tension Measurements at Microscopic Interfaces Using a Micropipet Technique. 2. Dynamics of Phospholipid Monolayer Formation and Equilibrium Tensions at the Water−Air Interface,” *Langmuir*, vol. 17, no. 18, pp. 5544–5550, Aug. 2001.

[81] R. R. Sauers, “Steric Attraction: The Far Side,” *J. Chem. Educ.*, vol. 73, no. 2, p. 114, Feb. 1996.

[82] G. Pu, M. a Borden, and M. L. Longo, “Collapse and shedding transitions in binary lipid monolayers coating microbubbles.,” *Langmuir*, vol. 22, no. 7, pp. 2993–9, Mar. 2006.

[83] M. a Borden, G. Pu, G. J. Runner, and M. L. Longo, “Surface phase behavior and microstructure of lipid/PEG-emulsifier monolayer-coated microbubbles.,” *Colloids Surf. B. Biointerfaces*, vol. 35, no. 3–4, pp. 209–23, Jun. 2004.

[84] M. a Borden, G. V Martinez, J. Ricker, N. Tsvetkova, M. Longo, R. J. Gillies, P. a Dayton, and K. W. Ferrara, “Lateral phase separation in lipid-coated microbubbles.,” *Langmuir*, vol. 22, no. 9, pp. 4291–7, Apr. 2006.

[85] M. A. Borden and M. L. Longo, “Dissolution Behavior of Lipid Monolayer-Coated , Air-Filled Microbubbles : Effect of Lipid Hydrophobic Chain Length,” no. 22, pp. 9225–9233, 2002.

[86] G. van Meer, D. R. Voelker, and G. W. Feigenson, “Membrane lipids: where they are and how they behave.,” *Nat. Rev. Mol. Cell Biol.*, vol. 9, no. 2, pp. 112–24, Mar. 2008.

[87] J. M. Seddon, “Structure of the inverted hexagonal (HII) phase, and non-lamellar phase transitions of lipids,” *Biochim. Biophys. Acta - Rev. Biomembr.*, vol. 1031, no. 1, pp. 1–69, 1990.

[88] N. G. Fisher, J. P. Christiansen, A. Klibanov, R. P. Taylor, S. Kaul, and J. R. Lindner, “Influence of microbubble surface charge on capillary transit and myocardial contrast enhancement.,” *J. Am. Coll. Cardiol.*, vol. 40, no. 4, pp. 811–9, Aug. 2002.

[89] T. Yu and W. Yeung, “Membrane Surface Charge and Lipid Signaling in Phagocytosis,” University of Toronto, 2008.

[90] I. Lentacker, B. G. De Geest, R. E. Vandenbroucke, L. Peeters, J. Demeester, S. C. De Smedt, and N. N. Sanders, “Ultrasound-responsive polymer-coated microbubbles that bind and protect DNA.,” *Langmuir*, vol. 22, no. 17, pp. 7273–8, Aug. 2006.

[91] M. L. Immordino, F. Dosio, and L. Cattel, “Stealth liposomes: review of the basic science, rationale, and clinical applications, existing and potential.,” *Int. J. Nanomedicine*, vol. 1, no. 3, pp. 297–315, Jan. 2006.

[92] D. Needham and D. Kim, “PEG-covered lipid surfaces: bilayers and monolayers.,” *Colloids Surf. B. Biointerfaces*, vol. 18, no. 3–4, pp. 183–195, Oct. 2000.

[93] C. Luna, K. Stroka, H. Bermudez, and H. Aranda-Espinoza, “Thermodynamics of monolayers formed by mixtures of phosphatidylcholine/phosphatidylserine,” *Colloids Surf B Biointerfaces*, vol. 85, no. 2, pp. 293–300, 2011.

[94] R. Gullapalli, M. Demirel, and P. Butler, “Molecular dynamics simulations of DiI-C18 bilayer (3) in a DPPC lipid,” *Phys Chem*, vol. 10, no. 24, pp. 3548–3560, 2012.

[95] B. a Kaufmann, C. L. Carr, J. T. Belcik, A. Xie, Q. Yue, S. Chadderdon, E. S. Caplan, J. Khangura, S. Bullens, S. Bunting, and J. R. Lindner, “Molecular imaging of the initial inflammatory response in atherosclerosis: implications for early detection of disease.,” *Arterioscler. Thromb. Vasc. Biol.*, vol. 30, no. 1, pp. 54–9, Jan. 2010.

[96] A. L. Klibanov, “Preparation of targeted microbubbles: ultrasound contrast agents for molecular imaging.,” *Med. Biol. Eng. Comput.*, vol. 47, no. 8, pp. 875–82, Aug. 2009.

[97] J. R. Lindner, P. a. Dayton, M. P. Coggins, K. Ley, J. Song, K. Ferrara, and S. Kaul, “Noninvasive Imaging of Inflammation by Ultrasound Detection of Phagocytosed Microbubbles,” *Circulation*, vol. 102, no. 5, pp. 531–538, Aug. 2000.

[98] J. R. Lindner, “Assessment of inflammation with contrast ultrasound.,” *Prog. Cardiovasc. Dis.*, vol. 44, no. 2, pp. 111–20, 2001.

[99] K. Chen, O. Gheysens, M. Rodriguez-porcel, A. M. Lutz, and I. Y. Chen, “ORIGINAL RESEARCH US Imaging of Tumor Angiogenesis with Microbubbles Targeted to Vascular Endothelial Purpose : Methods : Results : Conclusion :,” vol. 246, no. 2, 2008.

[100] D. R. Anderson, J. M. Tsutsui, F. Xie, S. J. Radio, and T. R. Porter, “The role of complement in the adherence of microbubbles to dysfunctional arterial endothelium and atherosclerotic plaque.,” *Cardiovasc. Res.*, vol. 73, no. 3, pp. 597–606, Feb. 2007.

[101] F. Xie, J. M. Tsutsui, J. Lof, E. C. Unger, J. Johanning, W. C. Culp, T. Matsunaga, and T. R. Porter, “Effectiveness of lipid microbubbles and ultrasound in declotting thrombosis.,” *Ultrasound Med. Biol.*, vol. 31, no. 7, pp. 979–85, Jul. 2005.

[102] A. M. Takalkar, A. L. Klibanov, J. J. Rychak, J. R. Lindner, and K. Ley, “Binding and detachment dynamics of microbubbles targeted to P-selectin under controlled shear flow.,” *J. Control. Release*, vol. 96, no. 3, pp. 473–82, May 2004.

[103] J. J. Rychak, J. R. Lindner, K. Ley, and A. L. Klibanov, “Deformable gas-filled microbubbles targeted to P-selectin.,” *J. Control. Release*, vol. 114, no. 3, pp. 288–99, Sep. 2006.

[104] A. S. Ham, A. L. Klibanov, and M. B. Lawrence, “Action at a distance: lengthening adhesion bonds with poly(ethylene glycol) spacers enhances mechanically stressed affinity for improved vascular targeting of microparticles.,” *Langmuir*, vol. 25, no. 17, pp. 10038–44, Sep. 2009.

[105] J. Loughran, C. Sennoga, R. J Eckersley, and M.-X. Tang, “Effect of ultrasound on adherent microbubble contrast agents.,” *Phys. Med. Biol.*, vol. 57, no. 21, pp. 6999–7014, Nov. 2012.

[106] C. C. Chen and M. a Borden, “The role of poly(ethylene glycol) brush architecture in complement activation on targeted microbubble surfaces.,” *Biomaterials*, vol. 32, no. 27, pp. 6579–87, Sep. 2011.

[107] J. Wu, H. Leong-poi, J. Bin, L. Yang, Y. Liao, Y. Liu, J. Cai, J. Xie, and Y. Liu, “Effi cacy of Contrast-enhanced US and Magnetic Microbubbles Targeted to Vascular Cell Adhesion Molecule – 1 for Molecular Imaging of Purpose : Methods : Results :,” vol. 260, no. 2, pp. 463–471, 2011.

[108] J. J. Rychak, A. L. Klibanov, and J. A. Hossack, “Acoustic radiation force enhances targeted delivery of ultrasound contrast microbubbles: in vitro verification.,” *IEEE Trans. Ultrason. Ferroelectr. Freq. Control*, vol. 52, no. 3, pp. 421–33, Mar. 2005.

[109] P. Dayton, A. Klibanov, G. Brandenburger, and K. Ferrara, “Acoustic radiation force in vivo: a mechanism to assist targeting of microbubbles.,” *Ultrasound Med. Biol.*, vol. 25, no. 8, pp. 1195–201, Oct. 1999.

[110] D. A. Sutherland, “Models of Ultrasound Contrast Agents,” no. October, 2008.

[111] A. Doinikov and A. Bouakaz, “Review of shell models for contrast agent microbubbles,” *IEEE transactions on ultrasonics, ferroelectrics, and frequency control*, vol. 58, no. 5, pp. 981–993, 2011.

[112] A. Doinikov and A. Bouakaz, “Review of Shell Models for Contrast Agent,” *IEEE transactions on ultrasonics, ferroelectrics, and frequency control*, vol. 58, no. 5, pp. 981–993, 2011.

[113] S. M. van der Meer, B. Dollet, M. M. Voormolen, C. T. Chin, A. Bouakaz, N. de Jong, M. Versluis, D. Lohse, and S. M. Van Der Meer, “Microbubble spectroscopy of ultrasound contrast agents,” *J. Acoust. Soc. Am.*, vol. 121, no. 1, p. 648, 2007.

[114] K. Sarkar, W. T. Shi, D. Chatterjee, and F. Forsberg, “Characterization of ultrasound contrast microbubbles using in vitro experiments and viscous and viscoelastic interface models for encapsulation,” *J. Acoust. Soc. Am.*, vol. 118, no. 1, p. 539, Jul. 2005.

[115] A. Prosperetti, “The thermal behaviour of oscillating gas bubbles,” *J. Fluid Mech.*, vol. 222, pp. 587–616, Jan. 1991.

[116] R. I. Nigmatulin, N. S. Khabeev, and F. B. Nagiev, “Dynamics, heat and mass transfer of vapour-gas bubbles in a liquid,” *Int. J. Heat Mass Transf.*, vol. 24, no. 6, pp. 1033–1044, Jun. 1981.

[117] J. B. Keller, “Bubble oscillations of large amplitude,” *J. Acoust. Soc. Am.*, vol. 68, no. 2, p. 628, Aug. 1980.

[118] C. Herring and U. S. O. of S. R. and Development, *Theory of the Pulsations of the Gas Bubble Produced by an Underwater Explosion*. Columbia Univ., Division of National Defense Research, 1941, p. 168.

[119] A. Prosperetti and A. Lezzi, “Bubble dynamics in a compressible liquid. Part 1. First-order theory,” *J. Fluid Mech.*, vol. 168, no. -1, p. 457, Apr. 2006.

[120] M. Minnaert, “XVI. On musical air-bubbles and the sounds of running water,” *Philos. Mag. Ser. 7*, vol. 16, no. 104, pp. 235–248, 1933.

[121] C. C. Church, “The effects of an elastic solid surface layer on the radial pulsations of gas bubbles,” *J. Acoust. Soc. Am.*, vol. 97, no. 3, p. 1510, Mar. 1995.

[122] L. Hoff, P. Sontum, and J. Hovem, “Oscillations of polymeric microbubbles: effect of the encapsulating shell,” *J. Acoust. Soc. Am.*, vol. 107, no. 4, pp. 2272–80, Apr. 2000.

[123] N. de Jong and L. Hoff, “Ultrasound scattering properties of Albunex microspheres,” *Ultrasonics*, vol. 31, no. 3, pp. 175–181, May 1993.

[124] N. de Jong, L. Hoff, T. Skotland, and N. Bom, “Absorption and scatter of encapsulated gas filled microspheres: Theoretical considerations and some measurements,” *Ultrasonics*, vol. 30, no. 2, pp. 95–103, Mar. 1992.

[125] D. Chatterjee and K. Sarkar, “A Newtonian rheological model for the interface of microbubble contrast agents.,” *Ultrasound Med. Biol.*, vol. 29, no. 12, pp. 1749 – 57, 2004.

[126] Q. Li, T. J. Matula, J. Tu, X. Guo, and D. Zhang, “Modeling complicated rheological behaviors in encapsulating shells of lipid-coated microbubbles accounting for nonlinear changes of both shell viscosity and elasticity.,” *Phys. Med. Biol.*, vol. 58, no. 4, pp. 985–98, Feb. 2013.

[127] K. Chetty, E. Stride, C. a Sennoga, J. V Hajnal, and R. J. Eckersley, “High-speed optical observations and simulation results of SonoVue microbubbles at low-pressure insonation.,” *IEEE Trans. Ultrason. Ferroelectr. Freq. Control*, vol. 55, no. 6, pp. 1333–42, Jan. 2008.

[128] J. Tu, J. Guan, Y. Qiu, and T. J. Matula, “Estimating the shell parameters of SonoVue microbubbles using light scattering.,” *J. Acoust. Soc. Am.*, vol. 126, no. 6, pp. 2954–62, Dec. 2009.

[129] P. Marmottant, S. van der Meer, M. Emmer, M. Versluis, N. de Jong, S. Hilgenfeldt, and D. Lohse, “A model for large amplitude oscillations of coated bubbles accounting for buckling and rupture,” *J. Acoust. Soc. Am.*, vol. 118, no. 6, p. 3499, Dec. 2005.

[130] L. Pocivavsek, S. L. Frey, K. Krishan, K. Gavrilov, P. Ruchala, A. J. Waring, F. J. Walther, M. Dennin, T. a Witten, and K. Y. C. Lee, “Lateral stress relaxation and collapse in lipid monolayers.,” *Soft Matter*, vol. 4, pp. 2019–2029, Jan. 2008.

[131] P. Marmottant, A. Bouakaz, N. de Jong, and C. Quilliet, “Buckling resistance of solid shell bubbles under ultrasound.,” *J. Acoust. Soc. Am.*, vol. 129, no. 3, pp. 1231–9, Mar. 2011.

[132] M. Overvelde, V. Garbin, J. Sijl, B. Dollet, N. de Jong, D. Lohse, and M. Versluis, “Nonlinear shell behavior of phospholipid-coated microbubbles.,” *Ultrasound Med. Biol.*, vol. 36, no. 12, pp. 2080–92, Dec. 2010.

[133] J. Sijl, M. Overvelde, B. Dollet, V. Garbin, N. de Jong, D. Lohse, and M. Versluis, “‘Compression-only’ behavior: a second-order nonlinear response of ultrasound contrast agent microbubbles.,” *J. Acoust. Soc. Am.*, vol. 129, no. 4, pp. 1729–39, Apr. 2011.

[134] S. Paul, A. Katiyar, K. Sarkar, D. Chatterjee, W. T. Shi, and F. Forsberg, “Material characterization of the encapsulation of an ultrasound contrast microbubble and its subharmonic response: strain-softening interfacial elasticity model.,” *J. Acoust. Soc. Am.*, vol. 127, no. 6, pp. 3846–57, Jun. 2010.

[135] A. A. Doinikov, J. F. Haac, and P. a Dayton, “Modeling of nonlinear viscous stress in encapsulating shells of lipid-coated contrast agent microbubbles.,” *Ultrasonics*, vol. 49, no. 2, pp. 269–75, Feb. 2009.

[136] J. Tu, J. E. Swalwell, D. Giraud, W. Cui, W. Chen, and T. J. Matula, “Microbubble sizing and shell characterization using flow cytometry.,” *IEEE Trans. Ultrason. Ferroelectr. Freq. Control*, vol. 58, no. 5, pp. 955–63, May 2011.

[137] M. Emmer, A. van Wamel, D. E. Goertz, and N. de Jong, “The onset of microbubble vibration.,” *Ultrasound Med. Biol.*, vol. 33, no. 6, pp. 941–9, Jun. 2007.

[138] Y. Zong, M. Wan, S. Wang, and G. Zhang, “Optimal design and experimental investigation of surfactant encapsulated microbubbles.,” *Ultrasonics*, vol. 44 Suppl 1, no. null, pp. e119–22, Dec. 2006.

[139] A. Katiyar, K. Sarkar, and P. Jain, “Effects of encapsulation elasticity on the stability of an encapsulated microbubble.,” *J. Colloid Interface Sci.*, vol. 336, no. 2, pp. 519–25, Aug. 2009.

[140] J. Gorce, M. Arditi, and M. Schneider, “Influence of Bubble Size Distribution on the Echogenicity of,” *Invest. Radiol.*, vol. 35, no. 11, pp. 661–671, 2000.

[141] L. H. Per, C. Sontum, B. Hoff, N. Imaging, and T. Nomegian, “Acoustic Properties of Shell-encapsulated, Gas-filled Ultrasound Contrast Agents.,” *IEEE Ultrason. Symp.*, pp. 1441–1444, 1996.

[142] Y. Gong, M. Cabodi, and T. Porter, “Pressure-dependent resonance frequency for lipid-coated microbubbles at low acoustic pressures,” *2010 IEEE Int. Ultrason. Symp.*, pp. 1932–1935, Oct. 2010.

[143] M.-X. Tang and R. J. Eckersley, “Frequency and pressure dependent attenuation and scattering by microbubbles.,” *Ultrasound Med. Biol.*, vol. 33, no. 1, pp. 164–8, Jan. 2007.

[144] S. M. Van Der Meer, M. Versluis, and D. Lohse, “The resonance frequency of SonoVue ™ as observed by high-speed optical imaging,” vol. 00, no. c, pp. 343–345, 2004.

[145] J. Sijl, H. J. Vos, T. Rozendal, N. de Jong, D. Lohse, and M. Versluis, “Combined optical and acoustical detection of single microbubble dynamics.,” *J. Acoust. Soc. Am.*, vol. 130, no. 5, pp. 3271–81, Nov. 2011.

[146] T. Faez, M. Emmer, M. Docter, J. Sijl, M. Versluis, and N. de Jong, “Characterizing the subharmonic response of phospholipid-coated microbubbles for carotid imaging.,” *Ultrasound Med. Biol.*, vol. 37, no. 6, pp. 958–70, Jun. 2011.

[147] K. E. Morgan, J. S. Allen, P. a Dayton, J. E. Chomas, a L. Klibaov, and K. W. Ferrara, “Experimental and theoretical evaluation of microbubble behavior: effect of transmitted phase and bubble size.,” *IEEE Trans. Ultrason. Ferroelectr. Freq. Control*, vol. 47, no. 6, pp. 1494–509, Jan. 2000.

[148] K. Chetty, C. A. Sennoga, J. V. Hajnal, R. J. Eckersley, and E. Stride, “P1F-4 High Speed Optical Observations and Simulation Results of Lipid Based Microbubbles at Low Insonation Pressures,” in *2006 IEEE Ultrasonics Symposium*, 2006, pp. 1354–1357.

[149] S. O. Nielsen, C. F. Lopez, P. B. Moore, J. C. Shelley, and M. L. Klein, “Molecular Dynamics Investigations of Lipid Langmuir Monolayers Using a Coarse-Grain Model,” *J. Phys. Chem. B*, vol. 107, no. 50, pp. 13911–13917, Dec. 2003.

[150] H. J. Vos, B. Dollet, J. G. Bosch, M. Versluis, and N. de Jong, “Nonspherical vibrations of microbubbles in contact with a wall: a pilot study at low mechanical index.,” *Ultrasound Med. Biol.*, vol. 34, no. 4, pp. 685–8, Apr. 2008.

[151] M. Strasberg, “The Pulsation Frequency of Nonspherical Gas Bubbles in Liquids,” *J. Acoust. Soc. Am.*, vol. 25, no. 3, p. 536, May 1953.

[152] D. Faccio, G. Tamošauskas, E. Rubino, J. Darginavičius, D. G. Papazoglou, S. Tzortzakis, a. Couairon, and a. Dubietis, “Cavitation dynamics and directional microbubble ejection induced by intense femtosecond laser pulses in liquids,” *Phys. Rev. E*, vol. 86, no. 3, p. 036304, Sep. 2012.

[153] S. W. Ohl, E. Klaseboer, and B. C. Khoo, “The dynamics of a non-equilibrium bubble near bio-materials.,” *Phys. Med. Biol.*, vol. 54, no. 20, pp. 6313–36, Oct. 2009.

[154] H. Chen, A. A. Brayman, W. Kreider, M. R. Bailey, and T. J. Matula, “Observations of translation and jetting of ultrasound-activated microbubbles in mesenteric microvessels.,” *Ultrasound Med. Biol.*, vol. 37, no. 12, pp. 2139–48, Dec. 2011.

[155] J. E. Blue, “Resonance of a Bubble on an Infinite Rigid Boundary,” *J. Acoust. Soc. Am.*, vol. 41, no. 2, p. 369, Feb. 1967.

[156] P. A. Shima and Y. Tomita, “The behavior of a spherical bubble near a solid wall in a compressible liquid,” *Ingenieur-Archiv*, vol. 51, no. 3–4, pp. 243–255, May 1981.

[157] K. Sato, Y. Tomita, and A. Shima, “Numerical analysis of a gas bubble near a rigid boundary in an oscillatory pressure field,” *J. Acoust. Soc. Am.*, vol. 95, no. 5, p. 2416, May 1994.

[158] A. A. Doinikov, L. Aired, and A. Bouakaz, “Acoustic scattering from a contrast agent microbubble near an elastic wall of finite thickness.,” *Phys. Med. Biol.*, vol. 56, no. 21, pp. 6951–67, Nov. 2011.

[159] A. V. Patil, P. Reynolds, D. Milner, and J. A. Hossack, “A 3D nonlinear FEA model for simulation of microbubble behavior,” in *2008 IEEE Ultrasonics Symposium*, 2008, pp. 985–988.

[160] S. Martynov, E. Kostson, N. Saffari, and E. Stride, “Forced vibrations of a bubble in a liquid-filled elastic vessel.,” *J. Acoust. Soc. Am.*, vol. 130, no. 5, pp. 2700–8, Nov. 2011.

[161] S. Martynov, E. Stride, and N. Saffari, “The natural frequencies of microbubble oscillation in elastic vessels.,” *J. Acoust. Soc. Am.*, vol. 126, no. 6, pp. 2963–72, Dec. 2009.

[162] E. Sassaroli and K. Hynynen, “Resonance frequency of microbubbles in small blood vessels: a numerical study.,” *Phys. Med. Biol.*, vol. 50, no. 22, pp. 5293–305, Nov. 2005.

[163] V. Garbin, D. Cojoc, E. Ferrari, E. Di Fabrizio, M. L. J. Overvelde, S. M. van der Meer, N. de Jong, D. Lohse, and M. Versluis, “Changes in microbubble dynamics near a boundary revealed by combined optical micromanipulation and high-speed imaging,” *Appl. Phys. Lett.*, vol. 90, no. 11, p. 114103, Mar. 2007.

[164] B. Helfield, B. Y. Leung, and D. E. Goertz, “The effect of boundary proximity on the fundamental and subharmonic emissions from individual microbubbles at higher frequencies,” in *Proceedings of Meetings on Acoustics*, 2013, vol. 19, no. 1, pp. 075096–075096.

[165] V. F. K. Bjerknes, *Fields of Force*. New York, Col. Univ. Press, 1906.

[166] P. O. Fort and A. A. Doinikov, *Bjerknes forces and translational bubble dynamics*, vol. 661, no. 2. 2005.

[167] P. Dayton, A. Goode, K. Morgan, S. Klibanov, G. Brandenburger, and K. Ferrara, “Action of microbubbles when insonified: experimental evidence,” in *1996 IEEE Ultrasonics Symposium. Proceedings*, vol. 2, pp. 1131–1134.

[168] M. A. Borden, M. R. Sarantos, S. M. Stieger, S. I. Simon, W. Katherine, and P. A. Dayton, “Ultrasound Radiation Force Modulates Ligand Availability on Targeted Contrast Agents,” vol. 5, no. 3, pp. 139–147, 2006.

[169] S. Zhao, M. Borden, S. H. Bloch, D. Kruse, K. W. Ferrara, and P. A. Dayton, “Radiation-force assisted targeting facilitates ultrasonic molecular imaging.,” *Mol. Imaging*, vol. 3, no. 3, pp. 135–48, Jul. 2004.

[170] P. Palanchon, P. Tortoli, A. Bouakaz, M. Versluis, and N. de Jong, “Optical observations of acoustical radiation force effects on individual air bubbles.,” *IEEE Trans. Ultrason. Ferroelectr. Freq. Control*, vol. 52, no. 1, pp. 104–10, Jan. 2005.

[171] M. Versluis, V. Garbin, B. Dollet, L. Van Wijngaarden, N. De Jong, D. Lohse, L. Wijngaarden, and N. Jong, “Secondary Bjerknes forces between ultrasound contrast agent microbubbles,” *J. Acoust. Soc. Am.*, vol. 123, no. 5, p. 3111, 2008.

[172] R. Mettin, I. Akhatov, U. Parlitz, C. Ohl, and W. Lauterborn, “Bjerknes forces between small cavitation bubbles in a strong acoustic field,” *Phys. Rev. E*, vol. 56, no. 3, pp. 2924–2931, Sep. 1997.

[173] Y. Zhang, X. Guo, D. Zhang, and X. Gong, “Evaluation of the effects of secondary radiation Force on aggregation of ultrasound contrast agents,” no. August, pp. 2–5, 2010.

[174] V. Garbin, M. Overvelde, B. Dollet, N. de Jong, D. Lohse, and M. Versluis, “Unbinding of targeted ultrasound contrast agent microbubbles by secondary acoustic forces.,” *Phys. Med. Biol.*, vol. 56, no. 19, pp. 6161–77, Oct. 2011.

[175] J. E. E. Chomas, P. Dayton, J. Allen, K. Morgan, and K. W. W. Ferrara, “Mechanisms of contrast agent destruction.,” *IEEE Trans. Ultrason. Ferroelectr. Freq. Control*, vol. 48, no. 1, pp. 232–48, Jan. 2001.

[176] H. Vos, N. de Jong, and P. Tortoli, “Microbubble Characterization Through Acoustically Induced Deflation,” *IEEE Trans. Ultrason. Ferroelectr. Freq. Control*, vol. 57, no. 1, 2010.

[177] J. E. Chomas, P. Dayton, D. May, and K. Ferrara, “Threshold of fragmentation for ultrasonic contrast agents.,” *J. Biomed. Opt.*, vol. 6, no. 2, pp. 141–50, Apr. 2001.

[178] J. E. Chomas, P. A. Dayton, D. May, J. Allen, A. Klibanov, and K. Ferrara, “Optical observation of contrast agent destruction,” *Appl. Phys. Lett.*, vol. 77, no. 7, p. 1056, Aug. 2000.

[179] C. Yeh, S. Su, and W. Chen, “Destruction Threshold Parameters Estimation for Ultrasonic Contrast Agents,” vol. 25, no. 4, pp. 159–163, 2005.

[180] S. Dicker, M. Mleczko, G. Schmitz, and S. P. Wrenn, “Determination of microbubble cavitation threshold pressure as function of shell chemistry,” *Bubble Sci. Eng. Technol.*, vol. 2, no. 2, pp. 55–64, Dec. 2010.

[181] R. V Shohet and P. a Grayburn, “Potential bioeffects of ultrasonic destruction of microbubble contrast agents.,” *J. Am. Coll. Cardiol.*, vol. 47, no. 7, pp. 1469–70, Apr. 2006.

[182] H. Chen, A. a. Brayman, T. J. Matula, and A. P. Evan, “Vascular damage by ultrasound-activated microbubble induced vessel invagination,” *2010 IEEE Int. Ultrason. Symp.*, pp. 678–681, Oct. 2010.

[183] P. Li, W. F. Armstrong, and D. L. Miller, “Impact of myocardial contrast echocardiography on vascular permeability: comparison of three different contrast agents.,” *Ultrasound Med. Biol.*, vol. 30, no. 1, pp. 83–91, Jan. 2004.

[184] D. M. Skyba, R. J. Price, a. Z. Linka, T. C. Skalak, and S. Kaul, “Direct In Vivo Visualization of Intravascular Destruction of Microbubbles by Ultrasound and its Local Effects on Tissue,” *Circulation*, vol. 98, no. 4, pp. 290–293, Jul. 1998.

[185] J. L. Tlaxca, C. R. Anderson, A. L. Klibanov, B. Lowrey, J. a Hossack, J. S. Alexander, M. B. Lawrence, and J. J. Rychak, “Analysis of in vitro transfection by sonoporation using cationic and neutral microbubbles.,” *Ultrasound Med. Biol.*, vol. 36, no. 11, pp. 1907–18, Nov. 2010.

[186] K. Wei, A. R. Jayaweera, S. Firoozan, A. Linka, D. M. Skyba, and S. Kaul, “Quantification of Myocardial Blood Flow With Ultrasound-Induced Destruction of Microbubbles Administered as a Constant Venous Infusion,” *Circulation*, vol. 97, no. 5, pp. 473–483, Feb. 1998.

[187] P. Frinking, A. Bouakaz, J. Kirkhorn, F. J. Cate, N. Jong, F. J. ten Cate, and N. de Jong, “Ultrasound Contrast Imaging : Current and New Potential Methods,” *Ultrasound Med. Biol.*, vol. 26, no. 6, pp. 965–975, 2000.

[188] W. T. Shi and F. Forsberg, “Ultrasonic Characterisation of the Non-linear Properties of Contrast Microbubbles” *Ultrasound Med. Biol.*, vol. 26, no. 1, pp. 93–104, 2000.

[189] P. N. Burns, D. Hope Simpson, and M. A. Averkiou, “Nonlinear imaging,” *Ultrasound Med. Biol.*, vol. 26, pp. S19–S22, May 2000.

[190] R. A. Heckemann, D. O. Cosgrove, M. J. K. Blomley, R. J. Eckersley, C. J. Harvey, and Y. Mine, “Liver Lesions : Intermittent US Can Increase Conspicuity with Microbubble Contrast Material — Early Experience 1,” 2000.

[191] M. Hasegawa, Y. Saiki, H. Kayano, and T. Katagiri, “[Assessment of myocardial perfusion with second harmonic imaging--using intravenous injection of Albunex and Levovist].,” *Nihon Rinsho.*, vol. 56, no. 4, pp. 903–8, Apr. 1998.

[192] P. N. Burns, S. R. Wilson, and D. H. Simpson, “Pulse inversion imaging of liver blood flow: improved method for characterizing focal masses with microbubble contrast.,” *Invest. Radiol.*, vol. 35, no. 1, pp. 58–71, Jan. 2000.

[193] J. Kirkhorn, S. Frigstadt, and H. Top, “Comparison of Pulse Inversion and Second Harmonic for Ultrasound Contrast Imaging,” pp. 1897–1901, 2000.

[194] M.-X. Tang, N. Kamiyama, and R. J. Eckersley, “Effects of nonlinear propagation in ultrasound contrast agent imaging.,” *Ultrasound Med. Biol.*, vol. 36, no. 3, pp. 459–66, Mar. 2010.

[195] G. Brock-Fisher, M. Poland, and P. Rafter, “Means for increasing sensitivity in non-linear ultrasound imaging systems,” 26-Nov-1996.

[196] R. J. Eckersley, C. T. Chin, and P. N. Burns, “Optimising phase and amplitude modulation schemes for imaging microbubble contrast agents at low acoustic power.,” *Ultrasound Med. Biol.*, vol. 31, no. 2, pp. 213–9, Feb. 2005.

[197] J. Powers, P. Burns, and J. Souquet, “Imaging instrumentation for ultrasound contrast agents,” in in *Advances in Echo Imaging Using Contrast Enhancement SE - 8*, N. Nanda, R. Schlief, and B. Goldberg, Eds. Springer Netherlands, 1997, pp. 139–170.

[198] A. Katiyar and K. Sarkar, “Excitation threshold for subharmonic generation from contrast microbubbles.,” *J. Acoust. Soc. Am.*, vol. 130, no. 5, pp. 3137–47, Nov. 2011.

[199] J. Sijl, B. Dollet, M. Overvelde, V. Garbin, T. Rozendal, N. Jong, D. Lohse, M. Versluis, and N. de Jong, “Subharmonic behavior of phospholipid-coated ultrasound contrast agent microbubbles.,” *J. Acoust. Soc. Am.*, vol. 128, no. 5, pp. 3239–52, Nov. 2010.

[200] B. L. Helfield, E. Cherin, F. S. Foster, and D. E. Goertz, “Investigating the subharmonic response of individual phospholipid encapsulated microbubbles at high frequencies: a comparative study of five agents.,” *Ultrasound Med. Biol.*, vol. 38, no. 5, pp. 846–63, May 2012.

[201] P. J. a Frinking, J. Brochot, and M. Arditi, “Subharmonic scattering of phospholipid-shell microbubbles at low acoustic pressure amplitudes.,” *IEEE Trans. Ultrason. Ferroelectr. Freq. Control*, vol. 57, no. 8, pp. 1762–71, Aug. 2010.

[202] R. Gessner and P. a Dayton, “Advances in molecular imaging with ultrasound.,” *Mol. Imaging*, vol. 9, no. 3, pp. 117–27, Jun. 2010.

[203] A Needles, O. Couture, and F. S. Foster, “A method for differentiating targeted microbubbles in real time using subharmonic micro-ultrasound and interframe filtering.,” *Ultrasound Med. Biol.*, vol. 35, no. 9, pp. 1564–73, Sep. 2009.

[204] X. Hu, H. Zheng, D. E. Kruse, P. Sutcliffe, D. N. Stephens, and K. W. Ferrara, “A sensitive TLRH targeted imaging technique for ultrasonic molecular imaging.,” *IEEE Trans. Ultrason. Ferroelectr. Freq. Control*, vol. 57, no. 2, pp. 305–16, Jan. 2010.

[205] S. M. van der Meer, N. de Jong, M. Versluis, D. Lohse, V. Garbin, E. Ferrari, D. Cojoc, E. Di Fabrizio, M. L. J. Overvelde, S. M. Meer, N. Jong, and E. Fabrizio, “1F-2 Optical Trapping of Ultrasound Contrast Agent Microbubbles: Study of the Bubble-Wall and Bubble-Bubble Interaction in Ultrasound,” in *2006 IEEE Ultrasonics Symposium*, 2006, pp. 513–516.

[206] M. Emmer, H. J. Vos, D. E. Goertz, A. van Wamel, M. Versluis, and N. de Jong, “Pressure-dependent attenuation and scattering of phospholipid-coated microbubbles at low acoustic pressures.,” *Ultrasound Med. Biol.*, vol. 35, no. 1, pp. 102–11, Jan. 2009.

[207] D. E. Goertz, N. Jong, A. F. W. Steen, N. de Jong, and A. F. W. van der Steen, “Attenuation and size distribution measurements of Definity and manipulated Definity populations.,” *Ultrasound Med. Biol.*, vol. 33, no. 9, pp. 1376–88, Sep. 2007.

[208] N. de Jong, L. Hoff, and N. Jong, “Ultrasound scattering properties of Albunex microspheres,” *Ultrasonics*, vol. 31, no. 3, pp. 175–181, May 1993.

[209] J. M. Gorce, M. Arditi, and M. Schneider, “Influence of bubble size distribution on the echogenicity of ultrasound contrast agents: a study of SonoVue.,” *Invest. Radiol.*, vol. 35, no. 11, pp. 661–71, Nov. 2000.

[210] A. Prosperetti, “Application of the subharmonic threshold to the measurement of the damping of oscillating gas bubbles,” *J. Acoust. Soc. Am.*, vol. 61, no. 1, p. 11, Jan. 1977.

[211] E. Talu, K. Hettiarachchi, S. Zhao, R. L. Powell, A. P. Lee, L. Longo, and P. A. Dayton, “Possible Method for Improving Sensitivity in Molecular Imaging,” vol. 6, no. 6, pp. 384–392, 2008.

[212] J. E. Streeter, R. Gessner, I. Miles, and P. A. Dayton, “Improving Sensitivity in Ultrasound Molecular Imaging by Tailoring Contrast Agent Size Distribution : In Vivo Studies,” vol. 9, no. 2, pp. 87–95, 2010.

[213] J. A. Feshitan, C. C. Chen, J. J. Kwan, and M. A. Borden, “Microbubble size isolation by differential centrifugation.,” *J. Colloid Interface Sci.*, vol. 329, no. 2, pp. 316–24, Jan. 2009.

[214] J. H. Xu, S. W. Li, G. G. Chen, and G. S. Luo, “Formation of monodisperse microbubbles in a microfluidic device,” *AIChE J.*, vol. 52, no. 6, pp. 2254–2259, Jun. 2006.

[215] P. a. Dayton, H. Nguyen, E. Talu, K. Hettiarachchi, a. P. Lee, R. L. Powell, and M. L. Longo, “P2A-8 Lipid-Stabilized Monodisperse Microbubbles Produced by Flow Focusing for Use as Ultrasound Contrast Agents,” *2006 IEEE Ultrason. Symp.*, pp. 1568–1571, 2006.

[216] B. J. Schmidt, I. Sousa, A. a van Beek, and M. R. Böhmer, “Adhesion and ultrasound-induced delivery from monodisperse microbubbles in a parallel plate flow cell.,” *J. Control. Release*, vol. 131, no. 1, pp. 19–26, Oct. 2008.

[217] E. Stride and M. Edirisinghe, “Novel microbubble preparation technologies,” *Soft Matter*, vol. 4, no. 12, p. 2350, 2008.

[218] C. C. Chen, S. Wu, J. D. Finan, B. M. Iii, and E. E. Konofagou, “An Experimental Study on the Apparent Stiffness of Size-Isolated Microbubbles Used for Blood-Brain Barrier Opening Applications,” pp. 1–4.

[219] V. Sboros, E. Glynos, S. D. Pye, C. M. Moran, M. Butler, J. Ross, R. Short, W. N. McDicken, and V. Koutsos, “Nanointerrogation of ultrasonic contrast agent microbubbles using atomic force microscopy.,” *Ultrasound Med. Biol.*, vol. 32, no. 4, pp. 579–85, Apr. 2006.

[220] V. Sboros, E. Glynos, S. D. Pye, C. M. Moran, M. Butler, J. a Ross, W. N. McDicken, and V. Koutsos, “Nanomechanical probing of microbubbles using the atomic force microscope.,” *Ultrasonics*, vol. 46, no. 4, pp. 349–54, Nov. 2007.

[221] R. H. Abou-Saleh, S. a Peyman, K. Critchley, S. D. Evans, and N. H. Thomson, “Nanomechanics of lipid encapsulated microbubbles with functional coatings.,” *Langmuir*, vol. 29, no. 12, pp. 4096–103, Mar. 2013.

[222] E. C. Gelderblom, H. J. Vos, F. Mastik, T. Faez, Y. Luan, T. J. A. Kokhuis, A. F. W. van der Steen, D. Lohse, N. de Jong, and M. Versluis, “Brandaris 128 ultra-high-speed imaging facility: 10 years of operation, updates, and enhanced features.,” *Rev. Sci. Instrum.*, vol. 83, no. 10, p. 103706, Oct. 2012.

[223] D. H. Thomas, M. Butler, T. Anderson, M. Emmer, H. Vos, M. Borden, E. Stride, N. Jong, V. Sboros, and N. de Jong, “The ‘quasi-stable’ lipid shelled microbubble in response to consecutive ultrasound pulses,” *Appl. Phys. Lett.*, vol. 101, no. 7, p. 071601, Aug. 2012.

[224] D. H. Thomas, M. Butler, N. Pelekasis, T. Anderson, E. Stride, and V. Sboros, “The acoustic signature of decaying resonant phospholipid microbubbles.,” *Phys. Med. Biol.*, vol. 58, no. 3, pp. 589–99, Feb. 2013.

[225] V. Garbin, B. Dollet, M. Overvelde, D. Cojoc, E. Di Fabrizio, L. van Wijngaarden, A. Prosperetti, N. de Jong, D. Lohse, and M. Versluis, “History force on coated microbubbles propelled by ultrasound,” *Phys. Fluids*, vol. 21, no. 9, p. 092003, 2009.

[226] T. Faez, I. Skachkov, M. Versluis, K. Kooiman, and N. de Jong, “In vivo characterization of ultrasound contrast agents: microbubble spectroscopy in a chicken embryo.,” *Ultrasound Med. Biol.*, vol. 38, no. 9, pp. 1608–17, Sep. 2012.

[227] H. J. B. Couto, D. G. Nunes, R. Neumann, and S. C. a. França, “Micro-bubble size distribution measurements by laser diffraction technique,” *Miner. Eng.*, vol. 22, no. 4, pp. 330–335, Mar. 2009.

[228] G. R. R. Lockwood, D. H. Turnball, D. A. Christopher, and F. S. Foster, “Beyond 30 MHz [applications of high-frequency ultrasound imaging],” *IEEE Eng. Med. Biol. Mag.*, vol. 15, no. 6, pp. 60–71, 1996.

[229] W. T. Shi, F. Forsberg, and E. C. Everbach, “Acoustic Detection of Microbubble Destruction in Gaseous Contrast Agents,” pp. 2189–2190, 1990.

[230] J. Guan, T. J. Matula, and M. Averkiou, “Imaging the destruction of individual ultrasound contrast microbubbles with diagnostic ultrasound,” *Acoust. Res. Lett. Online*, vol. 5, no. 4, p. 165, 2004.

[231] V. Sboros, C. M. Moran, S. D. Pye, and W. N. McDicken, “The behaviour of individual contrast agent microbubbles,” *Ultrasound Med. Biol.*, vol. 29, no. 5, pp. 687–694, May 2003.

[232] J. Sijl, E. Gaud, P. J. A. Frinking, M. Arditi, N. de Jong, D. Lohse, and M. Versluis, “Acoustic characterization of single ultrasound contrast agent microbubbles.,” *J. Acoust. Soc. Am.*, vol. 124, no. 6, pp. 4091–7, Dec. 2008.

[233] N. Dejong, “Mechanical Index,” *Eur. J. Echocardiogr.*, vol. 3, no. 1, pp. 73–74, Mar. 2002.

[234] G. Threlfall, H. J. Wu, K. Li, B. Aldham, J. Scoble, I. D. Sutalo, A. Raicevic, L. Pontes-Braz, B. Lee, M. Schneider-Kolsky, A. Ooi, G. Coia, and R. Manasseh, “Quantitative guidelines for the prediction of ultrasound contrast agent destruction during injection.,” *Ultrasound Med. Biol.*, vol. 39, no. 10, pp. 1838–47, Oct. 2013.

[235] J. R. Lindner, “Microbubbles in medical imaging: current applications and future directions.,” *Nat. Rev. Drug Discov.*, vol. 3, no. 6, pp. 527–32, Jun. 2004.

[236] “Molecular ultrasound imaging using microbubble contrast agents,” *Front. Biosci.*, vol. 12, pp. 5124–5142, 2007.

[237] S. a Moestue, I. S. Gribbestad, and R. Hansen, “Intravascular targets for molecular contrast-enhanced ultrasound imaging.,” *Int. J. Mol. Sci.*, vol. 13, no. 6, pp. 6679–97, Jan. 2012.

[238] C. F. Caskey, D. E. Kruse, P. a. Dayton, T. K. Kitano, and K. W. Ferrara, “Microbubble oscillation in tubes with diameters of 12, 25, and 195 microns,” *Appl. Phys. Lett.*, vol. 88, no. 3, p. 033902, 2006.

[239] C. F. Caskey, S. M. Stieger, S. Qin, P. a Dayton, and K. W. Ferrara, “Direct observations of ultrasound microbubble contrast agent interaction with the microvessel wall.,” *J. Acoust. Soc. Am.*, vol. 122, no. 2, pp. 1191–200, Aug. 2007.

[240] N. de Jong, H. J. Vos, P. Tortoli, and F. Guidi, “P1F-5 Simultaneous Optical and Acoustical Observation of Microbubbles Behaviour,” *2006 IEEE Ultrason. Symp.*, pp. 1358–1361, 2006.

[241] D. E. Kruse, P. a. Dayton, K. W. Ferrara, and S. Zhao, “1F-5 Detection of Echoes from Adherent Targeted Microbubbles,” *2006 IEEE Ultrason. Symp.*, pp. 525–528, 2006.

[242] H. J. Vos, N. de Jong, R. Mori, J. Viti, F. Guidi, P. Tortoli, and J. Sijl, “Ultrafast framing optical and acoustical recording of nonlinearly oscillating microbubbles,” *2009 IEEE Int. Ultrason. Symp.*, pp. 1817–1820, Sep. 2009.

[243] F. Guidi, P. Tortoli, H. J. Vos, and N. De Jong, “Simultaneous Optical and Acoustical Observation of Microbubbles Behaviour,” pp. 1358–1361, 2006.

[244] C. A. Sennoga, J. S. Yeh, J. M. Seddon, S. Nourshargh, R. J. Eckersley, D. O. Haskard, D. O. Cosgrove, and P. Nihoyannopoulos, *Microbulles ciblées pour l'imagerie ultrasonore*. Paris: Springer Paris, 2007, pp. 321–328.

[245] C. a Sennoga, V. Mahue, J. Loughran, J. Casey, J. M. Seddon, M. Tang, and R. J. Eckersley, "On sizing and counting of microbubbles using optical microscopy.," *Ultrasound Med. Biol.*, vol. 36, no. 12, pp. 2093–6, Dec. 2010.

[246] B. Helfield, E. Cherin, S. Foster, D. E. Goertz, and C. Sim, "The Influence of Attachment on the Nonlinear Behaviour of Lipid Encapsulated Microbubbles at High Frequencies," pp. 951–954, 2011.

[247] F. Forsberg, W. T. Shi, and B. B. Goldberg, "Subharmonic imaging of contrast agents.," *Ultrasonics*, vol. 38, no. 1–8, pp. 93–8, Mar. 2000.

[248] T. Faez, G. Renaud, M. Defontaine, S. Calle, and N. de Jong, "Dynamic manipulation of the subharmonic scattering of phospholipid-coated microbubbles.," *Phys. Med. Biol.*, vol. 56, no. 19, pp. 6459–73, Oct. 2011.

[249] A. Katiyar, K. Sarkar, and F. Forsberg, "Modeling subharmonic response from contrast microbubbles as a function of ambient static pressure.," *J. Acoust. Soc. Am.*, vol. 129, no. 4, pp. 2325–35, Apr. 2011.

[250] C. a Macdonald, V. Sboros, J. Gomatam, S. D. Pye, C. M. Moran, and W. Norman McDicken, "A numerical investigation of the resonance of gas-filled microbubbles: resonance dependence on acoustic pressure amplitude.," *Ultrasonics*, vol. 43, no. 2, pp. 113–22, Dec. 2004.

[251] W. T. Shi, F. Forsberg, J. S. Raichlen, L. Needleman, and B. B. Goldberg, "Pressure dependence of subharmonic signals from contrast microbubbles," *Ultrasound in Medicine and Biology*, 1999. [Online]. Available: http://www.sciencedirect.com.iclibezp1.cc.ic.ac.uk/science/article/pii/S030156299800163X?np=y. [Accessed: 05-Jul-2013].

[252] A. Eller, "Generation of Subharmonics of Order One-Half by Bubbles in a Sound Field," *J. Acoust. Soc. Am.*, vol. 46, no. 3B, p. 722, Aug. 1969.

[253] E. Biagi, L. Breschi, E. Vannacci, and L. Masotti, "Subharmonic emissions from microbubbles: effect of the driving pulse shape.," *IEEE Trans. Ultrason. Ferroelectr. Freq. Control*, vol. 53, no. 11, pp. 2174–82, Nov. 2006.

[254] C. O. Adebajo, J. A. Talwalkar, J. J. Poterucha, W. R. Kim, and M. R. Charlton, "Ultrasound-based transient elastography for the detection of hepatic fibrosis in patients with recurrent hepatitis C virus after liver transplantation: a systematic review and meta-analysis.," *Liver Transpl.*, vol. 18, no. 3, pp. 323–31, Mar. 2012.

[255] A. Lorenz, H. Ermert, H. J. Sommerfeld, M. Garcia-Schürmann, T. Senge, and S. Philippou, "[Ultrasound elastography of the prostate. A new technique for tumor detection].," *Ultraschall Med.*, vol. 21, no. 1, pp. 8–15, Feb. 2000.

[256] L. Aired, A. A. Doinikov, A. Bouakaz, U. Inserm, C. Erl, and C. H. U. Bretonneau, "Effect of an elastic wall on the behavior of encapsulated microbubbles," no. April, pp. 1625–1630, 2012.

[257] C. Devendran, P. Rogers, I. A. N. Gralinski, and A. Neild, “Particle Manipulation and Separation in an Open Microfluidic Chamber,” *Proc. 2013 Int. Congr. Ultrason.*, no. Icu, pp. 978–981, 2013.

[258] N. A. Hosny, G. Mohamedi, P. Rademeyer, J. Owen, Y. Wu, M.-X. Tang, R. J. Eckersley, E. Stride, and M. K. Kuimova, “Mapping microbubble viscosity using fluorescence lifetime imaging of molecular rotors.,” *Proc. Natl. Acad. Sci. U. S. A.*, vol. 110, no. 23, pp. 9225–30, Jun. 2013.

[259] Olympus and Panametrics, “Ultrasonic Transducers Technical Notes,” 2006.

[260] M. R. Sprague, E. Chérin, and F. S. Foster, “Function Calibration Method : Application to Microbubble Backscattering Cross-Section Measurements at High Frequency,” vol. 58, no. 6, 2011.

9 Appendix

9.1 Transducer calibration

9.1.1 Beam width

The focal region of the transducers is dependent upon a number of factors such as driving frequency. What this means in practice for constant experimental conditions is that as the driving frequency is increased the area of focus decreases in size in accordance with Equation 9-1 [259]. The caveat of this is that the alignment becomes increasingly more important as higher frequencies are examined.

$$B_{D,axial} = 1.02\frac{F_l\lambda}{T_D}$$

Equation 9-1

$B_{D,axial}$ is the -6dB beam diameter, F_l is the transducer focal length (≈78mm), λ is the wavelength and T_D is the transducer element diameter. At 2 MHz this gives a beam width of approximately 2 mm, reducing to 0.7 mm at 6MHz

To confirm these as values they were also determined experimentally. Briefly, a calibrated hydrophone (HPM1/1 Precision Acoustics, Dorset UK) was positioned at the focus, by sweeping the hydrophone through the acoustic field a picture of the field could be built. The experimental results yielded a beam width of 2.5mm at 2MHz reducing to 1.mm at 6MHz. The larger experimental results could be somewhat expected due to the accuracy of the hydrophone (≈13% at the frequency ranges in question) and the physical size of the hydrophone tip (1mm)

9.1.2 Pressure at focus

The pressure at the focus was calibrated to ensure that the pulse sequence desired could be faithfully reproduced experimentally at the focus. By positioning the same calibrated needle hydrophone as described in Section 9.1.1 at the focus and driving the transducer through a range of voltages and frequencies the pressure at the focus can be determined. The transducer was driven using 10 cycle narrowband pulses at frequencies ranging from 2 – 6 MHz in 0.5 MHz steps and at applied voltages from 0.05 V (the lowest setting available without the addition of signal attenuators)

to 0.5 V (half the dynamic range of the system). The results are presented below in Figure 9-1. Each frequency displays an essentially linear pressure response with increasing applied voltage. Plateaus can be observed for some frequencies at pressures > 350 kPa, this was due to the saturation of the hydrophone at those frequency/pressure combinations. The different gradients observed are due to the transducer sensitivity at different frequencies which needs to be accounted for.

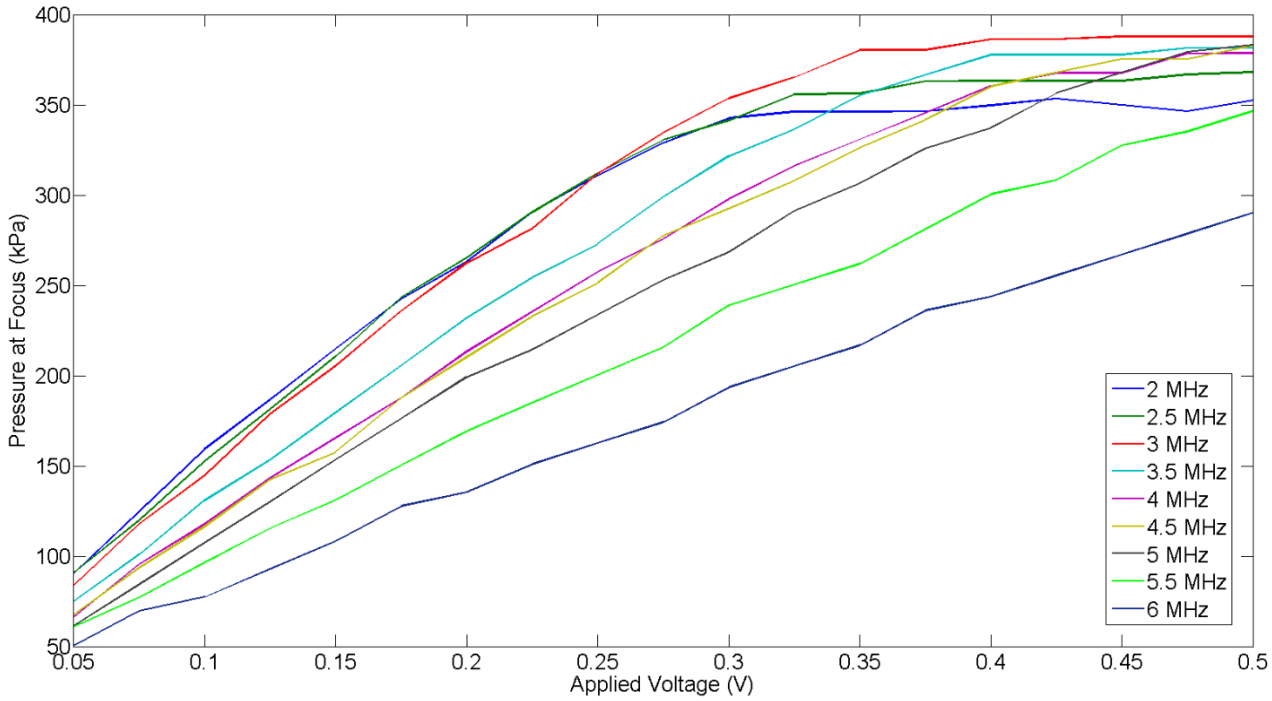

Figure 9-1: Pressure at focus for as a function of applied frequency and voltage.

9.1.3 Frequency Response

Throughout the bandwidth of the transducer the sensitivity of response at different frequencies varies, peak sensitivity is found at the centre frequency. To correct the received signals for the transducer sensitivity the receive transfer function, R(f), needs to be obtained. This is also required to compare experimentally gathered results to simulated data.

The determination of the receive transfer response was conducted following the procedure demonstrated by Sprague et al. [260]. Briefly, this procedure involves taking two measurements. The first is a pulse-echo (PE) measurement taken with a plane reflector of known reflection coefficient ($\Gamma_{reflector}$, Equation 9-3 where Z is the acoustic impedance of the medium (1) and reflector (2), an

aluminium plate was used for these experiments. $\Gamma_{reflector} = 0.843$) placed at the focus of the transducer. The PEs are conducted using narrowband pulses (10 cycles) covering the full bandwidth of the transducer (0.1 – 9 MHz in 0.25 MHz steps for the 3.5 centre frequency transducer used in Chapters 3 and 4; 0.1 – 2 MHz in 0.1 MHz steps for the 1 MHz centre frequency transducer used in Chapter 5), this gives a voltage reading as a function of frequency (V(f)). The second measurement required is the receive pressure at twice the focal distance, this is recorded using a calibrated needle hydrophone (HPM1/1 Precision Acoustics, Dorset UK) and gives the pressure at the face of a virtual transducer ($P_{hydrophone}(f)$). The receive transfer function is then found by Equation 9-2.

$$R(f) = \frac{V(f)}{\Gamma_{reflector} . P_{hydrophone}(f)}$$

Equation 9-2

$$\Gamma_{reflector} = E_R = \frac{Z_2 - Z_1}{Z_2 + Z_1}$$

Equation 9-3

The receive transfer functions for the two receive transducers is shown below Figure 9-2

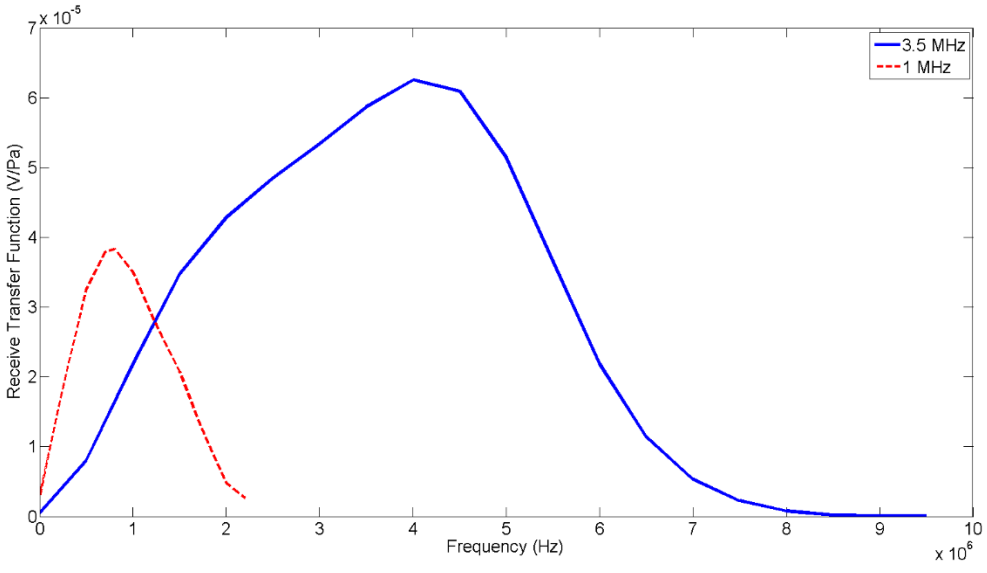

Figure 9-2: Receive transfer functions for the two receive transducers used throughout this thesis. 3.5 MHz centre frequency (Blue solid line) as used in Chapters 3 and 4, 1 MHz centre frequency transducer (Red dashed line) as used in Chapter 5.

9.2 Matlab Code

The following is the MatLab script used for the simulation of MB using 4 different theoretical models as described in Chapter 6. Due to the method of coding there are essentially two parallel streamof simulation; one for the elastic wall model with both types of shell model and the other for the just the two types of shell model.

9.2.1 Simulation launcher and parameter selection

```
function [dat R1 scatp modelsel simconst simvar]=simlauncher4;

% clear all

% frequency, initial radius, distance to wall, elasticity, shell viscosity
% and buckling radius can all be ranges of values. The resultant matrix
% will be a 7 dimensional matrix. The first column is the waveform/power
% spectrum and the next 6 dimensions are the variables above. If the
% Marmottant model is chosen a 6 dimensional matrix will be returned
% because distance to wall is no longer a variable.

% dat is the simulated pulse
% R1 and scatp are the multidimensional array outputs for radius and
% scattered pressure respectively
% modsel is the model type used
% simvar and simconst hold the simulation parameters


[dat n m modelsel simconst simvar] = Modelvariables; % pulse creator and
variable set up

%% Doinikov + Marmottant
if modelsel==1




R1=zeros(m,length(simvar.centfreq),length(simvar.R0),length(simvar.d),lengt
h(simvar.chi),length(simvar.kappa_s),length(simvar.buckling));

scatp=zeros(m,length(simvar.centfreq),length(simvar.R0),length(simvar.d),le
ngth(simvar.chi),length(simvar.kappa_s),length(simvar.buckling));



    for j=1:n-1; % centfrequncy
        for k=1:length(simvar.R0) % Initial Radius
            for l=1:length(simvar.d) % wall distance
                for s=1:length(simvar.chi) % elasticity
                    for b=1:length(simvar.kappa_s) % viscosity
```

```
                        for v=1:length(simvar.buckling) %buckling radius

                            [R1(:,j,k,l,s,b,v) scatp(:,j,k,l,s,b,v)]=...
                                simsetup(dat(:,[1
(j+1)]),simvar.R0(k),simvar.d(l),simvar.buckling(v),...

simvar.chi(s),simvar.kappa_s(b),simconst,modelsel);

                            str=['Elastic wall + marmottant' '   f0='
num2str(simvar.centfreq(j)) '   R0=' num2str(simvar.R0(k))...
                                '   d=' num2str(simvar.d(l)) '   chi='
num2str(simvar.chi(s)) ...
                                '   kappa_s=' num2str(simvar.kappa_s(b)) '
Rb=' num2str(simvar.buckling(v))];
                            disp(str)

                        end
                    end
                end
            end
        end
    end

%% Doinikov + de Jong
elseif modelsel==2




R1=zeros(m,length(simvar.centfreq),length(simvar.R0),length(simvar.d),lengt
h(simvar.chi),length(simvar.kappa_s),length(simvar.buckling));

scatp=zeros(m,length(simvar.centfreq),length(simvar.R0),length(simvar.d),le
ngth(simvar.chi),length(simvar.kappa_s),length(simvar.buckling));



    for j=1:n-1; % centfrequncy
        for k=1:length(simvar.R0) % Initial Radius
            for l=1:length(simvar.d) % wall distance
                for s=1:length(simvar.chi) % elasticity
                    for b=1:length(simvar.kappa_s) % viscosity
                        for v=1:length(simvar.buckling) %buckling radius

                            [R1(:,j,k,l,s,b,v) scatp(:,j,k,l,s,b,v)]=...
                                simsetup(dat(:,[1
(j+1)]),simvar.R0(k),simvar.d(l),simvar.buckling(v)...

,simvar.chi(s),simvar.kappa_s(b),simconst,modelsel);

                            str=['Elastic wall + de Jong' '   f0='
num2str(simvar.centfreq(j)) '   R0=' num2str(simvar.R0(k))...
                                '   d=' num2str(simvar.d(l)) '   chi='
num2str(simvar.chi(s)) ...
                                '   kappa_s=' num2str(simvar.kappa_s(b)) '
Rb=' num2str(simvar.buckling(v))];
                            disp(str)

                        end
                    end
```

```
                end
            end
        end
    end

%% straight Marmottant
elseif modelsel==3
    d=0;

R1=zeros(m,length(simvar.centfreq),length(simvar.R0),length(simvar.chi),len
gth(simvar.kappa_s),length(simvar.buckling));

scatp=zeros(m,length(simvar.centfreq),length(simvar.R0),length(simvar.chi),
length(simvar.kappa_s),length(simvar.buckling));

    for j=1:n-1;
        for k=1:length(simvar.R0)
            for s=1:length(simvar.chi) % elasticity
                for b=1:length(simvar.kappa_s) % viscosity
                    for v=1:length(simvar.buckling) %buckling radius

                        [R1(:,j,k,s,b,v) scatp(:,j,k,s,b,v)]= ...
                            sim_RP_marm(dat(:,[1
j+1]),simvar.R0(k),simvar.buckling(v),simvar.chi(s),simvar.kappa_s(b),simco
nst,modelsel);

                        str=['Marmottant' '   f0='
num2str(simvar.centfreq(j)) '   R0=' num2str(simvar.R0(k)) ...
                            '   chi=' num2str(simvar.chi(s)) '   kappa_s='
num2str(simvar.kappa_s(b)) ...
                            '   Rb=' num2str(simvar.buckling(v))];
                        disp(str)

                    end
                end
            end
        end
    end


%% Straight de Jong
elseif modelsel==4
    d=0;

R1=zeros(m,length(simvar.centfreq),length(simvar.R0),length(simvar.chi),len
gth(simvar.kappa_s),length(simvar.buckling));

scatp=zeros(m,length(simvar.centfreq),length(simvar.R0),length(simvar.chi),
length(simvar.kappa_s),length(simvar.buckling));

    for j=1:n-1;
        for k=1:length(simvar.R0)
            for s=1:length(simvar.chi) % elasticity
                for b=1:length(simvar.kappa_s) % viscosity
                    for v=1:length(simvar.buckling) %buckling radius

                        [R1(:,j,k,s,b,v) scatp(:,j,k,s,b,v)]= ...
                            sim_RP_marm(dat(:,[1
j+1]),simvar.R0(k),simvar.buckling(v),simvar.chi(s),simvar.kappa_s(b),simco
nst,modelsel);
```

```
                        str=['de Jong' '   f0=' num2str(simvar.centfreq(j))
'   R0=' num2str(simvar.R0(k)) ...
                            '   chi=' num2str(simvar.chi(s)) '   kappa_s='
num2str(simvar.kappa_s(b)) ...
                            '   Rb=' num2str(simvar.buckling(v))];
                        disp(str)

                    end
                end
            end
        end
    end



    pspect=0;


end
```

9.2.2 Pulse creation and variable setup

```
function [dat n m modelsel simconst simvar] = Modelvariables;

% Pulse creator and variable/constant selection

% Model selection
liststring={'Elastic Wall + Marmottant','Elastic Wall + De
Jong','Marmottant','De Jong'};

[modelsel,v]=listdlg('PromptString','Select a
model:','SelectionMode','single','ListString',liststring);

if v==0
    disp('Choose a model you fool!')
    return

else
    if v==1

        % Dialogue Box for Constants
        promptc={'Enter Number of Cycles:',...
            'Peak Acoustic Pressure (kPa):','Phase (Multiple of Pi):','Wall
density (kg/m^3):','Wall Poissons Ratio:'...
            ,'Wall Thickness (μm):','Distance to Transducer (m):','Time
step (s):','Tranducer Response Correction (0=No Correction, 1=1MHz,
2=3.5MHz):'...
            ,'Fluid Density (kg/m^3):', 'Water/Gas Interface Tension
(N/m):','Fluid Viscosity (Pa.s):','Ambiant Pressure (kPa):','Polytropic
Index'};
        namec='Model Constants - Single Values';
        nlinesc=1;
        defc={'10','200','0.5','1060','0.34','10','0.078','1e-
9','2','1000','0.072','0.001','101.3','1.095'};
        options.Resize='on';
        options.Windowstyle='normal';
        const=inputdlg(promptc,namec,nlinesc,defc,options);


        simconst.cyc=[(str2num(const{1,1}))];
        simconst.pressure=[(str2num(const{2,1}))*10^3];
        simconst.phi=[(str2num(const{3,1}))];
        simconst.rho2=[(str2num(const{4,1}))];
        simconst.p_ratio=[(str2num(const{5,1}))];
        simconst.h=[(str2num(const{6,1}))*10^-6];
        simconst.L=[(str2num(const{7,1}))];
        simconst.dt=[(str2num(const{8,1}))];
        simconst.tdx=[(str2num(const{9,1}))];
        simconst.rho1=[(str2num(const{10,1}))];
        simconst.rho3=[(str2num(const{10,1}))]; %assuming mediums 1 and 3
in doinikov model
        simconst.sigma_w=[(str2num(const{11,1}))];
        simconst.eta=[(str2num(const{12,1}))];
        simconst.p0=[(str2num(const{13,1}))*10^3];
        simconst.gamma=[(str2num(const{14,1}))];

        %Dialogue box for Variables
```

```
        promptv={'Enter Bubble Radius (μm):','Distance to Wall (Multiple of
R0):','Buckling Radius (Multiple of R0):',...
            'Shell elasticity (N/m):','Shell Viscosity (Pa.s):','Pulse
Centre Frequency (MHz)'};

        namev='Model Variables - Can be multiples or ranges';
        nlinesv=1;

        defv={'2','1','1','0.51','0.72e-8','2'};
        varib=inputdlg(promptv,namev,nlinesv,defv);


        simvar.R0=[(str2num(varib{1,1}))*10^-6];
        simvar.d=[(str2num(varib{2,1}))];
        simvar.buckling=[(str2num(varib{3,1}))];
        simvar.chi=[(str2num(varib{4,1}))];
        simvar.kappa_s=[(str2num(varib{5,1}))];
        simvar.centfreq=[(str2num(varib{6,1}))*10^6];

        %pulse creation

        for k=1:length(simvar.centfreq)
            plength{k}=simconst.cyc/simvar.centfreq(k);
            time{k}=0:simconst.dt:plength{k};

p{k}=simconst.pressure*(cos(2*pi*simvar.centfreq(k)*time{k}+simconst.phi*pi
));
            gauss{k}=gausswin(length(p{k}));
            p{k}=p{k}.*gauss{k}';
            plengthmax(k)=max(plength{k});
        end
        plengthmax=max(plengthmax);
        tmax=0:simconst.dt:plengthmax;
        mid=tmax(ceil(end/2));
        midind=find(tmax==mid);
        Pulse=zeros(length(simvar.centfreq),length(tmax));
        for k=1:length(simvar.centfreq)
            startind(k)=floor(midind-(length(time{k}))/2);
        end
        for k=1:length(simvar.centfreq)
            Pulse(k,startind(k)+1:startind(k)+length(time{k}))=p{k};
        end


        pad=zeros(floor(1.5*length(tmax)),length(simvar.centfreq)); %zeros
1.3 times the length of pulse
        pad(((length(pad))/2)-(length(tmax)/2):((length(pad))/2)-
(length(tmax)/2)-1+(length(tmax)),:)=Pulse';
        tpad=0:simconst.dt:(1.5*plengthmax);

        pulse(:,1)=tpad;
        pulse(:,2:(length(simvar.centfreq))+1)=pad;


        dat=pulse;
        [m n]=size(dat);

    end
end
```

9.2.3 Simulation setup for Doinikov Models

```
function [R1 scatp]= simsetup
(input,R0,d,buckling,chi,kappa_s,simconst,modelsel)


%Input is pulse as the output of Modelvariables, must run Modelvariables.m
first

p=input(:,2);
t=input(:,1);

dt=t(2)-t(1);

nt=length(t);
R1=zeros(nt,1)+R0;
dR1=zeros(nt,1);

%% send to solver for determining R and dR

for j=3:nt
    rr=RungeKutta_doinikov(j*dt,[R1(j-1);dR1(j-
1)],dt,p(j),R0,d,buckling,chi,kappa_s,simconst,modelsel);
    R1(j)=rr(1);
    dR1(j)=rr(2);
end

ddR1=[0; diff(dR1)]/dt;

%% find scattered pressure

beta    = simconst.rho2*(simconst.p_ratio/(1-simconst.p_ratio)); % wall
material properties


scatp=((simconst.rho1/simconst.L)*(R1.^2.*ddR1+2*R1.*dR1.^2))...
    *((4*beta*simconst.rho3)/((simconst.rho1 +beta)*(beta+simconst.rho3)));

pause(0.01);

end
```

9.2.4 Simulation setup for Marmottant models

```
function [R1 scatp]= sim_RP_marm
(input,R0,buckling,chi,kappa_s,simconst,modelsel)

% simulation setup for the Marmottant variations of model

p=input(:,2);
t=input(:,1);

dt=t(2)-t(1);

nt=length(t);
R1=zeros(nt,1)+R0;
dR1=zeros(nt,1);

%Send to Runge Kutta solver

for j=3:nt
    rr=RungeKutta_marm(j*dt,[R1(j-1);dR1(j-
1)],dt,p(j),R0,buckling,chi,kappa_s,simconst,modelsel);
    R1(j)=rr(1);
    dR1(j)=rr(2);
end
ddR1=[0; diff(dR1)]/dt;

%determine scattered pressure

scatp=simconst.rho1/simconst.L*(R1.^2.*ddR1+2*R1.*dR1.^2);

pause(0.01);

end
```

9.2.5 Runge-Kutta setup – Doinikov elastic wall model

```
function
r=RungeKutta_doinikov(t0,r0,dt,p,R0,d,buckling,chi,kappa_s,simconst,modelse
l)
%this function carry out 1-step Runge-Kutta method to solve the ODE defined
%in RPNNP
%t0: the initial time point
%r0: the intial condition including radius and its derivative at t0
%R0: the equilibrim radius, different from r0
%dt: time step
%p:  acoustic pressure at t0


k1=dt*doinikov_model(t0,r0,p,dt,R0,d,buckling,chi,kappa_s,simconst,modelsel
);
k2=dt*doinikov_model(t0+dt/2,r0+k1/2,p,dt,R0,d,buckling,chi,kappa_s,simcons
t,modelsel);
k3=dt*doinikov_model(t0+dt/2,r0+k2/2,p,dt,R0,d,buckling,chi,kappa_s,simcons
t,modelsel);
k4=dt*doinikov_model(t0+dt,r0+k3,p,dt,R0,d,buckling,chi,kappa_s,simconst,mo
delsel);

r=r0+(k1+2*k2+2*k3+k4)./6;
```

9.2.6 Runge-Kutta setup – Marmottant model

```
function
r=RungeKutta_marm(t0,r0,dt,p,R0,buckling,chi,kappa_s,simconst,modelsel)


%this function carry out 1-step Runge-Kutta method to solve the ODE defined
%in RPNNP
%t0: the initial time point
%r0: the intial condition including radius and its derivative at t0
%R0: the equilibrim radius, different from r0
%dt: time step
%p:  acoustic pressure at t0
%omega: central frequency of insonation

k1=dt*RP_Mammotant_JC(t0,r0,p,R0,buckling,chi,kappa_s,simconst,modelsel);
k2=dt*RP_Mammotant_JC(t0+dt/2,r0+k1/2,p,R0,buckling,chi,kappa_s,simconst,mo
delsel);
k3=dt*RP_Mammotant_JC(t0+dt/2,r0+k2/2,p,R0,buckling,chi,kappa_s,simconst,mo
delsel);
k4=dt*RP_Mammotant_JC(t0+dt,r0+k3,p,R0,buckling,chi,kappa_s,simconst,models
el);

r=r0+(k1+2*k2+2*k3+k4)./6;
end
```

9.2.7 Time point calculator for Radius using Doinikov model

```
function
r1=doinikov_model(t0,r0,p,dt,R0,d,buckling,chi,kappa_s,simconst,modelsel)


r=r0(1);
dr=r0(2);

c0      = 1580;      % speed of sound
a       = 0.1976*R0; % van der waals radius of bubble, see paper
beta    = simconst.rho2*(simconst.p_ratio/(1-simconst.p_ratio)); % wall
material properties
d       = d*R0;      % distance to wall, in terms of bubble radii

z1=(simconst.rho1-beta)/(simconst.rho1+beta); %terms from paper so I don't
have to write them continuously
z2=(beta-simconst.rho3)/(beta+simconst.rho3);


%% --- Marmottant et al. version of Rayleigh Plesset ---

%
r_buckling=buckling*R0; %buckling radius as a function of R0
s_breakup = 0.13;
% s_breakup=1; %resistant bubble
s_ruptured = simconst.sigma_w;
r_breakup = r_buckling*sqrt(1+(s_breakup/chi));
r_ruptured = r_buckling*sqrt(1+(simconst.sigma_w/chi));

if r <= r_buckling % This is Sigma(R)
    sigmaR = 0;
elseif r>= r_breakup
    sigmaR = s_ruptured;
else
    sigmaR = chi*(((r^2)/(r_buckling^2))-1);
end


if R0 <= r_buckling   % This is Sigma(R0)
    sigmaR0 = 0;
elseif R0>= r_breakup
    sigmaR0 = s_ruptured;
else
    sigmaR0 = chi*(((R0^2)/(r_buckling^2))-1);
end
rho1=simconst.rho1;
p0=simconst.p0;

gamma=simconst.gamma;
sigma_w=simconst.sigma_w;
eta=simconst.eta;
h=simconst.h;

if modelsel==1
```

```
    ddr=(((1/rho1)*((p0+(2*sigmaR0/R0))*((r/R0)^-(3*gamma))*(1-
(((3*gamma)/c0)*dr))...
        -p0-p-((2*sigmaR)/r)-((4*eta*dr)/r)-((4*kappa_s*dr)/(r^2))))...
        -((3*(dr^2)/2)*(1-z1*((2*r)/(3*d))-
z2*((2*r)/(3*(d+h)))+z1*z2*((2*r)/(3*h)))))...
        /(r*(1-z1*(r/(2*d))-z2*(r/(2*(d+h)))+z1*z2*(r/(2*h))));


elseif modelsel==2;


    ddr=(((1/rho1)*((p0+(2*sigma_w/R0))*((r/R0)^-(3*gamma))*(1-
(((3*gamma)/c0)*dr))...
        -p0-p-((2*sigma_w)/r)-4*chi*((1/R0)-(1/r))-((4*eta*dr)/r)-
((4*kappa_s*dr)/(r^2))))...
        -((3*(dr^2)/2)*(1-z1*((2*r)/(3*d))-
z2*((2*r)/(3*(d+h)))+z1*z2*((2*r)/(3*h)))))...
        /(r*(1-z1*(r/(2*d))-z2*(r/(2*(d+h)))+z1*z2*(r/(2*h))));

end

r1= [dr; ddr];

end
```

9.2.8 Time point calculator for Radius using the Marmottant Model

```
function r1 =
RP_Mammotant_JC(t0,r0,p,R0,buckling,chi,kappa_s,simconst,modelsel)

r=r0(1);
dr=r0(2);

c0      = 1580;      % speed of sound
rho1    = simconst.rho1;      % density surrounding medium
eta     = simconst.eta;    % viscosity
p0      = simconst.p0;   % atmospheric pressure
gamma   = simconst.gamma;     % ratio of heat capacity at constant pressure
and constant volume
sigma_w = simconst.sigma_w;     % free surface tension


%% --- Marmottant et al. version of Rayleigh Plesset ---


r_buckling=buckling*R0;
s_breakup = 0.13;
% s_breakup = 1;
% s_breakup = 0;
s_ruptured = sigma_w;

if s_breakup==1
r_breakup = r_buckling*sqrt(1+(s_breakup/chi));

else
    r_breakup = r_buckling*sqrt(1+(s_breakup/chi));
end

r_ruptured = r_buckling*sqrt(1+(sigma_w/chi));


if r <= r_buckling
    s_R = 0;

elseif r>= r_breakup
    s_R = s_ruptured;

else
    s_R = chi*(((r^2)/(r_buckling^2))-1);

end

if R0 <= r_buckling
    sigmaR0 = 0;
elseif R0>= r_breakup
    sigmaR0 = s_ruptured;
else
    sigmaR0 = chi*(((R0^2)/(r_buckling^2))-1);
end

if  modelsel==3;
```

```
    ddr = ((1/rho1)*(((p0+((2*sigmaR0)/R0))*((r/R0)^-(3*gamma))*(1-
(((3*gamma)/c0)*dr))).../r;
        -p0-((2*s_R)/r)-((4*eta*dr)/r)-((4*kappa_s*dr)/(r^2))-p)-
((3/2)*(dr^2)))/r;



    %% Using the De Jong variation of the shell properties term. Infinite
elastic state valid for small oscillations
elseif modelsel==4;

    ddr = ((1/rho1)*(((p0+((2*sigma_w)/R0))*((r/R0)^-(3*gamma))*(1-
(((3*gamma)/c0)*dr))).../r;
        -p0-((2*sigma_w)/r)-4*chi*((1/R0)-(1/r))-((4*eta*dr)/r)-
((4*kappa_s*dr)/(r^2))-p)-((3/2)*(dr^2)))/r;

end

r1= [dr; ddr];
end
```